



INSTITUTE
OF
NAVAL ARCHITECTURE
AND
OCEAN ENGINEERING



Polish Maritime Research

No 1 (109) 2021
Vol. 28

ADDRESS OF PUBLISHER
& EDITOR'S OFFICE:

GDAŃSK UNIVERSITY
OF TECHNOLOGY

Institute
of Naval Architecture
and Ocean Engineering
G. Narutowicza 11/12
80-233 Gdańsk, POLAND

EDITORIAL STAFF:

Wiesław Tarełko
| Editor in Chief
Janusz Kozak
| Deputy Editors-in-Chief
Wojciech Litwin
| Deputy Editors-in-Chief

Price:
single issue: 25 PLN

Prices for abroad
single issue:
- in Europe EURO 15
- overseas USD 20

WEB:
pg.edu.pl/pmr

e-mail : pmr@pg.edu.pl

ISSN 1233-2585

CONTENS

4	Hossein Tahmasvand, Hamid Zeraatgar <i>A COMBINED METHOD TO PREDICT IMPACT PRESSURE ON PLANING CRAFT</i>
16	Sebastian Bielicki <i>PREDICTION OF SHIP MOTIONS IN IRREGULAR WAVES BASED ON RESPONSE AMPLITUDE OPERATORS EVALUATED EXPERIMENTALLY IN NOISE WAVES</i>
28	Boyang Li, Rui Zhang, Yajing Li, Baoshou Zhang, Chao Guo <i>STUDY OF A NEW TYPE OF FLETTNER ROTOR IN MERCHANT SHIPS</i>
42	Ewelina Ciba <i>HEAVE MOTION OF A VERTICAL CYLINDER WITH HEAVE PLATES</i>
48	Wenbin Lai, Yonghe Xie, Detang Li <i>NUMERICAL STUDY ON THE OPTIMIZATION OF HYDRODYNAMIC PERFORMANCE OF OSCILLATING BUOY WAVE ENERGY CONVERTER</i>
59	Zhaoyi Zhu, Xiaowen Li, Qinglin Chen, Yingqiang Cai, Yunfeng Xiong <i>SIMULATIONS AND TESTS OF COMPOSITE MARINE STRUCTURES UNDER LOW-VELOCITY IMPACT</i>
72	Przemysław Król <i>HYDRODYNAMIC STATE OF ART REVIEW: ROTOR – STATOR MARINE PROPULSOR SYSTEMS DESIGN</i>
83	Fatih Okumuş, Araks Ekmekçioğlu, Selin Soner Kara <i>MODELLING SHIPS MAIN AND AUXILIARY ENGINE POWERS WITH REGRESSION-BASED MACHINE LEARNING ALGORITHMS</i>
97	Valerii Kuznetsov, Boris Dymo, Svitlana Kuznetsova, Mykola Bondarenko, Andrii Voloshyn <i>IMPROVEMENT OF THE CARGO FLEET VESSELS POWER PLANTS ECOLOGICAL INDEXES BY DEVELOPMENT OF THE EXHAUST GAS SYSTEMS</i>
105	Mengqi Cui, Yingwei Lu, Jiahao He, Lei Ji, Hui Wang, Shaojun Liu <i>A COMPARATIVE LIFE CYCLE ASSESSMENT OF MARINE DESOX SYSTEMS</i>
116	Jerzy Girtler, Jacek Rudnicki <i>THE MATTER OF DECISION-MAKING CONTROL OVER OPERATION PROCESSES OF MARINE POWER PLANT SYSTEMS WITH THE USE OF THEIR MODELS IN THE FORM OF SEMI-MARKOV DECISION-MAKING PROCESSES</i>
127	Ryszard Buczkowski, Bartłomiej Żyliński <i>FINITE ELEMENT FATIGUE ANALYSIS OF UNSUPPORTED CRANE</i>

**ADDRESS OF PUBLISHER
& EDITOR'S OFFICE:**

**GDAŃSK UNIVERSITY
OF TECHNOLOGY**

**Institute
of Naval Architecture
and Ocean Engineering
G. Narutowicza 11/12
80-233 Gdańsk, POLAND**

- 136 Xiaofeng Xu, Deqing Cui, Yun Li, Yingjie Xiao**
*RESEARCH ON SHIP TRAJECTORY EXTRACTION BASED ON MULTI-
ATTRIBUTE DBSCAN OPTIMISATION ALGORITHM*
- 149 Zaopeng Dong, Yang Liu, Hao Wang, Tao Qin**
*METHOD OF COOPERATIVE FORMATION CONTROL FOR UNDERACTUATED
USVS BASED ON NONLINEAR BACKSTEPPING AND CASCADE SYSTEM THEORY*
- 163 Józef Lisowski**
*COMPUTATIONAL INTELLIGENCE IN MARINE CONTROL ENGINEERING
EDUCATION*

Editorial

POLISH MARITIME RESEARCH is the scientific journal with a worldwide circulation. This journal is published quarterly (four times a year) by Gdansk University of Technology (GUT). On September, 1994, the first issue of POLISH MARITIME RESEARCH was published. The main objective of this journal is to present original research, innovative scientific ideas, and significant findings and application in the field of :

Naval Architecture, Ocean Engineering and Underwater Technology,

The scope of the journal covers selected issues related to all phases of product lifecycle and corresponding technologies for offshore floating and fixed structures and their components.

All researchers are invited to submit their original papers for peer review and publications related to methods of the design; production and manufacturing; maintenance and operational processes of such technical items as:

- all types of vessels and their equipment,
- fixed and floating offshore units and their components,
- autonomous underwater vehicle (AUV) and remotely operated vehicle (ROV).

We welcome submissions from these fields in the following technical topics:

- ship hydrodynamics: buoyancy and stability; ship resistance and propulsion, etc.,
 - structural integrity of ship and offshore unit structures: materials; welding; fatigue and fracture, etc.,
 - marine equipment: ship and offshore unit power plants: overboarding equipment; etc.
-

Scientific Board

Chairman : Prof. JERZY GIRTLEK - Gdańsk University of Technology, Poland

Vice-chairman : Prof. CARLOS GUEDES SOARES, Universidade de Lisboa, Lisbon, Portugal

Vice-chairman : Prof. MIROSŁAW L. WYSZYŃSKI - University of Birmingham, United Kingdom

Prof. POUL ANDERSEN
Technical University of Denmark
Kongens Lyngby
Denmark

Prof. STOJCE DIMOV ILCEV
Durban University of Technology
Durban
South Africa

Prof. JERZY MERKISZ
Poznan University of Technology
Poznan
Poland

Prof. JIAHN-HORNG CHEN
National Taiwan Ocean University
Keelung
Taiwan

Prof. YORDAN GARBATOV
Universidade de Lisboa,
Lisbon
Portugal

Prof. VALERI NIEKRASOV
Admiral Makarov National University
of Shipbuilding
Mikolaiv
Ukraine

Prof. VINCENZO CRUPI
University of Messina
Messina
Italy

Prof. STANISŁAW GUCMA
Maritime University of Szczecin
Szczecin
Poland

Prof. SERHIY SERBIN
Admiral Makarov National
University of Shipbuilding
Mikolaiv
Ukraine

Prof. MAREK DZIDA
Gdansk University of Technology
Gdansk
Poland

Prof. ANTONI ISKRA
Poznan University of Technology
Poznan
Poland

Prof. JOZEF SZALA
UTP University of Science and
Technology
Bydgoszcz
Poland

Dr. KATRIEN ELOOT,
Flanders Hydraulics Research,
Antwerpen
Belgium

Prof. JAN KICINSKI
Institute of Fluid-Flow Machinery -
Polish Academy of Sciences
Gdansk
Poland

Prof. HOANG ANH TUAN
Ho Chi Minh City
University of Technology
(HUTECH)
Ho Chi Minh
Vietnam

Prof. ODD MAGNUS FALTINSEN
Norwegian University of Science and
Technology
Trondheim
Norway

Prof. ZBIGNIEW KORCZEWSKI
Gdansk University of Technology
Gdansk
Poland

Prof. TADEUSZ SZELANGIEWICZ
Maritime University of Szczecin
Szczecin
Poland

Prof. MASSIMO FIGARI
University of Genova
Genova
Italy

Prof. JOZEF LISOWSKI
Gdynia Maritime University
Gdynia
Poland

Prof. DRACOS VASSALOS
University of Strathclyde
Glasgow
United Kingdom

Prof. HASSAN GHASSEMI
Amirkabir University of Technology
Tehran
Iran

Prof. JERZY EDWARD MATUSIAK
Aalto University
Espoo
Finland

A COMBINED METHOD TO PREDICT IMPACT PRESSURE ON PLANING CRAFT

Hossein Tahmasvand

Amirkabir University of Technology, Iran

Hamid Zeraatgar*

Amirkabir University of Technology, Iran

* Corresponding author: hamidz@aut.ac.ir (H. Zeraatgar)

ABSTRACT

Prediction of the pressure distribution on a planing craft in waves deeply affects its structural design and safe operation. In this paper, the possibility of pressure prediction for the planing craft in waves is studied. A combined method is formulated by which craft motions in waves are computed using a 2.5D method, and the impact pressure is anticipated by the equivalent wedge method. Experiments are conducted to record the vertical acceleration and pressure time trends on a model. Comparing the results of the combined method with the experiments indicates that this approach successfully predicts the heave and pitch motions and the time evolution of the acceleration and pressure. The method presents good estimations for the peaks of the acceleration and pressure. Using the combined method, a parametric study on maximum peak acceleration and pressure is also conducted for various forward velocities and wave heights. It has been shown that the combined method is a fast and reliable tool for maximum peak pressure prediction. The method may be employed for structural design and optimization.

Keywords: impact pressure; acceleration; 2.5D method; equivalent wedge method; planing craft.

INTRODUCTION

Accurate prediction of the pressure distribution on a planing craft plays a major role in the design of a safe structure. Both instantaneous impact pressure and mean force are important for a structure exposed to the impact of water. A very sharp peak of short duration is the most important feature of the impact pressure and acceleration. The impact totally disappears in heave and pitch motions. Therefore, when a method correctly predicts the motions, it does not guarantee that the pressure distribution, especially the peak pressure, has been evaluated properly.

Various methods such as experimental, semi-empirical, numerical and computational fluid dynamics (CFD) methods

have been employed to analyse the dynamics of planing craft in waves. Fridsma [1] experimentally examined the motions of different prismatic planing models in regular waves. Savitsky et al. [2] presented relations for added resistance, vertical acceleration, and buoyancy force in the wave, using the results of Fridsma [1]. Martin [3] introduced a linear model for the dynamics of planing craft in the frequency domain. The linear model presented by Martin was the first model utilised for the dynamics of planing craft. Zarnick [4], based on Martin's model, developed a nonlinear mathematical model for the planar motion of planing craft in the time domain. Many researchers, including Hicks et al. [5], Akers [6], Van Deyzen [7], Sayeed [8], Ruscilli [9], and Pennino [10], have attempted to improve the Zarnick model.

Based on the reviewed literature, the 2.5D method (developed by Zarnick [4]) is a fast and reliable means for the prediction of the heave and pitch motions and the vertical acceleration of planing craft in waves [7]. The 2.5D method computes the motion in waves based on momentum changes and does not provide an estimation of the pressure. As far as the pressure distribution on the planing craft is concerned, Von Karman [11] and Wagner [12] presented an analytical method based on potential theory for the two-dimensional (2D) wedge in water entry. Many researchers developed Wagner's method further [13, 14]. They only estimated the pressure on 2D wedges in water entry, and few studies have addressed the pressure distribution on a planing craft in waves. Smiley [15, 16] recorded the pressure distribution on V-shaped planing craft having a range of dead-rise angles at several trim angles in calm water. Gray et al. [17], according to the results of Smiley, developed a regression formula for three-dimensional pressure distribution on a V-shaped prismatic planing craft. Rosen and Garne [18] experimentally measured the bottom pressure on a high-speed craft in waves. Rosen [19] presented an interpolation method for calculating the pressure distribution in waves. Camilleri et al. [20] conducted full-scale trials on a high-speed craft in waves and studied the pressure, accelerations, and strain time trends.

Despite providing valuable insights into the pressure distribution on planing craft by the experimental and numerical methods, the analytical/regression approach is more attractive to engineers for structural design and optimisation. Several regression formulae based on experimental, analytical, and numerical methods were introduced to estimate the impact pressure on planing craft. They are extensively applied for structural design in the rules of classification societies [21]. Allen et al. [22] presented a regression method to calculate the impact pressure for structural design. Razola et al. [21] re-formulated and evaluated the impact pressure using the Allen method [22]. They combined the 2.5D method and a pressure shape function modelling technique. Ghadimi et al. [23] presented a mathematical model based on 2D+t theory for predicting the pressure distribution of a hard-chine planing craft in planing and semi-planing modes. Ghasemi et al. [24] developed a mathematical model based on the Savitsky model to study the performance of stepped planing hulls. Jones and Allen [25] proposed the "equivalent wedge method" to estimate the pressure distribution for given motion in waves. The equivalent wedge method includes the three-dimensional flow effect. It seems that the equivalent wedge method is more realistic than the shape function technique. The above review indicates that few analytical/regression methods of pressure estimation on planing hulls are available, while it is crucial for structural design. The available methods are also under development to better comply with the real sea environment.

Following Razola et al.'s [21] approach, this study introduces pressure calculation on planing craft in waves by combining the 2.5D method and the equivalent wedge method. The 2.5D method is a reliable method for motion and acceleration prediction. One should note that a good estimation of acceleration by the 2.5D method does not necessarily

mean a good estimation of the pressure distribution on the structure. On the other hand, the equivalent wedge method is a robust method to estimate the pressure distribution, if motion as input is appropriately calculated. That is why a combination of the 2.5D method and the equivalent wedge method is employed.

In this study, a computer code is initially developed based on the 2.5D method. Then, the 2.5D method is combined with the equivalent wedge method to calculate the pressure distribution on any points on the craft. Furthermore, a model test is conducted to record accelerations and pressure for validation of the combined method results. Finally, using the combined method, a parametric study is carried out on the maximum peak acceleration and the maximum peak pressure of a planing craft.

THE COMBINED METHOD FOR CALCULATING THE IMPACT PRESSURE

In this section, a draft of the 2.5D method is first presented. Then, the equivalent wedge method, proposed by Jones and Allen [25], is reviewed. Finally, these two methods are combined.

REVIEW OF THE 2.5D METHOD

Having considered practical planing craft lengths and the sea wavelengths, it is assumed that the wavelengths are generally larger than the craft length and the wave slopes are small. Additionally, craft are V-shaped, hard chine with constant forward speed encountering regular head waves.

Fig. 1 shows a schematic of a planing craft in the wave. Two coordinate systems are considered; an earth-fixed coordinate system (x, z) that represents craft forward (x -axis) and downward (z -axis) motions, and a body-fixed coordinate system (ξ, ζ) where ξ is parallel to the keel-line, and ζ is perpendicular to it. Thrust force (T), normal force (N), drag force (D) and weight of craft (W) are the main forces exerted on the craft. The normal force is the sum of the hydrodynamic and buoyancy forces.

By the use of Newton's second law in the earth-fixed coordinate system, the following equations of motions are obtained for two degrees of freedom pitch (θ) and heave (z_{CG}):

$$M\ddot{z}_{CG} = T_z - N \cos\theta + D \sin\theta + W \quad (1)$$

$$I\ddot{\theta} = N x_c - D x_d + T x_p \quad (2)$$

where M and I are the craft mass and moment of inertia, respectively. x_c , x_d and x_p are the vertical distances of the forces N , D and T from the centre of gravity, respectively.

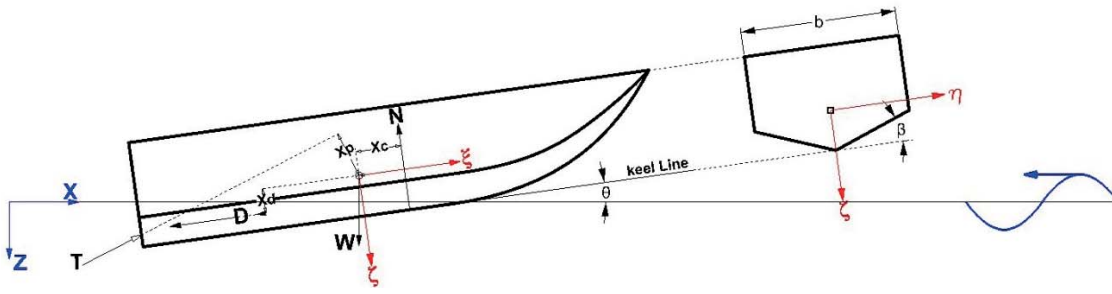


Fig. 1. Definition of coordinate systems and forces on a craft

According to the 2.5D method, the planing craft forces in waves are the sum of a series of two-dimensional forces on its 2D wedge sections. The hydrodynamic force perpendicular to the unit length of each 2D section, f , is calculated from the following equation [4]:

$$f = - \left\{ \frac{D}{Dt} (m_a V) + C_{D,C} \rho b V^2 \right\} \quad (3)$$

where m_a , $C_{D,C}$, b and V are the added mass coefficient, cross-flow drag coefficient, beam and vertical velocity of each section, respectively. The cross-flow drag coefficient is $C_{D,C} = \cos\beta$ for wedge sections [26], where β is the dead-rise angle. The buoyancy force of a 2D wedge section is a coefficient of the submerged volume relative to the static water level surface as $f_B = -\rho g A$, where a is the buoyancy force coefficient ($a=0.5$ [26]), and A is the submerged area of the wedge section.

The instantaneous hydro-mechanic forces exerted on the wetted length (l) of the craft are an integration of the instantaneous forces on the 2D sections along the wetted length:

$$F_z(t) = \int_l f \cos\theta d\xi + \int_l f_B d\xi \quad (4)$$

The hydro-mechanic moment about CG is also calculated by integrating the product of the normal force per unit length and the corresponding moment arm along the wetted length:

$$F_\theta(t) = \int_l f(\xi, t) \xi d\xi + \int_l f_B \xi d\xi \quad (5)$$

By assuming $x_c = 0$ and ignoring $D \sin \theta$, g due to relatively small θ , two coupled non-linear differential equations are concluded:

$$(M + M_a \cos^2\theta) \ddot{z}_{CG} - (Q_a \cos\theta) \ddot{\theta} = F'_z + W \quad (6)$$

$$(-Q_a \cos\theta) \ddot{z}_{CG} + (I + I_a) \ddot{\theta} = F'_\theta \quad (7)$$

where M_a , Q_a , and I_a are the added mass of the craft, pitch-induced added mass to heave, and pitch-added moment of inertia, respectively. Finally F'_z , and F'_θ are calculated as follows:

$$F'_z = F_z - \left((M_a \cos^2\theta) \ddot{z}_{CG} - (Q_a \cos\theta) \ddot{\theta} \right) \quad (8)$$

$$F'_\theta = F_\theta - \left((-Q_a \cos\theta) \ddot{z}_{CG} + I_a \ddot{\theta} \right) \quad (9)$$

Equations (8) and (9) are solved by using the Runge-Kutta integration.

REVIEW OF THE EQUIVALENT WEDGE METHOD

In the equivalent wedge method, a 3D planing hull is divided into a set of incremental wedge portions. It is assumed that each portion is a part of an equivalent prismatic wedge, which has the same width, dead-rise angle, and trim. The parameters such as submerged depth and dead-rise angle are determined in the middle section of the portion. The centreline pressure distribution of the prismatic wedge is calculated using the trim, dead-rise angle, beam, and wetted length. The pressure distribution on the centreline of the portion is a portion of the pressure distribution of the prismatic wedge, as seen in Fig. 2. The transverse pressure distribution is computed using the centreline pressure.

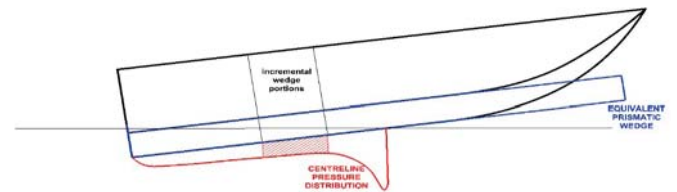


Fig. 2. Pressure distribution on the centreline of an equivalent wedge

The prismatic wedge is composed of chine-wet and chine-dry sections (see Fig. 3). The centreline pressure distribution of the prismatic wedge in the wet-chine sections of the prismatic wedge is estimated as follows [17]:

$$\frac{P_c}{\frac{1}{2}\rho V^2} = \left[1 - \left(\frac{\mu - \cos\theta}{1 - \mu\cos\theta + \sin\theta\sqrt{1-\mu^2}} \right) \right] \cos\beta \quad (10)$$

where θ , β and V are the trim angle, dead-rise angle and vertical relative velocity of the equivalent wedge, and μ is equivalent to the longitudinal coordinate of a section ($-1 \leq \mu \leq 1$). $\mu = -1$, $\mu = \cos\theta$ and $\mu = 1$ represent sections of the transom, maximum pressure and fore end of the waterline of the prismatic wedge, respectively.

The centreline pressure on the dry-chine sections of the prismatic wedge is obtained by averaging the pressure distribution predicted by Eq. (10) with the centreline distribution predicted by immersing wedge theory (Eq. (12)).

The transverse pressure distribution is computed using the centreline pressure. It was presented in [17] for the section with wet-chine as follows:

$$\frac{P}{P_c} = 1 - \left(\frac{\cos\varepsilon}{1 + \sin\varepsilon} \right)^{2n} \quad (11)$$

where $n = (\pi - 2\beta)/\pi$, P_c is the pressure on the keel, and ε is equivalent to the transverse coordinate of a point on a section ($0 \leq \varepsilon \leq \pi/2$). $\varepsilon = \pi/2$ and $\varepsilon = 0$ represent $\eta = 0$ and $\eta = C$, respectively. The transverse pressure distribution for dry-chine sections is computed as follows [17]:

$$\frac{P}{\frac{1}{2}\rho V^2} = \left[\frac{\pi \cot\alpha}{\sqrt{1 - (\eta/w)}} - \frac{1}{(w/\eta)^2 - 1} \right] \sin^2\theta \quad (12)$$

$$\alpha = \tan^{-1} \left(\frac{\pi}{2} \sqrt{\frac{\sin^2\beta + K^2 \tan^2\theta}{K^2 - 2K \sin^2\beta - K^2 \sin^2\beta \tan^2\theta}} \right) \quad (13)$$

$$K \approx \frac{\pi}{2} \left(1 - \frac{3 \tan^2\beta \cos\beta}{1.7\pi^2} - \frac{\tan\beta \sin^2\beta}{3.3\pi} \right) \quad (14)$$

$$\frac{\eta}{2b} = k \cos\beta \int_{\varepsilon}^{\pi/2} [(1 + \sin\varepsilon)^n (\cos\varepsilon)^{1-n} \sin\varepsilon] d\varepsilon \quad (15)$$

$$\frac{1}{k} = 4 \cos\beta \int_0^{\pi/2} [(1 + \sin\varepsilon)^n (\cos\varepsilon)^{1-n} \sin\varepsilon] d\varepsilon \quad (16)$$

where ρ and w are the water density and half of the wetted width. w is presented as follows:

$$\frac{w}{c} = \frac{\lambda_t - \xi}{\lambda_t - \lambda_{wc}}, \quad \xi > \lambda_{wc} \quad (17)$$

$$\lambda_{wc} = \lambda_t - \frac{\tan\beta}{\pi \tan\theta} \quad (18)$$

where λ_t and λ_{wc} are the total wetted length and the wetted chine region length relative to the beam, respectively (see Fig. 3).

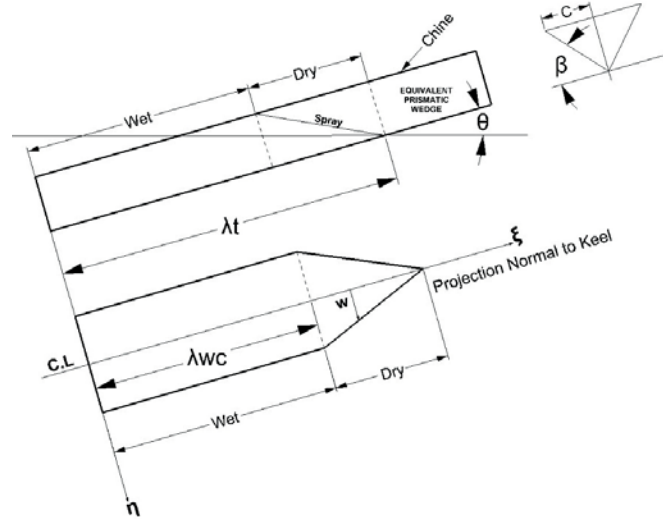


Fig. 3. Equivalent prismatic wedge

THE COMBINED METHOD

A procedure is developed to implement a combination of the 2.5D method and the equivalent wedge method for estimation of the pressure distribution on a planing hull. The procedure is shown in Fig. 4 and a summary of the procedure steps is as follows:

- 1) Planing craft specifications, in a certain regular wave, at given forward speed, are input data to this method.
- 2) The hydrodynamic forces and hydrodynamic moment are calculated as a function of time using Eqs. (8) and (9).
- 3) Accelerations, velocities and displacements are calculated through solving Eqs. (6) and (7) using the Runge-Kutta method,
- 4) Velocities and displacements are substituted into Eq. (10) and Eq. (12) to estimate the pressure distribution.

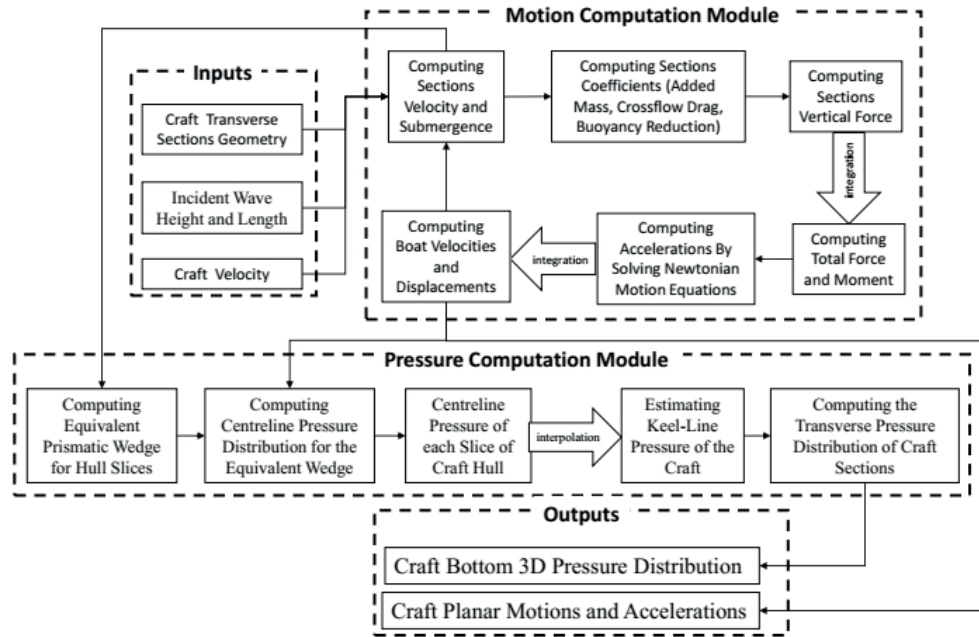


Fig. 4. Procedure of the combined method for the pressure prediction

EXPERIMENTAL SET-UP

To validate the combined method, a set of experiments on a planing craft in waves is conducted in the towing tank of the National Iranian Marine Laboratory (NIMALA) [27]. A planing hull with a hard chine V-shape, variable dead-rise angle and length of 23 meters is chosen for the experiment [28]. A model of 1 m is manufactured based on the main particulars given in Table 1. Fig. 5 shows the body plan and the position of the pressure transducers. Five PCB-102B04 pressure transducers are mounted at specified places on desired sections for recording the hydrodynamic pressure, and a Triaxial mini (5 mg) high sensitivity PCB-356A32 accelerometer is mounted at the centreline of Sec. 2 for recording the vertical acceleration. Following Zeraatgar et al.'s [29] recommendation, the data are recorded at a sampling rate of 25 kHz.

Tab. 1. Main particulars of the planing hull model

Description	Symbol	Value
Length between perpendiculars (m)	LBP	0.936
Moulded breadth at chine (m)	B	0.197
Draft at aft perpendicular (m)	TA	0.064
Draft at fore perpendicular (m)	TF	0.041
Displacement (kg)	Δ	6.5
Longitudinal centre of gravity (m)	LCG	0.372
Vertical centre of gravity (m)	VCG	0.040
Pitch radius of gyration (m)	K_{yy}	0.291

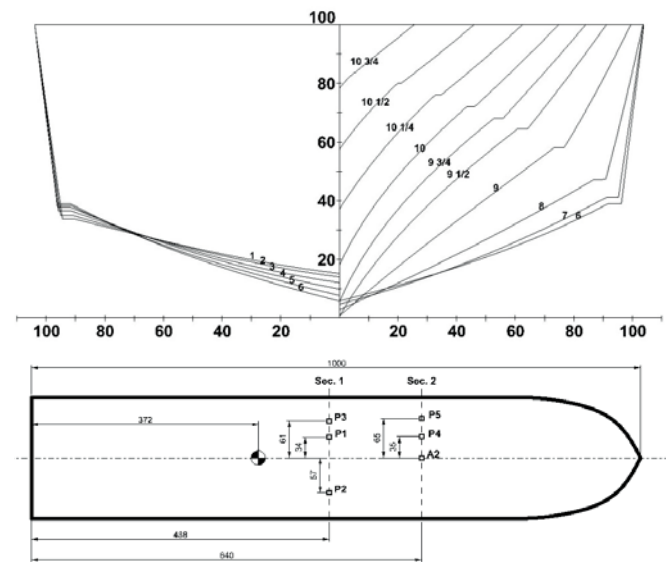


Fig. 5. Body plan of the planing hull model, and the position of pressure transducers on the model (measures are in millimeters)

Experimental Procedure

According to ITTC recommended procedures for seakeeping tests (Procedure 7.5-02-05-04), the model is towed at the intersection of the longitudinal centre of gravity and the thrust line. The model is restrained in surge, sway, roll and yaw and free to pitch and heave (Fig. 6). To adjust the towing direction, first tests are performed in calm water at a speed of 6 m/s to record the rise-up and trim of the model. These are measured as 3.6 cm for rise-up and 3.0 degrees for the trim angle.

Tests are conducted in regular waves having a height of 3.5 cm and wavelength of 300 cm at a speed of 6 m/s. The model under testing is shown in Fig. 7. The pressure and acceleration are recorded in analogue form and transferred

to the signal conditioner to be amplified. The amplifier has three gain factors: 1, 10 and 100. Knowing the approximate pressure in advance, the gain factor of the signal conditioner is appropriately selected. This kind of amplification prevents measurement of low pressure using a pressure transducer with a large measurement range, which may induce large error. The measured pressure is filtered employing the moving average with caution so that no physical peaks are lost.

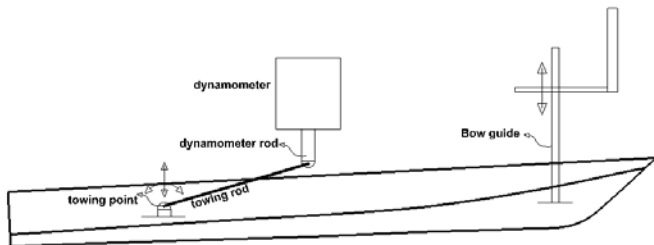


Fig. 6. Towing mechanism



Fig. 7. Model under testing in NIMALA towing tank

RESULTS AND DISCUSSION

VALIDATION OF THE COMBINED METHOD

The model attitude in the calm water recorded in the experiment is compared with the results of the combined method in Table 2. The combined method broadly complies with the experiment.

Table 2. Rise-up and trim of the model, the combined method in comparison with experiment

Title	Rise-up (cm)	Trim (degree)
Experiment	3.6	3.0
Combined method	3.3	2.8
Difference (%)	-8.3	-6.6

Due to the failure of the potentiometer in the experiment for heave and pitch measurement, the combined method results are compared with the available data, Fridsma's [1]

test results in regular waves. Fridsma's A-model, presented in Table 3, is considered for the heave and pitch evaluation of the combined method. In Fig. 8, the heave and pitch of the combined method are compared with Fridsma's results, where C_λ is the wavelength coefficient defined as $C_\lambda = (L/\lambda) [C_\Delta / (L/b)^2]^{1/3}$, C_Δ is the load coefficient defined as $\Delta / (\rho g b^3)$, and Δ , b , L and λ are the displacement, beam, hull length and wavelength, respectively. As can be seen, the results of the combined method are in good agreement with Fridsma's experiment.

Tab. 3. Characteristics of Model A of Fridsma [1]

L (m)	L/b	β (deg)	C_Δ	LCG	K_{yy}	V / \sqrt{L}
1.143	5	20	0.608	0.41L	0.25L	6

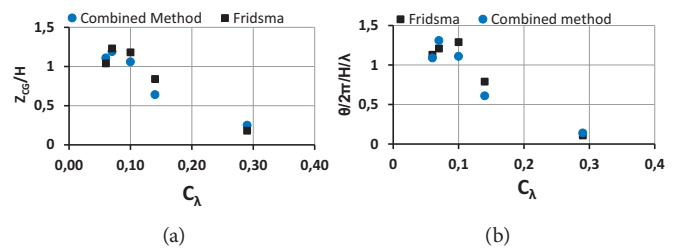


Fig. 8. A comparison of the predicted dimensionless a) heave and b) pitch motions with the experimental data reported by Fridsma [1]

A detailed insight into the validation of the combined method is achieved by comparing the acceleration and pressure with the experiment. A comparison of the vertical acceleration between the combined method and the experiment is shown in Fig. 9. The acceleration trend is almost repeating in each encounter period, which is about 0.37 seconds. In Table 4, an average of 30 acceleration peaks is presented for the combined method and the experiment. The relative differences are -3.6% and +0.44% for the negative and positive peak accelerations, and 9.4% for the average positive peak duration. The low relative differences show that the method accurately anticipates the peaks of accelerations. Therefore, the combined method is regarded as a reliable method for predicting the impact acceleration.

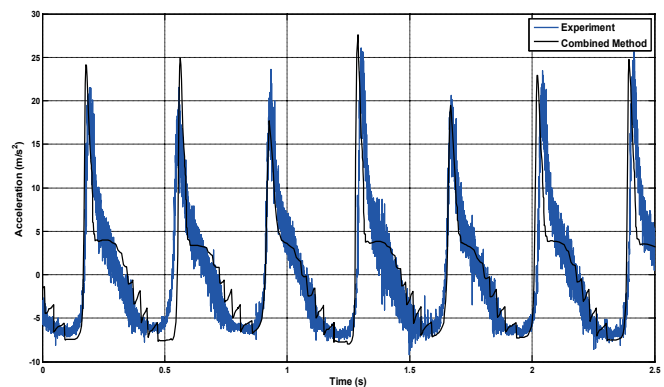


Fig. 9. A comparison between predicted and recorded acceleration at Sec. 2 ($V=6$ m/s, $H=3.5$ cm, $L_w=300$ cm)

Tab. 4. Average of the negative and positive peak acceleration and average of the positive peak duration

Parameter	2.5D	Experiment	Difference %
Ave. of negative peak acc. (m/s ²)	-7.2	-7.0	-3.6
Ave. of positive peak acc. (m/s ²)	22.6	22.5	0.44
Ave. of positive peak duration (s)	0.053	0.048	9.4

The major concern of this study is the prediction of pressure distribution by the combined method, especially the impact pressure. In Fig. 10 and Fig. 11, the predicted pressure at several points on Sec. 1 and Sec. 2 is compared with the experiment. The combined method results and the recorded pressure time trends are both repeating in each encounter period and have the same number of peaks. They both show a high peak pressure and a low peak pressure in each encounter period. The calculated and recorded results show almost the same instant for both peaks. Within an encounter period, between the high peak and low peak and between the low peak and the next high peak, the general trends are almost the same. Hence, it may be concluded that the time trend of the combined method follows the same trend as the experiment.

As observed in Fig. 10 and Fig. 11, the pressure in the experiment is positive during the first part of an encounter period and negative/positive for the second part. The negative pressure most likely happens as the sensor fully emerges. Although the pressure predicted by the combined method is positive during the first part of each encounter period, it returns to zero in the second part of the same period. This is because, in the combined method, it is presumed that the pressure is zero in air.

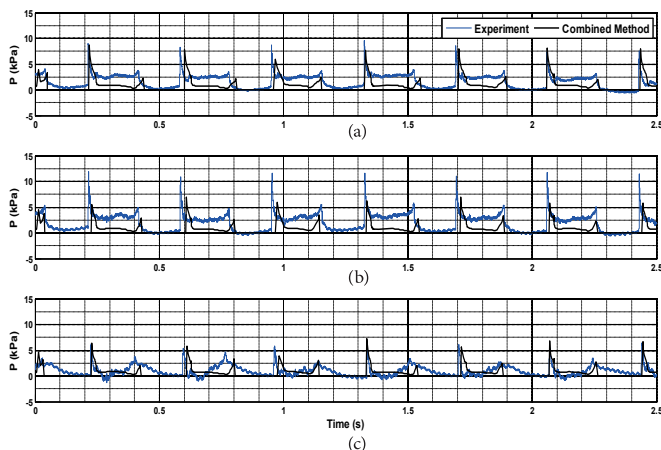


Fig. 10. Comparing predicted pressure by the combined method with the experiment at a) Point#1, b) Point#2, c) Point#3 ($V=6$ m/s, $H=3.5$ cm, $L_w=300$ cm)

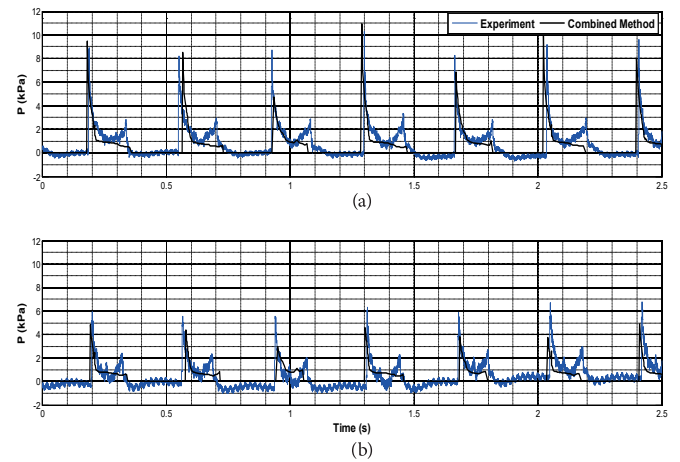


Fig. 11. Comparing predicted pressure by the combined method with the experiment at (a) Point#4, and (b) Point#5 ($V=6$ m/s, $H=3.5$ cm, $L_w=300$ cm)

In Table 5, the averages of high and low peak pressure at five locations are shown in an encounter period. It presents the results of the combined method and the experiment for average pressure and relative differences for the five considered points. The differences of the high peak ranges from +1.3% to -39.2%, while the differences of the low peak range from -15.1% to -66.6%. This means that the combined method tends to have a random error for the high peak, but shows a biased error for the low peak.

The combined method considerably underpredicts the high peak pressure at Sec.1, point #2, as described above. However, for the other points, the differences are not as large as at point #2. Despite this discrepancy, the developed code is utilised for the parametric study.

Tab. 5. The average low and high pressure peaks for the combined method and experiment

Parameter	Combined method	Experiment	Difference %
	Sec. 1, point #1		
Ave. High Peak (kPa)	9.740	8.716	11.7
Ave. Low Peak (kPa)	3.143	3.701	-15.1
Sec. 1, point #2			
Ave. High Peak (kPa)	6.925	11.383	-39.2
Ave. Low Peak (kPa)	2.306	5.160	-55.3
Sec. 1, point #3			
Ave. High Peak (kPa)	5.748	5.674	1.3
Ave. Low Peak (kPa)	2.640	3.640	-27.5
Sec. 2, point #4			
Ave. High Peak (kPa)	10.480	10.280	1.9
Ave. Low Peak (kPa)	1.105	3.306	-66.6
Sec. 2, point #5			
Ave. High Peak (kPa)	4.420	5.777	-23.5
Ave. Low Peak (kPa)	0.777	2.273	-65.8

Tracing of two-peak pressure in one encounter period

Recalling Fig. 10 and Fig. 11, it is observed that two peaks occur, i.e. a high peak and a low peak for an encounter period. For both the experiment and the combined method, the pressure between the high peak and the low peak is positive. However, between the low peak and the next high peak, the combined method returns to positive/zero pressure, while the experiment records positive/negative. The high peak pressure occurs as soon as the water surface passes the sensor. After the sensor is fully submerged, the pressure instantly drops. It further reduces as the chine becomes wet. Increase (decrease) of relative velocity gradually increases (decreases) the pressure. To find out the reason for the low peak, the above conditions have to be traced.

Fig. 12 shows the submergence (H), vertical position of the chine and point #4, time trends of calculated pressure (P) and vertical relative velocity (V) on sensor 4. The vertical relative velocity for the point #4 at the considered condition is always positive. This means that the combined method always has the water entry condition for this case. Let's consider the equation of relative velocity as follows:

$$V = \dot{x}_{CG} \sin\theta - \dot{\theta}\xi + (\dot{z}_{CG} - w_z) \cos\theta \quad (19)$$

where \dot{x}_{CG} is the forward speed of the model (6 m/s for this case) and w_z is the vertical velocity of the wave profile. In Eq. (19), the term $\dot{x}_{CG} \sin\theta$ is always positive and dominant in comparison with the other terms. That is why the relative velocity is always positive for the considered point. Certainly, however, this may not happen for all points on the model.

In Fig. 12, an encounter period is selected to investigate the pressure peaks. In this figure, line t_1 is the beginning of water entry of the sensor, t_2 is the instant of chine wetting, t_3 is the start of chine-wet to be chine-dry and t_4 is the instant when the sensor fully emerges from the water. The high peak occurs at an instant when the sensor is fully immersee in the water. Then, the chine becomes wet at t_2 , and the pressure gradually drops due to the gradual decrease of the relative velocity. The low peak occurs between t_3 and t_4 when the chine becomes dry again. After t_4 , the sensor fully emerges from the water and zero pressure occurs. Analysis of the physical phenomena on the pressure sensor fully supports the two peaks of pressure in one encounter period.

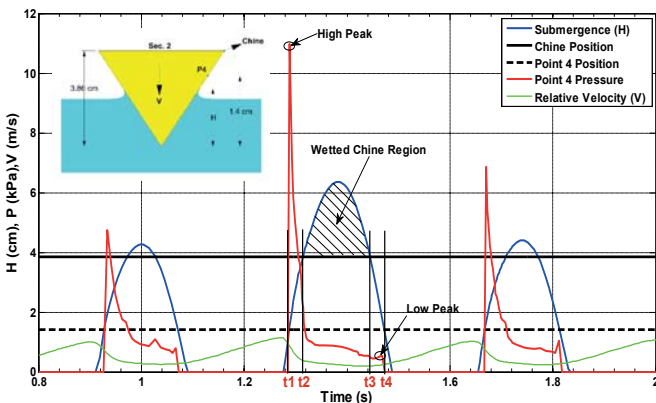


Fig. 12. Time series of submergence, predicted pressure and relative velocity

Parametric study

The fast pressure calculation made possible by the combined method makes it a powerful tool for conducting a parametric study on the acceleration and pressure. A parametric study on the craft specified in Fig. 5 and Table 1 is performed for different forward speeds and wave heights. The considered cases and corresponding running attitudes are presented in Table 6. In addition, Fig. 13 shows the sections and points where the pressure and acceleration are calculated, respectively.

Tab. 6. The considered cases and corresponding running attitudes

No.	H/B	Forward speed (m/s)	Mean trim (deg)	Mean rise-up (cm)
1-1	0.3404	4.0	7.4	1.5
1-2	0.3404	4.5	6.2	1.8
1-3	0.3404	5.0	5.6	2.2
1-4	0.3404	5.5	4.9	2.4
1-5	0.3404	6.0	4.4	2.5
2-1	0.222	5.0	6.2	2.5
2-2	0.167	5.0	6.3	2.5
2-3	0.111	5.0	6.3	2.5

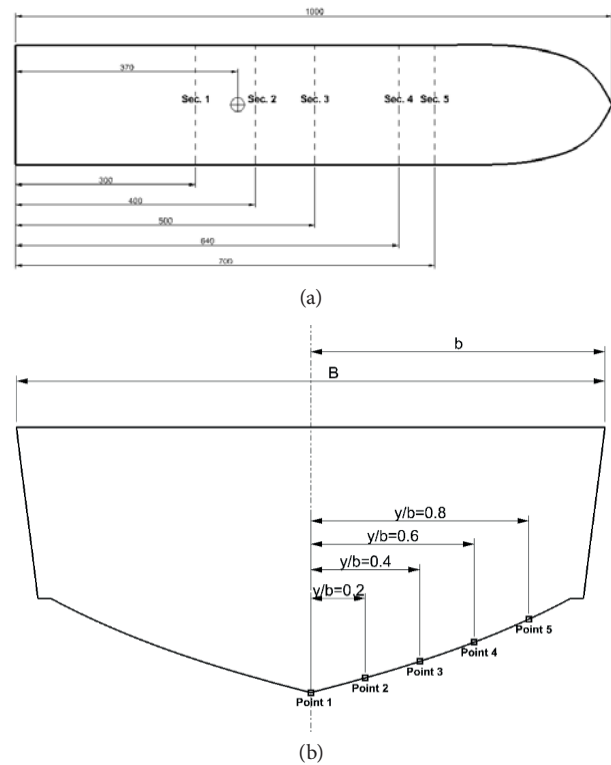


Fig. 13. (a) Longitudinal coordinate of sections and (b) positions of pressure calculation points (measures are in millimeters).

Vertical acceleration

The mean peak acceleration versus Froude number (Fn) are plotted in Fig. 14 for several sections. The term "mean peak" is defined as the average value of ten peaks from a single wave record. All sections show a rapid increase in the maximum peak acceleration as the Froude number increases. For the considered planing hull, a 46% increase of the Froude

number results in about a 120% increase of the maximum peak acceleration. It is also observed that the acceleration increases from the aft sections to the fore sections. In the case of $Fn=1.8$, a section at $x/L=0.3$ has the maximum peak acceleration of 20 m/s^2 , while a section at $x/L=0.7$ has 50 m/s^2 . As one may expect, both the parameters of the Froude number and the location of the section significantly affect the maximum peak acceleration.

The acceleration versus the distance from the transom is shown in Fig. 15 for different wave heights at the forward speed of 5 m/s ($Fn=1.6$). The maximum peak acceleration rapidly increases from aft to fore, for all wave heights similar to the Froude number. In addition, an increase in wave height significantly increases the maximum peak acceleration. The maximum peak acceleration of about 11 m/s^2 occurs at $x/L=0.7$ at a wave height of $H/B=0.111$, while it increases to 45 m/s^2 at $H/B=0.28$, more than four times.

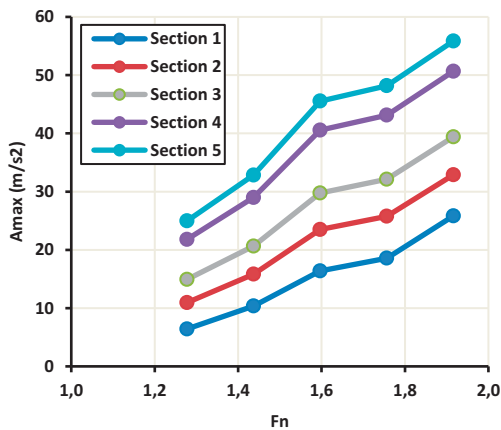


Fig. 14. Mean peak accelerations for different Froude number and positions at $H/b=0.28$

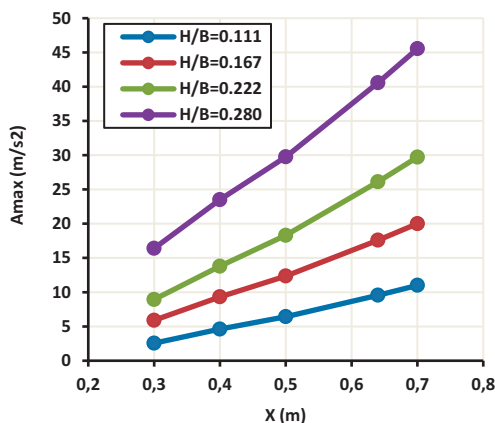


Fig. 15. Mean peak accelerations on craft sections for several wave heights at $V=5 \text{ m/s}$

PRESSURE

Three parameters, including local dead-rise angles, local vertical relative velocity and the chine-wet/chine-dry condition, govern the maximum peak pressure. The

dead-rise angle distribution is shown in Fig. 16. As can be seen, the dead-rise angle starts at the transom by 11 degrees and increases slowly to 20 degrees to $x/L=0.6$, then rapidly increases to 50 degrees at $x/L=0.9$ and remains at 50 degrees to $x/L=1.0$.

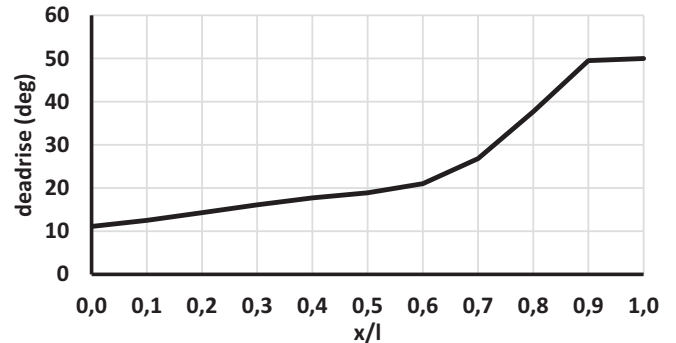


Fig. 16 Dead-rise angle distribution of the model.

On the other hand, the vertical relative velocity is typically higher far from the centre of gravity. Fig. 17 shows the peak of vertical relative velocity at different positions for a range of wave heights. The peak of vertical relative velocity increases with the increasing wave height and approaching the fore of the craft.

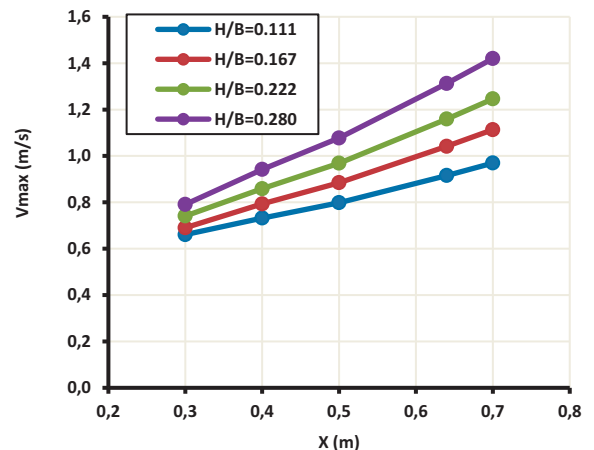


Fig. 17. Peak vertical relative velocity at different positions at $V=5 \text{ m/s}$

Overall, the pressure is a function of both the relative velocity and a dead-rise angle of more than a first-order. Therefore, the pressure at the fore part should increase due to a higher vertical relative velocity and should decrease due to a higher dead-rise angle, at the same time. The contradiction between the two effects may result in a non-monotonic pressure distribution. Additionally, the chine-wet condition drops the pressure to atmospheric pressure at the chine and significantly reduces the pressure in places near the chine. The sections located on aft to amid-ship frequently become chine-wet.

In Fig. 18, the maximum peak pressure of five sections at five points across each section ($y/b=0, 0.2, 0.4, 0.6, 0.8$) for

a range of wave heights are presented. Fig. 18 (a) demonstrates the maximum peak pressure on the keel-line as a function of the wave height along the keel length. The pressure along the craft's length is divided into two parts, the aft part from $x/L=0.3$ to the amid-ship and the fore part starting from the centre of gravity to $x/L=0.7$. At $H/B=0.111$, the pressure from the transom to the amid-ship increases, while from amid-ship to fore perpendicular it rapidly decreases. This trend changes as the wave height increases. For example, at a wave height of $H/B=0.28$, the pressure rapidly increases from $x/L=0.3$ to $x/L=0.65$ and continues with an almost constant value. Approximately the same trend can be seen in Fig. 18 (b), a point on the hull close to the keel line.

As the y -coordinate of the point under consideration increases, shown in Fig. 18 (a) to Fig. 18 (d), a tendency of pressure decrease is observed, especially for the fore part of the craft length. The aft part of the craft has almost the same pressure. Fig. 18 (d) and (e) ($y/b=0.6$ and 0.8) show a tendency to yield the zero pressure for some sections located on $x/L=0.7$. The tendency to zero pressure is most likely related

to the unsubmerged condition of the sections at the fore. Furthermore, the maximum pressure curves have a fracture and decrease all at once ahead of $x/l=0.6$, as seen in Fig. 18 (a) to (e). This is because of the steep increase of the dead-rise angle in these sections.

An important engineering solution to keep the pressure and acceleration low in the fore part of the planing craft is to keep the dead-rise angle constant from transom to amid-ship, but with a rapid increase from amid-ship to the fore perpendicular. This study shows that this solution works effectively, and sometimes less pressure at the fore perpendicular is observed. It may be recommended to employ a kind of parametric study to find out the best geometry of the craft for the elimination of high-pressure especially in the fore of a craft.

Moreover, the results indicate that the combined method may be employed as a powerful tool to modify planing hulls design to achieve an even pressure distribution along the length of the planing craft.

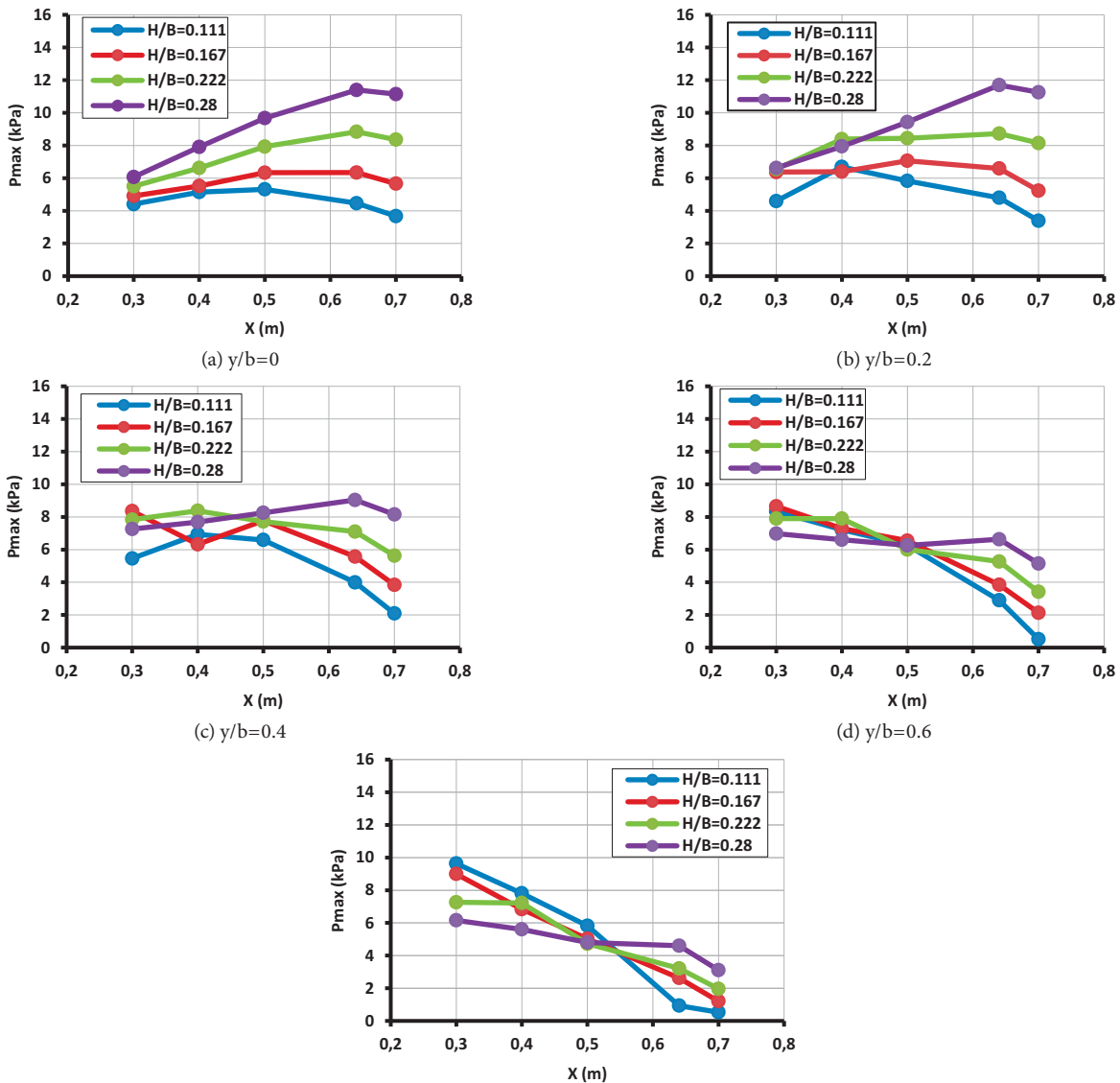


Fig. 18. Maximum pressure at a) $y/b=0$, b) $y/b=0.2$, c) $y/b=0.4$, d) $y/b=0.6$ and e) $y/b=0.8$ relative to the distance from the transom at $V=5$ m/s.

CONCLUSIONS

In this study, a computer code is developed based on combining the 2.5D method with the equivalent wedge method for calculation of the impact pressure on planing hulls in waves. The computer code also calculates heave and pitch motions as well as acceleration. A planing model was tested in calm water and regular waves with a wave height of 3.5 cm and wavelength of 300 cm at a speed of 6 m/s, and the recorded acceleration and pressure were compared with the results of the combined method. The calculated results in comparison with model experiment show a good agreement for heave and pitch motions, and acceleration. The pressure trend resulting from calculation is also in good agreement with the experiment, while the pressure peaks have relatively low agreement with the experiment. The combined method is utilised for a parametric study on acceleration and pressure for various velocities and wave heights. The parametric study reveals that the pressure and acceleration are evenly distributed along the craft, if the dead-rise angle is constant from transom to amid-ship, and gradually increases from amid-ship to the fore perpendicular. This study suggests that the optimum deadrise angle distribution along a planing craft should be extracted from an analysis similar to that presented in this paper.

REFERENCES

1. Fridsma G. (1969): *A systematic study of the rough-water performance of planing boats*. Stevens Inst of Tech, Hoboken, NJ, Davidson Lab.
2. Savitsky D., Brown P. W. (1976): *Procedures for hydrodynamic evaluation of planing hulls in smooth and rough water*. Marine Technology, 13(4), 381-400.
3. Martin M. (1976): *Theoretical Prediction of Motions of High-Speed Planing Boats in Waves*. Journal of Ship Research, 22(3), 98.
4. Zarnick E. E. (1978): *A nonlinear mathematical model of motions of a planing boat in regular waves*. David W Taylor Naval Ship Research and Development Center, Bethesda, MD.
5. Hicks J. D., Troesch A. W., Jiang C. (1995): *Simulation and nonlinear dynamics analysis of planing hulls*. Journal of Offshore Mechanics and Arctic Engineering, 17(1), 38-45.
6. Akers R. H. (1999): *Dynamic analysis of planing hulls in the vertical plane*. Proceedings of the Society of Naval Architects and Marine Engineers, New England Section.
7. Van Deyzen A. (2008): *A nonlinear mathematical model of motions of a planing monohull in head seas*. In Proceedings of the 6th International Conference on High Performance Marine Vehicles (HIPER'08).
8. Sayeed T. M. (2010): *Numerical simulation of planing hull in regular waves*. Memorial University of Newfoundland.
9. Ruscelli D. (2009): *Dynamics of high-speed craft*. PhD Thesis, University of Genoa, Genoa.
10. Pennino S. (2014): *Vertical Motion Assessment for Planing Hulls*. PhD Thesis, University of Naples Federico II, Naples, Italy.
11. Von Karman T. (1929): *The impact on seaplane floats during landing*. National Advisory Committee on Aeronautics, Washington, DC.
12. Wagner H. (1932): *Über Stoß- und Gleitvorgänge an der Oberfläche von Flüssigkeiten*. ZAMM-Journal of Applied Mathematics and Mechanics/Zeitschrift für Angewandte Mathematik und Mechanik, 12(4), 193-215.
13. Howison S., Ockendon J., Wilson S. (1991): *Incompressible water-entry problems at small deadrise angles*. Journal of Fluid Mechanics, 222, 215-230.
14. Oliver J. M. (2002): *Water entry and related problems*. PhD Thesis, University of Oxford.
15. Smiley R. F. (1951): *A Semiempirical Procedure for Computing the Water-Pressure Distribution on Flat and V-Bottom Prismatic Surfaces During Impact or Planing*. National Advisory Committee for Aeronautics, Washington, DC.
16. Smiley R. F. (1952): *Water-pressure distribution during landings of a prismatic model having an angle of dead rise of 22 1/2 degrees and beam-loading coefficients of 0.48 and 0.97*. National Advisory Committee for Aeronautics, Washington, DC.
17. Gray H. P., Allen R. G., Jones R. R. (1972): *Prediction of Three-Dimensional Pressure Distributions of V-Shaped Prismatic Wedges during Impact or Planing*. David W Taylor Naval Ship Research and Development Center, Bethesda, MD.
18. Rosén A., Garme K. (2004): *Model experiment addressing the impact pressure distribution on planing craft in waves*. International Journal of Small Craft Technology, 146.
19. Rosén A. (2005): *Impact pressure distribution reconstruction from discrete point measurements*. International Shipbuilding Progress, 52(1), 91-107.
20. Camilleri J., Taunton D., Temarel P. (2018): *Full-scale measurements of slamming loads and responses on high-speed planing craft in waves*. Journal of Fluids and Structures, 81, 201-229.

21. Razola M., Rosén A., Garme K. (2014): *Allen and Jones revisited*. Ocean Engineering, 89, 119-133.
22. Allen R. G., Jones R. R., Taylor D. W. (1978): *A simplified method for determining structural design-limit pressures on high performance marine vehicles*. In Advanced Marine Vehicles Conference.
23. Ghadimi P., Tavakoli S., Dashtimanesh A. (2016): *Calm water performance of hard-chine vessels in semi-planing and planing regimes*. Polish Maritime Research, 23(4), 23-45.
24. Ghassemi H., Kamarlouei M., Veysi S. T. G. (2015): *A hydrodynamic methodology and CFD analysis for performance prediction of stepped planing hulls*. Polish Maritime Research, 22(2), 23-31.
25. Jones R. R., Allen R. G. (1972): *A Semiempirical Computerized Method for Predicting Three-Dimensional Hull-Water Impact Pressure Distributions and Forces on High-Performance Hulls*. David W Taylor Naval Ship Research and Development Center, Bethesda, MD.
26. Shuford Jr C. L. (1958): *A theoretical and experimental study of planing surfaces including effects of cross section and plan form*. National Advisory Committee for Aeronautics, Washington, DC.
27. *ITTC Member Organisations*. Available from: <https://ittc.info/members/member-organisations/national-iranian-marine-laboratory-nimala/>.
28. Yang S.-I., et al. (1996): *The Prediction of Resistance of a 23m Class Planing Hull*. Journal of Hydrospace Technology, 2(2), 68-79.
29. Zeraatgar H., et al. (2019): *Sampling rate effect on wedge pressure record in water entry by experiment*. Ocean Engineering, 179, 51-58.

CONTACT WITH THE AUTHORS

Hossein Tahmasvand

e-mail: tahmasvand@aut.ac.ir
Amirkabir University of Technology,
Hafez, 15875-4413 Tehran,

IRAN

Hamid Zeraatgar

e-mail: hamidz@aut.ac.ir
Amirkabir University of Technology,
Hafez, 15875-4413 Tehran,

IRAN

PREDICTION OF SHIP MOTIONS IN IRREGULAR WAVES BASED ON RESPONSE AMPLITUDE OPERATORS EVALUATED EXPERIMENTALLY IN NOISE WAVES

Sebastian Bielicki

Maritime Advanced Research Centre, Gdańsk, Poland

ABSTRACT

The most common methods for predicting ship roll motions in a specified sea state are direct measurements of motions in a representative irregular wave realisation (time domain) or calculations of motions from response amplitude operators (RAOs) in the frequency domain. The result of the first method is valid only for the tested sea state, whilst the second method is more flexible but less accurate. RAO-based predictions are calculated assuming a linear model of ship motions in waves. RAO functions are usually evaluated by means of tests in regular waves for a limited number of frequencies and a constant wave amplitude. This approach is time-consuming and the discrete form of the RAO functions obtained for a limited number of frequencies may lead to discrepancies in the prediction of seakeeping and often does not allow the actual amplitude of the response in resonant frequency to be determined. Another challenge is the appropriate selection of wave amplitude for tests due to the considerable influence of viscous damping on roll response in irregular sea waves. There are alternative methods for the experimental determination of RAO functions and one of them is presented in this study. The presented approach allows RAO functions to be evaluated in one run by the generation of irregular waves characterised by a white or coloured noise spectrum. This method reduces the experiment duration, with almost continuous RAO characteristics obtained. The flat (white noise) and linear (coloured noise) wave spectral energy characteristics are considered in the experiment and the obtained predictions are compared with the results of accurate measurements in irregular waves.

Keywords: seakeeping, roll motions, noise, ship motions, experiments

INTRODUCTION

There are significant challenges concerning the safety and operability aspects of a ship. These issues are especially important for severe sea conditions during operations in open sea. Some may focus on dynamic positioning issues and the influence of ship propulsion systems, such as bow tunnel thrusters on ship motions [1], while others may focus on operability based on the assessment of ship motions as a response to wave excitations [2]. In the last decade, a large number of computational analyses concerning ship motions in waves have been published [3, 4, 5, 6, 7, 8]. However, experiments at the model scale along with full-scale

trials [9] are still the most accurate approaches for checking operability criteria, but the cost of model tests sometimes limits the number of considered cases. This study focuses on an experimental approach to roll motion prediction as it plays a very important role in the assessment of ship operability [2], as well as having a significant influence on ship safety during operations in severe seas [10]. These motions are mostly important for station keeping vessels in the offshore industry during operations in the vicinity of platforms in open seas.

Roll motion is the response motion of a vessel exposed to sea waves. The most appropriate method for the prediction of ship response in a seaway is to carry out an experiment in irregular waves representing the considered sea conditions.

However, this method is usually limited to only a couple of representative sea states. This approach is applicable if the operability is not the main goal of the analysis, meaning that the ship's seakeeping characteristics are regarded as long term and over long distances. For this purpose, the assumption of a linear response of the marine system to random excitation was developed in the first half of the twentieth century.

THEORETICAL BACKGROUND

The response of ship motions to ocean waves is considered as an input/output system with a known linear characteristic (Fig. 1). This characteristic is called the response amplitude operator (RAO) and is a function of wave frequency [11]. The response motions are irregular like sea waves. By taking a known wave energy spectrum into consideration with a known ship's response frequency characteristic (RAO), the response spectra can be calculated. With response spectra, the statistical properties of this response can be found.

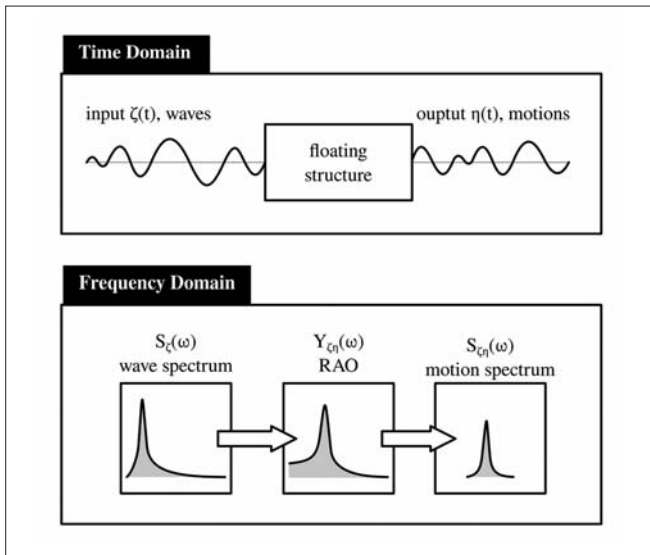


Fig. 1. Linear relationship between wave (input) and motions (response)

Based on an ocean wave representation in spectral form, the wave energy in the frequency domain is given by [12]:

$$S_{\zeta}(\omega)d\omega = \frac{1}{2} \zeta_A^2(\omega) \quad (1)$$

where:

- S_{ζ} – density of wave energy
- $d\omega$ – differential of angular frequency
- ω – wave angular frequency
- ζ_A – wave amplitude

and by analogy, the energy spectrum of the response is:

$$S_{\zeta\eta}(\omega)d\omega = \frac{1}{2} \eta_A^2(\omega) \quad (2)$$

where:

- $S_{\zeta\eta}$ – density of response energy
- η_A – response amplitude

The linear response characteristic Y_{η} known as the RAO is:

$$Y_{\eta}(\omega) = \frac{\eta_A(\omega)}{\zeta_A(\omega)} \quad (3)$$

By rearranging Eq. (3), the response amplitude is:

$$\eta_A(\omega) = \zeta_A(\omega)Y_{\eta}(\omega) \quad (4)$$

and by combining Eqs. (2)–(4), the response spectrum may be shown as:

$$S_{\zeta\eta}(\omega)d\omega = \frac{1}{2} \zeta_A^2(\omega)Y_{\eta}^2(\omega). \quad (5)$$

Furthermore, when considering Eq. (1), the response spectrum is:

$$S_{\zeta\eta}(\omega)d\omega = S_{\zeta}(\omega) d\omega Y_{\eta}^2(\omega). \quad (6)$$

The wave and the ship's response are random processes with a Gaussian distribution function around a zero mean [13]; thus, the root mean square value of signal is expressed by:

$$\eta_{RMS} = \sqrt{m_{0\eta}} \quad (7)$$

where the zeroth moment in Eq. (7) is:

$$m_{0\eta} = \int_0^{\infty} S_{\zeta\eta}(\omega)d\omega. \quad (8)$$

The above is valid as the response amplitude η_A is proportional to the wave amplitude ζ_A .

The linearized equation of response motion is [12]:

$$(M + A)\ddot{\eta} + B\dot{\eta} + C\eta = F_W \quad (9)$$

where for linear motions, F_W is the wave force acting on a particular direction, and for angular motions, F_W is the moment about the axis of rotation. The $M + A$ component is the sum of the inertia properties, such as the mass for linear motions and the moment of inertia for rotations and added mass A . The B and C components are hydrodynamic damping and restoring coefficients, respectively. Furthermore, Eq. (9) may be normalised by $M + A$ to reach:

$$\ddot{\eta} + \nu_{\phi} \dot{\eta} + \omega_{\eta}^2 \eta = f_W \quad (10)$$

where ν_{η} and ω_{η} are the dimensionless damping coefficient and natural frequency, respectively. The damping coefficient must have a linear characteristic so that the assumption of the proportionality of the response and excitation is valid. This assumption gives a good approximation for all motions except the roll when the nonlinear viscous damping is significantly higher than the damping occurring from the generation of waves. However, the roll motion damping nonlinearity may be included in the equation of motion, if it depends only on the amplitude of the resulting roll motion.

Equation (6) is key to predicting roll motions in the considered sea state with a specified spectral energy

density $S_{\zeta_\eta}(\omega)$. The transfer function of roll motions Y_{ζ_φ} is usually established by experiments in regular waves with a constant amplitude or slope, whilst the RAO of roll motion is a narrow band and the tests are carried out for multiple frequencies ω within a certain range around the resonant frequency ω_φ . Since viscous damping phenomena depend on the level of roll amplitude, the constant wave amplitude- or slope-based RAO must be corrected to the expected response in the considered sea state. This means that predictions from regular wave experiments should be complemented by the characteristics of roll damping established either by roll decay test or other ones. This approach is thus rather time-consuming, so this study presents an alternative, less time-consuming method for RAO evaluation.

Equation (6) may be modified to the form:

$$S_{N_\varphi}(\omega_i) = S_N(\omega_i)Y_\varphi^2(\omega_i) \quad (11)$$

where the input to the system here is the noise energy density spectrum $S_N(\omega)$, which may have a constant value over the frequencies ω (white noise (WN)) or may proportionally increase (blue noise (BN)) or decrease (pink noise (PN)) with the frequencies ω . The $d\omega$ part of the equation is always greater than zero and might be deleted. By transforming Eq. (10), the RAO can be found as:

$$Y_\varphi(\omega_i) = \sqrt{\frac{S_{N_\varphi}(\omega_i)}{S_N(\omega_i)}} \quad (12)$$

The discrete roll motion RAO, in dimensionless form, where the roll angle is related to the wave slope angle $\alpha_A = k\zeta_A$, can be further approximated by [14]:

$$Y_{\alpha_\varphi}(\omega_i) = \frac{\kappa_\varphi}{\sqrt{\left(1 - \frac{\omega^2}{\omega_\varphi^2}\right)^2 + \left(2\nu_\varphi \frac{\omega}{\omega_\varphi^2}\right)^2}} \quad (13)$$

where dimensionless damping is found as $\nu_\varphi = \frac{B}{(M+A)}$.

Equation (13) simplifies the ship roll response because sway and yaw coupling is neglected and the contribution of the diffraction component might be compensated by the modified Froude-Krylov heeling moment reduction factor [14]:

$$\kappa_\varphi(\omega_i) = \beta_0 e^{-\beta_1 \omega^2} \quad (14)$$

where the coefficients β_0 and β_1 in function are determined by least squares approximation of the RAO evaluated by noise measurements according to Eq. (13). In addition, it is shown that the damping of roll motions in noise waves is equal to the damping in the demanded sea state with the same total energy, meaning that the root mean square (RMS) values of the input waves (noise and wind wave spectral form) are equal. The next key feature of the proposed method is that changes in damping are assumed linear, related to the RMS of the generated noise signal. This means that to find the damping coefficient for the prediction of roll motions, the RMS of the generated noise waves should lay within the RMS values of the demanded sea states. The damping coefficient

can be read from the linear characteristic of the RMS values, as shown in Fig. 2.

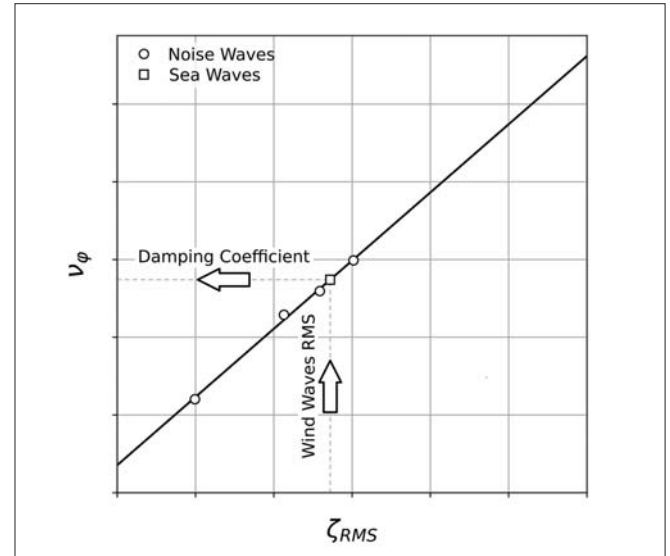


Fig. 2. Linear characteristic of roll damping coefficient

As far as we have a linear characteristic for the damping coefficients from noise measurements, the number of runs may be limited.

MODEL TESTS

Model tests were carried out for three models of vessels. The tests were carried out in a Maritime Advanced Centre (CTO) towing tank no. 2 equipped with a flap type wave maker and active wave absorber. The rectangular shape tank has a length of 50 m, a breadth of 7 m and an adjustable depth, which for the purposes of the current analyses was set to represent deep water conditions. The models were tested only in beam seas. The main dimensions of the hull models are presented in Table 1.

Tab. 1. Main particulars of tested hull models

	HM#01	HM#02	HM#03
L_{pp} [m]	3.585	3.553	3.212
B [m]	0.708	0.770	0.952
T [m]	0.196	0.205	0.363
C_B [-]	0.92	0.78	0.70
$T\varphi$ [S]	2.47	2.16	3.02
Scale factor	53.0	24.0	17.0

The models were tested in different irregular waves representing the demanded sea states and appropriate noise wave realisation [15], [16]. One of the models was tested in regular waves. The detailed configuration of the test cases is presented in Table 2.

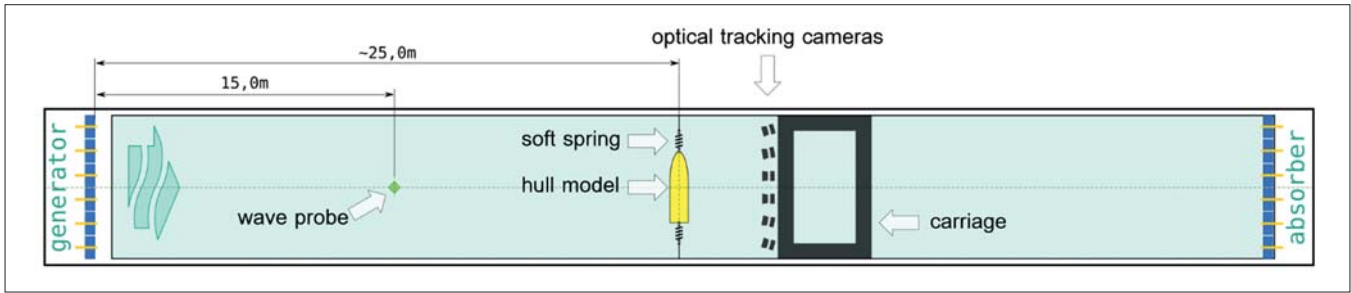


Fig. 3 Experimental setup in CTO towing tank no. 2

Tab. 2. Test configurations

Wave (HM#01)	RMS [mm]	Peak Period [s]	Wave (HM#02)	RMS [mm]	Peak Period [s]	Wave (HM#03)	RMS [mm]	Peak Period [s]
(ITTC)			(JONSWAP)			(JONSWAP)		
I1.1	12.8	2.43	I1.2	28.8	1.42	I1.3	16.8	1.85
I2.1	27.2	2.45	I2.2	46.5	1.87	I2.2	36.0	2.70
I3.1	36.0	2.48	I3.2	55.9	2.00	I3.2	48.4	2.90
			I4.2	89.9	2.53			
(Noise)			(Noise)			(Noise)		
WN1.1	21.3		WN1.2	37.6		WN1.2	24.4	
WN2.1	25.9		WN2.2	46.3		WN2.2	36.0	
WN3.1	9.9		WN3.2	23.8		WN3.2	48.4	
WN4.1	30.2		PN1.2	38.4				
			PN2.2	47.0				
			BN1.2	36.7				
			BN2.2	23.1				
(Regular)								
R0.1	25.3							

During the tests model was set in perpendicular to wave propagation direction. The wave probe was positioned in front of the model, 10 m fore from wave generator, and the measured wave train was undisturbed by model itself. The hull motions in 6DOF (degrees of freedom) was measured with the use of 6 motion capture cameras system. Hull model was restrained in sway and surge motions by the soft spring anchoring system mounted to model at the centre line at the water level. The test set up is presented in Fig. 3

The tests in regular waves were carried out in constant regular wave double amplitude of 1/50 of the model length [17]. This level of regular wave amplitude is recommended by procedures issued by the International Towing Tank Conference (ITTC) [17].

The irregular waves were set to represent a wide variety of irregular waves with the most popular wave spectra, such as the ITTC – two parameter Pierson-Moskowitz [18] and JONSWAP [19]. The general parameters representing the generated wave spectra are presented in Table 2 and an example of a measured wave spectrum and its theoretical representation is presented in Fig. 4.

The noise spectra were prepared to obtain a narrow band width as the expected RAO will be within the range of wave

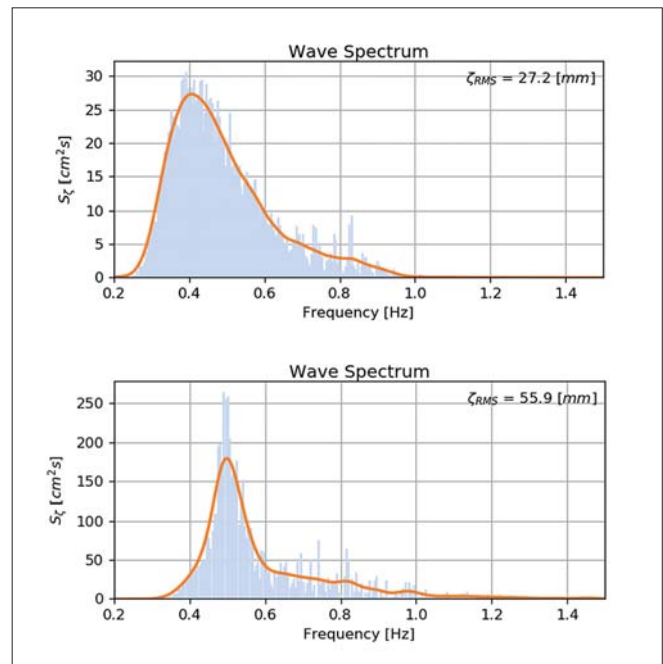


Fig. 4. Spectra of wind waves (top – I2.1 ITTC, bottom – I3.2 JONSWAP)

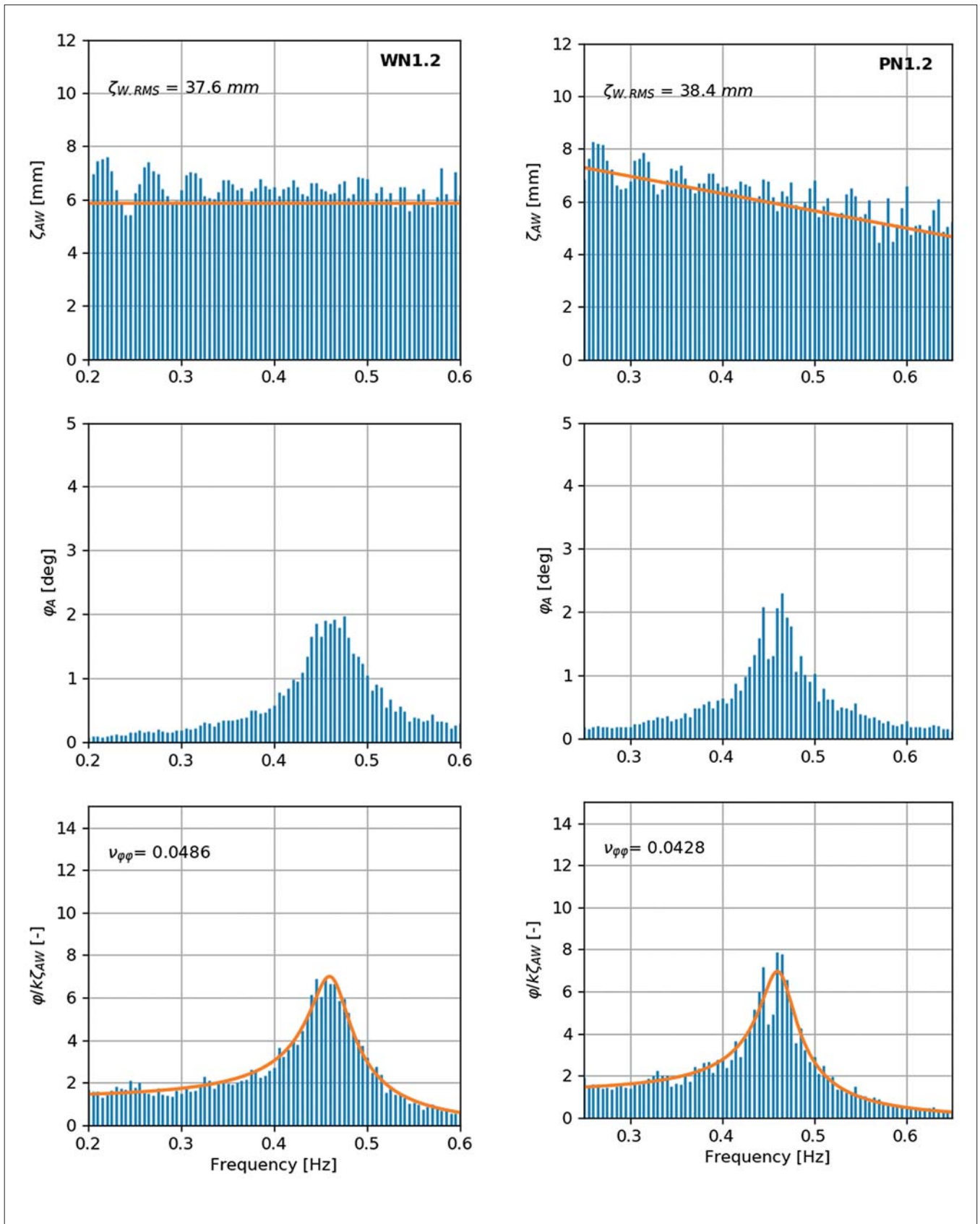


Fig. 5. Comparison of noise measurements – white, HM#02 (left) vs. pink, HM#02 (right)

frequencies. In addition, the amplitude of signal was tuned to the energy of noise within the range of the demanded sea

energy. Examples of the generated noise amplitude spectra with certain RMS values are presented in Fig. 5 and Fig. 6.

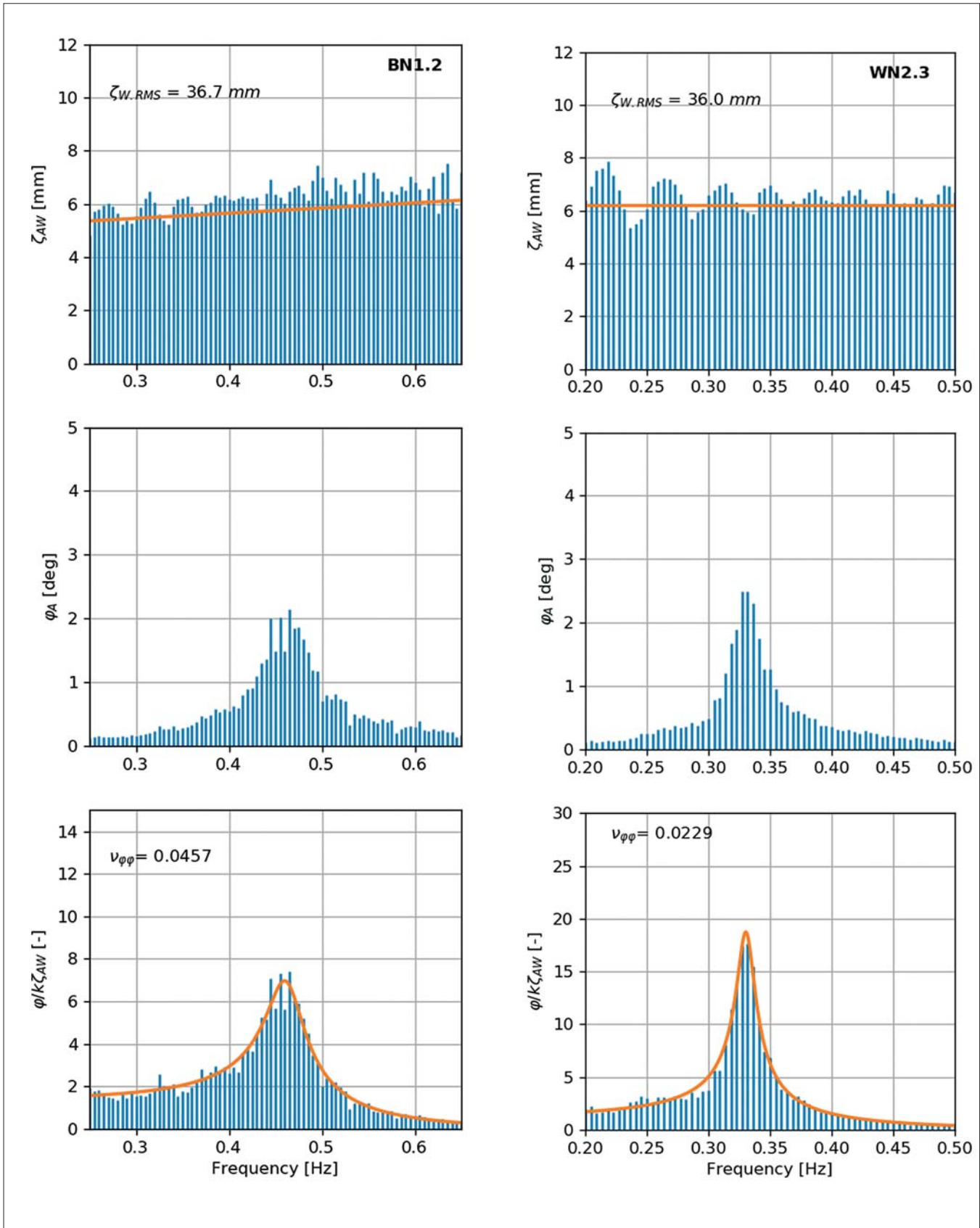


Fig. 6. Comparison of noise measurements – blue, HM#02 (left) vs. white, HM#03 (right)

Fig. 7 presents the relationship between the RMS values of the generated noise waves and the damping coefficients achieved from the approximation of RAOs by Eq. (13).

Figures 7–10 present the RAO functions evaluated from the results of measurements in noise waves.

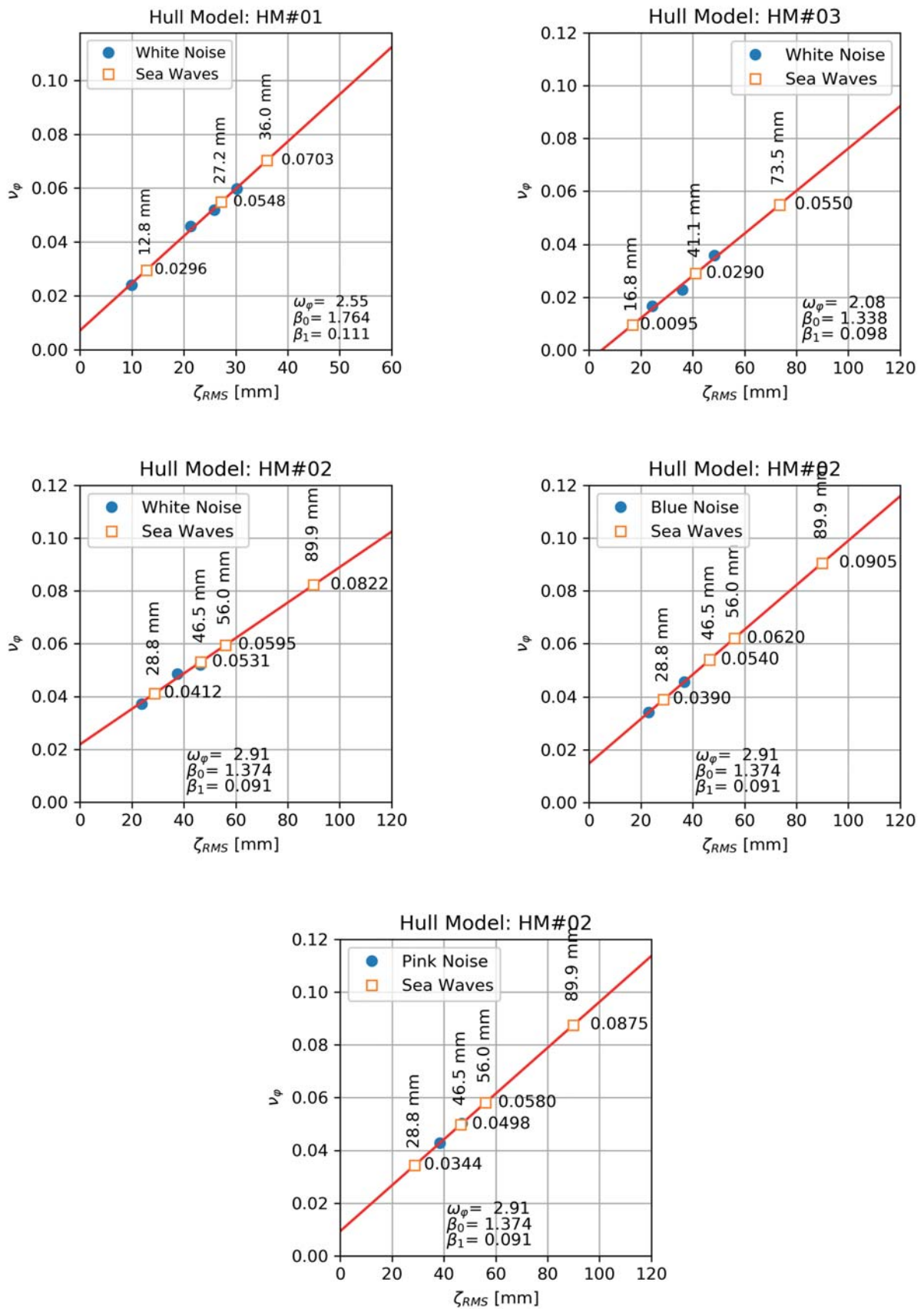


Fig. 7. Relation between damping coefficient and wave RMS

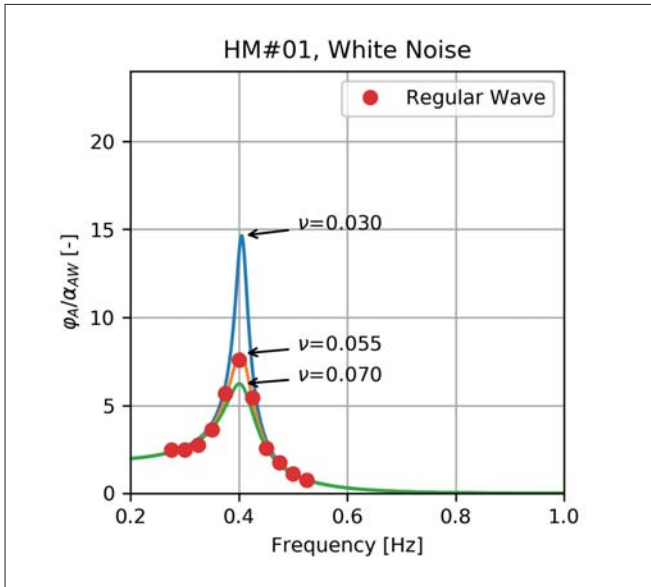


Fig. 8. HM#01, approximated transfer functions

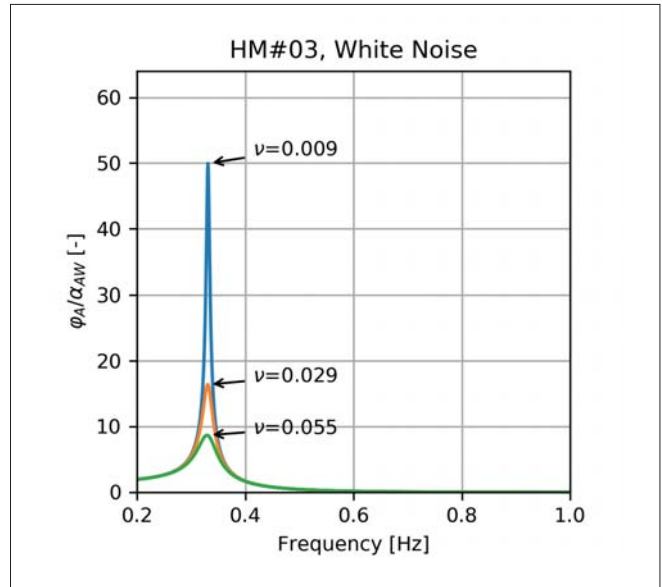


Fig. 10. HM#03, approximated transfer functions

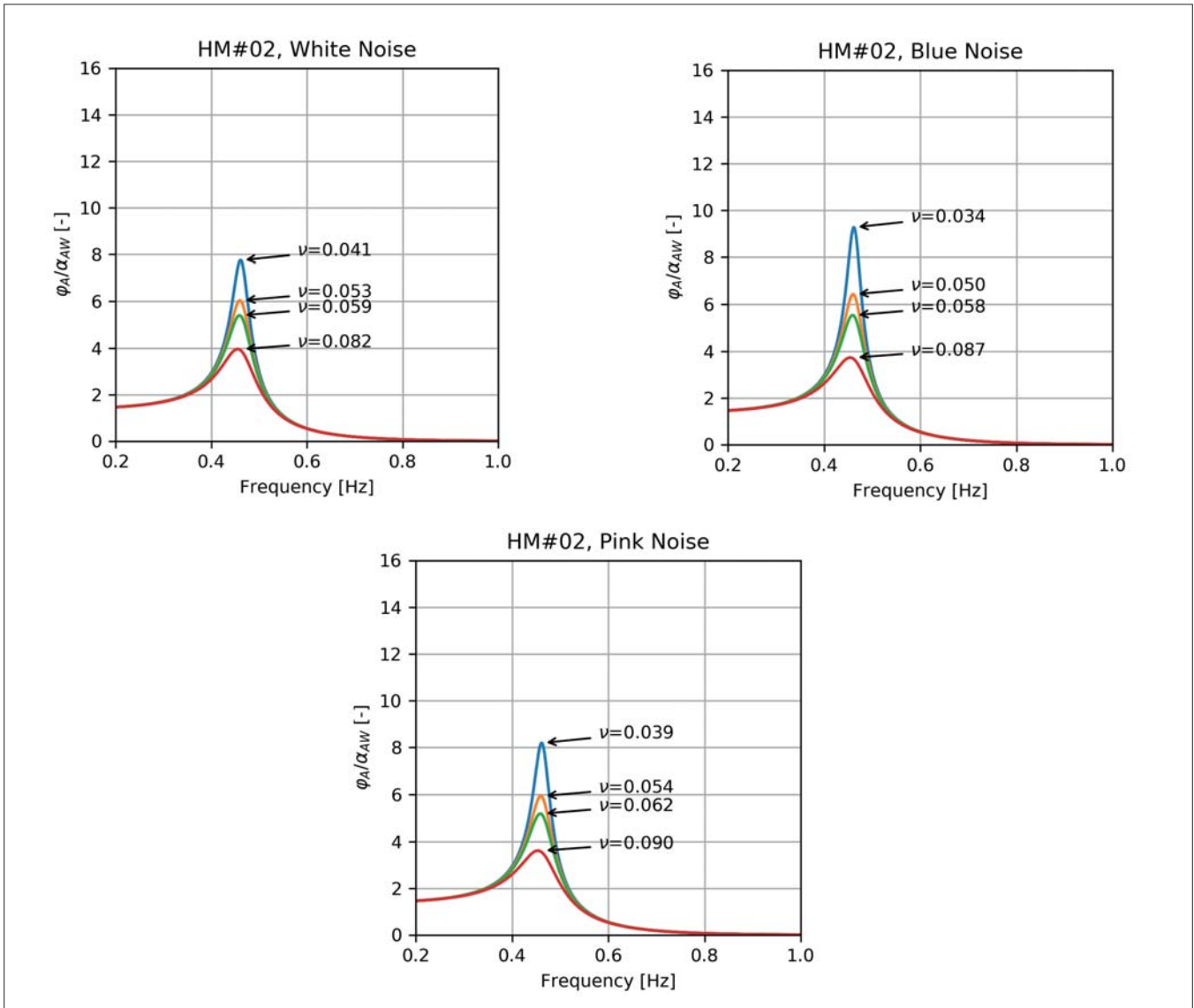


Fig. 9. HM#02, approximated transfer functions

UNCERTAINTY ANALYSIS

Uncertainty analysis (UA) was analysed in two types: Type A and Type B [20]. The RAO curves which were used to final predictions were subjected to UA. The source of errors in Type B analysis is mainly the wave probe error $\varepsilon(\zeta)$ evaluated in probe calibration process and motion tracking system angular precision error $\varepsilon(\varphi)$ provided by manufacturer. The probability distribution of expected value as well as its errors is assumed here as rectangular (uniform) thus uncertainty of measured signal is given by formula:

$$u(\zeta_{AW}) = \frac{\varepsilon(\zeta)}{N\sqrt{3}} \quad (15)$$

$$u(\varphi_A) = \frac{\varepsilon(\varphi)}{N\sqrt{3}} \quad (16)$$

The value N in formulas (18) and (19) is the number of harmonics in considered amplitude spectrum.

The dimensionless RAO function Y_φ might be calculated by formula (3), and is established by indirect measurements. The combined uncertainty is calculated then by partial derivatives of formula (3) as follows:

$$u_B(Y_\varphi) = \sqrt{\left(\frac{\delta Y_\varphi}{\delta \zeta_{AW}}\right)^2 u^2(\zeta_{AW}) + \left(\frac{\delta Y_\varphi}{\delta \varphi_A}\right)^2 u^2(\varphi_A)} \quad (17)$$

The main source of errors in Type A uncertainty here is the deviation from approximated and measured RAO characteristics, thus the Type A uncertainty $u_A(Y_\varphi)$ is equal to root mean square error of approximation given by equation (16).

The total uncertainty is then calculated as root of sum squared uncertainties of Type A and B:

$$u(Y_\varphi) = \sqrt{u_A^2(Y_\varphi) + u_B^2(Y_\varphi)} \quad (18)$$

The percentage of total uncertainty in maximum RAO value $Y_\varphi(f_{RES})$ at resonant frequency f_{RES} is calculated from formula:

$$\frac{u(Y_\varphi)}{Y_\varphi(f_{RES})} \cdot 100\% \quad (19)$$

and it is presented in Fig. 11 to Fig. 13 as a function of wave frequency

Finally the uncertainty of predicted RMS values of roll motions, from approximated RAO of noise measurements, are calculated as combined uncertainty from formula:

$$u(\varphi_{RMS}) = \frac{\delta \varphi_{RMS}}{\delta Y_\varphi} \Delta Y_\varphi \quad (20)$$

where root mean square function of roll motions is calculated from combined formulas (6), (7) and (8) as follows:

$$\varphi_{RMS} = \sqrt{\int S_\zeta(\omega) \cdot Y_\varphi^2(\omega) d\omega} \quad (21)$$

and the total uncertainty of RAO function is found from:

$$\Delta Y_\varphi = \int u(Y_\varphi) d\omega \quad (22)$$

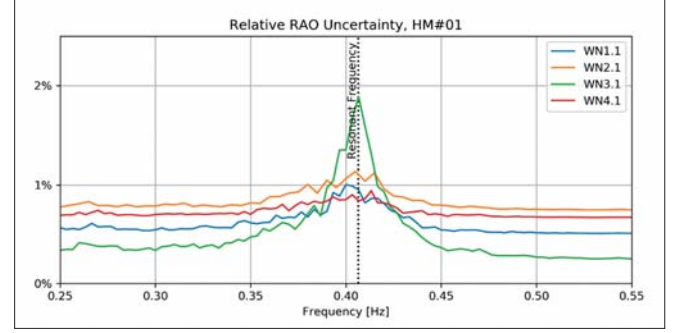


Fig. 11 Relative RAO uncertainty HM#01

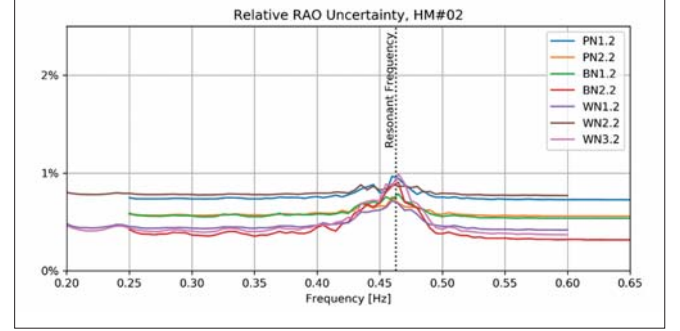


Fig. 12 Relative RAO uncertainty HM#02

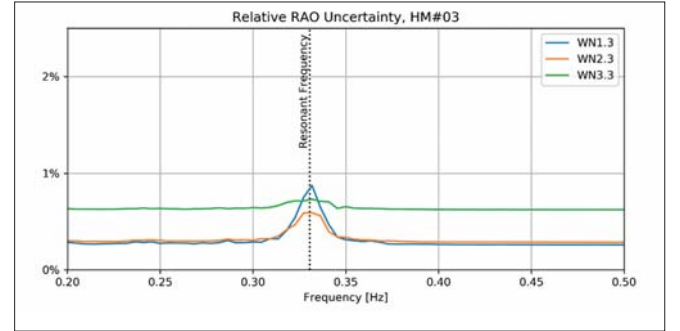


Fig. 13 Relative RAO uncertainty HM#03

Uncertainty of roll RMS from direct measurements in irregular waves is equal to:

$$u(\varphi_{RMS}) = \frac{\varepsilon(\varphi)}{\sqrt{3}} \quad (23)$$

RESULTS OF ANALYSES

Equation (13) with modified Froude-Krylov coefficients fits very well to the RAOs evaluated from noise wave experiments. The values of the damping coefficients lie on a straight line in all considered configurations of the tests (Fig. 7). Table 3 presents the results of predictions from direct measurements in the modelled sea waves compared to the predictions calculated from the RAOs. The predicted and measured RMS values were then plotted against each other (Fig. 14). The straight red line depicts the ideal correlation between prediction and measurements, while the grey lines represent $\pm 5\%$ margin of the actual values.

Tab. 3. Comparison of roll motion RMS values (measurements in irregular waves and noise RAO-based predictions)

	Noise	$u(\varphi_{RMS})$	Irregular	$u(\varphi_{RMS})$	Regular	Description
11.1	2.42	0.04	2.23	0.06	1.67	HM#01
12.1	3.63	0.09	3.36	0.06	3.57	
13.1	4.15	0.13	4.13	0.06	4.75	
11.2	0.95	0.05	1.01	0.06	N/A	HM#02.BN
12.2	5.21	0.10	5.01	0.06	N/A	
13.2	7.46	0.13	7.14	0.06	N/A	
14.2	8.62	0.24	8.75	0.06	N/A	
11.2	0.92	0.07	1.01	0.06	N/A	HM#02.PN
12.2	4.99	0.14	5.01	0.06	N/A	
13.2	7.15	0.18	7.14	0.06	N/A	
14.2	8.47	0.32	8.75	0.06	N/A	
11.2	0.90	0.04	1.01	0.06	N/A	HM#02.WN
12.2	5.04	0.08	5.01	0.06	N/A	
13.2	7.34	0.11	7.14	0.06	N/A	
14.2	8.92	0.19	8.75	0.06	N/A	
11.3	0.41	0.05	0.34	0.06	N/A	HM#03
12.3	4.77	0.15	4.54	0.06	N/A	
13.3	6.51	0.32	7.25	0.06	N/A	

The predicted and measured values were analysed by means of Pearson's correlation factor R_{fo} and the root mean square error (RMSE) given by [21]:

$$R_{fo} = \frac{1}{N} \sum_i^N y_{fi} y_{oi} \quad (24)$$

$$RMSE_{fo} = \sqrt{\frac{1}{N} \sum_i^N (Y_{fi} - Y_{fo})^2} \quad (25)$$

where

$$R_{fo} = \frac{Y_{fi} - \mu_f}{\sigma_f} y_{fi} y_{oi} = \frac{Y_{oi} - \mu_o}{\sigma_o} \quad (26)$$

The R_{fo} correlation coefficient quantifies the statistically linear correlation between observations (measurements) Y_o and predictions Y_f . The squared value of R_{fo} varies within between 0 and 1.

CONCLUSIONS

The method presented in this study may be used as an alternative experimental approach to evaluate RAOs. The experiments were carried out in irregular waves with wide bandwidth spectra of colour noise character. The approach might be considered as similar to that proposed by (Bielicki, Bednarek and Kraskowski [22]) where the noise measurements were applied to find predicted roll motions in considered sea states. The approach presented in [22] approximates RAO functions to noise measurements and Froude-Krylov moment in Eq. (13) is calculated basing on different formulae with

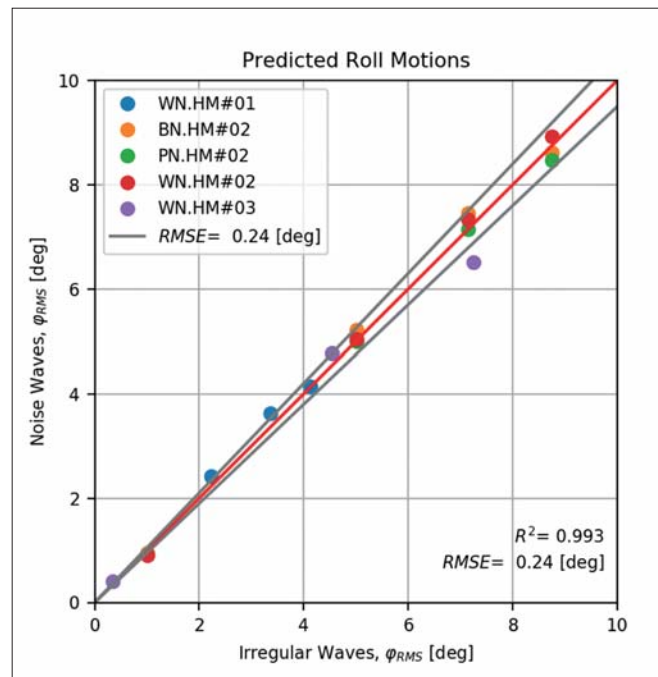


Fig. 14. Correlation plot of measurements against prediction

correction depending on the level of noise input signal. The damping factor is obtained there from roll decay tests and adjusted to considered sea state by iteration. The method presented here allows to apply modified Froude-Krylov moment from Eq. (14), which arises from measurements.

Besides the damping coefficient is found from the least square approximation of Eq. (13) directly – it exclude the necessity of roll decay tests. Finally the main outcome of the method presented here is that the damping coefficient varies linearly with the RMS values of noise generated waves. The last feature allows to predict roll motions in variety of sea states basing on limited measurements in noise waves. Thus the predicted roll motions in multiple sea state conditions fit reasonably well with measurements in selected irregular waves (sea conditions), as confirmed by a squared Pearson's correlation above 0.99 and a RMSE below 0.25 [deg]. The noise wave-based measurement may be extended for other motions, like heave and pitch.

ACKNOWLEDGEMENTS

This research was financed by the Ministry of Science and Higher Education of the Republic of Poland and by the Maritime Advanced Research Centre CTO S.A.

REFERENCES

1. M. Reichel, "Longitudinal motion due to action of tunnel thrusters," *Polish Maritime Research*, vol. 25, no. Special Issue, pp. 74–79, 2018.
2. H. Olszewski and H. Ghaemi, "New concept of numerical ship motion modelling for total ship operability analysis by integrating ship and environment under one overall system," *Polish Maritime Research Special Issue*, no. DOI: 10.2478/pomr-2018-0020, pp. 36–41, 2018.
3. S. Mousaviraad, P. Carrica, J. Huang and F. Stern, "CFD Prediction of Ship Response to Severe Ocean Waves and Wind," in *27th Symposium on Naval Hydrodynamics*, Seoul, Korea, 2008.
4. C. D. Simonsen, J. F. Otzen, S. Joncquez and F. Stern, "EFD and CFD for KCS heaving and pitching in regular head waves," *Journal of Marine Science and Technology (Japan)*, vol. 18, no. DOI: 10.1007/s00773-013-0219-0, pp. 435–459, 2013.
5. B. J. Guo, S. Steen and G. B. Deng, "Seakeeping prediction of KVLCC2 in head waves with RANS," *Applied Ocean Research*, vol. 35, no. DOI: 10.1016/j.apor.2011.12.003, pp. 56–67, 2012.
6. K. Niklas and H. Pruszko, "Full scale CFD seakeeping simulations for case study ship redesigned from V-shaped bulbous bow to X-bow hull form," *Applied Ocean Research*, vol. 89, no. DOI: 10.1016/j.apor.2019.05.011, pp. 188–201, 2019.
7. J. Jia, Z. Chen, C. Chen i H. Ren, „Time-domain hydroelastic analysis of nonlinear motions and loads on a large bow flare ship in high irregular seas,” *Journal of Marine Science and Technology (Japan)*, tom 25(2), pp. 426–454, 2020.
8. J. Jiao, S. Sun, J. Lee, C. Adenya, H. Ren, C. Chen and D. Wang, "A comprehensive study on the seakeeping performance of high speed hybrid ships by 2.5D theoretical calculation and different scaled model experiments," *Ocean Engineering*, vol. 160, pp. 197–223, 2018.
9. J. Jiao, C. Chen i H. Ren, „A comprehensive study on ship motion and load responses in short-crested irregular waves,” *International Journal of Naval Architecture and Ocean Engineering*, tom 11, nr DOI: 10.1016/j.ijnaoe.2018.07.003, pp. 364–369, 2019.
10. X. Wu, L. Tao i Y. Li, „Nonlinear roll damping of ship motions in waves,” *Journal of Offshore Mechanics and Arctic Engineering*, tom 127, nr DOI: 10.1115/1.1951780, pp. 205–211, 2005.
11. M. St. Denis and W. Pierson, "On the motion of ships in confused seas," *Soc. Nav. Archit. Mar. Eng.*, vol. Trans. 61, pp. 280–354, 1953.
12. J. Journee and W. Massie, *Introduction in Offshore Hydromechanics*, Delft: Delft University of Technology, 2001.
13. O. Rice, "Mathematical Analyses of Random Noise," *Bell System Technical Journal*, Vols. Vols. 23, 24, 1945.
14. J. Dudziak, *Teoria Okrętu*, Gdańsk: Fundacja Promocji Przemysłu Okrętowego i Gospodarki Morskiej, 2008.
15. S. Chakrabarti, „Physical Model Testing of Floating Offshore Structures,” w *Dynamic Positioning Conference*, Houston, USA, 1998.
16. M. Drzewiecki and W. Sulisz, "Generation and propagation of nonlinear waves in a towing tank," *Polish Maritime Research*, no. DOI: 10.2478/pomr-2019-0014, pp. 125–133, 2019.
17. ITTC, "Report of the Seakeeping Committee," in *Proceedings of 12th International Towing Tank Conference*, The Hague, 1978.
18. W. J. Pierson and L. Moskowitz, "A proposed spectral from for fully developed wind seas based on the similarity theory of S.A. Kitaigorodskii," *Journal of Geophysical Research*, vol. 69, pp. 5181–5203, 1964.
19. K. Hasselmann et al., „Measurement of wind-wave growth and swell decay during the Joint Nort Sea Wave Project (JONSWAP)," *Deutschen Hydrographischen Institut*, Hamburg, 1973.

20. "Evaluation of measurement data – Guide to the expression of uncertainty in measurement," in *JCGM 100:2008*, 2008.
21. A. Barnston, "Correspondence Among the Correlation, RMSE and Heidke Forecast Verification Measures," American Meteorological Society, Climate Analysis Center, NMC/NWS/NOAA, Washington D.C., 1992.
22. S. Bielicki, A. Bednarek and M. Kraskowski, "Evaluation of Response Amplitude Operator of Ship Roll Motions," in *Proceedings of the ASME 2017 36th International Conference on Ocean, Offshore and Arctic Engineering*, Trondheim, 2017.

CONTACT WITH THE AUTHOR

Sebastian Bielicki

e-mail: sebastian.bielicki@cto.gda.pl

Centrum Techniki Okrętowej S.A.
Szczecińska 65, 80-392 Gdańsk

POLAND

STUDY OF A NEW TYPE OF FLETTNER ROTOR IN MERCHANT SHIPS

Boyang Li ¹

Rui Zhang ¹

Yajing Li ¹

Baoshou Zhang ^{2*}

Chao Guo ¹

¹ College of Electromechanical Engineering, Qingdao University of Science and Technology, Qingdao, Shandong, China

² School of Aerospace Engineering, Tsinghua University, Beijing, China

* Corresponding author: sxsdzbs@126.com (B. Zhang)

ABSTRACT

Wind energy is a clean and renewable source of energy. This study seeks to explore the potential for utilising wind power for merchant ships. A new type of Flettner rotor (rotating cylinder) mounted on the superstructure of a ship is proposed and numerically simulated. The construction and installation of the rotating cylinder is designed and a numerical simulation of the ship-mounted cylinder is carried out, using the commercially available CFD code Ansys Fluent to obtain parameters such as lift and drag coefficient of the cylinder in different conditions. Specifically, it is found that the cylinder type superstructure can play a certain role in reducing the effect of friction by comparing traditional and cylindrical superstructures; the rotating cylinder can generate auxiliary thrust for the ship. After analysis, the wind speed around the cylinder and spin ratio will have a direct influence on its thrust effect; there is an inflection point in the lift coefficient with the increase of α ; the thrust coefficient (8.63) reaches the maximum environmental wind speed at 10 m/s and spin ratio is 2.5. For the rotating cylinder, the greater the environmental wind, the greater the thrust contribution generated under the same spin ratio conditions. The maximum thrust can reach 750,000 N; the cylinder's auxiliary propulsion contribution shows a better advantage in $\alpha = 2.0$. The effective power generated by the cylinder reaches a maximum of 2,240 kW for environmental wind speed = 20 m/s and $\alpha = 1.0$.

Keywords: Ship propulsion; Flettner rotor; Wind energy; Rotating cylinder; Numerical simulation

INTRODUCTION

Due to the increased volume of seaborne cargo transactions around the world, the number of merchant ships is increasing. Ships not only consume a large amount of fuel during a voyage but they also produce exhaust gas, polluting the environment by burning fuel. In order to reduce harmful emissions from ships and promote the application of new cleaner energy, IMO puts forward higher requirements for emissions from ships. "Green ship" has become the current trend in the development of the ship industry and it is has become urgent to find new, alternative clean energy [1–3]. Wind energy is a kind of renewable energy with the advantages of abundant reserves, wide distribution and pollution-free [4, 5]. The wind energy over the ocean is more abundant because the sea is open and wind friction

is small. There are great advantages for the application of wind energy to ships sailing in the ocean.

In terms of wind energy utilisation by ships, scholars at home and abroad have carried out many related studies, including: traditional sails, Flettner rotor auxiliary propulsion, kite auxiliary propulsion, and airfoil sail auxiliary propulsion [6–9]. Among them, the Flettner rotor is a reasonable system, regarding the utilisation of wind energy on ships. It has a history of more than one hundred years of research. This kind of rotor propulsion is usually called "Flettner rotors". The first time such equipment was installed on a ship was in the early 1920s. Flettner rotors are mainly installed on the deck of a ship. One side of the Flettner rotors forms a low pressure area and the other side forms a high pressure area, so that it can generate lift (like a sail) to boost the ship, also known as the Magnus effect.

Nomenclature

D	Diameter of cylinder
H	Height of cylinder
A	Cross-sectional area of cylinder
ρ	Fluid density
ν	Kinematic viscosity is $1.45 \cdot 10^{-5}$ Pa/s
V_{ship}	Ship speed
$V_{en.}$	Environmental wind speed
V_a	Apparent wind speed
$Re = \frac{V_a * D}{\nu}$	Reynolds number
U_{tan}	Tangential velocity of cylinder
$\alpha = \frac{U_{tan}}{V_a}$	Spin ratio
ω	Angular velocity of rotating cylinder
$y+$	A non-dimensional wall distance

C_L	Lift coefficient
C_T	Thrust coefficient
C_D	Drag coefficient
C_H	Heel coefficient
C_f	Friction coefficient
T	Thrust
P_T	Thrust power
C_M	Moment coefficient
P_{motor}	Power consumption
$P_{ef.}$	Effective power
p	Static pressure
p_{∞}	Free flow pressure

$$C_p = \frac{p - p_{\infty}}{0.5 * \rho * V_a^2} \text{ Pressure coefficient}$$

Flettner rotors have been installed on some ships around the world and have been put into practical use. In 1924–1926, the German ship *Buckau* first installed a rotor device and conducted a sailing test, as shown in Fig. 1(a). An interesting example is the fact that the wind energy company Enercon launched a Flettner-driven cargo ship, named “E-Ship 1”. Compared with traditional cargo ships of the same size, in 2010 the Flettner rotors on “E-ship 1” (developed by Enercon) saved as much as 25% of the fuel that would normally be used (<https://www.evwind.es/2013/07/30/enercon-rotor-sail-ship-e-ship-1-saves-up-to-25-fuel/34733>). Since its maiden voyage in 2010, E-Ship 1 (developed for transporting Enercon wind turbine components) has covered more than 170,000 sea miles, as shown in Fig. 1(b). Then, in November 2014, a 9,700 ton ro-ro ship “Estraden” (owned by the Finnish

shipping company Bore) adopted Norsepower’s Flettner rotor plan. The ship sailed back and forth between the Netherlands and the United Kingdom, potentially saving 5% of fuel, as shown in Fig. 1(c). In January 2018, the 6,400 ton bulk carrier “Afros” (customised by the Greek shipowner Victoria Steamship) installed four Flettner rotors. In April 2018, Flettner rotors were installed on the “Viking Grace,” owned by Viking Cruises; they were 24 m high and 4 m in diameter, and it became the world’s first passenger ship using Flettner rotors technology. There are also practical applications of Flettner rotors on oil tankers. In August 2018, Maersk announced that two Flettner rotors, with a height of 30 m and a diameter of 5 m, were installed on an L2 tanker. This is the largest Flettner rotor in a practical application so far, as shown in Fig. 1(d).



Fig. 1. Flettner rotors in actual applications

There are also many practical cases in the application of Flettner rotors on medium and large merchant ships. Flettner rotors have become effective aids for ship navigation. Many experiments and numerical simulations have also been carried out on the utilisation of Flettner rotors to achieve ship propulsion. Bordogna et al. [10] studied a series of large wind tunnel tests on Flettner rotors, with the aim of better understanding the effect of the Reynolds number on the aerodynamic performance of Flettner rotors and, for aerodynamic performance, a velocity ratio of 2.5 was a key point. Marco et al. [11–13] assessed the impact of aspect ratio, spin ratio and end plate diameter on Flettner rotor performance; endplates installed on the Flettner rotor had a good effect. In reference [14], the relative position and velocity ratio of two Flettner rotors were tested and the conclusion was drawn that the velocity ratio and relative position were the decisive factors determining the influence of aerodynamic interaction on the performance of Flettner rotors. The flow structures with different Reynolds Numbers and different spin rates were discussed. Laminar and turbulence flow models were compared by Karabelas et al. [15]. Craft et al. [16] proposed that a superstructure disc on the rotors can result in a slight increase in the lift coefficient at high RPM. Traut et al. [17] studied numerical models of two wind power technologies, Flettner rotors and a towing kite, and proposed a technical method for evaluating the contribution of wind energy to ship propulsion, applying it to five different shipping routes. Salter pointed out a way of using Flettner rotors to achieve high-lift coefficients and high lift-drag ratios [18]. A study of a rotating cylinder with an endplate was conducted by Badalamenti and Prince [19], where spinning and stationary endplates were considered. The results of the study show that, although the endplate can significantly enhance the lift and improve the lift-to-drag ratio, the ultimate lift coefficient is always reached regardless of the endplate conditions.

According to the conditions generated by the Magnus effect, the magnitude of the Magnus force not only depends on the wind speed and the angular velocity of the Flettner rotors, but it is also affected by the wind-receiving area of the Flettner rotors. For Flettner rotors using the Magnus effect, a larger wind-receiving area produces greater boosting force [20–23]. In order to use wind energy more effectively and produce better boosting effects for ships, most Flettner rotors are installed in pairs on ships. The diameter range of the cylinder is between 1.5 m and 5 m, the height range is 15 m to 40 m and, in general, the number of Flettner rotors is 2 to 6 [24, 25]. However, a large number of Flettner rotor installations will increase the additional load capacity of the ship and will also occupy the ship's deck space. Installing multiple cylinders will reduce the ship's effective cargo space, especially for ships with high deck space utilisation; this reduces the economic value of merchant ships, such as container ships [26, 27].

It will be of great significance if a rotating cylinder can be designed that can not only assist the navigation of the ship but also save space on the ship's deck. Based on the above discussion, this article proposes a new type of Flettner rotor installation and method of use, such that the rotating cylinder

and superstructure are cleverly combined and a transparent cylinder is set on the outer side of the ship's superstructure. On the basis of not affecting the original functions of the superstructure, a huge-sized Flettner rotor and a new type of rotating cylinder was created. This can increase the wind-receiving area of the rotating cylinder so that the wind energy can be used to a greater extent and there is no need to install a separate cylinder on the deck. This saves installation space and it will not affect the layout of deck cargo spaces and machinery, or the loading and unloading of ships. This new type of vertical rotating cylinder uses the Magnus effect, as shown in Fig. 2. Harnessing the power of wind to generate thrust increases efficiency by reducing fuel consumption, bunker costs and harmful emissions. The new rotating cylinder can be installed on newly built ships, which will generate a large amount of thrust to assist the ship's navigation. In general, Flettner rotors can use a small proportion of ship auxiliary power to achieve rotation; its potential to save main engine fuel consumption can reach 3% to 25%. It has economic value for merchant ships.

THE STRUCTURE OF THE NEW ROTATING CYLINDER AND ITS INSTALLATION

The Flettner rotor usually works in lateral winds and the amount of thrust that it generates mainly depends on wind and ship speed. For merchant ships, the beneficial effects of the actual installation and use of the Flettner rotor depends on the size of the ship, the sailing area, and the operational profile. In order to analyse and evaluate the contribution of the new of type rotating cylinder, a 100,000 ton tanker ship was selected as an example of a ship fitted with a rotating cylinder. The number of superstructure floors of the merchant ship is 6. In order to avoid disturbing the observation of the ship's crew on the navigation deck, the highest edge of the cylinder is set up at the lower edge of the navigation deck; the lowest edge is set up at the upper edge of the superstructure on the first floor. This design does not affect the passing function of the personnel between the superstructure and the main deck. In addition, the navigation deck is circular and its diameter equal to the width of the ship, to ensure that the driver can easily watch the berthing process. Therefore, the specific structure of the new rotating cylinder is: a circular, hollow cylinder made of transparent material and enveloped in the middle part of the superstructure. It is driven by a motor to achieve rotation around the axis, and to obtain better rotor performance without affecting the original function of the superstructure. There is an endplate on the top of superstructure, as shown in Fig. 2. When the ship is sailing on the sea, the rotating cylinder is affected by lateral winds, which causes it to produce Magnus thrust. Besides this, the use of transparent materials for the rotating cylinder material can ensure sufficient light into the superstructure. There are emergency stop buttons on each floor of the superstructure; emergency stop buttons and life-saving hammers are installed on the floors near the lifeboat. The first purpose of this design is to make an emergency stop when the

rotating cylinder is in danger, the second is to stop the rotating cylinder when the ship encounters a dangerous situation; the relevant personnel then smash the transparent materials with a life-saving hammer to escape the scene in time.

The new rotating cylinder has great advantages. On the one hand, a major feature of the cylinder is its large diameter. This structure increases the wind-receiving area of the cylinder. It can be seen from the conditions that produce the Magnus effect force that increasing the wind area of the rotating cylinder also increases the lift of the cylinder. On the other hand, due to the windward surface usually being flat to the traditional ship's superstructure, the wind friction caused by the ship's sailing process is relatively large. When a rotating cylinder is set in the ship's superstructure. The cross-section of a cylinder is a circle and its sides are approximate streamlined. Therefore, the cylinder can reduce the friction of the superstructure. The shape of the superstructure will be compared and demonstrated in Section 4.1. Last but not least, all kinds of merchant ships have superstructures and the rotating cylinder can be appropriately improved, so the new rotating cylinder is suitable for many types of merchant ships.

The more common 100,000 ton class of ship was selected in this analysis, with the oil tanker "Bei Hai Wei Wang" of COSCO SHIPPING being the typical ship specifically used; some of its parameters are shown in Tab. 1. Generally, the height of a single deck of a merchant superstructure is 3.05 m, the height of the cylinder (H) is equal to about 4 decks in the middle of the superstructure (H = 12.5 m). In order to use the space as effectively as possible and to increase the area of the rotating cylinder, its diameter (D) should be as close to the width of the ship as possible; take D = 40 m. Moreover, the new rotating cylinder can ensure the normal basic functions of the ship's superstructure; the cylinder here is a cylinder with a diameter of 40 m and a height of 12.5 m. The endplate diameter is 42 m.

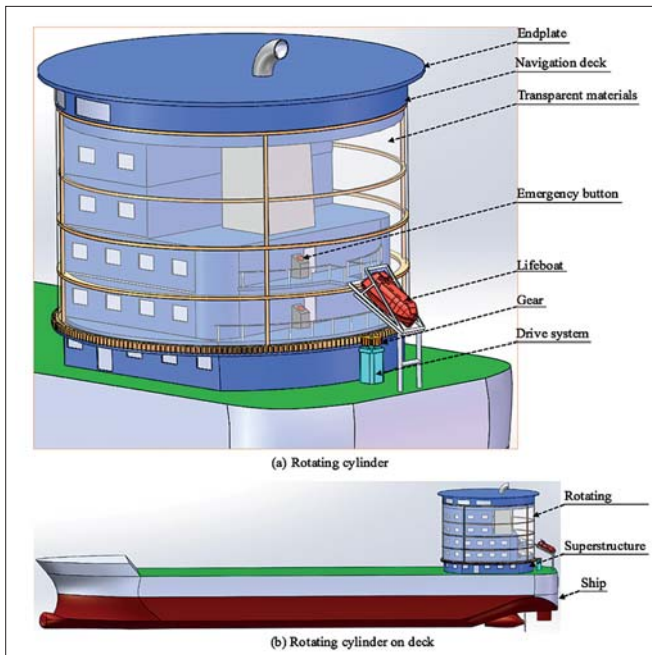


Fig. 2. The new rotating cylinder and its installation position on the ship

Tab. 1. Parameters of "Bei Hai Wei Wang"

Parameters	Value	Parameters	Value
Type	Aframax	Draft (m)	11.90
Length overall (m)	243.00	Deadweight (ton)	104404
Breadth moulded (m)	42.00	Main engine power (kW)	15260
Depth (m)	20.63	Maximum speed (knots)	15

PHYSICAL AND NUMERICAL MODELS

PHYSICAL COMPUTING MODELS

When the ship is subjected to the effects of environmental wind (V_{en}), the ship will be subjected to the Magnus effect force due to the existence of the rotating cylinder. If a sensor is installed to monitor the wind in real time, the starting, stopping and steering of the rotating cylinder can be adjusted in time with the change of wind direction, so as to ensure that the Magnus force on the cylinder is maximised along the ship's direction of travel. In order to explore the potential of the new rotating cylinder as a ship booster, it is important to consider that the wind acting on the cylinder is a vector sum of the environmental wind and the ship speed. According to Eq. 1, the apparent wind speed in the vicinity of the cylinder can be calculated as V_a , in Fig. 3(a). In the following simulation, both the lateral wind perpendicular to the ship and the ship's speed are considered; the ship's speed is fixed at 5 m/s (about 10 knots).

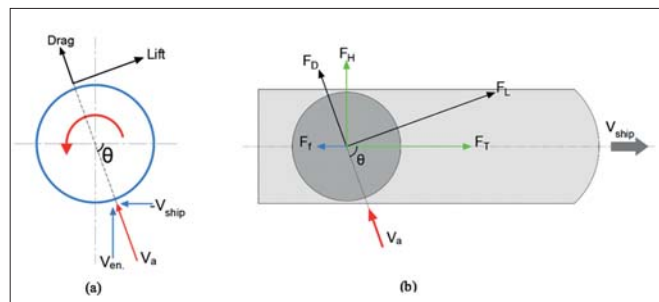


Fig. 3. Diagrams of apparent wind (a) and ship force (b)

The thrust (C_T) and heel coefficients (C_H) vary with the size and direction of the angular velocity of the cylinder and the apparent wind speed during the ship voyage. They are transformed by the lift coefficient (C_L), the drag coefficient (C_D) and the angle θ between the apparent wind speed and heading, as realised in Fig. 3. The equations Eq. (2) and (3) for calculating C_T and C_H are given [9].

$$V_a = V_{en} - V_{ship} \quad (1)$$

$$C_T = C_L * \sin^\theta - C_D * \cos^\theta \quad (2)$$

$$C_H = C_L * \cos^\theta + C_D * \sin^\theta \quad (3)$$

In the ship, the thrust force F_T and side force from the heel F_H are calculated based on the thrust coefficient C_T , heel

coefficient C_H , air density ρ , apparent wind speed V_a , and the sail area A according to equations (4) and (5). The diagram of ship forces is given in Fig. 3(b).

$$F_T = 0.5 * \rho * A * V_a^2 * C_T \quad (4)$$

$$F_H = 0.5 * \rho * A * V_a^2 * C_H \quad (5)$$

The power consumed by the motor rotating the cylinder and the lift, drag acting on the cylinder together determine the power value that can be generated by the rotating cylinder. The thrust obtained from the cylinder is calculated as a vector and projection of the lift and drag along the ship's course. The amount of power generated by the thrust and the power consumed by the motor are calculated, and they are given by the equations (6) and (7), where C_M is the Moment coefficient [17].

$$P_T = T * V_{ship} \quad (6)$$

$$P_{motor} = 0.5 * \rho * A * V_a^3 * C_M * \alpha \quad (7)$$

The effective power P_{ef} is calculated as the difference between the power delivered by the rotating cylinder and the power that is consumed by the motor to rotate it.

$$P_{ef} = P_T - P_{motor} \quad (8)$$

NUMERICAL MODELS

The purpose of the modelling was to simulate the lift, drag, thrust coefficient and other data of the rotating cylinder installed onto the ship's superstructure. This experiment used the CFD software 'Fluent' to carry out simulation calculations. The three-dimensional computational domain containing the rotating cylinder was established to obtain more accurate results. The SIMPLE algorithm was used to solve the N-S control equations and the two-order upstream scheme was chosen to ensure accuracy. The turbulence model chosen was the Realizable k- ϵ model [28–30]. The RANS equation was used as the basic equation for solving the computational domain around the rotating cylinder, which included the continuity Eq. (9) and the momentum Eq. (10). The simulations were performed in an unsteady way.

$$\nabla \cdot U = 0 \quad (9)$$

$$\rho \bar{u}_j \frac{\partial \bar{u}_i}{\partial x_j} = \rho \bar{f}_i + \frac{\partial}{\partial x_j} \left[-\bar{p} \delta_{ij} + \mu \left(\frac{\partial \bar{u}_i}{\partial x_j} + \frac{\partial \bar{u}_j}{\partial x_i} \right) - \rho \overline{u'_i u'_j} \right] \quad (10)$$

where ρ is the density of fluid; U is the relative velocity; μ is liquid viscousness; \bar{p} is static pressure; δ_{ij} is Kronecker delta; \bar{f}_i is the mass force term; $-\rho \overline{u'_i u'_j}$ is apparent stress owing to the fluctuating velocity field, generally referred to as the Reynolds stress.

COMPUTATIONAL DOMAIN AND BOUNDARY CONDITIONS

As shown in Fig. 4(a), the entire computational domain is shaped as a rectangle with a length of 22.5D, a width of 17.5D, and a height of 12.5D, where D is the diameter of the rotating cylinder, and the Cartesian coordinate system origin is centred at the bottom of the cylinder. The whole computational domain is arranged by coupling structured and unstructured grids, specifically tetrahedral grids near the ship; the grids around the rotating cylinder are encrypted; and layer boundary grids on the surface of the rotating cylinder are established [31, 32]. The other regions use structured grids, as in Fig. 4(b). Furthermore, the grid set up allowed a non-dimensional wall distance (y^+) value approximately equal to 1.0; the Max-Skewness is 0.84 and the blocking ratio is about 1.2%.

The computational domain is shown in Fig. 4(a). The right side and the front side of the ship are the inlet boundary, which adopts the velocity inlet boundary condition. The environmental wind direction is positive along the y-axis and the ship's sailing direction is positive along the x-axis; the wind speed condition is the apparent wind speed V_a and it is referenced to the above-mentioned apparent wind in Fig. 3(a). The outlet boundary adopts the pressure outlet boundary condition and the value is one atmospheric pressure. The wall is used at the top and bottom of the computational domain. The 1.5D range near the cylinder surface is the rotating area (circle), as shown in Fig. 4(b). The cylinder surface is a non-slip wall with a certain roughness and the cylindrical circle area is turned in a counter-clockwise direction.

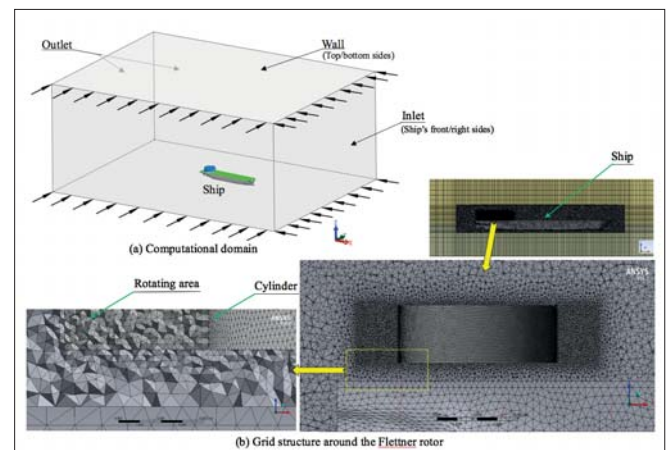


Fig. 4. Computational domain and boundary conditions

The 1.5D diameter rotating area is used to simulate the domain generated by the rotation of the cylinder, which is especially suitable for rotational movements [33]. It should be noted that the time step of the simulation is a function of

the angular velocity (ω). For the convergence of the numerical scheme, according to experience, there is a limitation on the maximum cell-based Courant-Friedrichs-Lewy (CFL) number in a time step [11]. Therefore, a larger angular velocity should correspond to a smaller value of time step.

GRID INDEPENDENCE ANALYSIS AND COMPARISON DATA VALIDATION

The grid independence study is performed by using four different grid densities with approximately 3,500,000, 4,000,000, 4,500,000 and 6,000,000 elements. The pressure coefficient C_p is used for comparing different grids when verifying the numerical method. The other conditions for this comparative validation were: 5-level wind, spin ratio α is 2, and Re is 3.08×10^7 . The C_p data curves, corresponding to the four grids, are shown in Fig. 5 and Table 2 shows the result of grid independency validation. It is concluded from the comparative analysis that the grid reaches 4,500,000 elements and further increases in grid density do not significantly affect the results. The error of the C_p is less than 0.4% when compared with the case of 6,000,000 elements. Therefore, the calculation of the efficiency and accuracy are taken into account and the numerical simulation is based on a grid of about 4,500,000 elements [34].

Tab. 2. Results for grid independency validation

Description	Scale	Element number	Average- C_p (35-40 s)	Error of average- C_p
Grid independence validation	Coarse	3,500,000	-0.747	1.1%
	Medium	4,000,000	-0.730	1.2%
	Fine	4,500,000	-0.736	0.4%
	Very fine	6,000,000	-0.739	0

In addition, since the objective conditions limited the experimental validation of the device, we simulated the example for the experiments performed by Bordogna

et al. using the CFD grid processing method and simulation procedure in the paper. The specific experimental conditions of the cylinder were $H = 3.73$ m, $D = 1$ m and $Re = 1.0 \times 10^6$ [10]. The results of the numerical simulation should be compared with experimental data. The simulation results are shown in Fig. 5(b) “Experimental data vs CFD simulation results” and it can be seen that the two results are generally consistent. Therefore, similarly, our simulations have some reliable accuracy in the study.

ANALYSIS OF THE RESULTS

To verify the characteristics and boosting effect of the new rotating cylinder, the characteristics of the rotating cylinder and the traditional superstructure (middle section) will be compared in Section *Comparison of different types of superstructure*. In Section *Discussion on spin ratios and wind levels*, the parameters of cylinder lift coefficient, drag coefficient, and thrust coefficient corresponding to different spin ratios under wind speed conditions of 5, 6, 7 and 8 levels, are investigated. In Section *Energy contribution to ship navigation*, the contribution of the rotating cylinder to the ship’s boosting is studied. In order to verify the influence of the variation of Reynolds number on the cylinder, a brief discussion is made in Section *The influence of Reynolds number on the performance of the new rotating cylinder*.

In order to obtain more realistic simulation results, the following apparent wind speed is the result of considering the combined effects of ship speed and environmental wind speed (see Fig. 3(a)). The ship speed is approximately 10 knots and environmental wind speed regulations are shown in Table 3.

Tab. 3. Environmental wind speed

Wind level	5	6	7	8
Environmental wind speed (m/s)	10	12	15	20

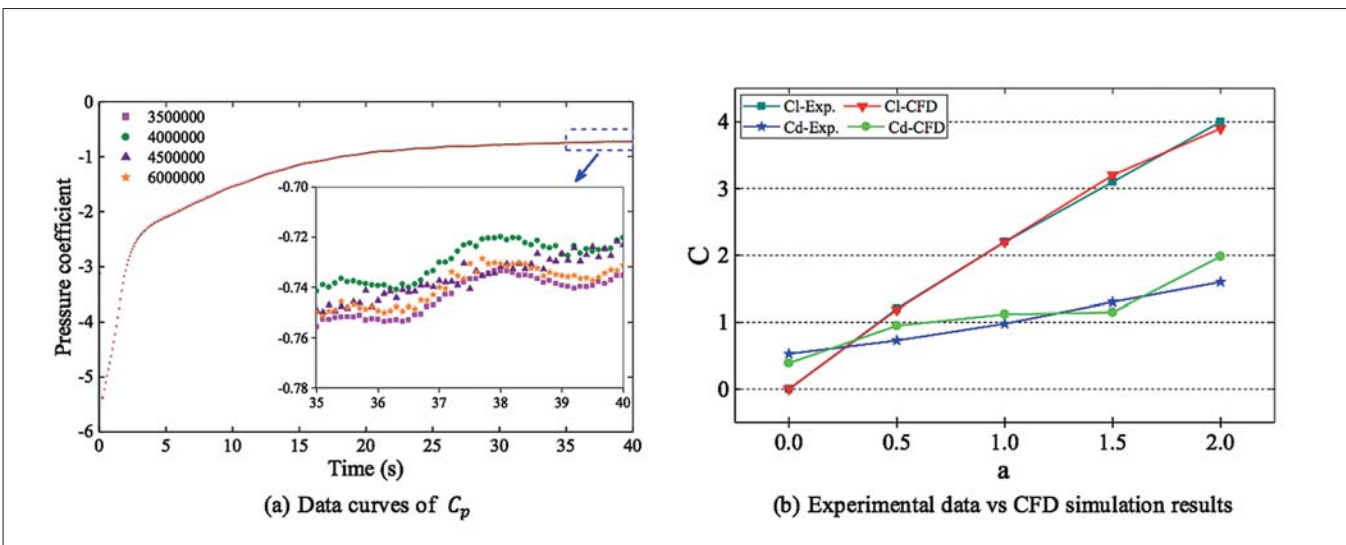


Fig. 5. Validation of the numerical method

COMPARISON OF DIFFERENT TYPES OF SUPERSTRUCTURE

COEFFICIENTS OF FORCE FOR ROTATING CYLINDER AND TRADITIONAL SUPERSTRUCTURE

The traditional superstructure consists of 4 to 6 floors; the middle 4 floors of the superstructure can be approximated into a rectangular shape, without considering the Navigation deck and the first-floor superstructure. In order to compare the effects of the new cylinder superstructure with the traditional superstructure on the ship's navigation, the friction coefficients (C_f) and heel coefficients (C_H) generated by the different types of superstructure are investigated under 5-level wind conditions. The volumetric parameters of the three superstructure types (traditional type, cylinder type and rotating cylinder type) are given in Table 4, and the three volumes are equal. The superstructure of the new rotating cylinder type is proposed in this paper, it is modified or added to the middle 4 floors of the superstructure on the basis of not affecting the function of the ship's superstructure.

The friction coefficient (C_f) graph and the average friction (F_f) bar graph for three types of superstructure are shown in Fig. 6(a). As can be seen, the friction coefficient of the traditional and cylinder superstructure is positive in 20 s, i.e. the friction generated by the superstructure of the ship's navigation process has always existed. The traditional type produces an average friction of 94,877.73 N; the cylinder's average friction is 4,833.31 N. Moreover, the friction coefficient of the traditional type is greater than the friction coefficient of the cylinder type. So, cylinder type superstructure has a certain effect on reducing wind friction compared to the traditional type. It is worth noting that the friction coefficient at 20 s is negative about the rotating cylinder type; its average friction of -151,520.34 N indicates that the superstructure of rotating cylinder type produced a forward thrust.

Tab. 4. Three types of superstructure

Type	Size (m)	α	Volume (m ³)
Traditional	35*35*12.5	0	15,700
Cylinder	40*12.5	0	
Rotating cylinder	40*12.5	2.0	

In Fig. 6(b), the heel coefficients (C_H) and average heel forces (F_H) for the three types of superstructures are shown, respectively. Three types of superstructure heel coefficient are positive, the cylinder type superstructure produces the smallest heel coefficient and the heel coefficient of the rotating cylinder type is the largest. By observing the three types of heel force it can be seen that the average lateral force of the traditional, cylinder, and rotating cylinder type superstructures are 55,772.91 N, 16,060.64 N and 79,515.39 N, respectively. Due to the additional friction generated by the rotating cylinder superstructure, as a result of Magnus forces acting on the rotating cylinder of $\alpha = 2.0$, the heel force for a rotating cylinder of the same size is greater than for a cylinder of $\alpha = 0$.

PRESSURE DISTRIBUTION AROUND THE SUPERSTRUCTURES

The three types of pressure distribution around the superstructures are given using the CFD-post processing function. Fig. 7 shows the wind pressure area around the superstructures on the mid-plane (in the middle of the cylinder in the z-axis).

It can be seen that the high-pressure area in all three figures is mainly located below the superstructures (because the y-axis direction is the environmental wind inlet, which has a value of 10 m/s). The maximum wind pressure in the high-pressure area of the traditional type superstructure can be seen as 95 Pa in Fig. 7(a). In Fig. 7(b), the maximum wind pressure around the cylinder type superstructure is 92 Pa and its high-pressure area is smaller. Fig. 7(c) shows

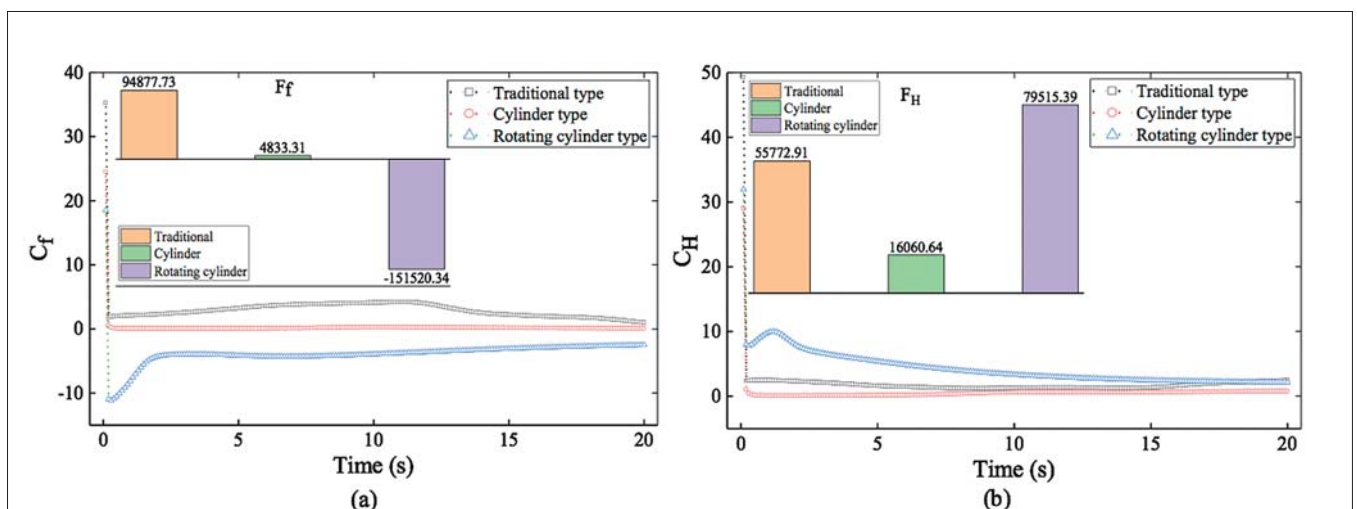


Fig. 6. Forces and force coefficients of the three types of superstructure

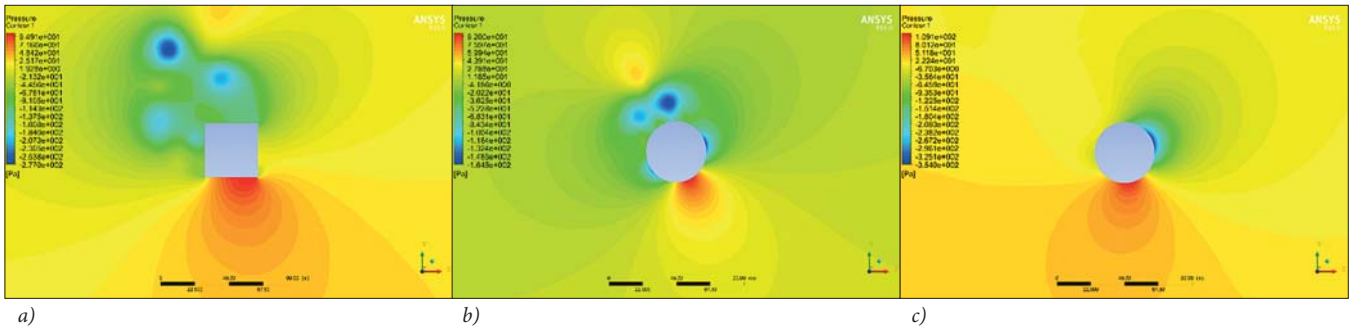


Fig. 7. Wind pressure area around the three kinds of superstructures on the mid-plane

the wind pressure around the rotating cylinder, which is also the main object of the simulation. The comparison with the other two graphs shows that the pressure of the rotating cylinder type and cylinder type superstructure are clearly different; the right side of the rotating cylinder (the direction of the ship's navigation) is a low pressure area, so, the whole rotating cylinder will be subjected to pressure along the x-direction. Due to the rotation of the cylinder, there is the Magnus effect around it, which creates a beneficial pressure differential. The ship is fitted with a rotating cylinder to take advantage of the lateral wind, which helps the ship move forward.

DISCUSSION ON SPIN RATIOS AND WIND LEVELS

THE EFFECTS OF DIFFERENT SPIN RATIOS ON THE LIFT AND DRAG COEFFICIENT FOR THE ROTATING CYLINDER

According to the relevant studies [11, 16], the environmental wind speed and the ship speed, as well as the angular velocity of the cylinder, have a significant influence on the lift coefficient of the rotating cylinder. The variation of the spin ratio (α)

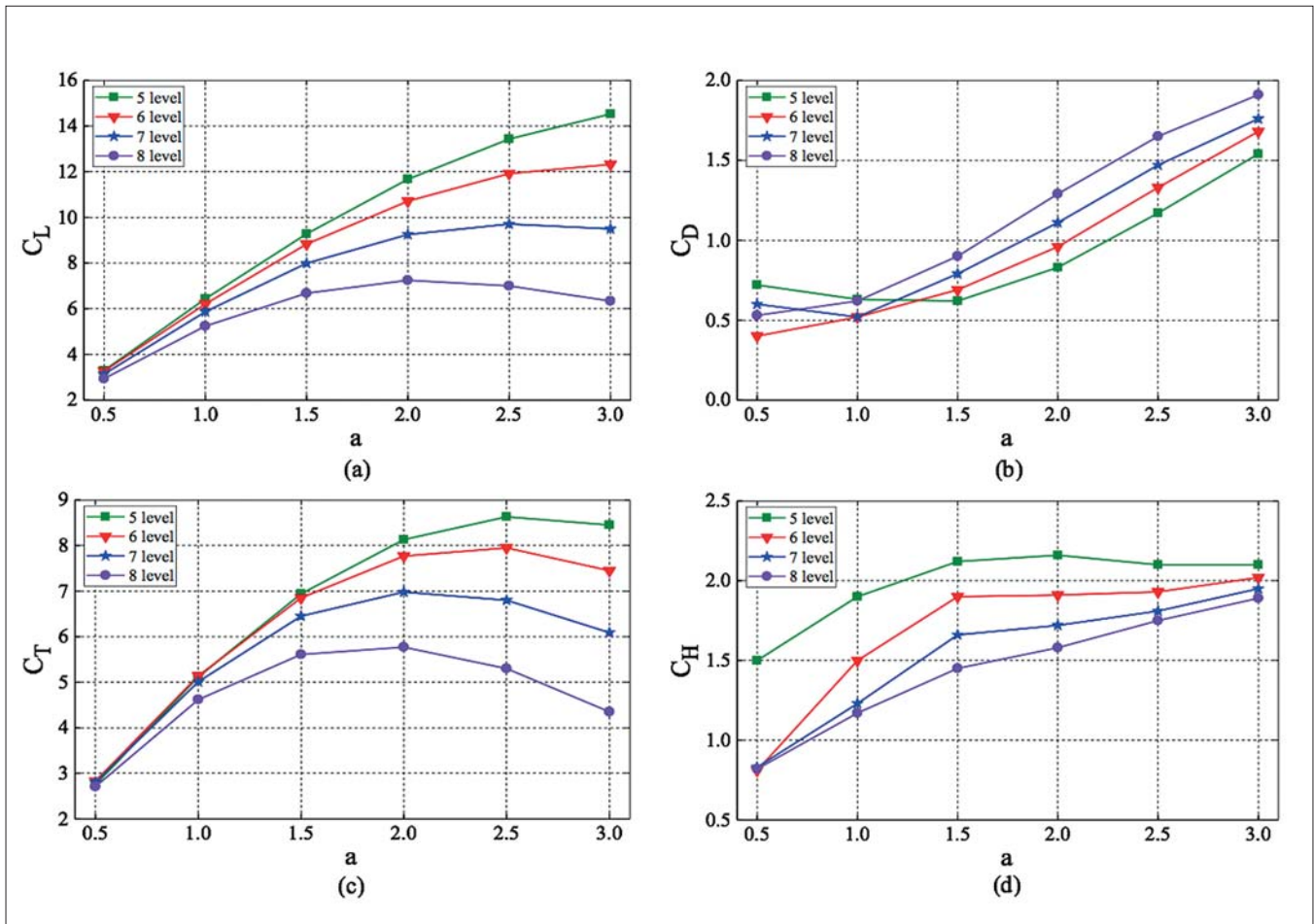


Fig. 8. The force coefficient of the rotating cylinder

affects the contribution of the rotating cylinder to navigation. In order to study the contribution of the rotating cylinder with different spin ratios, the changing effects of the spin ratio on the same rotating cylinder at different wind levels will be discussed separately. Specifically, the rotating cylinder lift coefficient (C_L), drag coefficient (C_D), thrust coefficient (C_T), and heel coefficient (C_H) is given to analysis and discussion. The force coefficient of the rotating cylinder is shown in Fig. 8.

Fig. 8 is the point line graph of the lift coefficient, drag coefficient, thrust coefficient and heel coefficient for a rotating cylinder in 5, 6, 7, and 8 level wind conditions. From the figure, it can be seen that the spin ratio has a significant impact on the force coefficient of the cylinder. Fig. 8(a) is the rotating cylinder lift coefficient graph. Wind levels of 5 and 6 correspond to the lift coefficient gradually increasing with an increase in spin ratio and the maximum lift coefficient can reach 14.53. Wind levels of 7 and 8 correspond to the lift coefficient and inflection points can be seen, wind level 7 corresponding to the lift coefficient's maximum value of 9.71, which appears when the spin ratio is 2.5. Level 8 corresponds to the maximum value of lift coefficient appearing at a spin ratio of 2.0.

Fig. 8(b) shows the drag coefficient of the rotating cylinder, the curves corresponding to wind levels 6, 7 and 8, showing an overall upward trend as the spin ratio increases. In the case of level 5 wind, the drag coefficient appears to be the smallest value when the spin ratio is 1.5, after which the coefficient becomes larger. By observing the directional trend of the drag coefficient curve, it can be assumed that, due to the Magnus effect, the drag coefficient becomes larger and larger as the spin ratio continues to increase. This trend of increasing drag coefficient is consistent with the results of Liu et al. [25].

In Fig. 8(c), it can be seen that the thrust coefficient first increases and then decreases with the increase in spin ratio for the rotating cylinder. The four kinds of wind inflection point are different. That is to say, the thrust coefficient of a cylinder has the best value with a change of spin ratio. This means that the thrust coefficient becomes smaller with an increase in environmental wind speed, but it does not mean that the cylindrical thrust contribution to the ship becomes smaller.

Fig. 8(d) shows the curves of heel coefficient for the rotating cylinder. It can be seen that the heel coefficients increase as the spin ratio increases, but their curve steepness becomes progressively smaller. At the same spin ratio, the heel coefficient of the rotating cylinder becomes smaller as the apparent wind speed increases. In addition, the maximum value of the thrust coefficient in Fig. 8(c) is 8.63 under the 5-level wind condition. The maximum value of heel coefficient in Fig. 8(d) is 2.16, which shows that the thrust contribution to the ship brought by the installation of the

rotating cylinder is much larger than the heel force generated by it. This also shows that the new type of rotating cylinder is very beneficial to the ship's sailing.

PRESSURE AROUND THE ROTATING CYLINDER AT DIFFERENT SPIN RATIOS

In order to better analyse the pressure values around the cylinder for different spin ratios, the pressure graphs are given spin ratios of 0.5, 1.0, 1.5, 2.0, 2.5 and 3.0 in a level 6 wind, respectively. As shown in Fig. 9, wind pressure area and contours are plotted around the cylinder on the mid-plane for different spin ratios. This Reynolds number is 3.59×10^7 .

It can be seen from the figure that a low pressure area appears on the right side of the cylinder; the presence of this pressure difference causes a thrust along the ship's sailing direction. Fig. 9(a) shows the pressure distribution for the spin ratio of 0.5, compared with the other images, the pressure difference around the cylinder along the x-axis direction in Fig 9(a) is the least obvious; it can be seen from the pressure contour in the figure that its maximum pressure difference is 515.7 Pa. In addition, as the spin ratio increases, the pressure difference around the cylinder along the x-axis direction becomes larger. At the spin ratio equal to 2.0, the maximum difference of the contour is reached at 900.3 Pa. This indicates that there is an optimal value of the spin ratio

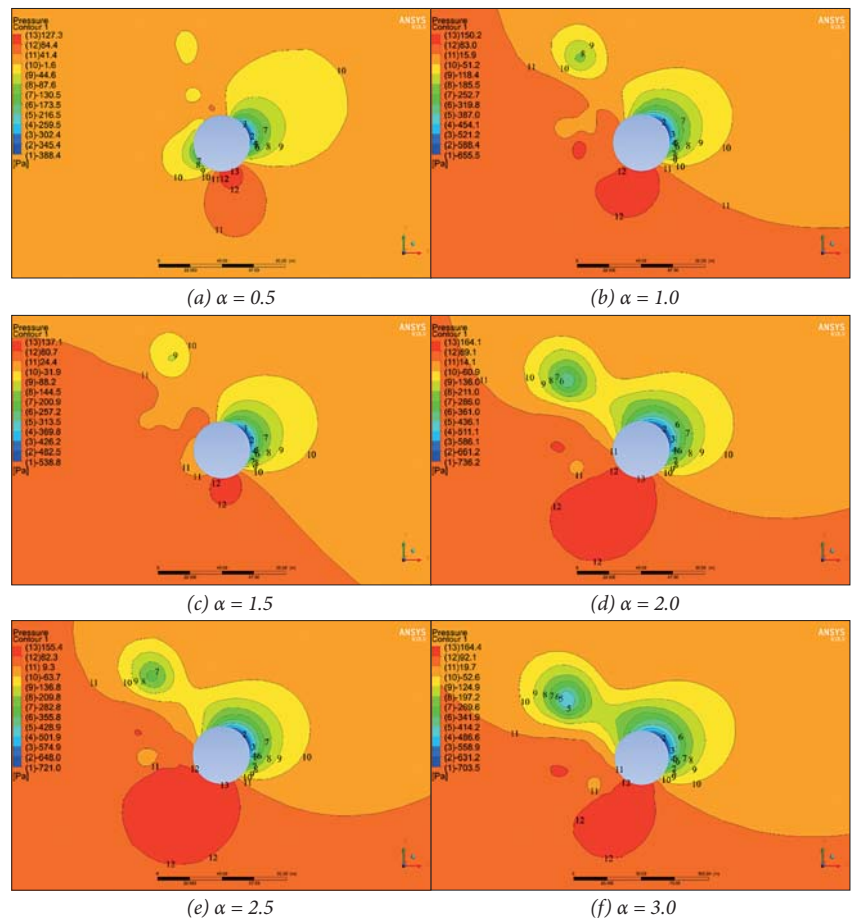


Fig. 9. Wing pressure area and contours plotted around the cylinder on the mid-plane for different spin ratios

of the new rotating cylinder of about 2.0. It can also be proved that the spin ratio is one of the main factors influencing the Magnus effect of the cylinder, by comparing the pressure. So, it is necessary to change the angular velocity of the rotating cylinder in real time according to the change of the environmental wind.

THRUST CONTRIBUTION OF ROTATING CYLINDER

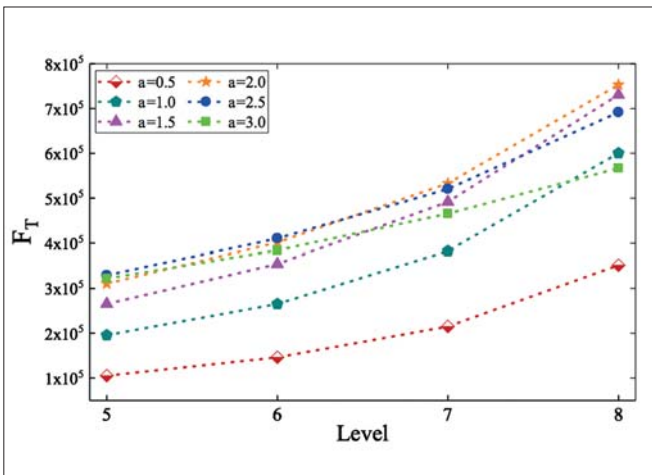


Fig. 10. Thrust of rotating cylinder

Fig. 10 shows the thrust curves of the rotating cylinders, corresponding to different wind levels for the six kinds of spin ratio conditions. As can be seen from the figure, the greater the environmental wind speed, the greater the thrust contribution generated by the cylinder in the same spin ratio. When the spin ratio is 0.5, the thrust is the smallest. In the four kinds of wind levels, the spin ratio of 2.5 corresponding to the cylinder thrust has been greater than the spin ratio of 3.0. The thrust corresponding to $\alpha = 1.5$ and 2.0 shows a steeper rise when the wind level increases. Finally, the two thrusts reach their maximum value of more than 750,000 N under the wind level 8 conditions. At the same time, this set of curves shows that it is not the larger spin ratio that corresponds to the rotating cylinder's thrust contribution. On the contrary, the rotating cylinder shows a better advantage when $\alpha = 2.0$.

ENERGY CONTRIBUTION TO SHIP NAVIGATION

The power consumed by an electric motor and the lift and thrust acting on the cylinder determine the power of the main engine that a rotating cylinder can replace. It is necessary to study the actual energy contribution of the rotating cylinder to the ship. Due to the existence of the Magnus effect, the rotating cylinder generates positive thrust that provides the ship's navigation. The thrust power (P_r) and effective power (P_{ef}) of the rotating cylinder corresponding to different spin ratios are analysed in Fig. 11.

As shown in Fig. 11, the four bar graphs indicate the thrust power and effective power corresponding to the

wind conditions of levels 5, 6, 7 and 8, respectively. On the whole, the thrust power shows a tendency to increase and then decrease as the spin ratio increases; the maximum thrust power for wind levels of 5 and 6 are 1,649,351 W and 2,057,131 W respectively at the spin ratio of 2.5; the maximum thrust power for wind levels of 7 and 8 are 2,669,711 W and 3,763,193 W at the spin ratio of 2.0.

More valuable than the thrust power of information is the effective power of the rotating cylinder, since it considers the removal of the motor power (P_{motor}). In combination with the analysis in Fig. 11 and Table 5, it can be seen in Fig. 11(a) that the maximum effective power value is 1,125,122 W at a spin ratio of 1.5. In Fig. 11(b), the maximum effective power value is 1,436,422 W at a spin ratio of 1.5 under level 6 wind. Similarly, the maximum effective power in Fig. 11(c) is 1,827,413 W. However, as can be seen in Fig. 11(d), the maximum effective power corresponding to level 8 occurs at a spin ratio of 1.0, which is 2,248,611 W. A comparison of the maximum effective power in the four cases shows that the maximum effective power of the rotating cylinder becomes larger as the environmental wind speed increases. Table 5 shows that, when the maximum effective power occurs, the effective power of the rotating cylinder can reach 75 to 85% of its thrust power, which also shows that the contribution of the rotating cylinder to the ship's propulsion is much larger than the energy consumed by its own rotation.

Tab. 5. Value comparison of maximum power

Wind level	Maximum effective power (W)	Spin ratio	Thrust power (W)	Effective power/Thrust power
5	1,125,122	1.5	1,331,002	85%
6	1,436,422	1.5	1,775,421	81%
7	1,827,413	1.5	2,464,121	74%
8	2,248,611	1.0	3,006,123	75%

THE INFLUENCE OF REYNOLDS NUMBER ON THE PERFORMANCE OF THE NEW ROTATING CYLINDER

The experimental study by Bordogna et al. showed that the Reynolds number is one of the factors affecting the lift coefficient and drag coefficient of a rotating cylinder [10, 15]. We conducted a simple comparative analysis of the lift coefficient, drag coefficient and thrust value of the new rotating cylinder under several different Reynolds number conditions. The specific simulation still refers to the ship's sailing speed of 5 m/s and the air kinematic viscosity $\nu = 1.45 \times 10^{-5}$ Pa/s. Fig. 12 shows the lift coefficient and drag coefficient of the rotating cylinder when the spin ratio is 1.5 and 2.5.

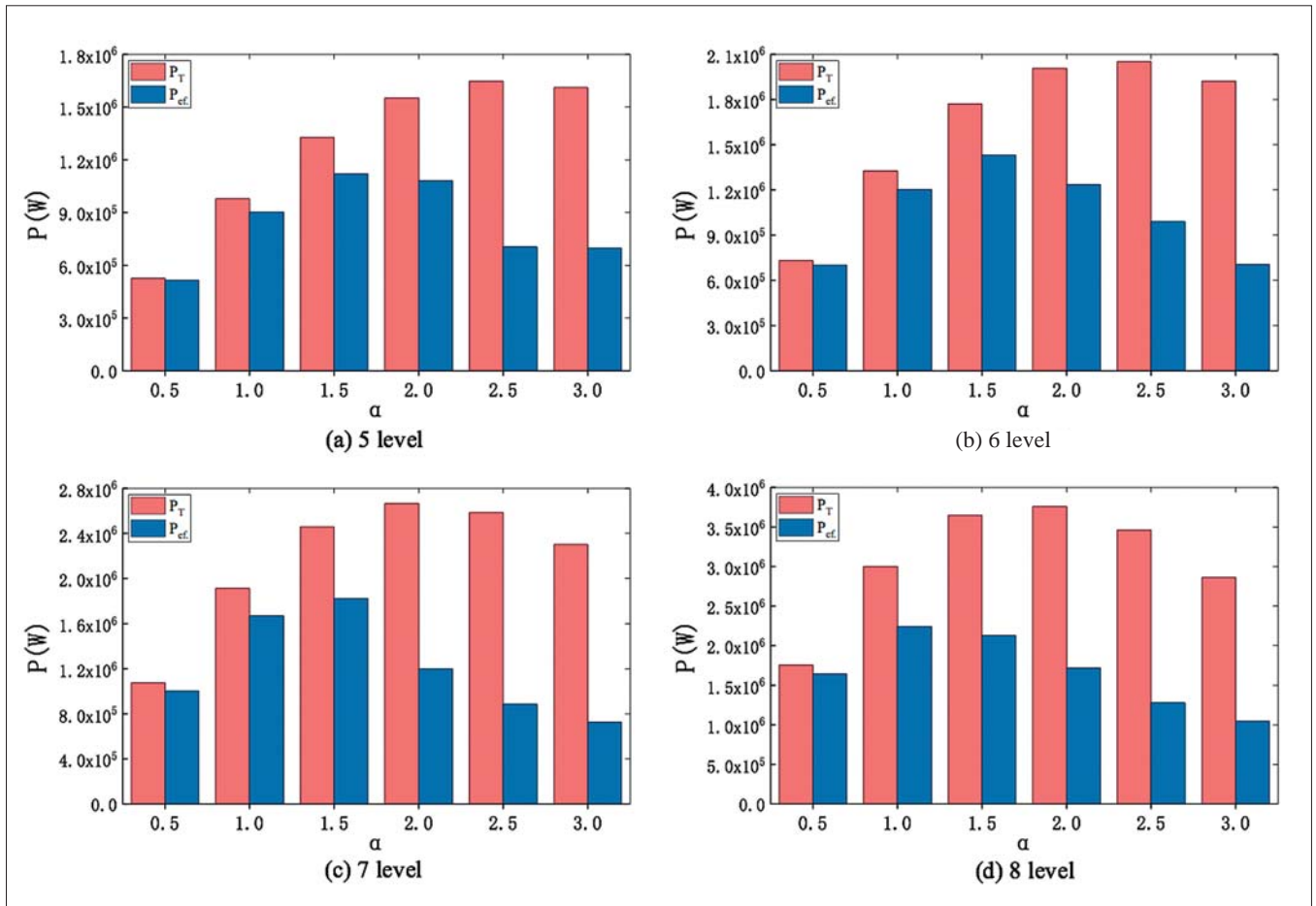


Fig. 11. The thrust power and effective power of the rotating cylinder

Fig. 12 shows the parameter comparison graph of the rotating cylinder under different Reynolds number conditions, in which the bar graph shows the lift coefficient and drag coefficient; the point line graph is its thrust. The spin ratios in Figs. 12(a) and (b) are 1.5 and 2.5, respectively. It can be seen from the figure that, as the Reynolds number increases, the lift coefficient of the rotating cylinder gradually decreases, and the drag coefficient gradually increases; the thrust curve of the ship shows an upward trend. When the spin ratio is 1.5, the maximum thrust of the rotating cylinder reaches 730,492 N as the Reynolds number reaches

5.69×10^7 . When the spin ratio is 2.5, the maximum thrust reaches 691,213 N.

OTHER ENVIRONMENTAL WIND SPEED DIRECTIONS

In this section, the thrust coefficients and thrust forces of the rotating cylinder along the ship's sailing direction are plotted for several cases where the heel angle (θ) of the environmental wind speed is 0, 60, 90, 120 and 180 degrees, respectively. The results are shown in Fig. 13(a) and Fig. 13(b).

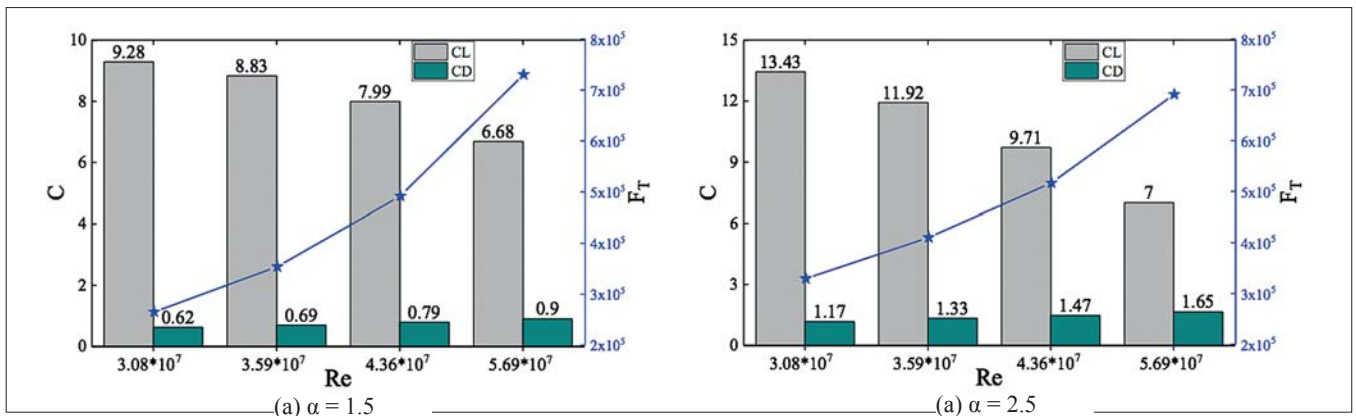


Fig. 12. The lift, drag coefficient and thrust values of the rotating cylinder under different Reynolds number

Specifically, the ship's speed is maintained at 5 m/s and the environmental wind speed is the more common 5-level wind, 10 m/s. When the heel angle is 0 and 180 degrees, the spin ratio of the cylinder is 0; in other cases, the spin ratio is taken to be 2.0.

From Fig. 13, we can see that the thrust coefficient and thrust force are different for different wind directions under the same value of environmental wind. When the heel angle of environmental wind is 0° , the ship is sailing upwind and the thrust coefficient is -0.66 . The thrust is also negative, which is normal. When $\theta = 120^\circ$, the thrust coefficient reaches its maximum value of 12.7. However, the maximum value of thrust is 311,233 N when the heel angle is 90° . Similarly, the thrust coefficient and the thrust of the rotating cylinder show a trend of increasing and then decreasing with the increase of the heel angle of the environmental wind. In addition, when $\theta = 180^\circ$ (i.e. the ship is sailing downwind and the device is not rotating), the cross section of the cylinder can be regarded as a traditional sail and its thrust coefficient is 0.55, which is smaller compared to the rotating cylinder. This also proves the advantages of the Flettner rotor in ship propulsion.

CONCLUSIONS

This research proposes a new type of rotating cylinder and its installation method: the superstructure and Flettner rotor are combined organically, which creates a rotating cylinder installed on the superstructure. The Magnus force generated by the Magnus effect provides part of the thrust of the ship. A ship model with a rotating cylinder outside the superstructure is established and related simulations are carried out to obtain the performance of the new rotating cylinder under different wind levels and different spin ratios. Simulations show that the new rotating cylinder has a significant effect and it can produce greater thrust power. Specifically, a typical ship was chosen (a 100,000 ton oil tanker) and the rotating cylinder with a diameter of 40 m was designed. Through numerical simulation, the maximum effective power that the new

rotating cylinder can provide is about 2,240 kW. The specific conclusions are as follows:

1. By comparing and discussing the force coefficient and surrounding pressure of the traditional superstructure, cylindrical superstructure, and rotating cylinder superstructures, it was found that, under the three equal volume conditions, the traditional superstructure and the cylinder superstructure have friction, and the cylinder superstructure has a certain effect on reducing wind drag compared to a traditional design. It is worth noting that the rotating cylinder has the Magnus effect, which generates thrust for the ship.
2. The lift and thrust coefficients of the rotating cylinder under different wind levels are compared. There are inflection points of the lift coefficient and the thrust coefficient as the spin ratio increases. The inflection points of different wind levels correspond to different spin ratios; this indicates that both the wind speed around the rotating cylinder and the spin ratio will have a direct impact on the boosting effect of the rotating cylinder. When the wind level is 5 and the spin ratio is 2.5, the thrust coefficient reaches its maximum, which is 8.63. In addition, as the spin ratio increases, the drag coefficient and the heel coefficient generally tend to increase.
3. When comparing the pressure around the rotating cylinder with different spin ratios at the level 6 wind condition, it can be seen that the pressure changes with the change of the spin ratio. At the spin ratio equal to 2.0, the maximum difference of the contour appears to be 900.3 Pa in Fig 9.
4. Under the same spin ratio conditions, the greater the environmental wind speed, the greater the thrust contribution generated by the rotating cylinder. With an increase in the wind level, the thrust corresponding to the spin ratio equal to 1.5 and 2.0 shows a greater steepness of rise. Under the level 8 wind condition, the thrust of the two reaches their maximum, exceeding 750,000 N. In addition, it is not that a larger spin ratio contributes more to the thrust of the corresponding rotating cylinder. On the

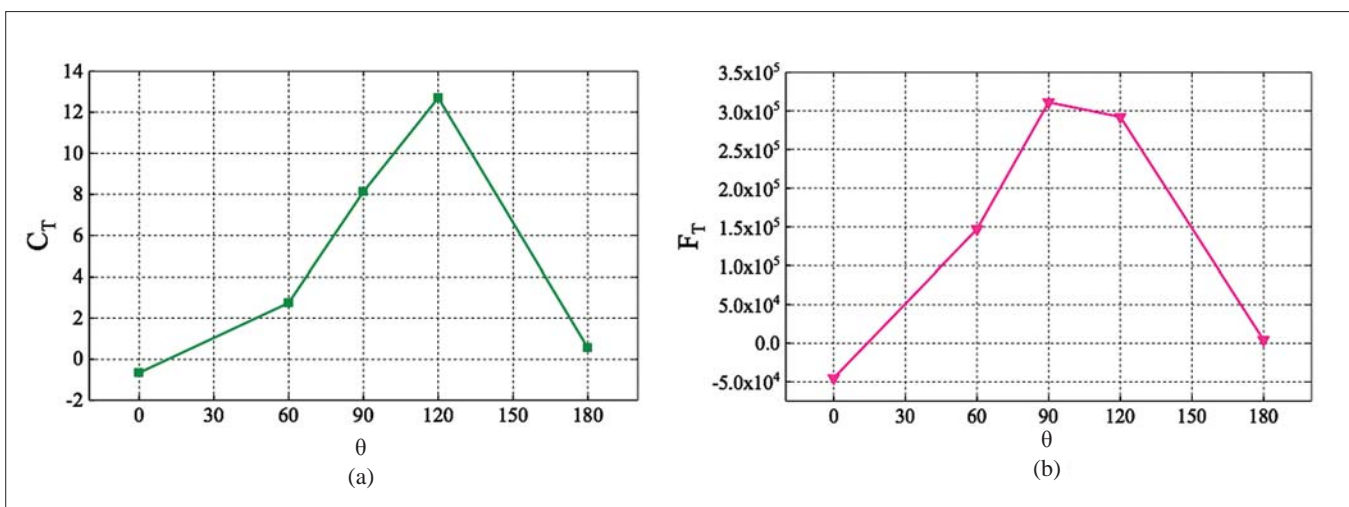


Fig. 13. The thrust coefficient and thrust of the rotating cylinder for other environmental wind speed directions

contrary, when the spin ratio is 2.0, the rotating cylinder shows a better advantage.

5. As the spin ratio increases, the thrust power of the rotating cylinder first increases and then decreases. Higher wind levels correspond to higher thrust power peaks. In addition, the spin ratios corresponding to the maximum effective power under the four wind levels are different: the maximum effective power of the level 8 wind is the largest and the corresponding spin ratio is 1.0; the other three spin ratios are 1.5. It is worth noting that when the maximum effective power appears, the effective power of the rotating cylinder can reach about 75 to 85% of the thrust power it generates. This also shows that the contribution of the rotating cylinder to the navigation of the ship is far greater than the power consumed by its own rotation.
6. After comparing the influence of the Reynolds number on the force coefficient and thrust of the new rotating cylinder, it was found that: when the Reynolds number increases, the lift coefficient of the rotating cylinder decreases, and the drag coefficient increases; the ship thrust curve shows an upward trend. In addition, the thrust coefficient and thrust force are different for different wind directions under the same value of environmental wind from Fig. 13.

The object of this research is a rotating cylinder installed on the superstructure of a ship. Simulations mainly verified the influence of several common wind levels and spin ratios on the new rotating cylinder. The results proved that there is a good feasibility for the installation of the new rotating cylinder on ships. The research can provide a theoretical basis for later engineering experiments and installation.

ACKNOWLEDGEMENTS

This work was supported by the National Science Foundation of China (Grant No. 61572404) and Tsinghua University's Shuimu Scholar Program (2020SM027).

REFERENCES

1. L. Zhen, Y. W. Wu, S. A. Wang, et al. 'Green technology adoption for fleet deployment in a shipping network'. *Transportation Research Part B: Methodological*, 139 (2020), 388-410.
2. A. Halff, L. Younes, T. Boersma. 'The likely implications of the new IMO standards on the shipping industry'. *Energy Policy*, 126 (2019), 277-286.
3. Y. P. Yuan, J. X. Wang, X. P. Yan, et al. 'A review of multi-energy hybrid power system for ships'. *Renewable and Sustainable Energy Reviews*, 132 (2020), 110081.
4. P. Cheng, N. Liang, R. Y. Li, et al. 'Analysis of Influence of Ship Roll on Ship Power System with Renewable Energy'. *Energies* 2020, 13, 1, doi:10.3390/en13010001.
5. Y. Y. Xie, W. Q. Guo, Q. W. Wu, et al. 'Robust MPC-based bidding strategy for wind storage systems in real-time energy and regulation markets'. *Electrical Power and Energy Systems*, 124 (2021), 106361.
6. Y. Wang. 'The working principle and practical application of rotor sail'. *Shanghai Energy Conservation*, 2018 (11), doi:10.13770/j.cnki.issn2095-705x.2018.11.010.
7. L. Talluri, D.K. Nalianda, E. Giuliani. 'Techno economic and environmental assessment of Flettner rotors for marine propulsion'. *Ocean Engineering*, 154 (2018), 1-15.
8. K. Roncin, M. Behrel, P. Iachkine, et al. 'Benchmark Sea Trials on a 6-Meter Boat Powered by Kite'. *Applied Science*, 2020, 10, 6148; doi:10.3390/app10186148.
9. R. H. Lu and J. W. Ringsberg. 'Ship energy performance study of three windassisted ship propulsion technologies including a parametric study of the Flettner rotor technology'. *Ships and Offshore Structures*, doi: 10.1080/17445302.2019.1612544.
10. G. Bordogna, S. Muggiasca, S. Giappino, et al. 'Experiments on a Flettner rotor at critical and supercritical Reynolds numbers'. *Journal of Wind Engineering & Industrial Aerodynamics*, 188 (2019), 19-29.
11. A. De Marco, S. Mancini, C. Pensa, et al. 'Flettner Rotor Concept for Marine Applications: A Systematic Study'. *International Journal of Rotating Machinery*, doi:10.1155/2016/3458750.
12. A. De Marco, S. Mancini, C. Pensa, et al. 'Marine application of Flettner rotors: numerical study on a systematic variation of geometric factor by DOE approach', in *Proceedings of the 6th International Conference on Computational Methods in Marine Engineering (MARINE'15)*, Rome, Italy, June 2015.
13. A. Thom. 'Effects of discs on the air forces on a rotating cylinder', *Reports & Memoranda 1623*, Aerospace Research Council, 1934.
14. G. Bordogna, S. Muggiasca, S. Giappino, et al. 'The effects of the aerodynamic interaction on the performance of two Flettner rotors'. *Journal of Wind Engineering & Industrial Aerodynamics*, <https://doi.org/10.1016/j.jweia.2019.104024>.
15. S.J. Karabelas, B.C. Koumroglou, C.D. Argyropoulos, et al. 'High Reynolds number turbulent flow past a rotating cylinder'. *Applied Mathematical Modelling*, 36 (2012), 379-398.
16. T. Craft, N. Johnson, B. Launder. 'Back to the Future? A Re-examination of the Aerodynamics of Flettner-Thom Rotors for Maritime Propulsion'. *Flow Turbulence Combust*, doi: 10.1007/s10494-013-9486-4.
17. M. Traut, P. Gilbert, C. Walsh, et al. 'Propulsive power contribution of a kite and a Flettner rotor on selected shipping routes'. *Applied Energy*, 113 (2014), 362-372.
18. S. Salter, G. Sortino, J. Latham. 'Sea-going hardware for the cloud albedo method of reversing global warming'. *Phil. Trans. R. Soc. A*, (2008), 366, 3989-4006, doi:10.1098/rsta.2008.0136.
19. C. Badalamenti, S. A. Prince. 'Effects of endplates on a rotating cylinder in crossflow', in *Proceedings of the*

- 26th AIAA Applied Aerodynamics Conference, Honolulu, Hawaii, USA, August 2008.
20. F. Tillig, J. W. Ringsberg, et al. 'Design, operation and analysis of wind-assisted cargo ships'. *Ocean Engineering*, 211 (2020), 107603.
 21. X. Y. Lu. 'Study on aerodynamic Performance of Vertical Magnus Wind Turbine'. University of Xiang Tan, May 2019.
 22. A. Sedaghat, I. Samani, M. Ahmadi-Baloutaki, et al. 'Computational study on novel circulating aerofoils for use in Magnus wind turbine blades'. *Energy*, 91 (2015), 393-403.
 23. A. Sedaghat. 'Magnus type wind turbines: Prospectus and challenges in design and modelling'. *Renewable Energy*, 62 (2014), 619-628.
 24. J. Seifert. 'A review of the Magnus effect in aeronautics'. *Progress in Aerospace Sciences*, 55 (2012), 17-45.
 25. X. Y. Liu, Y. X. Wang, J. J. Liang et al. 'CFD Analysis of Aerodynamic Characteristics of Ship's Wind-Assisted Rotor Sail. *Navigation of China*', doi: 1000-4653 (2019) 04-0046-05.
 26. G. Dong, P. T. Lee. 'Environmental effects of emission control areas and reduced speed zones on container ship operation'. *Journal of Cleaner Production*, <https://doi.org/10.1016/j.jclepro.2020.122582>.
 27. N. R. Ammar, I. S. Seddiek. 'Enhancing energy efficiency for new generations of containerized shipping'. *Ocean Engineering*, 215 (2020), 107887.
 28. D. Wang, P. L.-F. Liu. 'An ISPH with $k-\epsilon$ closure for simulating turbulence under solitary waves'. *Coastal Engineering*, 157 (2020), 103657.
 29. B. J. Guo, S. Steen. 'Comparison of numerical methods for wave generation by VOF-based numerical wave tank'. *Proceedings of the ASME 2011 30th International Conference on Ocean, Offshore and Arctic Engineering*. OMAE 2011-49777.
 30. D. Moreira, N. Mathias, T. Morais. 'Dual flapping foil system for propulsion and harnessing wave energy: A 2D parametric study for unaligned foil configurations'. *Ocean Engineering*, 215 (2020), 107875.
 31. M. Terziev, T. Tezdogan, A. Incecik. 'Modelling the hydrodynamic effect of abrupt water depth changes on a ship travelling in restricted waters using CFD'. *Ships and Offshore Structures*, doi: 10.1080/17445302.2020.1816731.
 32. I. Razzgallah, S. Kaidi, H. Smaoui, et al. 'The impact of free surface modelling on hydrodynamic forces for ship navigating in inland waterways: water depth, drift angle, and ship speed effect'. *Journal of Marine Science and Technology*, <https://doi.org/10.1007/s00773-018-0566-y>.
 33. D. J. Wang, K. Liu, P. Huo, et al. 'Motions of an unmanned catamaran ship with fixed tandem hydrofoils in regular head waves'. *Journal of Marine Science and Technology*, <https://doi.org/10.1007/s00773-018-0583-x>.
 34. B. S. Zhang, B. W. Song, Z. Y. Mao, et al. 'Hydrokinetic energy harnessing by spring-mounted oscillators in FIM with different cross sections: From triangle to circle'. *Energy*, 189 (2019), 116249.

CONTACT WITH THE AUTHORS

Baoshou Zhang

e-mail: sxsdzbs@126.com

School of Aerospace Engineering
Tsinghua University
Beijing 100084
CHINA

BOYANG LI

e-mail: qdlby@126.com

College of Electromechanical Engineering Qingdao
University of Science and Technology Qingdao, 266061
Shandong
CHINA

RUI ZHANG

e-mail: qustzr@163.com

College of Electromechanical Engineering Qingdao
University of Science and Technology Qingdao, 266061
Shandong
CHINA

YAJING LI

e-mail: sdlijaying@126.com

College of Electromechanical Engineering Qingdao
University of Science and Technology Qingdao, 266061
Shandong
CHINA

CHAO GUO

e-mail: sdqdc@126.com

College of Electromechanical Engineering Qingdao
University of Science and Technology Qingdao, 266061
Shandong
CHINA

HEAVE MOTION OF A VERTICAL CYLINDER WITH HEAVE PLATES

Ewelina Ciba

Gdańsk University of Technology, Poland

ABSTRACT

The shape of a vertical cylinder resembles the classic form of a spar platform. Spar platforms are floating platforms that are successfully used in waters of great depths and have several advantages that mean they are readily used in the oil industry. Many of these advantages are also relevant to their application for offshore wind turbines, which is currently being considered. In the hydrodynamic analysis of spar platforms, the determination of their hydrodynamic coefficients plays an important role. They can be determined based on the free decay test. The study presents a method for determining the hydrodynamic coefficients of an object based on the free decay test. The results of free oscillation calculations with the help of numerical fluid mechanics tools are presented and compared with the results of the experiment and analytical solution. The application of determined coefficients and their significance for floating platforms are discussed. The influence of change in the form of an additional damping element on the behaviour of spar structures is shown.

Keywords: spar platforms, heave plates, damping coefficient, added mass coefficient

INTRODUCTION

A spar is a type of floating platform designed for great depths. The structure of a spar platform is a vertical cylinder with positive buoyancy with an appropriate system of anchoring the platform to the seabed. They are always stable because their centre of buoyancy is above the centre of gravity. They can be used as mobile drilling rigs and their cable system (catenary) is easy to install, use and carry [1].

However, with long wave periods, the phenomenon of resonance may appear, which is largely influenced by damping related to water viscosity [2, 3]. In [4], several alternative hull shapes that improve the damping in the vertical movement of the structure are presented. The best of the presented solutions is a heave plate, a damping plate attached to the floating structure that has a distinct advantage in reducing the motion response of a floating structure by increasing the added mass and damping.

This solution has become very popular and consistent results of analyses of its effectiveness can be found in the literature. The increase in the added mass, the damping coefficient and the related increase of the natural period under the influence of the heave plate have also been confirmed [5, 6, 7].

Conventional offshore structure behavior calculations in offshore conditions are based on the potential theory and do not take into account viscous damping. This is a good approximation, but in some cases the viscosity should be included. Especially for the near resonance frequency [8]. The importance of viscosity also increases with the presence of edges in the structure, which was demonstrated by comparing the behavior of the hemispherical, rounded base and flat base structures in [9]

The resulting vortices and their impact on the drag coefficient depending on the geometry of the heave plate are shown e.g. in [10] or [11].

A good technique is to supplement linear theories with viscous drag coefficients obtained from experimental studies or calculations using the RANSE (Reynolds-Averaged Navier Stokes) model with turbulence models. This approach is described in [9] and [8]. The possibility to consider the effect of viscosity is also available in the commercial Ansys Aqwa software. Software uses three dimensional panel method to solve linearized hydrodynamic radiation and diffraction problem in frequency domain [12]

Potential flow solutions with added viscosity factors allow you to get good results in a reasonable amount of time. Time-consuming RANSE calculations are performed only once to calculate the coefficients, and then a series of analyzes can be performed for different conditions and configurations with faster models based on the potential theory, extended by the coefficients mentioned.

In [13], modelling of the spar platform dynamics with the use of drag coefficient, inertia coefficient and added mass coefficient was presented. In addition, in [10], the added mass and damping coefficients related to the plate viscous damping were presented. One of the methods of estimating the viscous damping is to conduct free decay tests, as discussed in [7].

A very interesting and extensive analysis of the heaving plate impact using the CFD method is presented in [11] Detailed parametric studies were conducted numerically on spar with single and two heave plates. Effects of scaling ratio, diameter ratio, heave plate position to diameter of heave plate ratio, heave plate position to draft ratio, relative spacing and spacing between heave plates to draft ratio were examined. As a result, the ranges of the analyzed parameters were given for which the heave motion reduction is the greatest.

In recent years, there has been a dynamic development of offshore wind energy. There are concepts of wind turbines based on various types of supporting structures. The concept of a turbine based on a jack-up platform is described in [14]. A concept based on a tension leg platform was presented in [15]. Most often, however, due to the large depths of the planned installation areas, the concepts of offshore wind turbines are based on spar-type platforms, as presented in

[16, 5]. As a result, considerations regarding spar platforms are becoming very popular again. Due to the different nature of the forces acting in the case of offshore wind platforms than in the case of oil rigs, there are also new problems with the dynamics of these platforms related to the action of wind force.

This study presents the calculation results of the numerical fluid dynamics of the free decay test for a smooth cylinder and a cylinder with a heave plate (Fig. 1), and compares them with the results of analytical calculations and experiment.

The damping coefficients and the added mass coefficient are determined and compared with the values presented in the literature. The confirmation of the correctness of the applied method allows us to state that the computational fluid dynamics (CFD) calculations can be used to correctly estimate the hydrodynamic coefficients of the analysed platforms. This is of great importance in the process of designing a structure, as it allows to carry out extensive parametric analyses at a low cost and hence to choose the best solution, which should then be checked using model tests. Moreover, CFD methods allow for analyses of various shapes and configurations, which is not always possible with analytical methods.

MATHEMATICAL DESCRIPTION OF THE PROBLEM

Submerged, under the influence of the initial force, the cylinder will then make an oscillating motion relative to the equilibrium position, with the amplitude of the movement decreasing with time. A mathematical description of the problem can be found in the literature [17].

We assume that the moving body is a rigid body and we replace surface and volume forces by the movement of the point associated with the origin of the coordinate system. We also assume that the coefficients of the equation are constant over time, which causes the equation to become a linear. This assumption is only true for a small amplitude of motion. In this case, the deflection is not more than 6 cm so they can be used. The cylinder motion equation is given as:

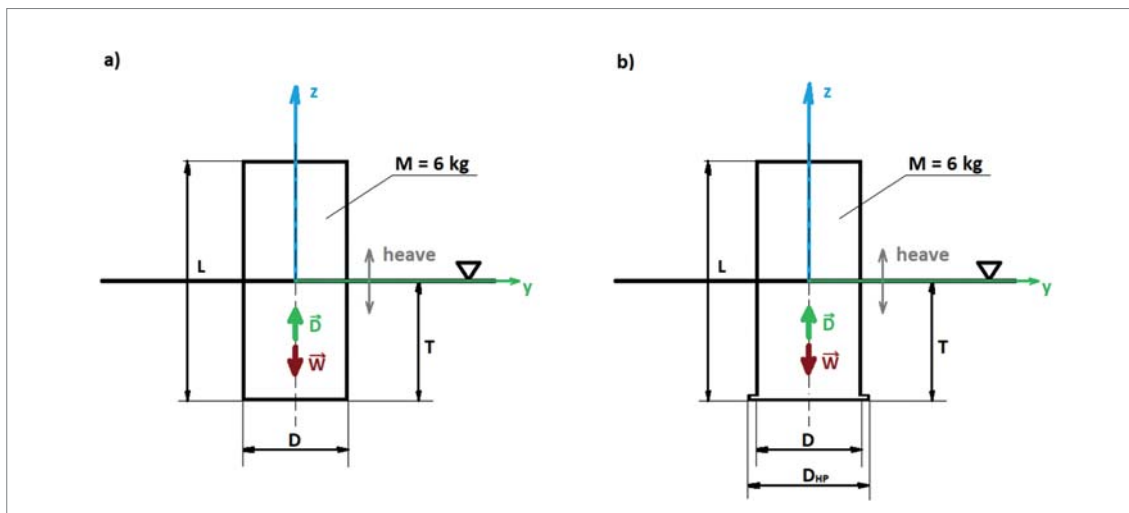


Fig. 1. Geometry of tested cylinders: a) smooth; b) with a heave plate

$$(m + a) \cdot \ddot{z} + b \cdot \dot{z} + c \cdot z = 0 \quad (1)$$

where:

z – vertical displacement [m]

m – solid mass of cylinder [kg]

a – hydrodynamic mass coefficient [kg]

b – hydrodynamic damping coefficient [kg/s]

c – restoring spring coefficient [kg/s²]

Equation (1) can be written as:

$$\ddot{z} + 2\nu \cdot \dot{z} + \omega_0^2 \cdot z = 0 \quad (2)$$

where the damping coefficient and the undamped natural frequency are defined as:

$$2\nu = \frac{b}{m + a} \quad \omega_0^2 = \frac{c}{m + a} \quad (3)$$

A non-dimensional damping coefficient κ is defined as:

$$\kappa = \frac{\nu}{\omega_0} = \frac{b}{2\sqrt{(m + a) \cdot c}} \quad (4)$$

By knowing the results of the free decay tests, we can calculate:

$$\kappa = \frac{1}{2\pi} \cdot \ln \left\{ \frac{z_{a_i} - z_{a_{i+1}}}{z_{a_{i+2}} - z_{a_{i+3}}} \right\} \quad (5)$$

Depending on the averaged displacement amplitude:

$$\overline{z_a} = \left\{ \frac{z_{a_i} - z_{a_{i+1}}}{z_{a_{i+2}} - z_{a_{i+3}}} \right\} \quad (6)$$

We calculate the hydrodynamic added mass coefficient as:

$$a = \frac{c}{\omega_0^2} - m \quad (7)$$

In the case of initial displacement z_a , Eq. (2) takes the form:

$$z = z_a e^{-\nu t} \left(\cos \omega_z t + \frac{\nu}{\omega_z} \sin \omega_z t \right) \quad (8)$$

Due to the fact that for the frequency of free oscillations $\omega_z^2 = \omega_0^2 - \nu^2$ and damping is small $\nu < 0.20$, $\nu^2 \ll \omega_0^2$, we can skip ν^2 and we can write that $\omega_z \approx \omega_0$.

RANSE CFD CALCULATIONS

CFD calculations were made using STAR-CCM+. Unsteady calculations were performed in the three-dimensional domain, using the volume of fluid and K-epsilon turbulence models. Cylinder displacements were modelled using the dynamic fluid body interaction module using an overset mesh. Each of the boundary walls was given a no-slip wall condition. The computational domain was prepared as in Fig. 2.

The shape of the second cylinder was changed by a heave plate with diameter DHP = 0.178 m and thickness $t = 0.005$ m. The transition between the edge of the ring and the cylinder wall is rounded at radius $r = 0.02$ m. The geometry of the cylinder with a heave plate is shown in Fig. 3.

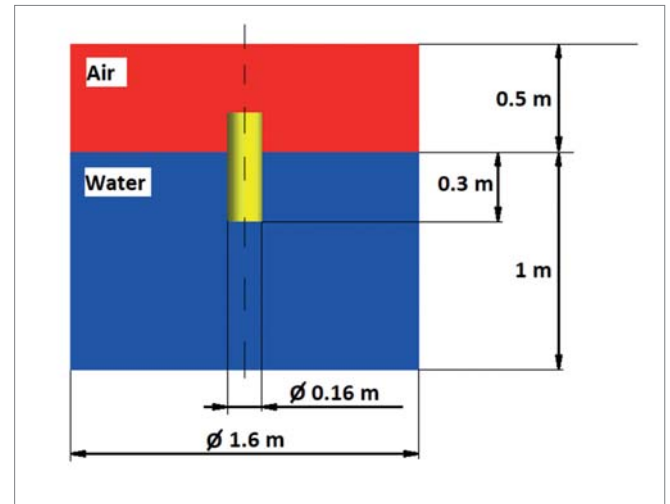


Fig. 2. Schematic of computational domain

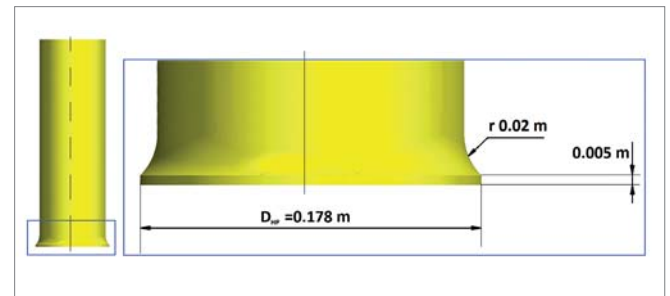


Fig. 3. Heave plate geometry

The assumed initial conditions were as follows: the share of water and air volume, and the initial pressure distribution of 1 atm above the free surface and hydrostatic pressure below the free surface. The cylinder was treated as a rigid body with one degree of freedom. The mass is equal to the displacement at draught 0.3 m, i.e. 6 kg. The initial solid velocity was assumed to force the initial cylinder displacement.

In the case of a smooth cylinder, the mesh was compacted around the cylinder (0.005 m) with a 0.002 m thick wall layer and two layers, by its expected displacement, and in the area of the free surface (0.01 m). The grid in the plane of symmetry with the division into moving and fixed parts is shown in Fig. 4. The number of grid elements was over 6 million.

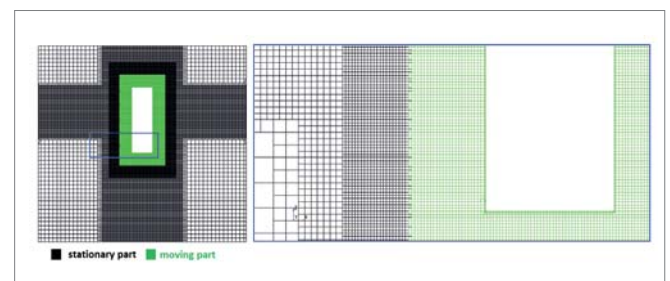


Fig. 4. Calculation grid in the plane of symmetry for smooth cylinder

In the case of a cylinder with an additional heave plate, the mesh was refinement in the plate area (0.002 m), the thickness of the prism layer was reduced to 0.0015 m and the number of layers was increased to seven. The mesh for the cylinder

with the plate is shown in Fig. 5. The number of elements was increased to over 7 million.

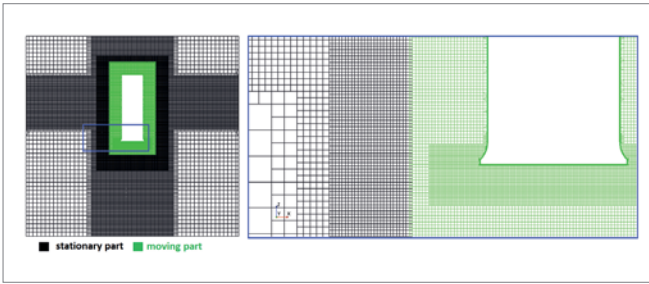


Fig. 5. Calculation grid for a cylinder with a heave plate

Calculations were performed for both cases with time step $t_k = 0.01$ s.

COMPARISON OF CALCULATION RESULTS WITH EXPERIMENT

In order to validate the calculations, an experiment was conducted whose conditions were equivalent. The same mass and geometry were used, and the resulting draft of the structure. The oscillation was forced by the application of an external force, the effect of which then ceased. The force was selected in such a way that the first free displacement was the same as in the performed calculations. The experiment was carried out in such a way that the weight of the appropriate mass and the accelerometer were placed inside the empty cylinder of the set geometry. Then, an initial draft greater than the one resulting from the displacement balance was forced and released, recording the accelerations of the oscillating cylinder. It was assumed that the cylinder only moves vertically. Its slight deviations have been neglected. Two series of tests were performed for each case. A photograph from the study is shown in Fig. 6.



Fig. 6. Model tests of a damping ring cylinder

As a result of the measurements, the acceleration changes over time were obtained. The measured values for one of the test series are shown in Fig. 7.

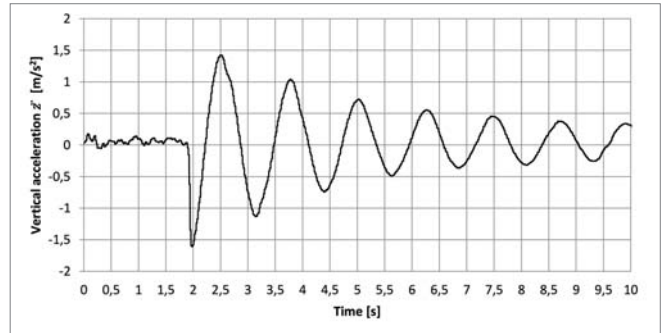


Fig. 7. Vertical cylinder acceleration measured for an example series of tests

Based on the measured accelerations, a displacement plot was created knowing that the amplitude is equal to the quotient of the acceleration and the square of the free vibration frequency at the points of maximum deflection.

$$z_a = \frac{\ddot{z}}{\omega_0^2} \quad (9)$$

The comparison of the displacement diagrams for both cases is shown in Fig. 8 for a smooth cylinder and in Fig. 9 for a cylinder with a heave plate.

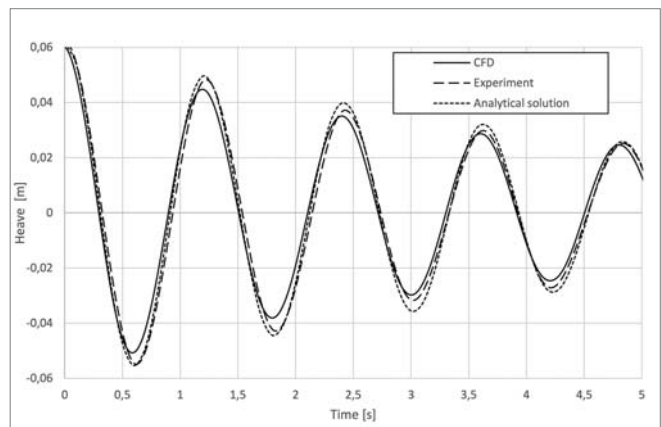


Fig. 8. Heaving a smooth cylinder

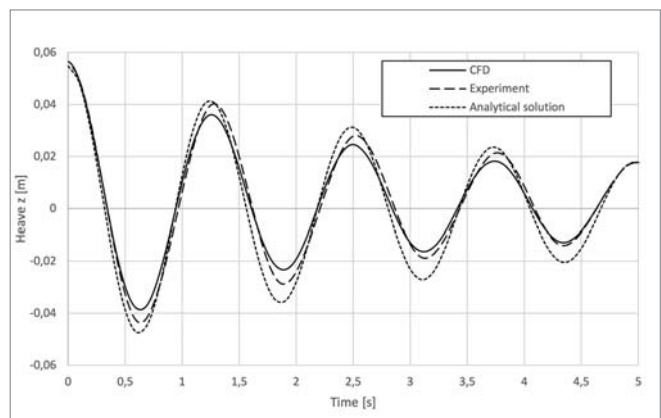


Fig. 9. Heaving a cylinder with a heave plate

To compare both cases, the non-dimensional damping coefficient κ (Eq. (5)) is shown in the plot depending on the average amplitude \bar{z}_a (Eq. (6)).

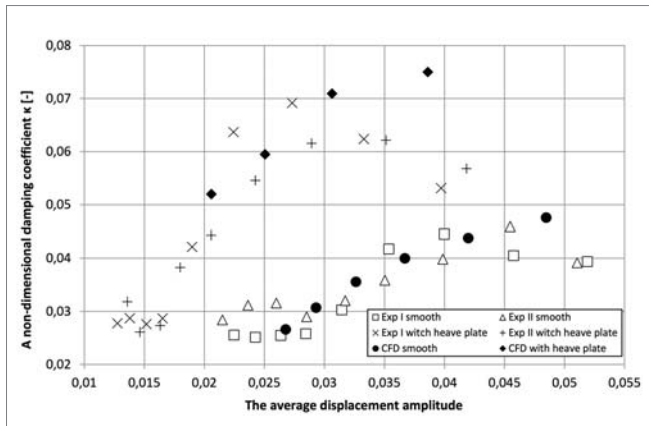


Fig. 10. A non-dimensional damping coefficient plot depending on the average displacement amplitude

The natural frequency ω_0 (Fig. 11) and the added mass coefficient a (Fig. 12) are also compared.

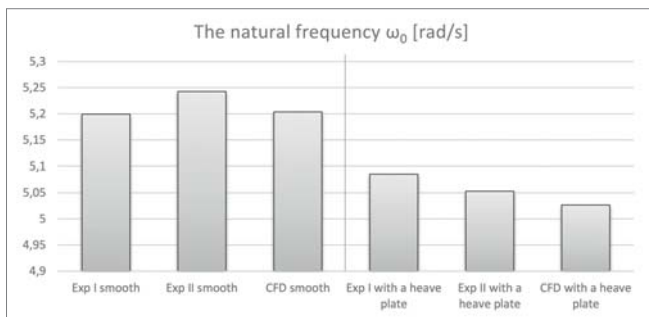


Fig. 11. Natural frequency

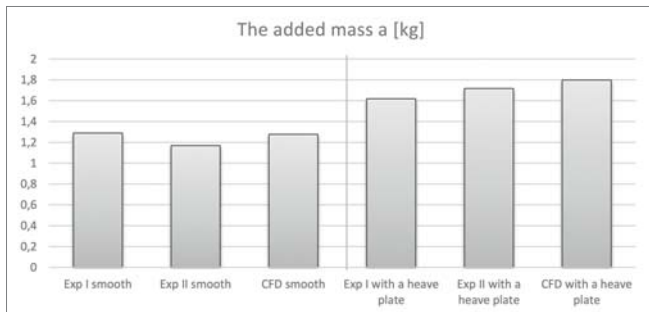


Fig. 12. Added mass coefficient

SUMMARY

The concepts of emerging wind platforms are often based on spar platforms and their modifications. This increases the interest in these platforms and the need for numerical analyses for the designed structures. Due to the time consuming nature of full RANSE CFD calculations, calculations by hybrid methods are a good solution, using much faster calculation methods based on hydrodynamic coefficients determined by RANSE CFD analyses and model tests. This study presents a method for determining such coefficients. Based on the results presented, it can be concluded that CFD calculations allow us to reliably map reality. In both cases, the large convergence of CFD calculation results, analytical solutions and experiment results was obtained, and the

differences in the dimensionless attenuation coefficient are not greater than the differences between the values obtained from both series of the experiment (fig. 11 and 12). The results of the calculations and the experiment differ for greater displacement amplitudes. Perhaps the calculations should be repeated with a shorter time step to improve convergence for these points.

As shown in the diagram (Fig. 10), the value of the damping coefficient depends on the displacement amplitude, and therefore the cylinder velocity. The conclusion is that when extending the calculations based on the potential method with coefficients related to viscosity, either the average damping coefficient for the anticipated speed range should be used or, if possible, the value of the coefficient as a function of velocity should be used.

Comparing the results for the cases of a smooth cylinder and a cylinder with an additional heave plate, even a slight change in shape whilst maintaining the same weight of the structure causes an increase in damping. An additional element also reduces the frequency of oscillations and causes an increase in the mass of the accompanying water. The obtained values of the coefficients are similar to those obtained by other methods presented in the literature. A further conclusion can be drawn from this that when designing the geometry of a spar platform, it is worth considering the use of additional damping elements of this type.

Confirmation of the correct application of CFD methods for the analysis of hydrodynamic coefficients is of great importance for the analysis of various concepts of additional damping elements for structures for offshore wind turbines. This will allow, at relatively low costs, for the analysis of many different solutions and we can select the best of them for model tests necessary to verify the obtained results. It is can be used to carry out calculations for plates with jagged edges, equipped with movable elements, and for flexible plates. CFD analyses allow us to carry out many series of calculations depending on changes in individual parameters of the elements (e.g. increasing the diameter of the plate) that will also help to trace the dependence of the coefficients on the selected parameters.

ACKNOWLEDGEMENT

The calculations were performed using a Simcenter STAR-CCM+ license.

REFERENCES

1. Jain A.K., Agarwal A.K. (2003): Dynamic Analysis of Offshore Spar Platforms. Defence Science Journal, Vol. 53, No. 2, pp. 211–219
2. Sharman K. T., Robertson A., Lewis J. (2019): *Heave Plate Hydrodynamics for Offshore Wind Turbine Applications*. EERA DeepWind, Trondheim

3. Liu Y, Yan H, Yung T. W. (2010): *Nonlinear Resonant Response of Deep Draft Platforms in Surface Waves*. ASME 2010 29th International Conference on Ocean, Offshore and Arctic Engineering
4. Bhatta D. D. (2007): *Computation of Added Mass and Damping Coefficients due to a Heaving Cylinder*. J. Appl. Math. Comput., 23, 127-140
5. Gilloteaux J. Ch., Bozonnet P. (2014): *Parametric Analysis of a Cylinder Like Shape Floating Platform Dedicated to Multi-Mega Watt Wind Turbine*. IFP Energies Nouvelles, Applied Mechanics division Rueil-Malmaison, France.
6. Fisher F. J., Gopalkrishnan R. (1998): *Some Observations on the Heave Behavior of Spar Platforms*. Journal of Offshore Mechanics and Arctic Engineering.
7. Koh H. J., Cho I. J. (2016): *Heave Motion Response of a Circular Cylinder with the Dual Damping Plates*. Ocean Engineering, 125, 95–102.
8. Zhao Ch., Cao F., Shi H. (2020): *Optimisation of heaving buoy wave energy converter using a combined numerical model* Applied Ocean Research 102 (2020) 102208
9. Gu, H., Stansby, P., Stallard, T., & Carpintero Moreno, E. (2018). *Drag, added mass and radiation damping of oscillating vertical cylindrical bodies in heave and surge in still water*. JOURNAL OF FLUIDS AND STRUCTURES, 82, 343–356. <https://doi.org/10.1016/j.jfluidstructs.2018.06.012>
10. Tao, L., Cai, S. (2004): *Heave Motion Suppression of a Spar with a Heave Plate*. Ocean Engineering.
11. A. Subbulakshmi, R. Sundaravadivelu (2016) *Heave damping of spar platform for offshore wind turbine with heave plate* Ocean Engineering 121 (2016) 24–36
12. S. Sudhakar, S. Nallayarasu (2011) *Influence of Heave Plate on Hydrodynamic Response of Spar* OMAE2011-49565
13. Haslum, H. A. (2000): *Simplified Methods Applied to Nonlinear Motion of Spar Platforms*. Norwegian University of Science and Technology, Trondheim.
14. Dymarski P. (2019): *Design of Jack-up Platform for 6 MW Wind Turbine: Parametric Analysis Based Dimensioning of Platform Legs*. Polish Maritime Research, 26, 183–197.
15. Żywicki J., Dymarski P., Ciba E., Dymarski C. (2017): *Design of Structure of Tension Leg Platform for 6 MW Offshore Wind Turbine Based On Fem Analysis*. Polish Maritime Research, Vol.–24, s1, 230–241
16. Dymarski P., Dymarski C., Ciba E. (2019): *Stability Analysis of the Floating Offshore Wind Turbine Support Structure of Cell Spar Type During its Installation*. Polish Maritime Research, Vol. 26, 4(104), 109–116.
17. Journee J. M. J., Massie W. W. (2001): *Offshore Hydromechanics*. Delft University of Technology.
18. Kim et al. M.-H. (2012): *Spar platforms: Technology and Analysis Methods*. American Society of Civil Engineers.

CONTACT WITH THE AUTHOR

Ewelina Ciba

e-mail: ewelina.ciba@pg.edu.pl

Gdańsk University of Technology
Narutowicza 11/12
80-233 Gdańsk
POLAND

NUMERICAL STUDY ON THE OPTIMIZATION OF HYDRODYNAMIC PERFORMANCE OF OSCILLATING BUOY WAVE ENERGY CONVERTER

Wenbin Lai

Yonghe Xie*

Detang Li

Zhejiang Ocean University, China

* Corresponding author: xieyh@zjou.edu.cn (Y. Xie)

ABSTRACT

The oscillating buoy wave energy converter (OBWEC) captures wave energy through the undulating movement of the buoy in the waves. In the process of capturing wave energy, the hydrodynamic performance of the buoy plays an important role. This paper designed the "Haida No. 1" OBWEC, in which the buoy adopts a form of swinging motion. In order to further improve the hydrodynamic performance of the buoy, a 2D numerical wave tank (NWT) model is established using ADINA software based on the working principle of the device. According to the motion equation of the buoy in the waves, the influence of the buoy shape, arm length, tilt angle, buoy draft, buoy width, wave height and Power Take-off (PTO) damping on the hydrodynamic performance of the buoy is studied. Finally, a series of physical experiments are performed on the device in a laboratory pool. The experimental results verify the consistency of the numerical results. The research results indicate that the energy conversion efficiency of the device can be improved by optimizing the hydrodynamic performance of the buoy. However, the absorption efficiency of a single buoy for wave energy is limited, so it is very difficult to achieve full absorption of wave energy.

Keywords: wave energy converter; hydrodynamic performance; numerical simulation; physical experiment

INTRODUCTION

In order to alleviate the pressure caused by the energy crisis and protect human health, it is very important to increase the development and utilization of clean and renewable energy [1, 2]. Among the many renewable energy sources, wave energy is becoming a hot spot in the world's new energy development due to its clean, environmentally friendly, renewable, and huge reserves. Its global reserves are as high as 2.5 billion kW [3, 4]. However, the difficulty of wave energy utilization is how to efficiently convert wave energy into electric energy [5, 6].

Currently, many types of wave energy converters (WECs) have been developed, and each type of WEC has its own advantages and disadvantages. However, high power generation costs, low energy conversion efficiency, reliability and safety are still the fundamental reasons why these WECs are difficult to commercialize widely [7, 8]. Considering several factors such as

the power generation cost, total efficiency, reliability and safety, the oscillating buoy wave energy converter (OBWEC) has obvious advantages compared with other WECs. OBWEC has the following advantages: simple structure, strong adaptability, convenient maintenance, relatively high energy conversion efficiency, and the core equipment of the device is located above the water surface so that there is no need to worry too much about seawater corrosion and sealing problems [9, 10]. In recent years, scholars all over the world have conducted a lot of research on OBWEC.

Zannutigh et al. studied the power and hydraulic performance of a floating WEC by changing the mooring system, the wave attack and the device orientation with respect to the incoming waves, and concluded that the CALM mooring system leads always to a larger power production than a spread mooring [11]. Sjolte et al. studied the effects of permanent magnet synchronous generators, inverter, and DC-links on the Power

Take-off (PTO) capabilities of the device, and found that the reactive control has limited potential for increasing the output of the device [12]. Neary et al. studied the feasibility of applying a classification system for wave resources to WEC classification, and concluded that the WEC response to extreme loads was found to vary considerably within the most energetic of the resource classes examined [13]. De Andrés et al. studied how the geometric tuning of a generic wave energy converter is affected by different climate scenarios, and concluded that the matchability of a device could be achieved via the PTO control or changing the geometric characteristics of a particular device [14]. Bedard et al. studied the impact of different footprint configurations and different mooring systems on the AquaBuOY device, and obtained the performance data of the device under different conditions [15]. Haraguchi et al. studied the feasibility of a point absorber with a tuned inertia mass to increase the power absorption and broaden the effective wave frequency range, and concluded that the energy conversion efficiency of the device can be improved by appropriately adjusting the spring stiffness and generator damping [16]. Homayoun et al. proposed a new concept of near-shore combined renewable energy system, and studied the hydrodynamic performance of WEC under four different buoy shapes, and concluded that the buoy with a curvature inward in the bottom has better hydrodynamic performance [17].

However, the problem of low energy conversion efficiency of OBWEC is still prominent. In order to further improve the energy conversion efficiency of OBWEC, Zhejiang Ocean University designed the “Haida No. 1” OBWEC, in which the buoy adopts a form of swinging motion [18], as shown in Fig. 1. According to the motion equation of the buoy in the wave, this paper studies the influence of the buoy shape, arm length, tilt angle, buoy draft, buoy width, wave height, and PTO damping on the hydrodynamic performance of the buoy. The conclusions can provide meaningful reference value for the design of other buoys.

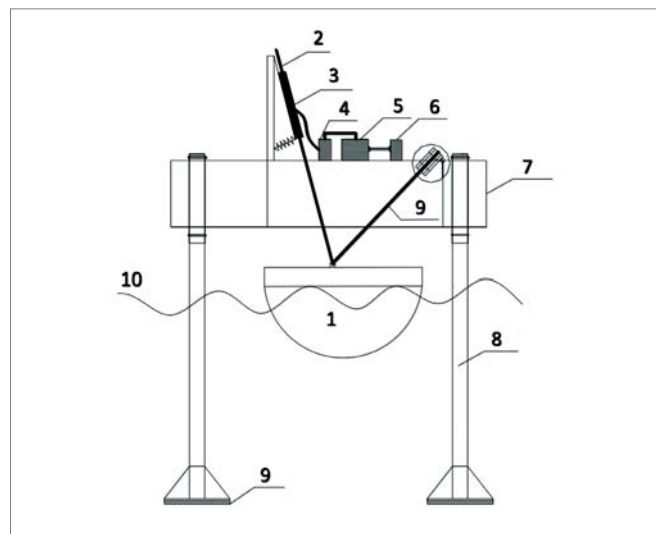
The remainder of the paper is organized as follows: Section 2 introduces the working principle of the “Haida No. 1” OBWEC. Section 3 derives the motion equation of the buoy in the waves. Section 4 uses ADINA software to establish a 2D numerical wave tank (NWT) model based on the working principle of the device. Section 5 studies the influence of the buoy shape, arm length, tilt angle, buoy draft, buoy width, wave height, and PTO damping on the hydrodynamic performance of the buoy based on the motion equation of the buoy in the waves. Section 6 establishes the physical model of the “Haida No. 1” OBWEC and conducts a series of wave condition experiments on the physical model in a laboratory pool to verify the correctness of the numerical results. Section 7 is the conclusion.

WORKING PRINCIPLE OF THE “HAIDA NO. 1” OBWEC

Fig. 1 shows the “Haida No. 1” OBWEC designed by our team, which is a variant of the heaving buoy WEC. The device is mainly composed of the wave energy capture system,

hydraulic transmission system, energy output system and control and protection system.

The working principle of the device is as follows: Firstly, the buoy moves up and down with the waves, and then captures wave energy from the waves and converts it into its own mechanical energy. Secondly, the buoy pushes the hydraulic piston to move up and down, and the hydraulic piston then drives the hydraulic cylinder to do work, thereby completing the conversion of the mechanical energy of the buoy into hydraulic energy. Thirdly, unstable hydraulic energy enters the accumulator, and after being adjusted by the accumulator, stable hydraulic energy is output. Finally, the stable hydraulic energy enters the hydraulic motor and drives the hydraulic motor to work, thereby driving the generator to convert the hydraulic energy into electrical energy.



1. Buoy; 2. Hydraulic piston; 3. Hydraulic cylinder; 4. Accumulator; 5. Hydraulic motor; 6. Generator; 7. Working platform; 8. Pile foot; 9. Crank; 10. Wave

Fig. 1. “Haida No. 1” OBWEC

MOTION EQUATION OF BUOY IN THE WAVES

As shown in Fig. 2, the wave energy capture system consists of a buoy and an arm. One end of the arm is fixedly connected to the buoy, and the other end of the arm is fixed at point O by a hinge. The buoy and arm form

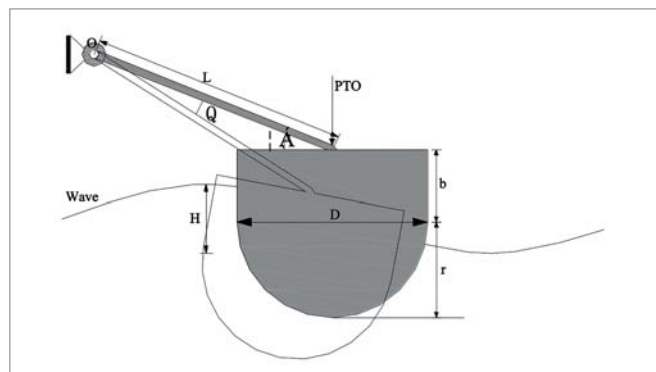


Fig. 2. Schematic diagram of buoy structure

a single-degree-of-freedom system, which is represented by its angular motion, θ . A linear PTO damper acts on the centre of the upper surface of the buoy. In regular wave theory, the motion equation of the buoy in the waves can be obtained by superimposing the effect of the PTO damping and incident wave on the buoy [19]:

$$(J + J_a) \ddot{\theta} = T_{Arch} - T_G + T_{rad} - T_{PTO} + T_{ext} \quad (1)$$

where J is the moment of inertia of the buoy and arm, J_a is the additional moment of inertia caused by the movement of the buoy, $\ddot{\theta}$ is the angular acceleration when the arm moves, T_{Arch} is the torque caused by Archimedes force, T_G is the torque caused by gravity, T_{rad} is the radiated wave torque caused by the radiated wave, T_{PTO} is the load torque caused by the PTO damping, T_{ext} is the exciting torque caused by the incident wave.

By identifying the terms in Eq. (1), the following well-known expressions are obtained:

$$\ddot{\theta} = \frac{T_{res} + T_{rad} - T_{PTO} + T_{ext}}{(J + J_a)} \quad (2)$$

where T_{res} is the hydrostatic restoring torque.

EXCITING TORQUE

The exciting torque T_{ext} is the torque of an incident wave acting on a buoy held fixed, which can be obtained by the following formula:

$$T_{ext} = \int_{-r}^b P(L \sin \alpha + z) dz \quad (3)$$

where P is the pressure of the incident wave on the buoy, L is the arm length, α is the tilt angle of the arm to the horizontal axis, b is the buoy freeboard, and r is the buoy draft.

HYDROSTATIC RESTORING TORQUE

The torque T_{Arch} is equal to the Archimedes force multiplied by the effective arm length:

$$T_{Arch} = V_{disp} \rho g L \cos\left(\frac{\pi}{2} - \alpha + \theta\right) \quad (4)$$

where V_{disp} is the volume of the submerged part of the buoy, ρ is the density of water, and g is the gravitational acceleration.

The torque T_G is equal to the weight of the buoy multiplied by the effective arm length:

$$T_G = mgL \cos\left(\frac{\pi}{2} - \alpha + \theta\right) \quad (5)$$

where m is the mass of the buoy.

Therefore, the hydrostatic restoring torque is:

$$T_{res} = T_{Arch} - T_G = (V_{disp} \rho - m) g L \cos\left(\frac{\pi}{2} - \alpha + \theta\right) \quad (6)$$

LOAD TORQUE

The load torque T_{PTO} is caused by the PTO force acting on the buoy. The PTO force can be obtained by the following relationship:

$$F_{PTO} = C \dot{\theta} L \sin\left(\frac{\pi}{2} - \alpha + \theta\right) \quad (7)$$

where C is the PTO damping coefficient.

Hence, the load torque is:

$$T_{PTO} = C \dot{\theta} L^2 \sin^2\left(\frac{\pi}{2} - \alpha + \theta\right) \quad (8)$$

RADIATING WAVE TORQUE

When the buoy moves in the waves with frequency ω , a radiating wave is generated. The radiating wave acting on the buoy will produce radiated wave torque, which can be described as:

$$T_{rad} = (-J_a \dot{\omega} - b_{hyd} \omega) L \cos\left(\frac{\pi}{2} - \alpha + \theta\right) \quad (9)$$

where b_{hyd} is the hydrodynamic damping coefficient.

According to the above motion equation of the buoy in the waves, the factors that affect the hydrodynamic performance of the buoy mainly include the buoy shape, arm length, tilt angle, buoy draft, buoy width, wave height, and PTO damping.

ESTABLISHMENT AND VERIFICATION OF NUMERICAL MODEL

ESTABLISHMENT OF NUMERICAL MODEL

According to the working principle of the ‘‘Haida No. 1’’ OBWEC, the numerical model of the buoy structure and corresponding fluid model of the computational domain are established respectively using ADINA software as shown in Fig. 3. In the numerical model of the buoy structure, in order to enable the buoy to rotate freely around the point O , a contact group, contact surface, contact pair, and friction system are defined at the hinge to control the movement of the buoy. In the fluid model of the computational domain, the upper boundary of the flow field is set as a free surface, and the lower boundary is set as a fixed wall. The left boundary is set as the incident wave boundary, and the right boundary is set as the fixed wall. In order to avoid the influence of the reflected wave on the buoy’s movement, the work is stopped before the reflected wave reaches the position of the buoy. In the flow field, the vertical grid resolution gradually increases from the fixed wall to the free surface; in the area behind the buoy, the horizontal grid resolution gradually decreases. The initial time step is set to 0.002 s, which can ensure that the implicit solver has sufficient accuracy [20].

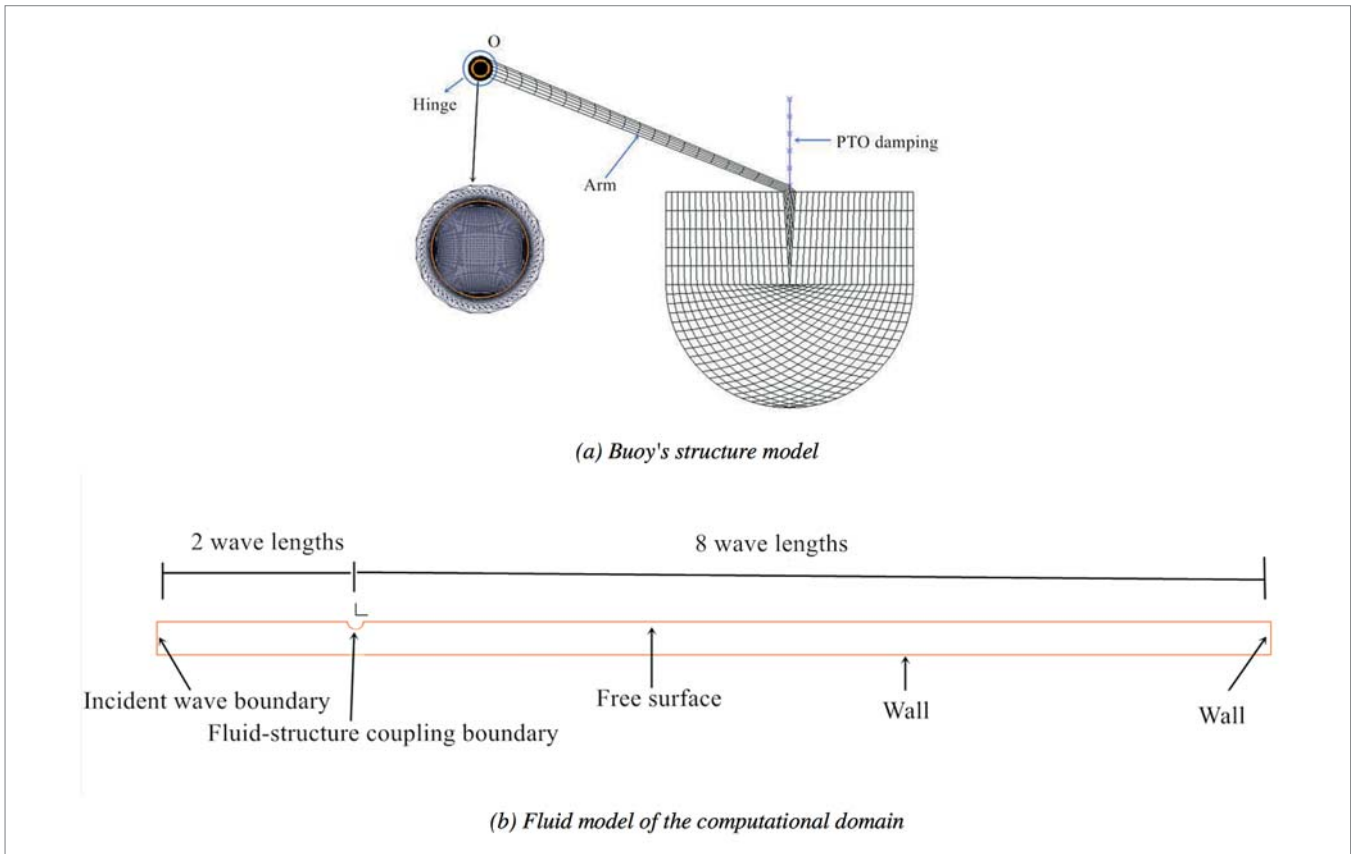


Fig. 3. Two-dimensional numerical model

VERIFICATION OF NUMERICAL RESULTS

Fig. 4 shows the time process of the incident wave height at the position of the buoy between the theoretical and numerical results under different wave periods, where the Z-displacement represents the distance from the wave surface to the horizontal plane. The water depth in the NWT is 10 m. It can be seen that no matter whether the wave period is 3.8 s or 4.2 s, there is a good agreement between the theoretical and numerical results, which verifies the accuracy of the NWT.

OPTIMIZATION OF HYDRODYNAMIC PERFORMANCE OF THE BUOY

OPTIMIZING TARGET PARAMETERS

The optimization target parameter of this paper is mainly the capture width ratio β of the buoy. The capture width ratio β of the buoy can be calculated by the following equation:

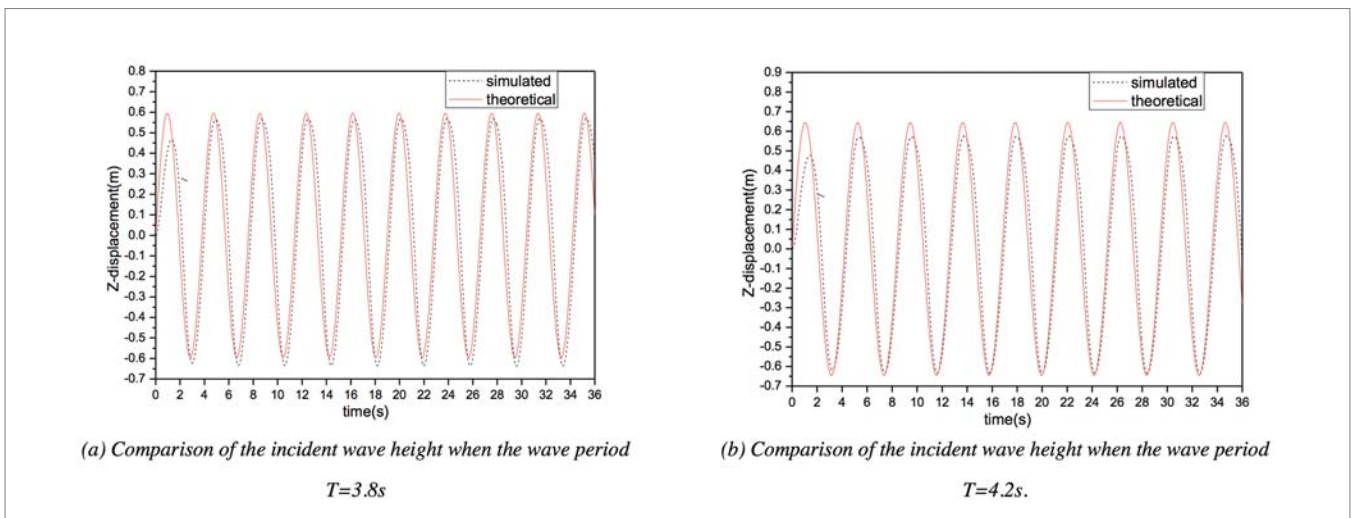


Fig. 4. Verification of numerical results

$$\beta = \frac{P_b}{P_{wave}} \quad (10)$$

where P_b is the average output power of the buoy, and is the average power of the incident wave on the buoy.

$$P_b = \frac{\int_{t_1}^{t_2} C \bar{v}^2}{t_2 - t_1} \quad (11)$$

$$P_{wave} = \frac{1}{32\pi} \rho g^2 H^2 T \bar{D} \approx 981 H^2 T D \quad (12)$$

where \bar{v} is the heave speed of the buoy, H is the wave height, T is the wave period, and \bar{D} is the lateral width of the buoy.

INFLUENCE OF ARM LENGTH ON THE HYDRODYNAMIC PERFORMANCE OF THE BUOY

In order to study the influence of the arm length L on the hydrodynamic performance of the buoy, the arm length L of the buoy is set to 1 m, 2 m, 3 m, 4 m, 5 m, 6 m, 7 m, and 8 m, respectively. The upper half of the buoy is a rectangle with a length of 4 m and a height of 2 m, and the lower half is a semicircle with a radius of 2 m. The tilt angle α is set to 20° , and the PTO damping coefficient $C = 5000 \text{ N} \cdot \text{s/m}$. When the wave period is 4.2 s, the heave Response Amplitude Operator (RAO) and capture width ratio of the buoy under different arm lengths are shown in Fig. 5.

It can be seen from Fig. 5 that when other parameters remain unchanged, as the arm length L increases, the heave RAO and capture width ratio of the buoy first increase, and then gradually stabilize. When the arm length L is less than 5 m,

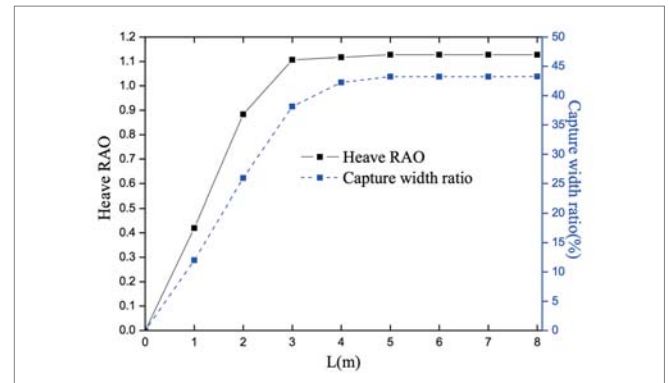


Fig. 5. Hydrodynamic performance of buoys under different arm lengths

the arm length has a greater influence on the hydrodynamic performance of the buoy. At this time, its hydrodynamic performance is basically proportional to the arm length. When the arm length L is greater than 5 m, the hydrodynamic performance of the buoy changes very little with the increase of the arm length, and finally remains unchanged.

The above conclusions demonstrate that the arm length has a great influence on the hydrodynamic performance of the buoy, especially when the arm length L is small. When the arm length reaches a certain value, its influence on the hydrodynamic performance of the buoy can be ignored. Therefore, when designing the arm length, it is necessary to choose a reasonable length to avoid wasting space with too long an arm, or reducing the hydrodynamic performance of the buoy with too short an arm.

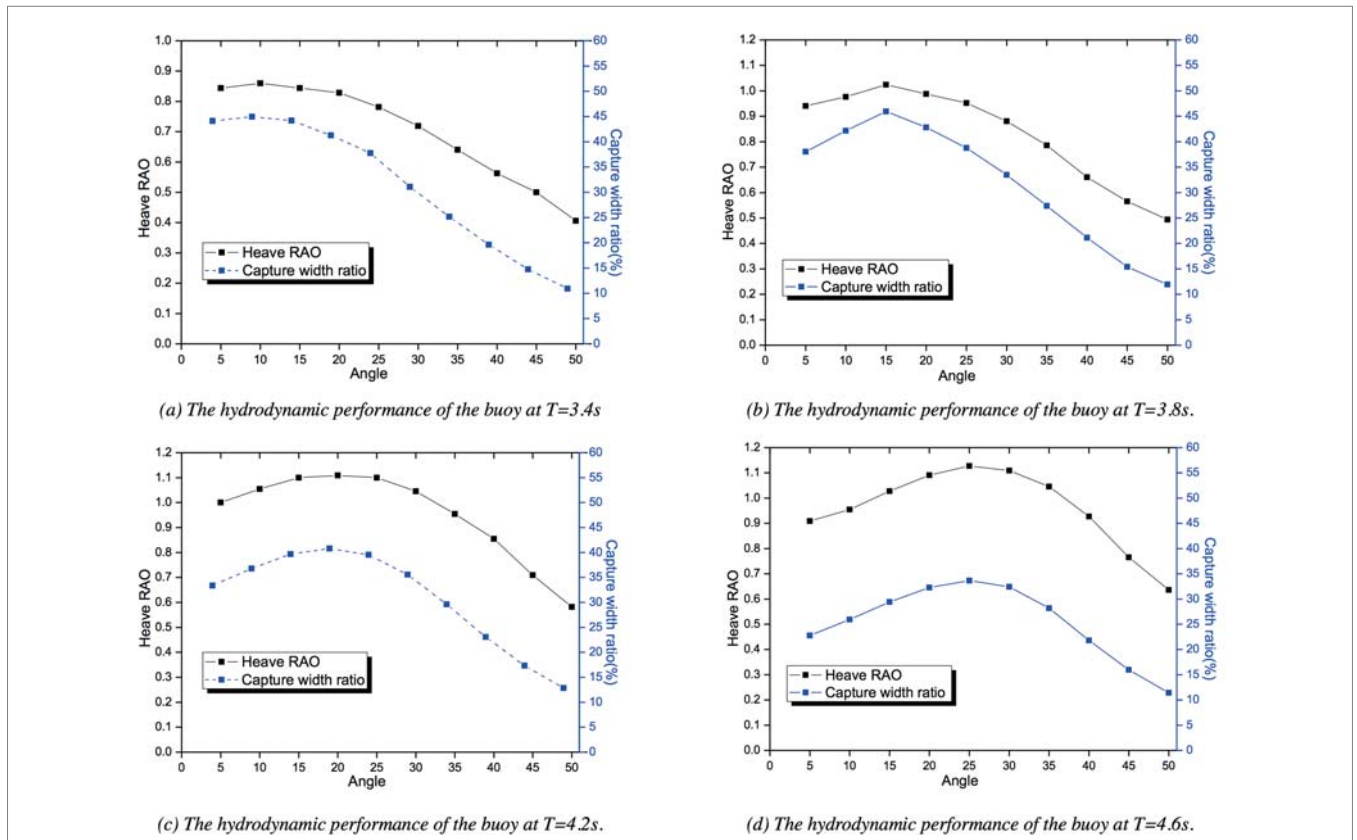


Fig. 6. Hydrodynamic performance of buoys under different tilt angles

INFLUENCE OF TILT ANGLE ON THE HYDRODYNAMIC PERFORMANCE OF THE BUOY

In order to study the influence of the tilt angle α on the hydrodynamic performance of the buoy, the arm length L is set to 5 m, and the other parameters are the same as above. The tilt angles α are set to 5°, 10°, 15°, 20°, 25°, 30°, 35°, 40°, 45°, and 50°, respectively. The influence of different tilt angles on the hydrodynamic performance of the buoy under wave periods of 3.4 s, 3.8 s, 4.2 s and 4.6 s are studied respectively as shown in Fig. 6.

When the wave period is 3.4 s, it can be seen from Fig. 6a that as the tilt angle increases, the heave RAO and capture width ratio of the buoy first increase and then decrease, and the change trend in the heave RAO and capture width ratio of the buoy is consistent. When the tilt angle is less than 10°, as the tilt angle increases, the heave RAO and capture width ratio of the buoy gradually increase. When the tilt angle is greater than 10°, as the tilt angle increases, the heave RAO and capture width ratio of the buoy gradually decrease. When the tilt angle is 10°, the heave RAO and capture width ratio of the buoy reach the maximum. At this time, its hydrodynamic performance is the best, and the maximum capture width ratio of the buoy is 44.97%.

Under other wave periods, the heave RAO and capture width of the buoy have the same changing trend as above. For the 3.8 s wave period, when the tilt angle is 15°, the heave RAO and capture width of the buoy reach the maximum,

and the maximum capture width ratio is 49.56%. For the 4.2 s wave period, when the tilt angle is 20°, the heave RAO and capture width of the buoy reach the maximum, and the maximum capture width ratio is 40.77%. For the 4.6 s wave period, when the tilt angle is 20°, the heave RAO and capture width of the buoy reach the maximum, and the maximum capture width ratio is 33.64%.

The above conclusions demonstrate that the tilt angle has a greater impact on the hydrodynamic performance of the buoy. For the same wave period, as the tilt angle increases, the capture width ratio of the buoy first increases and then decreases. Within a certain wave period, as the wave period increases, the optimal tilt angle also increases.

INFLUENCE OF BUOY SHAPE ON THE HYDRODYNAMIC PERFORMANCE OF THE BUOY

In order to study the influence of the buoy shape on the hydrodynamic performance of the buoy, the arm length L is set to 5 m, the tilt angle α is 20°, the wave period is 4.2 s, and the other parameters are the same as above. Keeping the buoy draft the same $r = 2$ m, and the buoy width the same $D = 4$ m, four different structures of the buoy shape and the corresponding fluid models are established by ADINA software as shown in Fig. 7.

Fig. 8a shows the heave RAO of different buoy shapes under the same wave period. From the bar graph, the heave RAO of buoy shape 2 is the largest, followed by buoy shape 3, buoy

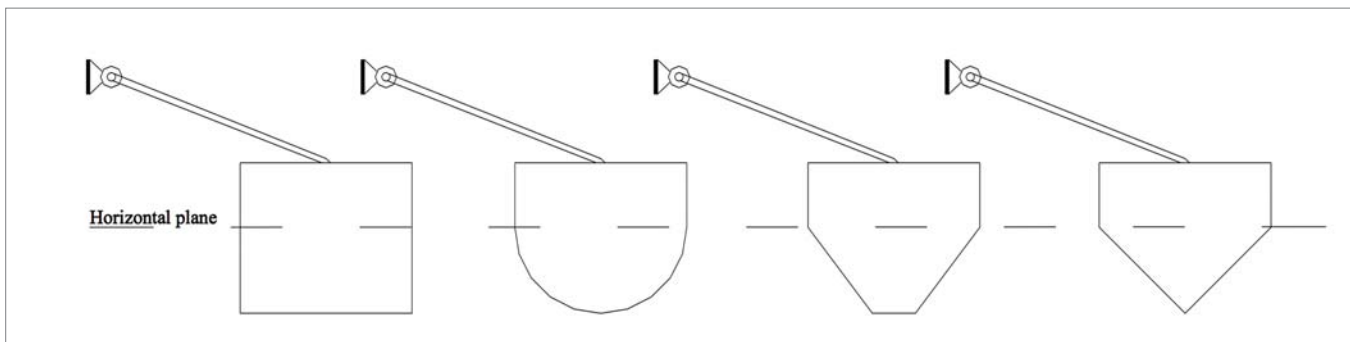


Fig. 7. Schematic diagram of buoy structure with different buoy shapes

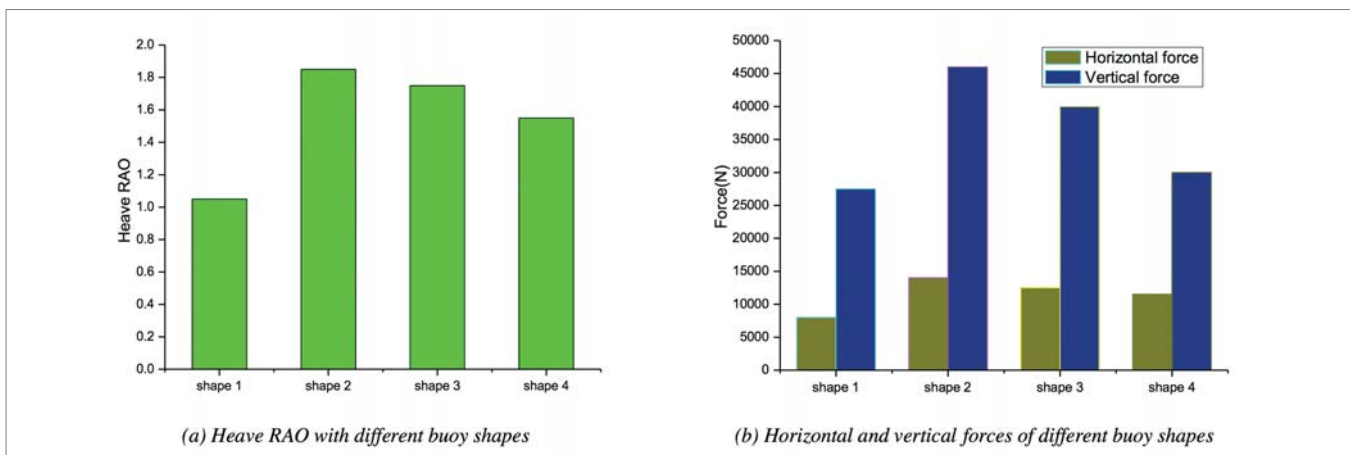


Fig. 8. Hydrodynamic performance of buoys under different buoy shapes

shape 4, and buoy shape 1. Fig. 8b shows the magnitude of the combined force received by different buoy shapes in the horizontal and vertical directions under the same wave. From the bar graph, the horizontal combined force and vertical combined force received by buoy shape 2 are both the largest, followed by buoy shape 3, buoy shape 4, and buoy shape 1. In the horizontal direction, the magnitude of the combined force on different buoy shapes does not change much; however, in the vertical direction, it changes greatly. According to Eq. (3), it can be seen that when the buoy draft is the same, the wave exciting force acting on the buoy is the same. Since the wave exciting force is the main external force received by the buoy in the horizontal direction, it causes the combined force received by the buoy in this direction to change very little. In the vertical direction, the buoy is not only subjected to the wave exciting force, buoyancy and gravity, but also subjected to fluid resistance. Since the fluid resistance of the buoy shape 2 is the smallest, the combined force received by it is the largest.

The above conclusions demonstrate that buoy shape 2 has better hydrodynamic performance than the other three buoy shapes under the same wave.

INFLUENCE OF BUOY WIDTH ON THE HYDRODYNAMIC PERFORMANCE OF THE BUOY

In order to study the influence of the buoy width D on the hydrodynamic performance of the buoy, the buoy draft r is set to 2 m, the arm length L is 5 m, the tilt angle α is 20° , and the other parameters are the same as above. We take two wave periods, $T = 3.4$ s and 3.8 s, and the corresponding wavelengths are 18 m and 22 m respectively. The buoy widths are set to 2 m, 3 m, 4 m, 5 m, 6 m, and 7 m, respectively. The influence of different buoy widths on the hydrodynamic performance of the buoy under the PTO damping coefficient of 2500 N · s/m, 5000 N · s/m, 7500 N · s/m, 10000 N · s/m, 12500 N · s/m, 15000 N · s/m, 17500 N · s/m, and 20000 N · s/m is studied respectively as shown in Fig. 9.

Fig. 9a shows the influence of different buoy widths on the hydrodynamic performance of the buoy for wave period

$T = 3.4$ s. It can be seen from the curve in the figure that for the buoy width of 2 m, when the PTO damping coefficient $C = 7500$ N · s/m, the capture width ratio of the buoy reaches the maximum, and the maximum capture width ratio is 37.94%. When the PTO damping coefficient is less than 7500 N · s/m, as the PTO damping coefficient increases, the capture width ratio of the buoy increases. When the PTO damping coefficient is greater than 7500 N · s/m, as the PTO damping coefficient increases, the capture width ratio of the buoy decreases. For other buoy widths, the change trend of the buoy's capture width ratio with the PTO damping coefficient is the same as above. When the buoy widths are 3 m, 4 m, 5 m, 6 m, and 7 m, the corresponding optimal capture width ratios are 41.57%, 41.62%, 39.68%, 35.95%, and 31.61%, respectively.

Fig. 9b shows the influence of different buoy widths on the hydrodynamic performance of the buoy for wave period $T = 3.8$ s. It can be seen from the curve in the figure that when the buoy widths are 2 m, 3 m, 4 m, 5 m, 6 m, and 7 m, the corresponding optimal capture width ratios are 33.71%, 38.80%, 40.41%, 41.22%, 35.85%, and 32.10%, respectively.

From the above conclusions, under the same wave period, as the buoy width increases, the buoy's maximum capture width first increases and then decreases. For the wave with a period of 3.4 s, the corresponding wavelength is 18 m, and the capture width ratio reaches the maximum when the buoy width is 4 m. For the wave period of 3.8 s, the corresponding wavelength is 22 m, and the capture width ratio reaches the maximum when the buoy width is 5 m. From the above, when the ratio of the wavelength to the buoy width is between 4 and 5, the buoy's capture width ratio is the largest.

INFLUENCE OF BUOY DRAFT ON THE HYDRODYNAMIC PERFORMANCE OF THE BUOY

In order to study the influence of the buoy draft r on the hydrodynamic performance of the buoy, the arm length L is set to 5 m, the buoy width D is 4 m, the tilt angle α is 20° , and the other parameters are the same as above. When the wave periods are 3.4 s and 4.2 s, and the corresponding wave heights

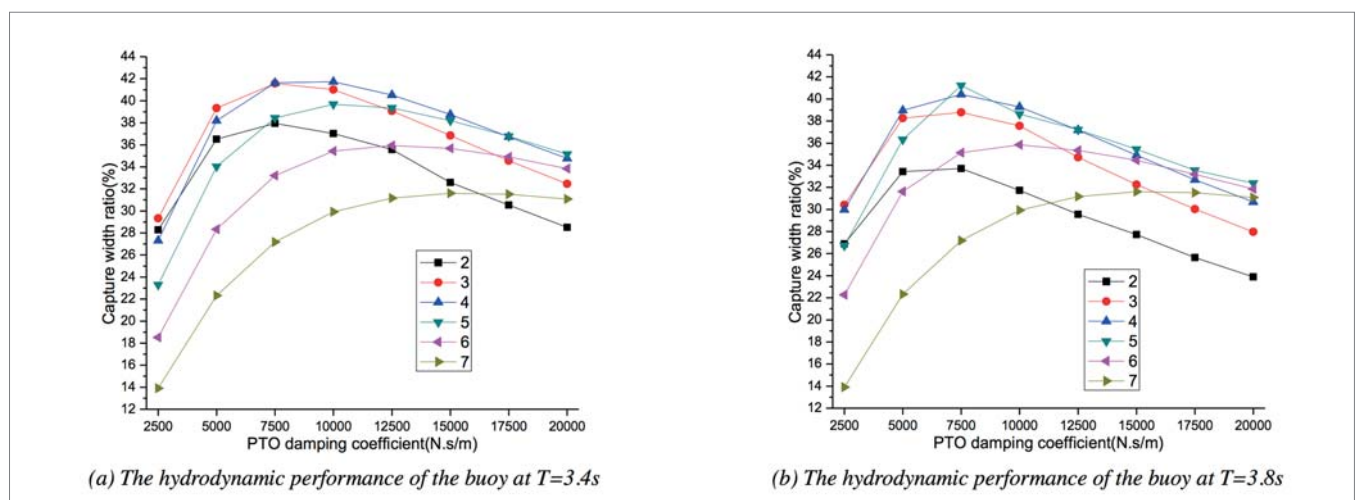


Fig. 9. Hydrodynamic performance of buoys under different buoy widths

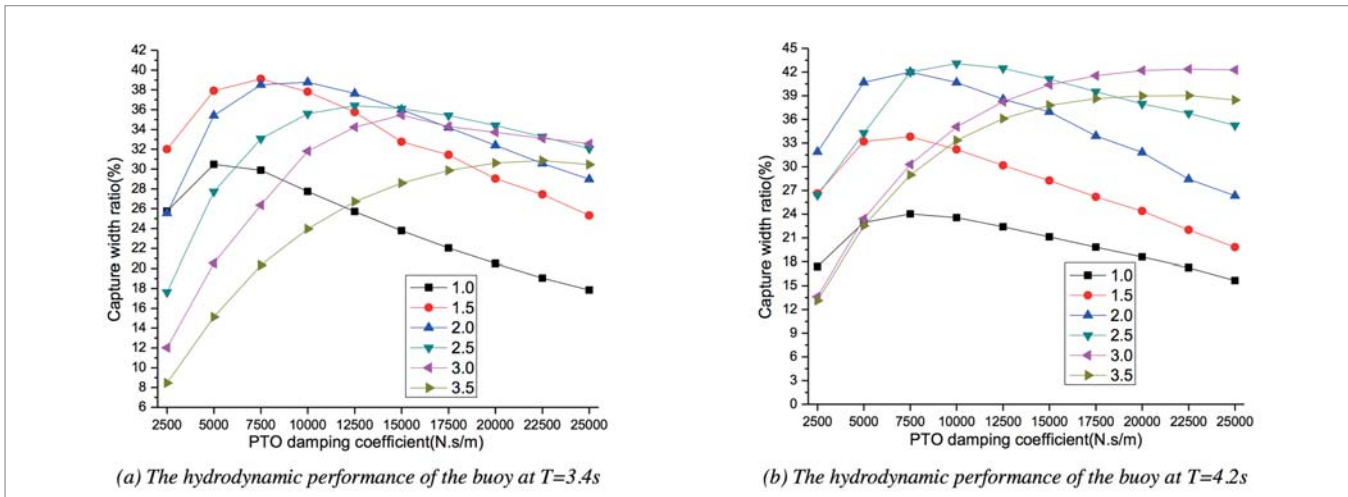


Fig. 10. Hydrodynamic performance of buoys under different buoy drafts

are 0.51 m and 0.94 m, respectively, the buoy drafts are set to 1.0 m, 1.5 m, 2.0 m, 2.5 m, 3.0 m, and 3.5 m, respectively. The influence of different buoy drafts on the hydrodynamic performance of the buoy under the PTO damping coefficients of 2500 N · s/m, 5000 N · s/m, 7500 N · s/m, 10000 N · s/m, 12500 N · s/m, 15000 N · s/m, 17500 N · s/m, and 20000 N · s/m is studied respectively as shown in Fig. 10.

Fig. 10a shows the influence of different buoy drafts on the hydrodynamic performance of the buoy for wave period $T = 3.4$ s. It can be seen from the curve in the figure that for the buoy draft of 1.0 m, when the PTO damping coefficient $C = 5000$ N · s/m, the capture width ratio of the buoy reaches the maximum, and the maximum value is 30.48%. When the PTO damping coefficient is less than 5000 N · s/m, as the PTO damping coefficient increases the capture width ratio of the buoy increases. When the PTO damping coefficient is greater than 5000 N · s/m, as the PTO damping coefficient increases the capture width ratio of the buoy decreases. For other buoy drafts, the change trend of the buoy's capture width ratio with the PTO damping coefficient is the same as above. When the buoy drafts are 1.5 m, 2.0 m, 2.5 m, 3.0 m, and 3.5 m, the corresponding optimal capture width ratios are 33.81%, 42.01%, 43.07%, 42.36%, and 39.02%, respectively.

Fig. 10b shows the influence of different buoy drafts on the hydrodynamic performance of the buoy for wave period $T = 4.2$ s. It can be seen from the curve in the figure that when the buoy drafts are 1.0 m, 1.5 m, 2.0 m, 2.5 m, 3.0 m, and 3.5 m, the corresponding optimal capture width ratios are 24.03%, 33.81%, 42.01%, 43.07%, 42.36%, and 39.02%, respectively.

From the above conclusions, for the wave with a period of 3.4 s and a wave height of 0.51 m, the capture width ratio of the buoy reaches the maximum when the buoy draft is about 1.5 m, and the maximum is 39.11%. For the wave with a period of 4.2 s and a wave height of 0.94 m, the capture width ratio of the buoy reaches the maximum when the buoy draft is about 2.5 m, and the maximum value is 43.07%. Under the same wave period, as the buoy draft increases the maximum capture

width ratio of the buoy first increases and then decreases. When the ratio of the buoy draft to the wave height is about 2.75, the buoy's capture width ratio is the largest.

INFLUENCE OF WAVE HEIGHT ON THE HYDRODYNAMIC PERFORMANCE OF THE BUOY

In order to study the influence of the wave height H on the hydrodynamic performance of the buoy, the buoy draft r is kept unchanged, the arm length L is 5 m, the buoy width is 4 m, the buoy draft r is 2 m, the tilt angle α is 20°, and the wave periods are 3.4 s and 4.2 s respectively. When the wave period is 3.4 s, the wave heights are set to 0.67 m, 0.74 m, 0.83 m, 0.91 m, 0.97 m and 1.05 m, respectively. When the wave period is 4.2 s, the wave heights are set to 0.94 m, 1.09 m, 1.24 m, 1.38 m, 1.51 m and 1.64 m, respectively. The influence of different wave heights on the hydrodynamic performance of the buoy under the PTO damping coefficient of 5000 N · s/m, 6000 N · s/m, 7000 N · s/m, 8000 N · s/m, 9000 N · s/m, and 10000 N · s/m is studied, respectively as shown in Fig. 11.

Fig. 11a shows the influence of different wave heights on the hydrodynamic performance of the buoy when the wave period is 3.4 s. It can be seen from the curve in the figure that for the wave height of 0.67 m, when the PTO damping coefficient = 9000, the capture width ratio of the buoy reaches the maximum, and the maximum value is 38.23%. When the PTO damping coefficient is less than 9000, as the PTO damping coefficient increases the buoy's capture width ratio increases. When the PTO damping coefficient is greater than 9000, as the PTO damping coefficient increases the buoy's capture width ratio decreases. For other wave heights, the variation trend of the buoy's capture width ratio with the PTO damping coefficient is the same as above. When the wave heights are 0.74 m, 0.83 m, 0.91 m, 0.97 m, and 1.05 m, the maximum capture width ratio of the buoy is 40.46%, 40.07%, 39.71%, 39.37%, and 39.15%, respectively. And the PTO damping coefficient corresponding to the maximum buoy capture width ratio is 9000 in all cases.

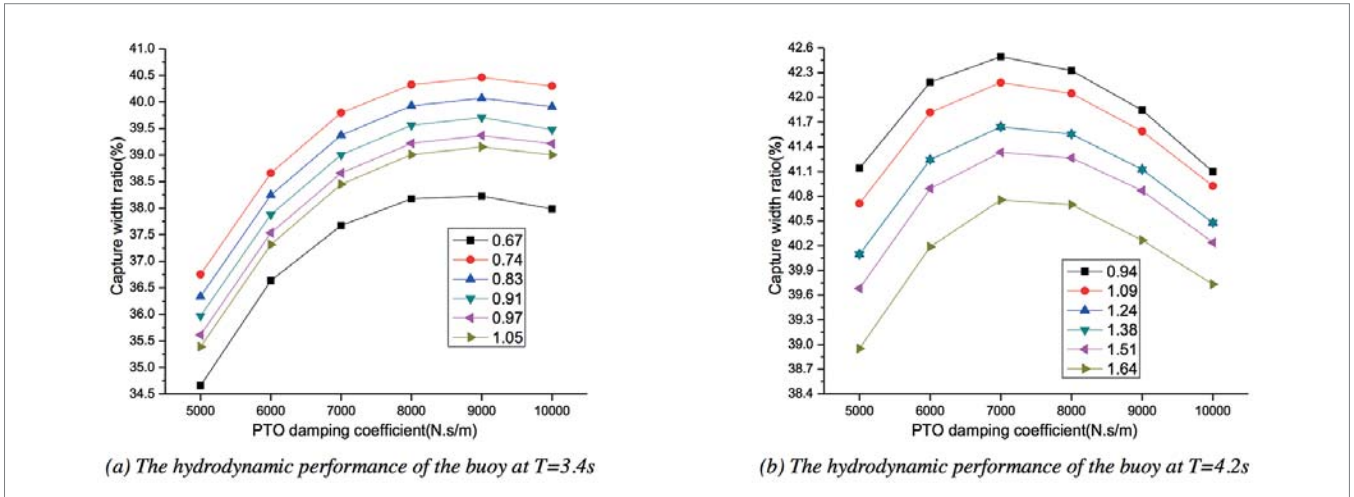


Fig. 11. Hydrodynamic performance of buoys under different wave heights

Fig. 11b shows the influence of different wave heights on the hydrodynamic performance of the buoy when the wave period is 4.2 s. It can be seen from the curve in the figure that when the wave heights are 0.94 m, 1.09 m, 1.24 m, 1.38 m, 1.51 m, 1.64 m, the corresponding optimal capture width ratios are 42.50%, 42.18%, 41.64%, 41.33%, 41.22%, and 40.75%, respectively. And the *PTO* damping coefficient corresponding to the maximum buoy capture width ratio is 7000 N · s/m in all cases.

From the above conclusions, under the same wave period, as the wave height increases, the buoy’s capture width ratio first increases and then decreases. The maximum capture width ratio of the buoy appears when the ratio of the buoy draft to the wave height is about 2.75, which is consistent with the conclusion of the previous section on the influence of the buoy draft on the hydrodynamic performance of the buoy. For the wave period of 3.4 s, the optimum *PTO* damping coefficient corresponding to the maximum capture width ratio of the buoy is $C = 9000 \text{ N} \cdot \text{s/m}$ in all cases. For the wave period of 4.2 s, the optimum *PTO* damping coefficient corresponding to the maximum capture width ratio of the buoy is all $C = 7000 \text{ N} \cdot \text{s/m}$ in all cases. The above shows that the optimal *PTO* damping coefficient is only related to the wave period, not the wave height.



Fig. 12. Physical model of “Haida No. 1”

EXPERIMENT AND RESULT ANALYSIS

In order to verify the consistency of the numerical results, an optimized physical model as shown in Fig. 12 is established based on the numerical results. In the physical model, the arm length L is 2.5 m, the tilt angle α is 20° , the buoy width D is 2 m, the buoy draft r is 1 m, and the buoy freeboard b is 0.5 m. The laboratory pool is 130 m long, 6 m wide and 4 m deep. One

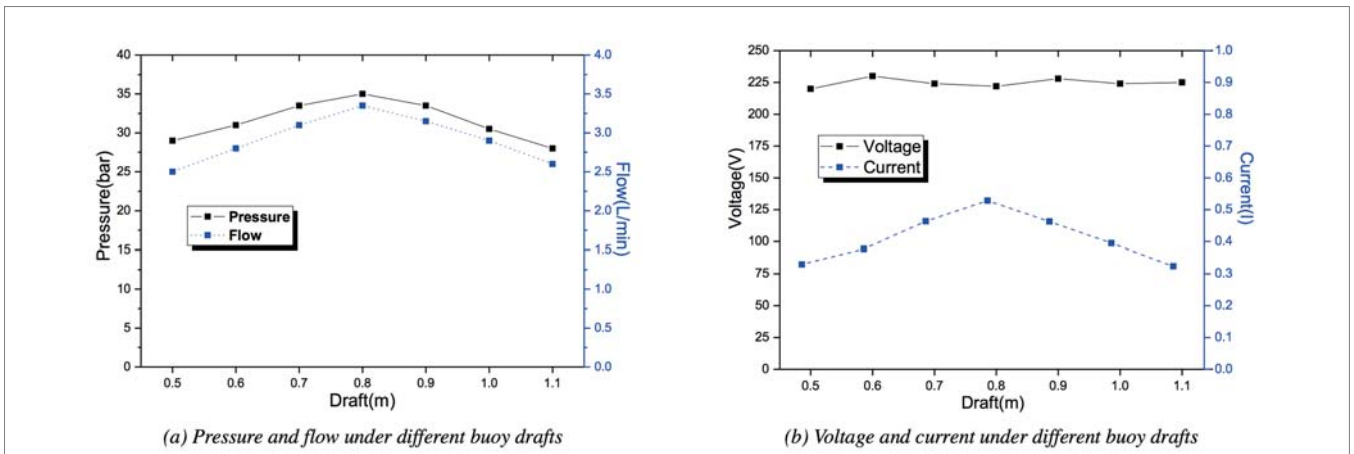


Fig. 13. Hydrodynamic performance of buoys under different buoy drafts

end of the laboratory pool is equipped with a hydraulic swing wave maker, and the other end is equipped with a sponge layer wave eliminator. The “Haida No. 1” OBWEC is installed at a distance of 30 m from the wave maker, and the influence of the reflected wave on the device can be ignored under the action of the sponge layer wave eliminator.

Fig. 13a shows the change curve of the pressure and flow in the hydraulic system for different buoy drafts when the wave period is 2.4 s and the corresponding wave height is 0.29 m. The product of pressure and flow in the hydraulic system represents the output power of the hydraulic system, which is proportional to the capture width ratio of the buoy. It can be seen from the curve in the figure that as the buoy’s draft increases, both the pressure and the flow rate first increase and then decrease. When the ratio of the buoy draft to the wave height is close to 2.75, the pressure and flow in the hydraulic system reach the maximum.

Fig. 13b shows the change curve of the output voltage and current for different buoy drafts when the wave period is 2.4 s and the corresponding wave height is 0.29 m. The product of the output voltage and current represents the total power output by the device, which is proportional to the capture width ratio of the buoy. It can be seen from the curve in the figure that when the ratio of the buoy draft to the wave height is close to 2.75, the output power reaches the maximum value, and the output voltage is relatively stable.

From the above conclusions, the experimental results verify the consistency of the numerical results.

CONCLUSION

In this paper, the “Haida No. 1” OBWEC is used as the research object, and its working principle is introduced. In order to further improve the energy conversion efficiency of the device, the influence of the arm length, tilt angle, buoy draft, buoy width, wave height, and *PTO* damping on the hydrodynamic performance of the buoy is studied based on the motion equation of the buoy in the waves. A physical model of “Haida No. 1” is established based on the numerical results, and the consistency of the numerical results is verified through a series of physical experiments. Based on the above results, the following conclusions are obtained:

1. The arm length L has a great influence on the hydrodynamic performance of the buoy. Under the same wave period, as the arm length increases, the hydrodynamic performance of the buoy first increases rapidly and then gradually remains unchanged. Therefore, when designing the arm length, it is necessary to choose a reasonable length to avoid wasting space with too long an arm, or reducing the hydrodynamic performance of the buoy with too short an arm.
2. The tilt angle α has a great influence on the hydrodynamic performance of the buoy. Under the same wave period, as the tilt angle increases, the hydrodynamic performance of the buoy first increases and then decreases. Within a certain range, as the wave period increases the optimal tilt angle gradually increases.
3. For the same wave period, as the buoy width D increases, the hydrodynamic performance of the buoy first increases and then decreases. When the ratio of the wavelength to the buoy width is between 4 and 5, the hydrodynamic performance of the buoy is the best.
4. The buoy shape 2 has better hydrodynamic performance than the other three buoy shapes in the same conditions.
5. For the same wave period, as the buoy draft r increases, the buoy’s hydrodynamic performance first increases and then decreases. When the buoy draft is about 2.75 times the wave height, the hydrodynamic performance of the buoy is optimal.
6. The *PTO* damping coefficient corresponding to the optimal hydrodynamic performance of the buoy is only related to the wave period, not to the wave height.

The above conclusions can provide a guide for optimizing the buoy’s hydrodynamic performance in similar WEC.

ACKNOWLEDGEMENTS

The authors acknowledge the National Natural Science Foundation of China (Grant: 51679217), and the Project of Ship Collaborative Innovation Centre of Jiangsu Province of China (Grant: HZ20180007).

REFERENCES

1. Panwar, N.L., S.C. Kaushik, and S. Kothari. ‘Role of renewable energy sources in environmental protection: A review Renewable and Sustainable Energy’, *Reviews*. 2011, doi: 10.1016/S1364-0321(99)00011-8.
2. Ellabban, O., H. Abu-Rub, and F. Blaabjerg. ‘Renewable energy resources: Current status, future prospects and their enabling technology’, *Renewable and Sustainable Energy Reviews*. 2014, doi: 10.1016/j.rser.2014.07.113.
3. Zheng, C.W., Q. Wang, and C.Y. Li. ‘An overview of medium-to long-term predictions of global wave energy resources’, *Renewable and Sustainable Energy Reviews*. 2017, doi: 10.1016/j.rser.2017.05.109.
4. Astariz, S., and G. Iglesias. ‘The economics of wave energy: A review’, *Renewable and Sustainable Energy Reviews*. 2015, doi: 10.1016/j.rser.2015.01.061.
5. Rosa-Santos, P., et al. ‘The CECO wave energy converter: Recent developments’, *Renewable Energy*. 2019, doi: 10.1016/j.renene.2019.02.081.
6. Zou, S., et al. ‘Optimal control of wave energy converters’, *Renewable Energy*. 2017, doi: 10.1016/j.renene.2016.11.036.
7. Zhang, W., and Y. Liu. ‘Simulation and experimental study in the process of wave energy conversion’, *Polish Maritime Research*. 2016, doi: 10.1515/pomr-2016-0056.

8. Sheng, W. 'Wave energy conversion and hydrodynamics modelling technologies: A review', *Renewable and Sustainable Energy Reviews*. 2019, doi: 10.1016/j.rser.2019.04.030.
9. Rusu, E., and F. Onea. 'A review of the technologies for wave energy extraction', *Clean Energy*. 2018, doi: 10.1093/ce/zky003.
10. Cordonnier, J., et al. 'SEAREV: Case study of the development of a wave energy converter', *Renewable Energy*. 2015, doi: 10.1016/j.renene.2015.01.061.
11. Zanuttigh, B., E. Angelelli, and J.P. Kofoed. 'Effects of mooring systems on the performance of a wave activated body energy converter', *Renewable Energy*. 2013, doi: 10.1016/j.renene.2013.02.006.
12. Sjolte, J., et al. 'Summary of performance after one year of operation with the lifesaver wave energy converter system', 10th European Wave and Tidal Energy Conference, Aalborg, Denmark, 2013.
13. Neary, V.S., et al. 'Classification systems for wave energy resources and WEC technologies', *International Marine Energy Journal*. 2018, doi: 10.36688/imej.1.71-79.
14. De Andrés, A.D., et al. 'Analysis of the geometric tunability of a WEC from a worldwide perspective', *International Conference on Offshore Mechanics and Arctic Engineering*. Vol. 45530. American Society of Mechanical Engineers, 2014.
15. Bedard, R., and G. Hagerman. 'E2I EPRI assessment offshore wave energy conversion devices', *Electrical Innovation Institute: Washington, DC, USA*, 2004.
16. Haraguchi, R., and T. Asai. 'Enhanced power absorption of a point absorber wave energy converter using a tuned inertial mass', *Energy*. 2020, doi: 10.1016/j.energy.2020. 117740.
17. Homayoun, E., H. Ghassemi, and H. Ghafari. 'Power performance of the combined monopile wind turbine and floating buoy with heave-type wave energy converter', *Polish Maritime Research*. 2019, doi: 10.2478/pomr-2019-0051.
18. Lai, W., D. Li, and Y. Xie. 'Simulation and experimental study of hydraulic cylinder in oscillating float-type wave energy converter', *Polish Maritime Research*. 2020, doi: 10.2478/pomr-2020-0024.
19. Sjolte, J., et al. 'Exploring the potential for increased production from the wave energy converter lifesaver by reactive control', *Energies*. 2013, doi: 10.3390/en6083706.
20. Han, Z., Z. Liu, and H. Shi. 'Numerical study on overtopping performance of a multi-level breakwater for wave energy conversion', *Ocean Engineering*. 2018, doi: 10.1016/j.oceaneng.2017.12.058.

CONTACT WITH THE AUTHORS

Yonghe Xie

e-mail: xieyh@zjou.edu.cn

Zhejiang Ocean University
Dinghai, 316022 Zhoushan

CHINA

Wenbin Lai

e-mail: 630880804@qq.com

Zhejiang Ocean University
Dinghai, 316022 Zhoushan

CHINA

Detang Li

e-mail: lidetang2008@163.com

Zhejiang Ocean University
Dinghai, 316022 Zhoushan

CHINA

SIMULATIONS AND TESTS OF COMPOSITE MARINE STRUCTURES UNDER LOW-VELOCITY IMPACT

Zhaoyi Zhu

Xiaowen Li*

Qinglin Chen

Yingqiang Cai

Yunfeng Xiong

Jimei University, School of Marine Engineering, China

Fujian Provincial Key Laboratory for Naval Architecture and Ocean Engineering

* Corresponding author: lixw2016@jmu.edu.cn (X. Li)

ABSTRACT

Due to their excellent performance, composite materials are increasingly used in the marine field. It is of great importance to study the low-velocity impact performance of composite laminates to ensure the operational safety of composite ship structures. Herein, low-velocity drop-weight impact tests were carried out on 12 types of GRP laminates with different layup forms. The impact-induced mechanical response characteristics of the GRP laminates were obtained. Based on the damage model and stiffness degradation criterion of the composite laminates, a low-velocity impact simulation model was proposed by writing a VUMAT subroutine and using the 3D Hashin failure criterion and the cohesive zone model. The fibre failure, matrix failure and interlaminar failure of the composite structures could be determined by this model. The predicted mechanical behaviours of the composite laminates with different layup forms were verified through comparisons with the impact test results, which revealed that the simulation model can well characterise the low-velocity impact process of the composite laminates. According to the damage morphologies of the impact and back sides, the influence of the different layup forms on the low-velocity impact damage of the GRP laminates was summarised. The layup form had great effects on the damage of the composite laminates. Especially, the outer 2-3 layers play a major role in the damage of the impact and the back side. For the same impact energy, the damage areas are larger for the back side than for the impact side, and there is a corresponding layup form to minimise the damage area. Through analyses of the time response relationships of impact force, impactor displacement, rebound velocity and absorbed energy, a better layup form of GRP laminates was obtained. Among the 12 plates, the maximum impact force, absorbed energy and damage area of the plate P_4 are the smallest, and it has better impact resistance than the others, and can be more in line with the requirements of composite ships. It is beneficial to study the low-velocity impact performance of composite ship structures.

Keywords: Low-velocity impact, marine structure, composites, test, finite element analysis

INTRODUCTION

Composite laminates are being increasingly used in lightweight structural components for a variety of engineering fields, such as the aerospace, automotive, marine and wind turbine sectors, because of their high strength-to-weight and stiffness-to-weight ratios, good fatigue performance and excellent corrosion resistance [1-3]. In the marine engineering field, fibre-reinforced composite materials can be used as hull panels, superstructure, main hull, propellers and fishing

tools, etc. [4-5]. However, due to their complicated operating environment, ships are often affected by various low-velocity impacts, such as collisions with other marine structures, floating objects, rocks, docks, and anchors. These low-velocity impacts often lead to internal damage to the composite hull structure, which cannot be observed by the human eye and severely affects the safety of the hull structure.

Based on a literature review, composite structures are more susceptible to impact damage than similar metallic structures. Although the surface of a composite structure may

not be visibly damaged or may sustain only slight pits after an impact, a large amount of matrix cracking and delamination damage may occur inside the laminates, and even some fibre fractures may occur. Even low-velocity, low-energy impacts can significantly reduce the mechanical properties of composite structures [6]. Moreover, due to the limitations of testing equipment and technology, internal damage can easily go undetected, which greatly reduces the safety of a ship during its service life. Therefore, at the beginning of the structural design of composite ships, it is of strategic importance to clarify the mechanical properties of composite laminates under low-velocity impact and improve the impact resistance of composite ship structures.

There are two main methods for studying the low-velocity impact of composite structures: mechanical tests and numerical simulations [7-14]. Common impact tests include drop-weight impact tests (ASTM D7136), Izod and Charpy impact tests (ASTM D256) and pendulum impact tests (ASTM D6110), among which the drop-weight impact method is most widely used. Considering that mechanical tests require more human effort and material resources, many researchers have begun to use numerical methods to simulate the low-velocity impact process of composite structures. Gliszczynski [14] dealt with experimental and numerical investigations of the composite plate subjected to low velocity impact. The numerical analyses were performed in the Ansys® environment. The implicit analyses were conducted with and without the implementation of the progressive failure algorithm and the application of the bilinear traction-separation law. High consistency of numerical and experimental results was achieved. The application of Hashin's criterion led to a valid prediction of the fibre failure areas and to overestimation of the matrix failure areas. Moura et al. [15-16] used Abaqus to simulate the low-velocity impact process, and the simulated delamination shape and area were in good agreement with their test results. However, their approach regarded the impact process as a quasi-static process and was unable to simulate the damage evolution process. Hou et al. [17] proposed a failure criterion for matrix and fibres to estimate the matrix cracking and fibre fracture of composite laminates under impact by revising the Tsai-Wu criterion. Luo et al. [18] applied an Abaqus subroutine to simulate the impact damage of laminates, and their simulation results were in good agreement with the experimental results. Wen et al. [19] used Ansys for damage analysis of composite materials, and their simulation results were in good agreement with the experimental results. Zhu et al. [20] established a composite damage simulation model through the VUMAT subroutine in Abaqus and found that the simulated damage area was in good agreement with the test results. Qiu et al. [4] investigated the impact responses and impact-induced damage of typical marine laminates by the FE method and found that the impact behaviours obtained in the simplified FE model are effective and can be comparable with experiments with a short computing time. Zhu et al. [21] used Abaqus for low velocity impact damage of composite laminates for ships, the typical failure modes were simulated by employing the 2D Hashin

criterion, and material degradation and a damage factor were taken into account in this model. The dynamic response and damage propagation of laminates were studied. The numerical results agree well with the experimental results. In a word, the numerical study of the low-velocity impact behaviour of laminates is more in-depth in the aerospace field, and the research on marine composite structures needs to be further developed.

Most of the research in the literature was based on finite element software and focused on simulating composite damage or improving failure criteria. In other words, different failure criteria were used to simulate the delamination damage, fibre failure and matrix damage of composite laminates to obtain a force-displacement curve to simulate the actual macroscopic state. With the increasing application of composites in the marine field, the low-velocity impact behaviour of composite hull structures has attracted more attention. There are challenges in using composite laminates in marine engineering, i.e., composites frequently suffer from the effects of impaction, including wave impaction, being hit by ships or other objects, missiles or bullets, and other special conditions. It is important to understand the impact behaviour of laminates. Hence, this study selected a composite yacht structure as the research object, and the mechanical behaviour of composite marine laminates under low-velocity impact was studied through mechanical testing and numerical simulation. The effects of 12 different layup forms on the impact resistance of composite laminates were tested and investigated. The results from this work provide a reference for the study of the low-velocity impact performance of composite ships.

EXPERIMENTAL METHOD

MATERIAL

The hull plate of a 75-foot glass-reinforced polymer (GRP) yacht was used as the base plate (No. P₁), and its layup form was used as the original layup. According to the original layup of P₁, an explorative design was carried out. Table 1 lists the specific layup forms. In the table, "A" represents CSM300, which is a chopped strand mat with an areal mass of 300 g/m²; "B" represents CSM225, which is a chopped strand mat with an areal mass of 225 g/m²; "C" represents EDJ300, which is a uniaxial cloth with an areal mass of 300 g/m²; and "D" stands for EDJ400, which is a uniaxial cloth with an areal mass of 400 g/m². The subscripts 0°, 90°, +45°, and -45° represent the fibre direction in a single ply, i.e., the angle between the fibre and the long side of the specimen. In order to make the layers design conform to the actual situation of the shipyard, the above four materials were selected. To investigate the influence of different layup forms on the low-velocity impact of the laminates, the layup sequence and angle were designed on the basis of the original layup. The design mainly followed the following principles:

- 1) Layup sequence: ensure that the sequence of the outermost layer N_1 to the third layer N_3 of the original layup remains unchanged and that the total number of chopped strand mats and uniaxial cloths remains unchanged, changing the position of the uniaxial cloths. And from the fourth layer, at least one layer of chopped strand mat should be laid between every two layers of uniaxial cloths.
- 2) Laying angle: ensure that the sequence and angle of the outermost layer N_1 to the third layer N_3 of the original layup remain unchanged and that the total number of chopped strand mats and uniaxial cloths remains unchanged, changing the layup angle of the uniaxial cloths.

Eleven different layup forms derived from the original layup are shown in Table 1. In the table, N_1 is the impact surface, N_2 - N_{12} are the internal layers, and N_{13} is the back surface of the impact laminates.

The GRP laminates in Table 1 were made by the wet layup process. The dimensions of the 12 GRP laminates were 350 mm × 350 mm. After the laminates were cured (Fig. 1), they were cut into rectangular plates with dimensions of 150 mm × 100 mm, as required by the test specification. To ensure the validity of the test results, three standard specimens were made for each layup form.

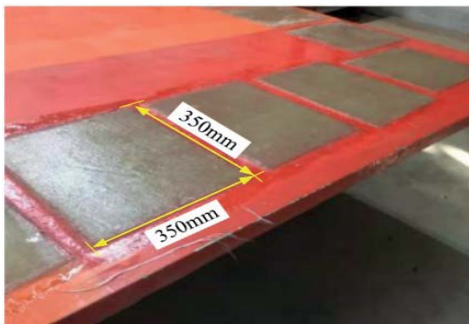


Fig. 1. GRP laminates with different layup forms

Tab. 1. Twelve layup forms used for the GRP laminates

Plate number	Layup sequence												
	N_1	N_2	N_3	N_4	N_5	N_6	N_7	N_8	N_9	N_{10}	N_{11}	N_{12}	N_{13}
P ₁	A	A	B	C _{0°}	C _{90°}	B	D _{0°}	D _{90°}	A	A	B	C _{90°}	C _{0°}
P ₂	A	A	B	C _{0°}	C _{90°}	B	C _{0°}	C _{90°}	A	A	B	D _{90°}	D _{0°}
P ₃	A	A	B	D _{0°}	D _{90°}	B	C _{0°}	C _{90°}	A	A	B	C _{90°}	C _{0°}
P ₄	A	A	B	C _{0°}	C _{90°}	B	D _{0°}	D _{90°}	B	C _{0°}	C _{90°}	A	A
P ₅	A	A	B	D _{0°}	D _{90°}	B	C _{0°}	C _{90°}	B	C _{0°}	C _{90°}	A	A
P ₆	A	A	B	C _{0°}	C _{90°}	B	C _{0°}	C _{90°}	B	D _{0°}	D _{90°}	A	A
P ₇	A	A	B	C _{+45°}	C _{-45°}	B	D _{0°}	D _{90°}	A	A	B	C _{90°}	C _{0°}
P ₈	A	A	B	C _{0°}	C _{90°}	B	D _{+45°}	D _{-45°}	A	A	B	C _{90°}	C _{0°}
P ₉	A	A	B	C _{0°}	C _{90°}	B	D _{0°}	D _{90°}	A	A	B	C _{+45°}	C _{-45°}
P ₁₀	A	A	B	C _{+45°}	C _{-45°}	B	D _{0°}	D _{90°}	A	A	B	C _{+45°}	C _{-45°}
P ₁₁	A	A	B	C _{0°}	C _{90°}	B	D _{+45°}	D _{-45°}	A	A	B	C _{+45°}	C _{-45°}
P ₁₂	A	A	B	C _{+45°}	C _{-45°}	B	D _{+45°}	D _{-45°}	A	A	B	C _{90°}	C _{0°}

IMPACT TESTS

Low-velocity impact tests were performed using an instrumented drop-weight testing machine (ZCJ1302-AD) in accordance with ASTM D7136. Low-velocity impact generally requires a speed less than 10 m/s [22-23], known as low-energy impact, which does not break through the composite plate but gives a permanent indentation in its surface. The tests were conducted with a drop-weight tower consisting of two rigid steel columns firmly connected to a metal gantry. The centre of the specimens was impacted with a hemispherical impactor. The impactor was connected to a piezoelectric sensor and was used to carry out the impacts and measure the impact force. The impact velocity was measured through a laser sensor, and an anti-rebound system was used to avoid producing multiple impacts on the same specimen. A rigid fixture was used to hold the specimens. The fixture was mounted onto a rigid steel base via four rigid clamps. Four lateral guiding pins were installed on the fixture to correctly position each specimen, and four clamps were used to hold the specimen during impact. Fig. 2 shows details of both the impactor and the fixture used in the tests. The specimens were placed on the steel base with a 125 mm × 75 mm cut-out. The initial impact conditions are shown in Table 2.

Tab. 2. Initial impact conditions

Impact energy (J)	Impactor mass (kg)	Impactor diameter (mm)	Impactor velocity (m/s)
25	2	12.5	4.98

Impact tests were conducted on the 12 different GRP specimens in the same environment. The tests were divided into 12 groups, and each group was used to carry out repeatability tests on 3 specimens with the same layup form. Fig. 3 shows the impact side and the back side of the 12 specimens after low-velocity impact. The number in the lower-left corner of the figure is the specimen group number (corresponding to the plate number in Table 1), and the number in the upper-right corner is the specimen number in each group.

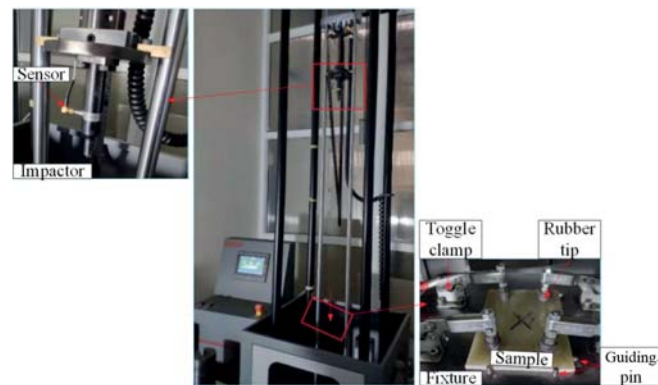
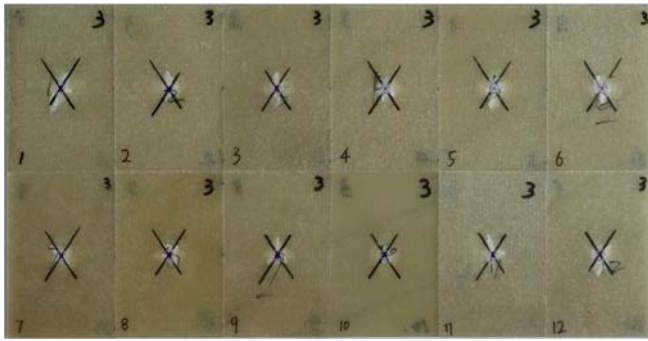
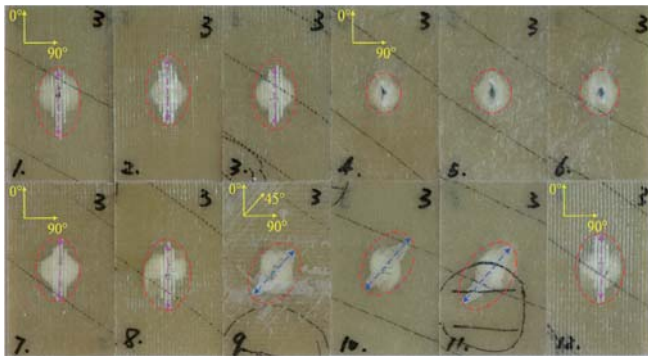


Fig. 2. Drop-weight testing machine



(a) The impact side



(b) The back side

Fig. 3. The damage morphology of 12 GRP specimens with different layout forms

NUMERICAL ANALYSIS

The impact behaviour of composite laminates, in which many failure mechanisms occur simultaneously and randomly, is more complex than that of metal materials. In particular, the impact damage of composite structures is a nonlinear problem involving various geometries, materials and contacts. Therefore, in the low-velocity impact simulation process of GRP structures, the damage model of the laminates should be clarified first to obtain effective numerical simulation results.

DAMAGE MODEL

Intralaminar damage

(1) Failure criteria

The failure modes of composites mainly include fibre failure, matrix failure and delamination failure. Fibre failure is divided into tensile and compressive fibre failure. Matrix failure is divided into tensile and compressive matrix failure. In the failure process of composite laminates, one failure mode is usually associated with others, or several failure modes occur together. Impact loads further complicate the failure of a composite structure. The literature [24-25] shows that some failure modes of composites have the same characteristics under dynamic and static loads. In other words, the failure mechanism of a composite is not related to the strain rate. Therefore, the failure criterion for quasi-static analysis can

be used in dynamic impact analysis. In this paper, the 3D Hashin criterion is used as the failure criterion [26-29]. The corresponding failure mode is as follows:

(1) Tensile fibre failure ($\sigma_{11} \geq 0$)

$$D_1 = \left(\frac{\sigma_{11}}{X_T} \right)^2 + \left(\frac{\tau_{12}}{S_{12}} \right)^2 + \left(\frac{\tau_{13}}{S_{13}} \right)^2 = \begin{cases} \geq 1 & \text{failure} \\ < 1 & \text{no failure} \end{cases} \quad (1)$$

(2) Compressive fibre failure ($\sigma_{11} < 0$)

$$D_2 = \left(\frac{\sigma_{11}}{X_C} \right)^2 = \begin{cases} \geq 1 & \text{failure} \\ < 1 & \text{no failure} \end{cases} \quad (2)$$

(3) Tensile matrix failure ($\sigma_{22} + \sigma_{33} \geq 0$)

$$D_3 = \left(\frac{\sigma_{22} + \sigma_{33}}{Y_T} \right)^2 + \frac{\tau_{12}^2 + \tau_{13}^2}{S_{12}^2} + \frac{\tau_{23}^2 - \sigma_{22}\sigma_{33}}{S_{23}^2} = \begin{cases} \geq 1 & \text{failure} \\ < 1 & \text{no failure} \end{cases} \quad (3)$$

(4) Compressive matrix failure ($\sigma_{22} + \sigma_{33} < 0$)

$$D_4 = \frac{\tau_{12}^2 + \tau_{13}^2}{S_{12}^2} + \frac{\sigma_{22} + \sigma_{33}}{Y_C} \left[\left(\frac{Y_C}{2S_{23}} \right)^2 - 1 \right] + \frac{\tau_{23}^2 - \sigma_{22}\sigma_{33}}{S_{23}^2} + \left(\frac{\sigma_{22} + \sigma_{33}}{2S_{23}} \right)^2 = \begin{cases} \geq 1 & \text{failure} \\ < 1 & \text{no failure} \end{cases} \quad (4)$$

In formulas (1)-(4), D_1 , D_2 , D_3 , and D_4 are the damage variables under different failure modes. X_T , X_C , Y_T and Y_C denote the tensile and compressive strengths of the single-layer plate in the fibre direction and transverse direction, respectively. S_{ij} is the shear strength of the single-layer plate corresponding to the ij direction. When the stress state of an element satisfies any of the failure criteria, the corresponding damage mode occurs in this element. When the stress state of an element satisfies more than one of the failure criteria at the same time, a variety of corresponding damage modes occur in this element.

(2) Stiffness degradation model

The 3D Hashin failure criterion can determine the stress-strain relationship of a composite single-layer plate when the initial damage occurs. After the initial damage, the structure does not immediately lose its bearing capacity. The damage progression in the structure, from the onset of initial damage to the complete collapse of the structure, is a gradual accumulation process, and its essence is that the material stiffness decreases continuously. Thus, the final failure of composite structures cannot be accurately predicted by the Hashin criterion alone. Therefore, the progressive failure analysis method is used [30-31]. After the Hashin criterion determines the initial damage, the material parameters in the damaged area are modified. To realise the effective transition from the undamaged area to the damaged area, the stress in the failure area is reduced according to a certain rule.

In the calculation process, if the stress state of the element meets the failure criterion, the stiffness degradation of the material is carried out. The elastic parameter of the element is multiplied by some reduction factor. With this material property degradation method, although the element has been damaged, it will continue to contribute to the stiffness of the laminate as long as it exists. In this paper, the Tan stiffness degradation criterion [32-33] is adopted, and the specific stiffness degradation scheme is shown in Table 3.

Tab. 3. Tan stiffness degradation criterion

Failure mode	Stiffness degradation
Tensile fibre failure	$E_{11}'=0.07E_{11}, G_{12}'=0.07G_{12}, G_{13}'=0.07G_{13},$ $\nu_{12}'=0.07\nu_{12}, \nu_{13}'=0.07\nu_{13}$
Compressive fibre failure	$E_{11}'=0.14E_{11}, G_{12}'=0.14G_{12}, G_{13}'=0.14G_{13},$ $\nu_{12}'=0.14\nu_{12}, \nu_{13}'=0.14\nu_{13}$
Tensile matrix failure	$E_{22}'=0.2E_{22}, E_{33}'=0.2E_{33}, G_{23}'=0.2G_{23},$ $\nu_{12}'=0.2\nu_{12}, \nu_{23}'=0.2\nu_{23}$
Compressive matrix failure	$E_{22}'=0.4E_{22}, E_{33}'=0.4E_{33}, G_{23}'=0.4G_{23},$ $\nu_{12}'=0.4\nu_{12}, \nu_{23}'=0.4\nu_{23}$

In the VUMAT subroutine of Abaqus, the state variables corresponding to the four failure modes are defined according to the Hashin criterion. The value of the state variable is 0 before the element failure, and is set to 1 when the failure occurs. Then the corresponding parameters are reduced according to Table 3. At the beginning of the incremental step, the state variables of the element (corresponding to various failure modes) are determined first, and the material parameters of this element are obtained (according to the stiffness degradation coefficient in Table 3). Second, the strain increment is applied and the stress is updated. Next, the Hashin criterion is used to determine whether a new failure occurs. If so, the corresponding state variable is set to 1 and the corresponding parameters are reduced. Finally, the stress under this incremental step is recalculated by using the new material parameters, and the incremental step of this element is over. Considering the irreversibility of the damage, once a state variable of the element is set to 1, the elastic parameters will not change after a reduction. When two or more failure modes occur in the same element, the minimum value of the degradation coefficient corresponding to different failure modes shall be taken. If there is an element with serious shape distortion, it will be deleted.

Interlaminar damage

The cohesive zone model based on the traction-separation constitutive relation was used to predict the interlaminar damage under low-velocity impact, and the damage constitutive relationship is shown in Fig. 4. The initiation of damage is based on a quadratic traction-separation law [34]; see formula (5). Once failure is initiated, it propagates following the element energy release rate. The mixed-mode damage evolution criterion (B-K criterion) proposed by Benzeggagh and Kenane was adopted to characterise the expansion law of interlaminar damage [35]; see formula (6).

$$\left(\frac{\langle\sigma_n\rangle}{N}\right)^2 + \left(\frac{\sigma_t}{S}\right)^2 + \left(\frac{\sigma_s}{T}\right)^2 \geq 1 \quad (5)$$

where σ_n , σ_t and σ_s represent normal traction and shear traction, respectively; $\langle\sigma_n\rangle=(\sigma_n+|\sigma_n|)/2$; and N, S and T are the normal strength and shear strength of the interface, respectively.

$$G_C = G_{IC} + (G_{IIC} - G_{IC}) \left(\frac{G_{IIC} + G_{IIIC}}{G_{IC} + G_{IIC} + G_{IIIC}} \right)^\eta \quad (6)$$

where G_C is the mixed-mode fracture toughness; G_{IC} , G_{IIC} and G_{IIIC} are the critical energy release rates of type I, type II and type III, respectively; and η is the B-K power law parameter and is related to the material. For carbon fibre or glass fibre reinforced resin composites, the value of η is in the range of 1-2[33,36-38]. Based on previous studies and finite element calculations, η is 1.45 in this paper.

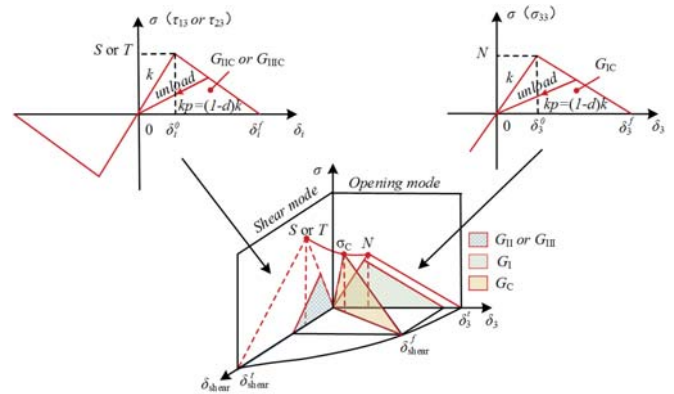


Fig. 4. Damage constitutive relation

MODELLING OF IMPACT ON COMPOSITE LAMINATES

Finite element model

According to the specific conditions of the low-velocity impact test, a finite element model was developed in Abaqus/Implicit, as shown in Fig. 5. The whole model was created in three parts, the impactor, laminate and the base. The hemispherical impactor and the base were simplified as analytical rigid bodies. The single-layer plate was discretised with 8-node reduced-integration solid elements (C3D8R), and the layers were connected by 0.02 mm 3D cohesive elements (COH3D8), which can simulate the mechanical behaviour between layers. The laminate model contains 129,600 solid elements and 124,200 cohesive elements. The dimensions of the laminate were 150 mm × 100 mm × 6.52 mm.

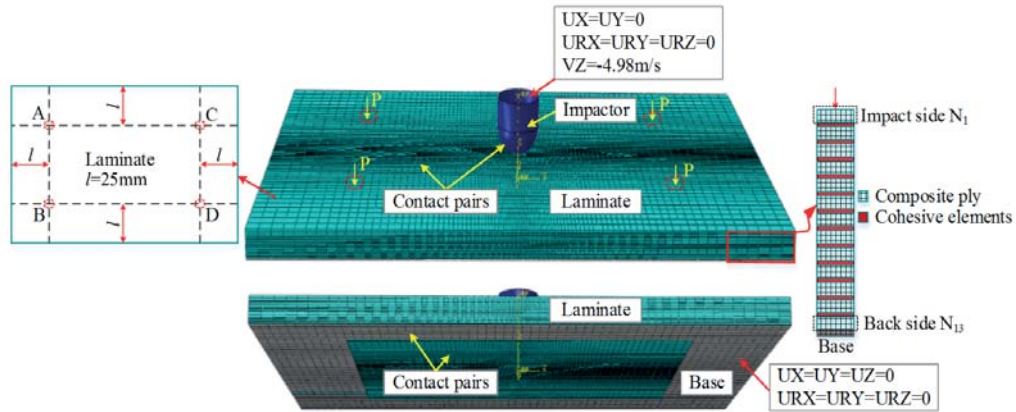


Fig. 5. Finite element model for impact analyses

In the experiment the analysed laminate was supported on the base and was additionally stabilised by four rubber tips of the toggle clamps. In order to simplify the boundary conditions and reflect the real experimental testing as much as possible, the rigid body displacement of the laminate was restricted by the fixture base and the toggle clamps. A standard surface-to-surface contact algorithm available in Abaqus/Implicit was used to simulate the impactor-laminate contact and the laminate-base contact during impact. And at the position of the rubber tips (red dotted line in Fig. 5), the force P along the Z axis was applied to simulate the restraint effect of the clamping element. And based on ASTM D7136 standard, the value of P is equal to -275 N . Compared with the specimen deformation, the deformation of the base during the impact process was negligible, so the base was set as a fixed constraint during the analysis process. The impactor was free in the Z direction and constrained in the X and Y directions.

Material properties

GRP laminates consist of two main materials, chopped strand mat and axial cloth, and their mechanical properties are shown in Table 4. In the table, X_T and X_C are the tensile and compressive strengths in the fibre direction, respectively; Y_T and Y_C are the tensile and compressive strengths in the orthogonal direction of the fibre, respectively; Z_T and Z_C are the tensile and compressive strengths in the thickness direction of the laminates, respectively; S_{12} , S_{13} , S_{23} are the shear strengths in the 12, 13, and 23 directions, respectively; ρ is the material density; and h is the thickness of a single-layer plate. The parameters of the cohesive interface elements are shown in Table 5. In the table, E is the elastic modulus of the interface layer, G_1 is the shear modulus in the 1 direction, and G_2 is the shear modulus in the 2 direction.

Table 4. Material properties used in the finite element analyses

Properties	Materials			
	A	B	C	D
E_1 (MPa)	13600	11600	23500	25600

Properties	Materials			
	A	B	C	D
E_2 (MPa)	13600	11600	6560	7120
E_3 (MPa)	10700	8062	6560	7120
ν_{12}	0.321	0.347	0.205	0.237
ν_{13}	0.127	0.139	0.205	0.237
ν_{23}	0.105	0.108	0.310	0.332
G_{12} (MPa)	7760	4602	2265	2473
G_{13} (MPa)	5200	3847	2265	2473
G_{23} (MPa)	5200	3847	1847	2011
X_T (MPa)	192	186	810	830
X_C (MPa)	260	250	475	490
Y_T (MPa)	192	186	58	63
Y_C (MPa)	260	250	145	160
Z_T (MPa)	76	70	58	63
Z_C (MPa)	320	310	145	160
S_{12} (MPa)	103	97	59	65
S_{13} (MPa)	66	60	59	65
S_{23} (MPa)	66	60	50	53
ρ (kg/cm ³)	1500	1320	1790	1800
h (mm)	0.55	0.34	0.375	0.5

Tab. 5. Interface properties used in the finite element analyses

Modulus (MPa)	Strength (MPa)	Energy release rate (N/mm)
$E = 3000$	$N = 20$	$G_{ic} = 0.249$
$G_1 = 1154$	$S = 25$	$G_{iic} = 0.733$
$G_2 = 1154$	$T = 25$	$G_{iiic} = 0.733$

Simulation of the low-velocity impact process of laminates

Low-velocity impact simulations were set up in accordance with the test performed in section 2.2. In Abaqus/Explicit, a VUMAT subroutine was used to define the material properties, damage criteria and damage evolution of the composite laminates. Based on the damage model in Section 3.1, the VUMAT subroutine was written in Fortran (Fig. 6). During calculation, this subroutine was used to assign user-defined material properties to the target model and iterate until the calculation was terminated. The specific analysis process is shown in Fig. 7. In each step, the VUMAT

subroutine obtains the value of stress and strain and the number of elements in the Abaqus main program, judges the damage state and degradation degree of each element, assesses the stress, strain, and damage factor, and then sends this information back to the Abaqus main program.

LOW-VELOCITY IMPACT RESULTS

ANALYSIS OF DAMAGE

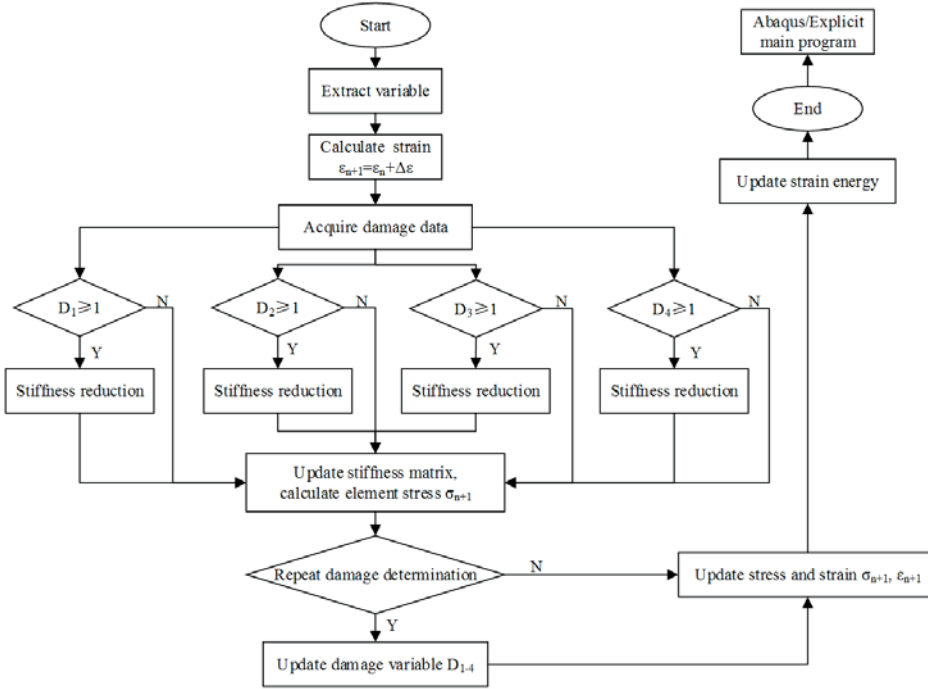


Fig. 6. VUMAT subroutine

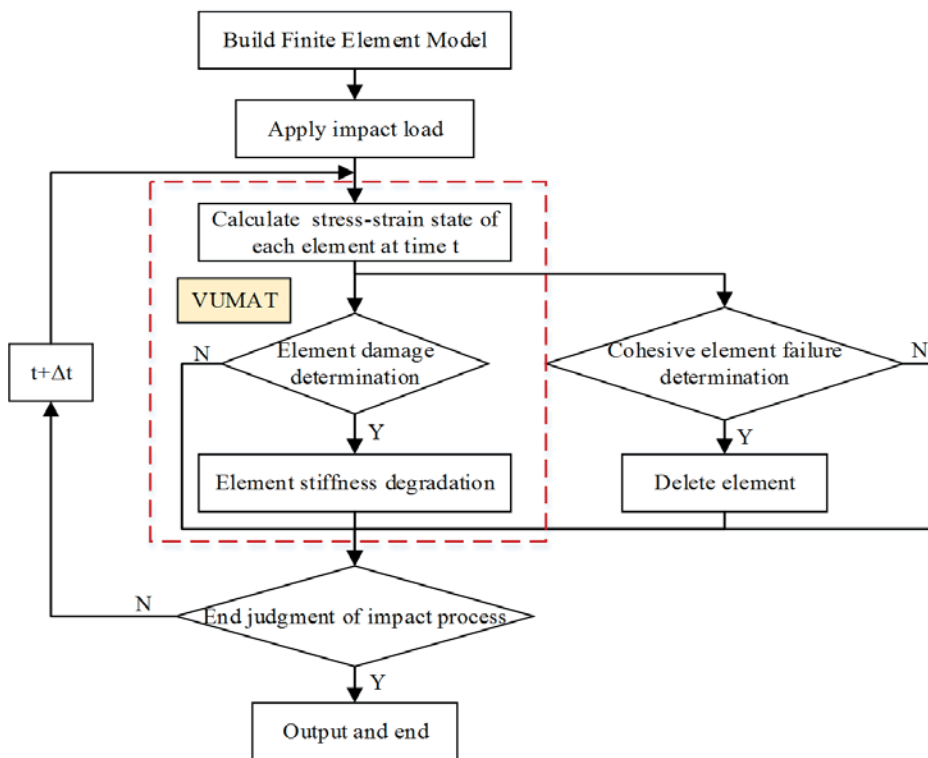


Fig. 7. Numerical analysis flow of the low-velocity impact of laminates

In the same environment, 25J impact tests were carried out on the 12 GRP specimens with different layup forms. Fig. 3 shows the impact and back sides of these specimens after low-velocity impact. The impact load produced varying degrees of fibre, matrix and delamination damage. It should be noted that each plate shown in Fig. 3 is one of three standard specimens and all the experimental values are the average of the three repeated tests. In the preliminary analysis of the results, attention was focused on the areas and the nature of the observed damage [13]. The initial damage occurred at the impact side, and the material at the impact point was plastically deformed. Due to the high contact force, the damage expanded rapidly to the interior of the laminate. As shown in Fig. 3(a), the damage morphology of the 12 plates is similar. There are obvious pits in the contact position between the impact side and the impactor. These pits are about 9 mm in diameter. It is well known that the damage is closely related to the layup form. The reason for this phenomenon is that the layup forms of N_1 - N_3 for all plates are consistent. In order to obtain more damage information, the back side of the tested specimens was analysed. By observing the damage characteristics shown in Fig. 3(b), it was found that the damage morphologies of P_4 - P_6 were similar, in which fine delamination damage could be seen in a radius of approximately 13 mm around the centre on the N_{13} plane. The damage morphologies of P_1 - P_3 , P_7 , P_8 and P_{12} were

similar, in which fine delamination damage could be seen in an ellipse with a long axis of approximately 58 mm and a short axis of approximately 40 mm around the centre, and there was clear fibre delamination damage in the 0° direction on the N₁₃ plane. The damage morphologies of P₉-P₁₁ were similar, in which fine delamination damage could be seen in an ellipse with a long axis of approximately 60 mm and a short axis of approximately 30 mm around the centre and there was obvious fibre delamination damage in the 45° direction on the N₁₃ plane. Therefore, these 12 plates can be divided into 4 groups, P₁-P₃, P₄-P₆, P₇, P₈, P₁₂ and P₉-P₁₁.

Taking the layup form of P₁ as a reference, the position and material of the changed layup were marked with symbols. Table 1 was simplified to make the comparative analysis more intuitive, as shown in Table 6. The analysis shows that the layup form of P₂ and P₃ is the closest to P₁; P₄, P₅ and P₆ have similar layup forms, but P₄ has a small difference; the layup forms of P₇, P₈, and P₁₂ are similar; P₉, P₁₀ and P₁₁ have similar layup forms. This is consistent with the experimental characterisation results shown in Fig. 3(b).

Tab. 6. The simplified layup forms of GRP laminates

Plate number	Layup sequence												
	N ₁	N ₂	N ₃	N ₄	N ₅	N ₆	N ₇	N ₈	N ₉	N ₁₀	N ₁₁	N ₁₂	N ₁₃
P ₁	A	A	B	C _{0°}	C _{90°}	B	D _{0°}	D _{90°}	A	A	B	C _{90°}	C _{0°}
P ₂	◇	□	..	◆	■	□	◇
P ₃				◆	■		◇	□					
P ₄									..	◇	□
P ₅				◆	■		◇	□	..	◇	□
P ₆							◇	□	..	◆	■
P ₇				△	▽								
P ₈							▲	▼					
P ₉				◇	□							△	▽
P ₁₀				△	▽							△	▽
P ₁₁							▲	▼				△	▽
P ₁₂				△	▽		▲	▼					

Note: △, ▽ stand for C+45°, C-45°; ▲, ▼ stand for D-45°, D+45°.

It was discovered that the damage morphology was closely related to the layup form of N₁₂ and N₁₃. N₁₂ and N₁₃ of P₄-P₆ were all chopped strand mats, which absorb more energy than uniaxial cloth, and the corresponding damage area was smaller. N₁₂ and N₁₃ of P₁-P₃, P₇, P₈ and P₁₂ were uniaxial fabrics laid at 90° and 0°, respectively; these plates exhibited obvious fibre delamination damage in the 0° direction. N₁₂ and N₁₃ of P₂ were uniaxial cloths with an areal mass of 400 g/m², whose strength was slightly higher than those of the 300 g/m² uniaxial cloth used in other laminates; accordingly, the damage area of P₂ was slightly smaller.

N₁₂ and N₁₃ of P₉-P₁₁ were uniaxial cloths laid at ±45°. There was fibre delamination damage in the ±45° direction, and the damage area was also slightly larger in these laminates. It is commonly known that the damage area is one of the important characteristics to judge the low-velocity impact damage of laminates. The included damage areas were divided into two parts: blue line outside - maximum damage area, yellow line inside - concentrated damage area, as shown in Fig. 8. With respect to the damage area, Fig. 8 shows the maximum damage area (MDA) and concentrated damage area (MDC) of the 12 tested specimens. The damage areas of each layer partially overlap and the MDC represents the overlapping region of the damage area. P₄ has the smallest maximum damage area and concentrated damage area. For the maximum damage scale indicated in Fig. 9, there is P₄ < P₅ < P₆ < P₃ < P₇ < P₂ < P₉ < P₁₀ < P₈ < P₁₂ < P₁ < P₁₁. Among the 12 layup forms, the tested specimens in which N₁₂ and N₁₃ were chopped strand mat had better impact resistance than the specimens where these layers were uniaxial cloths laid at 0° and 90° and slightly better than the specimens where these layers were uniaxial cloths laid at ±45°. Analysing the obtained results, it is easy to see that P₄ has a better layup form than the others.

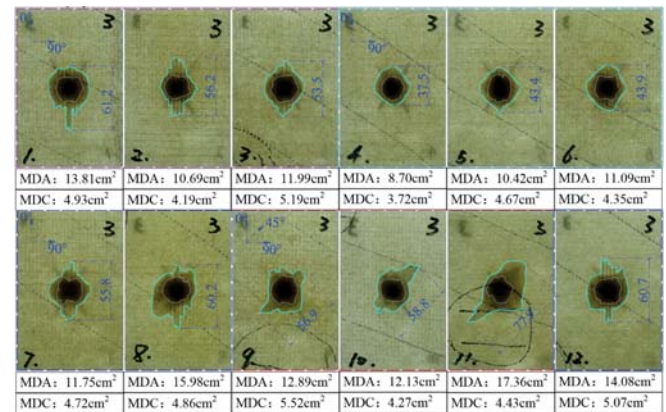


Fig. 8. The damage projection and areas of 12 tested specimens

ANALYSIS OF MECHANICAL RESPONSE

Fig. 9 shows the simulation process of P₁ under impact. Fig. 9(a) shows the state at the beginning of the impact, Fig. 9(b) shows the state at an impact time of 2.5 ms, and Fig. 9(c) shows the state after the impact. Based on P₁, the validity of the numerical simulation was verified. According to the results of the tests and simulations, the time response characteristics were analysed in terms of impact force, impactor displacement, impactor speed and absorbed energy. The mechanical behaviour of the GRP laminates under low-velocity impact was predicted.

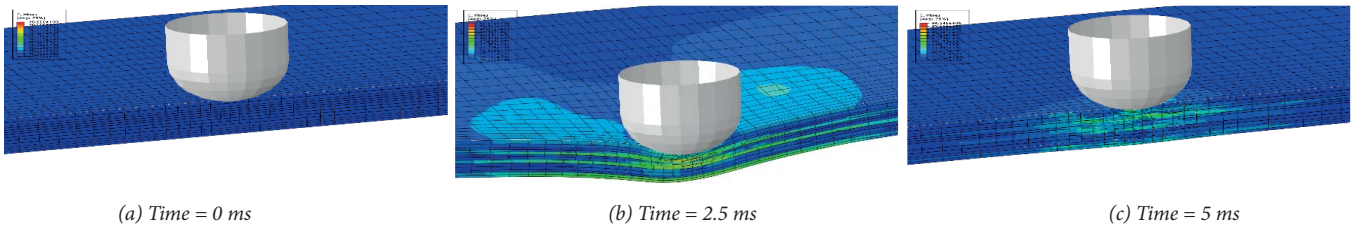


Fig. 9. Simulation process of P_1 under impact

Impact force–time response

The force–time histories of P_1 are represented in Fig. 10, in which the impact force and the time are represented by F and t , respectively. In the elastic phase, the force linearly increased to the initial damage threshold (F_H), at which time the initial damage caused the stiffness of the laminate to start to change. Between the initial damage threshold and the peak force, the curves fluctuated mainly due to the damage evolution within and between layers. After the impact force reached the peak (F_M), the impactor began to rebound until it separated from the laminates, and the impact force dropped to zero. A comparison shows that the trends from the test and simulation (FE) results of P_1 were relatively consistent. The simulation errors of the initial damage threshold and the peak force were 8.7% and 4.1%, respectively.

Fig. 10 shows that the simulation curve fluctuated slightly more than the test curve. One reason for this discrepancy is that the Tan stiffness degradation criterion was adopted in the simulation. After the elements reached the damage criterion, the stiffness suddenly decreased, which can cause a sudden change in the stiffness of the entire laminate and result in an unstable contact force. Another potential reason for this discrepancy is that the grid accuracy was not sufficient, and the stiffness degradation of a single element had a significant effect on the stiffness of the entire laminate. The fluctuations in the test curve were relatively gentle because the fibres in the laminates were sufficiently dense. From a macro perspective, damage to the fibres and the matrix occurred gradually. The rigidity of the laminates gradually decreased, so the fluctuations of the impact load were not very violent. After the impactor started to rebound, the impact force–time curves were relatively flat in both the test and the simulation. This was because the laminates were no longer damaged during the rebound process.

The test and simulation results of the maximum impact force of P_1 – P_{12} are shown in Fig. 11. In the test data, the maximum impact force of P_4 – P_6 was relatively low. A possible reason for this was that N_{12} and N_{13} were chopped strand mats with low stiffness, and a uniaxial cloth with greater stiffness was set in the middle of the laminate. Therefore, the stiffness of the entire laminate was relatively low, and the maximum impact force was lower. The maximum impact forces of P_1 – P_3 and P_7 – P_{12} were relatively high. A possible reason for this was that N_{12} and N_{13} were uniaxial cloths, the stiffness of the whole laminate was relatively high, and the maximum impact force increased accordingly. With different layout forms, the simulation results were consistent with the

experimental results. In terms of impact force alone, P_4 can effectively disperse the external force concentration, and its layout form is relatively good.

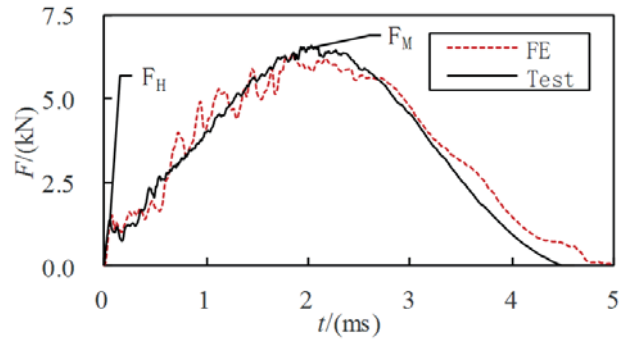


Fig. 10. Force-time histories of P_1

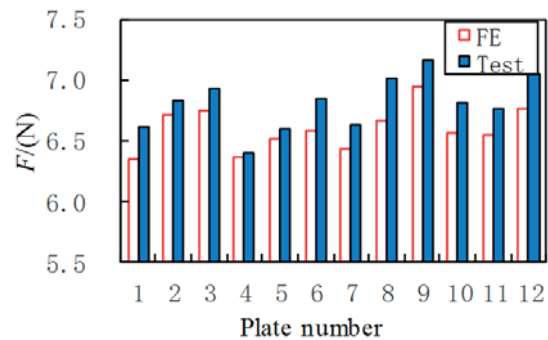


Fig. 11. Maximum impact force of P_1 – P_{12}

Impactor displacement–time response

The displacement–time histories of P_1 are shown in Fig. 12, in which the displacement is represented by D . A comparison shows that there was relatively good agreement between the test and simulation results; the maximum displacement error was only 2.1%. Hence, the simulation model can well reflect the displacement variation of the impactor during the impact process.

In Fig. 13, the experiment and simulation results of the maximum impactor displacement of P_1 – P_{12} were consistent. The maximum displacement of P_4 – P_6 was relatively large because N_{12} and N_{13} were chopped strand mats with low stiffness, and uniaxial cloth with high stiffness was set in the middle of the laminate. Therefore, the stiffness of the entire laminate was relatively low, and the corresponding maximum impactor displacement was relatively large. The maximum impactor displacements of P_1 – P_3 and P_7 – P_{12} were slightly smaller. The reason for this was that N_{12} and N_{13}

were uniaxial cloths. The stiffness of the whole laminate was relatively high, and the corresponding maximum impact force also increased accordingly. Under the same experimental conditions, the impactor displacement reflected the stiffness level of each laminate. Corresponding to different layup forms, the stiffness of the 12 laminates had the following relationship: $P_8 < P_{12} < P_7 < P_2 < P_9 < P_{10} < P_{11} < P_1 < P_3 < P_6 < P_5 < P_4$.

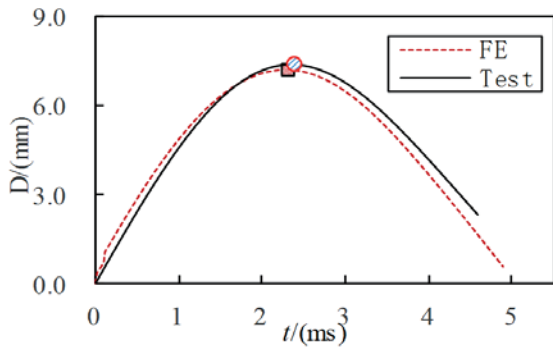


Fig. 12. Displacement-time histories of P_1

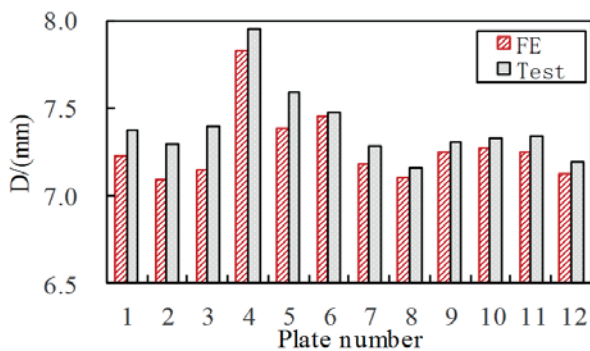


Fig. 13. Maximum impact displacements of P_1 - P_{12}

Rebound velocity/absorbed energy-time response

The tests and simulations recorded the velocity change of the impactor during the impact process, which includes two parts: impact and rebound. During the impact process, the impactor velocity gradually decreased over time; in the process of rebound, the velocity of the impactor gradually increased due to the rebound force of the laminates until the impactor was out of contact with the laminates. Fig. 14 shows the velocity change of the impactor corresponding to P_1 in the test and simulation, in which the velocity is represented by v . In this figure, the test and simulation results were basically consistent before the impactor displacement reached a maximum, but in the final stage of the impactor rebound, the simulation value gradually exceeded the experimental value. The error of the final rebound velocity was 11.7%. The reason for this discrepancy was that the Tan stiffness degradation criterion was adopted in the simulation. The elements still had a certain stiffness after damage, which led to a higher rebound speed of the impactor. Fig. 15 shows the test and simulation results of the final rebound velocity

of the impactor corresponding to P_1 - P_{12} . Similar to P_1 , the simulated value of the rebound velocity was higher than the experimental value, and the impactor corresponding to P_4 had the maximum rebound velocity.

In the whole impact process, the energy of the system, which was composed of a laminate and the impactor, was conserved. Therefore, the energy reduction of the impactor can be used to express the absorbed energy of the laminates. Fig. 16 shows the absorbed energy of P_1 during the impact process, in which the energy is represented by the letter “E”. Fig. 17 shows the final absorbed energy of P_1 - P_{12} . This figure shows that in both the simulation and the experiment, P_4 has the minimum absorbed energy. The hull plates need better impact resistance, such as a small damage area, less absorbed energy and so on. Thus, the carrying capacity of the hull structure can be maintained to a certain extent, and the water seepage efficiency can be reduced to ensure the safety of the ship. Therefore, its layup form is more in line with the requirements for composite ships, and can be used in the subsequent yacht design.

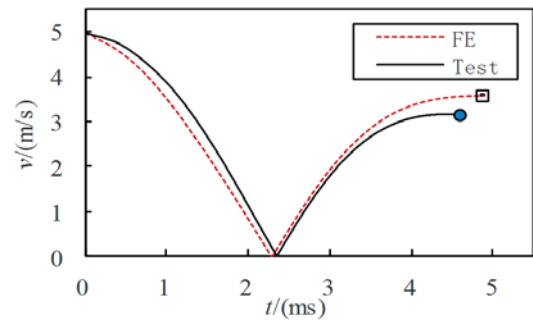


Fig. 14. Velocity-time histories of P_1

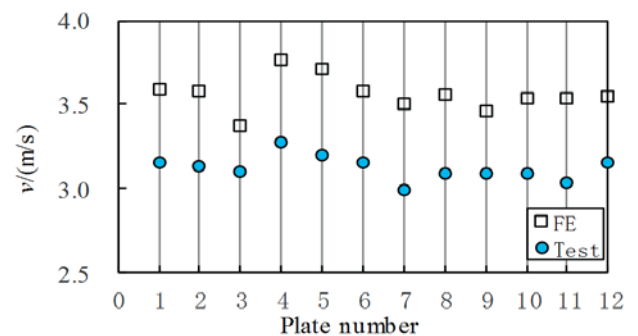


Fig. 15. Final rebound velocity of the impactor of P_1 - P_{12}

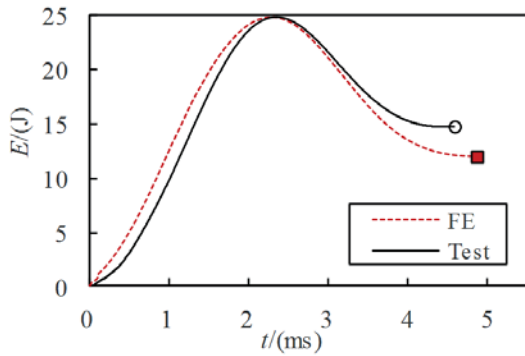


Fig. 16. Absorbed energy-time histories of P_1

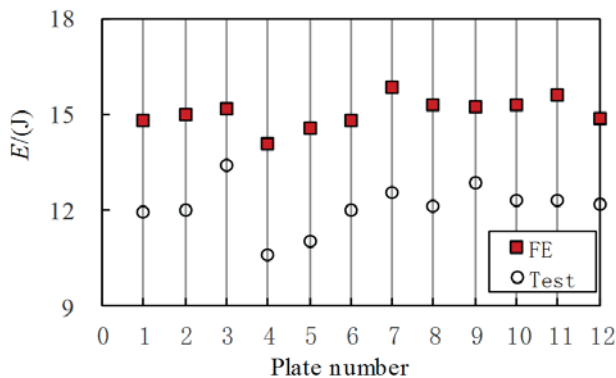


Fig. 17. Final absorbed energy of P_1 - P_{12}

CONCLUSION

In this investigation, experimental and numerical investigations of composite plates under low-velocity impact were conducted. The analysed plates were made of GRP laminate with 12 different layup forms. A simulation model was established by writing a VUMAT subroutine. The experimental research was carried out with the use of the impact drop tower. And the numerical analyses were performed in the Abaqus program. Hashin's criterion and the cohesive zone model were implemented as the damage initiation criterion of intralaminar and interlaminar damage. The Tan criterion and B-K criterion were used to characterise the stiffness degradation of intralaminar and interlaminar damage elements. Based on the experimental and numerical studies performed, it has been concluded that:

- 1) The initial damage occurred at the impact side, and the material at the impact point was plastically deformed, resulting in a circular pit with a diameter of about 9 mm. Due to the high contact force, the damage expanded rapidly to the interior of the laminate.
- 2) The low-velocity impact damage mainly occurs near the impact area. The damage areas for the same impact energy are larger for the back side than for the impact side. And the damage areas of each layer partially overlap.

- 3) The layup form had an important role in the damage on the impact side and back side of the composite laminates. Because of the same layup form of the first three layers, the pits diameter and damage areas of the impact side of the 12 plates are similar. And the damage on the back side of the specimens was closely related to the layup form of N_{12} and N_{13} .
- 4) For the same impact energy, there is a corresponding layup form to minimise the damage area. There are 12 layup forms in this paper, and the damage area of P_4 is the smallest.
- 5) In this paper, small cracks and fibre delaminations can be seen in the tested specimens under the low-velocity impact of 25J, but the energy is not enough to break the fibres on the back of the laminates.
- 6) Comparisons showed that the simulation and test results of the impact force, impactor displacement, rebound velocity and absorbed energy were in very good agreement. The validity of the numerical model is proved, and the numerical model can be successfully used for the initial prediction of the mechanical behaviour for composite laminates under low-velocity impact.
- 7) In this paper, the maximum impact force, absorbed energy and damage area of the plate P_4 are the smallest among the 12 plates. In comparison, it has better impact resistance than others, so it is more in line with the requirements of composite ships.

ACKNOWLEDGEMENTS

This work was financed by the National Natural Science Foundation of China (Grant No. 51909103) and the Project of Fujian Provincial Department of Education of China (Grant No. JAT190336).

REFERENCES

1. Li X., Zhu Z., Li Y., Hu Z. (2020): Design and mechanical analysis of a composite t-type connection structure for marine structures. *Polish Maritime Research*, 2020, 27(2): 145-157.
2. Tomasz F., Tomasz M. (2020): Validation process for computational model of full-scale segment for design of composite footbridge. *Polish Maritime Research*, 27(2): 158-167.
3. Li X., Zhu Z., Li Y., Hu Z., Dai L. (2020): A review on ultimate strength of composite-metal hybrid ships. *Journal of Ship Mechanics*, 24(05): 681-692.
4. Niksa-Rynkiewicz T., Landowski M., Szalewski P. (2020): Application of apriori algorithm in the lamination process in yacht production. *Polish Maritime Research*, 27(3): 59-70.

5. Qiu A., Fu K., Zhao C., et al. (2013): Numerical understanding the impact behaviors of marine composite laminates. 1st International Conference on Advanced Composites for Marine Engineering. 2013.
6. Thorsson S. I., Waas A. M., Rassaian M. (2018): Numerical investigation of composite laminates subject to low-velocity edge-on impact and compression after impact. *Composite Structures*, 203.
7. Liao B., Zhou J., Lin Y., et al. (2019): Low-velocity impact behavior and damage characteristics of CFRP laminates. *Chinese Journal of High Pressure Physics*, 33(04): 105-113.
8. Oliveira Ferreira G. F., et al. (2019): Computational analyses of composite plates under low-velocity impact loading. *Materials Today: Proceedings*, 2019, 8.
9. Thorsson S. I., Waas A. M., Rassaian M. (2018): Low-velocity impact predictions of composite laminates using a continuum shell based modeling approach part A: Impact study. *International Journal of Solids and Structures*, 155: 185-200.
10. Panettieri E., Fanteria D., Montemurro M., Froustey C. (2016): Low-velocity impact tests on carbon/epoxy composite laminates: A benchmark study. *Composites Part B*, 107: 9-21.
11. Shi Y., Pinna C., Soutis C. (2014): Modelling impact damage in composite laminates: A simulation of intra- and inter-laminar cracking. *Composite Structures*, 114.
12. Xu Y., Zuo H., Lu X., et al. (2019): Numerical analysis and tests for low-velocity impact damage evaluation of composite material. *Journal of Vibration and Shock*, 38(03): 149-155.
13. Gliszczynski A., et al. (2019): Barely visible impact damages of GFRP laminate profiles – An experimental study. *Composites Part B: Engineering*, 158: 10-17.
14. Gliszczynski A. (2018): Numerical and experimental investigations of the low velocity impact in GFRP plates. *Composites Part B Engineering*, 138: 181-193.
15. Moura M. D., Marques A. T. (2002): Prediction of low velocity impact damage in carbon-epoxy laminates. *Composite: Part A*, 33: 361-368.
16. Moura M. D., Goncalves J. P. (2004): Modelling the interaction between matrix cracking and delamination in carbon-epoxy laminates under low velocity impact. *Composites Science and Technology*, 64: 1021-1027.
17. Hou J. P., Petrinic N., Ruiz C., Hallett S. R. (2000): Prediction of impact damage in composite plates. *Composite Science and Technology*, 60: 273-281.
18. Luo R. K. (2000): The evaluation of impact damage in a composite plate with a hole[J]. *Composite Science and Technology*, 60: 49-58.
19. Wen W., Xu Y., Cui H. (2007): Damage analysis of laminated composites under low velocity impact loading. *Journal of Materials Engineering*, 7: 6-11.
20. Zhu W. (2012): Research on residual strength and fatigue performance of composite laminates with low-velocity impact damage. Dissertation, Nanjing: Nanjing University of Aeronautics and Astronautics.
21. Zhu D., Zhang W., et al. (2014): Studies of several influence factors of low-velocity impact damaged characterization on composite laminates. *Ship Science and Technology*, 11: 57-65.
22. Dong H., An X., et al. (2015): Progress in research on low velocity impact properties of fibre reinforced polymer matrix composite. *Journal of Materials Engineering*, 43(5): 89-100.
23. Zu Z. (2020): Experimental investigation on repeated low velocity impact damage and residual compressive strength of honeycomb sandwich panel. Dissertation, Shandong: Shandong University of Technology.
24. Guden M., Yildirim U., Hall I. W. (2004): Effect of strain rate on the compression behavior of a woven glass fiber/SC-15 composite. *Polymer Testing*, 23(6): 719-725.
25. Hosur M., Alexander J., Vaidya U., et al. (2004): Studies on the off-axis high strain rate compression loading composites. *Composite Structures*, 63(1): 75-85.
26. Hashin Z., Rotem A. (1973): A fatigue failure criterion for fiber reinforced materials. *Journal of Composite Materials*, 7(4): 448-464.
27. Hashin Z. (1980): Failure criteria for unidirectional fiber composites. *Journal of Applied Mechanics*, 47(2): 329-334.
28. Ferreira R. T. L., Ashcroft I. A. (2020): Optimal orientation of fibre composites for strength based on Hashin's criteria optimality conditions. *Structural and Multidisciplinary Optimization*, 61: 2155-2176.
29. Chaht F. L., Mokhtari M., Benzaama H. (2019): Using a Hashin Criteria to predict the damage of composite notched plate under traction and torsion behavior. *Fracture and Structural Integrity*, 13(50): 331-341.

30. Ha W. (2018): Study on failure modes and residual strength of composite laminates under low-velocity impact. Dissertation, Harbin: Harbin Institute of Technology.
31. Yang Y., Liu X., Wang Y. Q., et al. (2017): A progressive damage model for predicting damage evolution of laminated composites subjected to three-point bending. *Composites Science and Technology*, 151.
32. Sun X. (2018): Numerical simulation of gradual damage on bolt-bonded hole composite laminates. Dissertation, Harbin: Harbin Engineering University.
33. Shi J. (2015): The finite element analysis of the progressive damage of composite laminated plates based on ABAQUS. Dissertation, Shanxi: North University of China.
34. Abir M. R., Tay T. E., Ridha M., Lee H. P. (2017): Modelling damage growth in composites subjected to impact and compression after impact. *Composite Structures*, 168: 13-25.
35. Benzeggagh M. L., Kenane M. (1996): Measurement of mixed-mode delamination fracture toughness of unidirectional glass/epoxy composites with mixed-mode bending apparatus. *Composites Science and Technology*, 56(4): 439-449.
36. Chen Y., Yu Z., Wang H. (2012): Numerical modeling of scale effects on the responses of laminated composite plate under low velocity impact. *Chinese Journal of Solid Mechanics*, 33(6): 574-582.
37. Liu H. (2006): Numerical simulation of delamination damage in composite materials. Dissertation, Shanxi: Northwestern Polytechnical University.
38. Ji Z., Guan Z., Li Z. (2016): Damage resistance property of stiffened composite panels under low-velocity impact. *Journal of Beijing University of Aeronautics and Astronautics*, 42(04): 751-761.

CONTACT WITH THE AUTHORS

Xiaowen Li

e-mail: lixw2016@jmu.edu.cn

Jimei University, School of Marine Engineering,
No.176, Shigu Road, 361021 Xiamen,
Fujian Provincial Key Laboratory for Naval Architecture
and Ocean Engineering
CHINA

Zhaoyi Zhu

e-mail: 1988zhuzhaoyi@163.com

Jimei University, School of Marine Engineering,
No.176, Shigu Road, 361021 Xiamen,
Fujian Provincial Key Laboratory for Naval Architecture
and Ocean Engineering
CHINA

Qinglin Chen

e-mail: 199761000020@jmu.edu.cn

Jimei University, School of Marine Engineering,
No.176, Shigu Road, 361021 Xiamen,
Fujian Provincial Key Laboratory for Naval Architecture
and Ocean Engineering
CHINA

Yingqiang Cai

e-mail: 200661000102@jmu.edu.cn

Jimei University, School of Marine Engineering,
No.176, Shigu Road, 361021 Xiamen,
Fujian Provincial Key Laboratory for Naval Architecture
and Ocean Engineering
CHINA

Yunfeng Xiong

e-mail: 200561000043@jmu.edu.cn

Jimei University, School of Marine Engineering,
No.176, Shigu Road, 361021 Xiamen,
Fujian Provincial Key Laboratory for Naval Architecture
and Ocean Engineering
CHINA

HYDRODYNAMIC STATE OF ART REVIEW: ROTOR – STATOR MARINE PROPULSOR SYSTEMS DESIGN

Przemysław Król

Ship Design and Research Centre, Gdańsk, Poland

ABSTRACT

The paper covers the important topic of rotor–stator propulsor system design and operation. For the stand-alone marine screw propeller, both the design criteria for loading distribution and the theoretical efficiency limits are well described in the basic literature. This is in contrast to the combined propulsor system like a propeller cooperating with a pre-swirl device. The paper describes the current state of the art, summarising results obtained by various researchers by installing energy-saving devices on particular vessels. The design methods utilised are briefly outlined, with the main characteristics underlined. Rough analysis of the gathered data confirms the expected trend that a higher efficiency gain due to ESD installation is possible for a higher propeller loading.

Keywords: : energy-saving device, guide vane, pre-swirl stator, propulsor design, efficiency

INTRODUCTION

A vast amount of literature exists that covers the topic of marine propulsor design and its optimization. Due to rising environmental requirements, more attention is being paid nowadays to the propulsor efficiency. Consequently, energy-saving devices (ESDs) are gaining increasing interest from researchers and marine engineers. Important types of these are pre- and post-swirl devices, intended to recover rotational energy losses occurring during screw propeller operation. This paper addresses ESDs of various forms, but the main focus is on pre-swirl stators (PSS). The most important types of ESDs are presented in Fig. 1.

The pre-swirl stator is a system of rigid lifting foils, located before the operating propeller. These are meant to produce

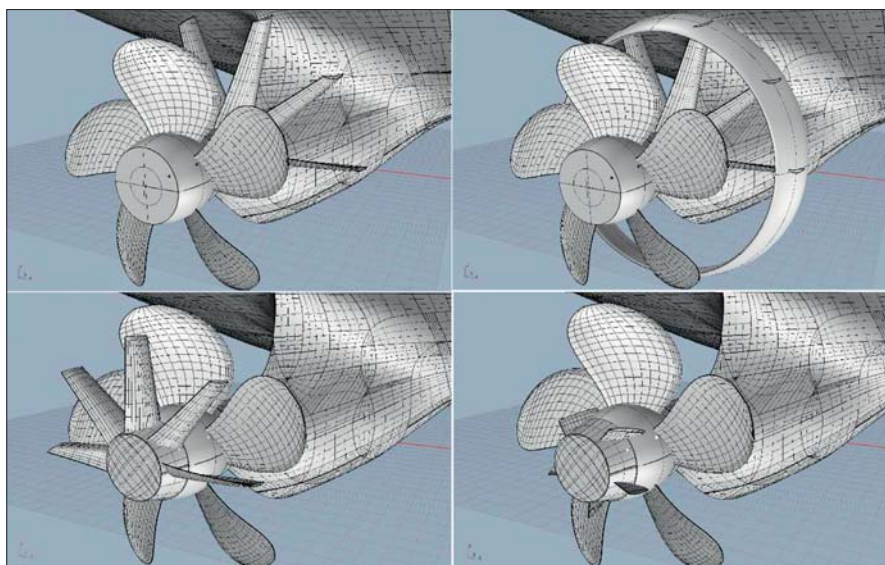


Fig. 1. Various kinds of ESDs (from upper left to bottom right): Pre-swirl stator, pre-swirl duct, post-swirl stator, propeller boss cap fins

counter-swirl, reducing the tangential losses of the propeller energy. In this way the propeller efficiency is altered, but the foils generate drag on themselves.

The pre-swirl duct (PSD) is a system of PSS foils shrouded with the duct. It combines the advantages of the PSS with equalling the velocity field inflowing to the operating propeller, which may improve the propulsor power profile as well as its cavitation/vibratory characteristics.

The post-swirl stator (PoSS) is based on the opposite concept to the PSS; the foils are located after the propeller, in its slipstream. The stator recovers energy lost by the propeller due to tangential losses by generating the thrust on its blades.

The propeller boss cap fins (PBCF) are a set of small lifting foils, located downstream from the propeller's trailing edge on the hub itself. Their role is to dispel the hub vortex shedding from the propeller and to recover some of the tangential losses.

A kind of PoSS that is present on most ships is a rudder. Its displacement effect is normally beneficial for the propeller by a slight increase of the effective wake fraction. Moreover, it may have a twisted leading edge and generate additional thrust, recovering the propeller's tangential losses.

This paper is divided into three parts: the first sketches the most important features of design methods met in the literature. The fluid flow models employed are named and ESD design criteria are mentioned. It should, however, be noted that the vast majority of modern studies adopt CFD computations combined with variational optimization of the parametrically described ESD.

The second, main, part of the paper summarises the most important results reported in each article. In the majority of studies, both numerical and experimental data were available, in which case the numerical data are mostly omitted in this review, due to space limitations.

The last, concluding, part of this review presents and compares the results reported in selected papers. In fact 'selected papers' means here 'all those for which it was possible'. This is due to the huge variety of data presented in the literature and difficulties with constructing a common base.

THE DESIGN METHODS

The stand-alone screw propeller has huge variety of well-recognised methods. This is somewhat contradictory to the propeller-ESD propulsor system, for which, due to the high complexity of the flow phenomena in such system, many more methods exist in the literature. None of them, however, can be stated as canonical or as reliable as classical approaches for a propeller operating alone. The reported methods can be distinguished mainly by the flow representation employed; it can be either an inviscid vortex flow model or a viscous one. A second factor is the stator particular that is undergoing the design process: it can be either the bound circulation distribution (in which case the stator foil's geometry results directly from it) or the geometry. In the latter case, the information on bound circulation is most often omitted in

Tab. 1. Design approach in selected papers

Paper	Designed particular	Design criterion	Flow model
[2]	Circulation distribution	Rotation cancellation	Vortex
[3]	Geometry	Optimization	Viscous
[4]	Circulation distribution	Optimization	Vortex
[5]	Circulation distribution	Optimization	Vortex
[7]	Circulation distribution	Optimization	Vortex
[8]	Circulation distribution	Rotation cancellation	Vortex
[9]	Geometry	Optimization	Viscous
[10]	Geometry	Optimization	Viscous
[11]	Circulation distribution	Optimization	Vortex
[12]	Geometry	Optimization	Viscous
[13]	Circulation distribution	Optimization	Vortex
[14]	Geometry	Optimization	Viscous
[15]	Geometry	Optimization	Viscous
[16]	Circulation distribution	Optimization	Vortex
[21]	Geometry	Optimization	Viscous
[22]	Geometry	Optimization	Viscous
[27]	Geometry	Optimization	Viscous
[29]	Geometry	Streamline adjustment	Viscous
[31]	Geometry	Optimization	Vortex
[32]	Circulation distribution	n/d	Viscous

the papers and it is in fact the only design concept available for the RANSE-based approach.

Among the vortex models, the most basic tool is the lifting line model (LLM), replacing stator foils with straight line bound vortices. This is a sufficient simplification for determination of the induced tangential velocity coming from the stator, which is in fact the vital part from the cooperating propeller point of view. In such approach, stator vortex wake deformation can be taken into account, which allows more accurate determination of the stator-induced axial velocity component [17]. Stators, with foils of high aspect ratio, may also be successfully designed with the LLM. Such approach seems, however, to be highly outmoded nowadays, as already in 1988 Kerwin used the lifting surface model (LLS) for this task [11]. The most advanced vortex flow model, the boundary element method (BEM), cannot be directly utilised in the design of the foil geometry for the prescribed loading. Thus it is rather addressed in the design via variational geometry optimization and/or analysis of the given propulsor system geometry. The decision on the stator's bound circulation magnitude is crucial for the efficiency of the propulsor system. Due to the lack of a theoretical criterion, variational optimization is done in most cases.

Vortex methods have several advantages which encourage many designers to use them, especially at the initial stages of work. The easy individual code implementation,

relatively short calculation time and the possibility of reverse problem solution are the main advantages of these. There are, however, serious limitations also. Computation of the vortex wake deformation, which could affect the designed foil's geometry, requires much care and may pose a difficulty in the case of heavily loaded stators, especially if the propeller-induced velocity field is to be taken into account during the simulation. Moreover, there are certain phenomena, like flow separation and vorticity dissipation, that cannot be included directly within the vortex model and have to be handled with semi-empirical formulas or in some other way. Flow separation is likely to occur on highly loaded profiles. Within the frame of the vortex model one can design a section with an arbitrary lift magnitude and distribution (even for NACAa = 1.0 mean line), but exceeding reasonable values will result in a failure to achieve the assumed loading in real fluid. Finding that limit may be done based upon systematic blade section profiles data, as collected in [1], and control of the lift force coefficient [7] or angle of attack [14] values.

Once the viscous flow model is adopted, most of the mentioned difficulties are driven away; the vortex wake shape, separation and vorticity dissipation are included directly in the simulation. Meanwhile, however, also all the advantages favouring vortex models are gone. Viscous calculations require notable computer resources and – what is most problematic – reverse problem solution is no longer possible. Instead, one has to employ optimization of both the stator and propeller geometries for the prescribed operating conditions. This may notably increase the required time of realization. Thus, optimization is required not only for the ESD geometry undergoing the design process but for the computational mesh also, to provide a sufficient balance between accuracy and the computational cost [15].

Despite using a much more sophisticated approach, RANSE can still provide only limited accuracy. A model test prognosis for an accelerating duct influence of 6.03% was already considered to be in sufficient agreement with CFD calculations, indicating a 5.15% reduction [3]. Similarly, for the pre-swirl stator a 5.2% power reduction, indicated by CFD, was outweighed by sea trials results of 6.8% [31]. This situation results probably from inaccuracies of local vortex phenomena modelling, which are responsible for an energy recovery effect. The accuracy may be improved if the relatively simpler turbulence model (e.g. $k-\omega$ SST) is replaced with the more sophisticated 7-equation RST model; the propeller-delivered power error may be decreased from around 4.0% to even 1.3% [15]. In the case of unsteady simulations, the time step turns out also to have vital importance [25], [26]. For this reason, new efforts on CFD development are currently being made, with self-propulsion conditions as a research topic [30], [33].

Correct modelling of such systems operation requires reference data for simulation validation, not only for propulsor operation but for the velocity fields also, such as is gathered in [6].

From a practical point of view, especially interesting is conducting the CFD calculations in full scale [15], [27], [31], although model-scale calculations are being conducted nowadays also [3], [12]. Both approaches have their advantages. One of the more important, shared by both, is getting a better insight into the complex flow phenomena involved in ESD operation [7], [12]. The main weight of interest remains in the velocity field and its alteration by ESD installation [28]. An important research field, however, is cavitation simulation [34].

Due to the issues outlined above, the most reasonable approach seems to be to start the design process with a vortex model to determine the initial geometry of the system (as shown e.g. in [9]). Once this is known, the optimization may be finalized by CFD simulation, conducted for a narrower number of cases.

ENERGY-SAVING EFFECT

A considerable number of papers upon the propeller–stator topic have been published, most of them reporting on the power reduction delivered, as provided by the ESD of the authors' design. The influence of the ESD is determined by means of either numerical calculations or model tests; in some cases, sea trials results are even provided. The completeness of the available data differs widely; in some cases not even the propeller diameter or ship speed are provided. This makes comprehensive analysis more difficult and less detailed than one would wish. In most papers, both numerical and experimental results are available. In such cases, only empirical data are repeated below, as the main focus of this study is ESD operation, not CFD development. Due to the requirements of further analyses, standard propeller loading coefficients like K_T , K_Q and C_T , C_N values were calculated (if these were not provided), based upon the data provided in the original papers.

$$K_T = \frac{T}{\rho n^2 D^4} \quad K_Q = \frac{Q}{\rho n^2 D^5} \quad (1)$$

$$C_T = \frac{T}{\frac{1}{8} \pi \rho D^2 V^2} \quad C_N = \frac{2 \pi n Q}{\frac{1}{8} \pi \rho D^2 V^3} \quad (2)$$

After some considerations, an effective advance speed for calculation of C_T , C_N was calculated using the advance ratio/effective wake coefficient determined with the ESD installed (if such value was available). Such approach was adopted due to the author's feeling that it better reflects propeller loading conditions, even if is not formally equal to the mean axial velocity experienced by operating the propeller. Unless stated otherwise, water density was taken as $\rho_M = 998.6 \text{ kg/m}^3$ for the model scale and $\rho_S = 1025.9 \text{ kg/m}^3$ for full scale.

The authors of each study adopted various vessels for their analyses. The main particulars of these are summarised in Table 2. A blank space was left if some data were not provided.

Tab. 2. Vessels analysed in particular studies

Paper	Ship type / Name	L_{pp} [m]	B [m]	T [m]	C_B [-]	D [m]	V_{DES} [knots]
[2]	Trawler						
[2]	Tanker						
[3]	Japanese Bulk Carrier (JSBC)	280.0	45.00	16.5		8.12	7.5
[3]	Tanker	333.0	60.0	20.5		10.5	
[4]	Cargo Vessels						
[5]	None						
[7]	Container Vessel					8.75	
[8]	Container Ship	286.0	48.20	14.8		9.60	22.0
[9]	VLCC	322.0	60.00	21.0		10.00	
[10], [24], [32]	Kriso Container Ship (KCS)	230.0	32.20	10.8	0.651		24.0
[12]	13,200 TEU Container Ship	350.0	48.2	14.5			20.0
[13]	n/a	319.0	60.00	21.0		10.00	16.21
[14]	KVLLC	320.0	58.00	20.8	0.810		15.5
[15]	Chemical Tanker	175.6	32.23	11.85	0.812	6.50	14.0
[17]	Nawigator XXI	54.13	10.5	3.15/3.20 ^a	0.626	2.26	13.0
[21]	n/a	174	32.20	11		6.10	15
[22]	6,500 TEU Container Ship						
[24]	KVLLC2						15.5
[27]	32500 DWT Bulk Carrier	171.5	28.40	10.0		5.20	11.5 / 12.0
[29]	180m Diamond 34 Bulk Carrier	176.8	30.00	9.75	0.800	5.60	14
[21]	Bulk Carrier "VALVOLINE"	182.0	32.00	11		5.80	15.0

a – given as T_A / T_F

UPSTREAM DEVICES

The main attention of this review is to the upstream ESDs. Table 3 (next page) summarises the results of the model tests and calculations conducted in each study. Where it was possible, the data for 'no ESD' conditions are provided here also. For such cases, a comment 'none' is put in the 'ESD type' column. The power-saving effect ΔP_D is defined according to the formula:

$$\Delta P_D = \frac{P_D^{No\ ESD} - P_D^{ESD}}{P_D^{No\ ESD}} \quad (3)$$

Selected papers are briefly discussed below. The paper [24] covers a vital topic; it is focused not on the design process itself but on the method of model tests extrapolation for the vessels with pre-swirl ESDs. The main issue is in fact the extrapolation of the effective wake fraction. The authors analyse the results of adopting known approaches (ITTC'78, ITTC'99) and their own. The main difference between the ITTC methods and the proposed one includes the fact that the pre-swirl devices not only produce rotational inflow but also alter the axial inflow, which should be treated separately during scaling. A wide range of model test results are given in the paper. Two vessels are taken into analysis: KVLLC2 (equipped with a pre-swirl duct) and KCS (equipped with a pre-swirl stator) and results of adopting the subsequent full-scale prognosis methods are compared.

Tab. 4. Full-scale propulsion prognosis via subsequent methods

Scaling method	ESD	Vessel	V_s [knots]	w_{ES} [-]	P_{DS} [kW]	n_s [rpm]
ITTC'78	None	KVLLC2	15.5	0.342	26226	71.73
ITTC'78	PSD	KVLLC2	15.5	0.363	24959	70.42
TTC'99	PSD	KVLLC2	15.5	0.383	24384	69.53
Moon et al., 2017	PSD	KVLLC2	15.5	0.367	24793	70.23
ITTC'78	None	KCS	24.0	0.254	43.672	106.28
ITTC'78	PSS	KCS	24.0	0.282	42.857	105.19
TTC'99	PSS	KCS	24.0	0.303	41.833	103.73
Moon et al., 2017	PSS	KCS	24.0	0.298	42.094	104.11

Paper [9] starts with an analysis of the energy losses occurring on the marine propeller, providing vital insight into possible recovery concepts. Axial losses are deduced via ideal propulsor theory. Rotational losses were taken as a remaining factor between the real propeller efficiency and the η_i determined via BEM, with no viscosity effects included.

The design of a pre-swirl duct was realised via variational optimization by means of FVM simulation. The vessel adopted for the design example was VLCC. The model tests were conducted both for 'bare hull' conditions and with ESD installed. The precise value of the delivered power prognosis was not given in the paper; only a quasi-propulsive efficiency increase of 5.1% was declared. This is at a similar level to the

Tab. 3. Upstream device installation effect

Paper	Ship type / Name	ESD type	ΔP_D [%]	V_S [kn]	n [rpm]	K_T [-]	$10K_Q$ [-]	C_T [-]	C_N [-]
[3]	JSBC	AD	6.0	7.5					
[3]	Tanker	PSD	3.5	8.1					
[5]	None	none	-			0.215	0.389	0.691	0.884
[5]	None	PSS	3.0			0.215	0.375	0.689	0.850
[7]	Container Vessel	none	-		100.2				
[7]	Container Vessel	PSS	5.0		96.0				
[9]	VLCC	none	-			0.163		2.050	
[9]	VLCC	PSD	5.1			0.186		2.952	
[10]	KCS	none	-	24.0	654.0 ^M				
[10]	KCS	PSS	3.9	24.0	639.0 ^M				
[13]	n/a	none	-	16.21	473.4 ^M	0.177	0.200	2.753	4.860
[13]	n/a	PSS	2.5	16.21	468.6 ^M	0.181	0.201	3.284	6.050
[13]	n/a	PSD	5.8	16.21	459.0 ^M	0.179	0.195	3.639	6.805
[14]	KVLLC	none	-	15.5	75.1				
[14]	KVLLC	PSS	5.6	15.5	70.9				
[15]	Chemical Tanker	none	-	14.0	86.4				
[15]	Chemical Tanker	PSS		14.0				1.570	2.703
[17]	Nawigator XXI	none	-	13.0	283.3	0.199	0.264	3.236	6.798
[17]	Nawigator XXI	PSS	10.0	13.0	273.6	0.225	0.283	4.890	11.258
[17]	Nawigator XXI	none	-	13.0	269.8	0.231	0.308	3.226	6.335
[17]	Nawigator XXI	PSS	7.4	13.0	257.7	0.255	0.327	4.825	10.589
[21]	n/a	none	-	15.0					3.698
[21]	n/a	PSD	3.3	15.0					5.716
[24]	KVLLC2	none	-	15.5	71.7				
[24]	KVLLC2	PSS	3.1	15.5	69.5				
[24]	KCS	none	-	24.0	106.3				
[24]	KCS	PSS	4.2	24.0	103.7				
[27]	32500 DWT Bulk Carrier	none	-	11.5	499.7 ^M		0.196		5.858
[27]	32500 DWT Bulk Carrier	PSS	2.5	11.5	486.2 ^M		0.208		8.915
[29]	180m Diamond 34 Bulk Carrier	none	-	14.0	559.2 ^M		0.207		
[29]	180m Diamond 34 Bulk Carrier	PSS	1.6	14.0	550.2 ^M		0.214		
[31]	Bulk Carrier "VALVOLINE"	PSS	6.8	15.0	123.0				

AD – accelerating duct; PSD – pre-swirl duct; PSS – pre-swirl stator; ^M – model-scale value

Tab. 5. Particulars of analysed propeller and its operation

D [m]	$P_{0.7}/D$ [-]	A_E/A_0 [-]	Z [-]	Z [-]	K_T [-]	η_i [-]	Axial losses [-]	Rotational losses [-]	$C_{T,a}$ [-]
10.0	0.714	0.4	4	0.40	0.1855	0.6038	0.3308	0.0355	2.952
				0.45	0.1630	0.6675	0.2718	0.0312	2.050
				0.50	0.1401	0.7285	0.2183	0.0268	1.427

a – calculated based on data provided in original paper

one reported in paper [13], where a power reduction at a level of 5.8% was declared from PSD installation (versus 2.5% from PSS application). The latter paper also provides detailed results of the model tests.

In paper [21] a 'Crown Duct' (CD) ESD device is discussed. Unlike in the case of a 'casual' PSD, the duct part is not located at the ESD's tip but rather in midspan. Some of the pre-swirl

foils end at the duct, but some of them extend beyond it or even start at it. The CD design is realised via variational optimization by means of FVM simulation. For the design example, a vessel of design speed $V_S = 15$ knots is adopted. The model tests were carried out both for a 'bare' hull and with CD installed, for two draughts (T_A , T_F values were not precisely defined). For full-scale prediction, the ITTC'99 procedure of effective wake

Tab. 6. Full- scale prognosis

$V_s=13.0$ knots	J_s [-]	w_{TS} [-]	η_{HS} [-]	η_{os} [-]	η_{DS} [-]	TS [kN]	Q_s [kNm]	n_s [rpm]	P_{DS} [kW]
CP745	0.396	0.371	1.221	0.444	0.566	124	37.1	289.3	1123
CP745+ST001 ^a	0.342	0.473	1.444	0.410	0.626	125	35.4	273.6	1014
CP745+ST001 ^b	0.340	0.476	1.452	0.408	0.627	125	35.4	273.0	1011
CP753	0.427	0.351	1.191	0.497	0.597	125	37.7	269.8	1065
CP753+ST002 ^a	0.367	0.468	1.419	0.438	0.645	126	36.5	257.7	986
CP753+ST002 ^b	0.363	0.474	1.435	0.434	0.646	126	36.5	257.0	982

a – scaling method according to ITTC'99; b – scaling method proposed in (Moon-Chan et al., 2017)

coefficient scaling was adopted and a power saving of 3.3% was declared. The paper gives detailed results of the model tests.

Paper [3] begins with presentation of the data for a validation case, which is a Japanese Bulk Carrier (JBC). For a speed around $V_s = 7.5$ knots ($Fr = 0.142$, as given in the paper), the model test prognosis for delivered power is $P_{DS} = 2863$ kW. The corresponding test after installing the ESD (an accelerating duct) yielded a delivered power prognosis of $P_{DS} = 2691$ kW. The resulting power reduction of 6.03% was considered to be in sufficient agreement with one determined via finite volume calculations (5.15%). FVM simulation was applied to design via optimization the geometry of the ESD for another vessel, the Tanker. For a speed around 8.1 knots ($Fr = 0.141$, as given in the paper), the model test prediction for the delivered power is $P_{DS} = 2813$ kW. The corresponding test after installing the ESD (a pre-swirl duct) brought a delivered power prediction of $P_{DS} = 2716$ kW. The resulting power reduction of 3.45% is closer to the one determined via FVM simulation (2.95%) than in the case of the JBC.

In paper [7] the pre-swirl stator is designed via the lifting line method, which is applied for optimization of the bound circulation distribution. For avoidance of flow separation on the stator, the local value of the lift coefficient C_L is kept below the prescribed margin (the precise value is not given in the paper). For the design case, a container vessel was adopted (the vessel particulars are not provided, the propeller diameter is $D = 8.75$ m). The model tests were conducted for a pre-swirl stator of diameter $2\Lambda = 9.10$ m, and two propellers revealed a possible delivered power reduction at a level of 5.0% along with a rate of revolution reduction by 4.2%. A quite similar concept is given in paper [14], where, however, the stator design is realised via the lifting surface method. It is assumed to cancel around 50% of the propeller slipstream rotation and have elliptic loading on each blade. Flow separation is avoided by limitation of the angle of attack to 15° . For the design example, the KVLLC with a design speed of $V_s = 15.5$ knots was adopted. The model tests were conducted for three configurations: without any ESD installed, with PSS as designed and with the same PSS but turned by 180° . The tests indicated a power reduction at a level of 5.6% and a propeller rate of revolution reduction at a level of 5.5%. Meanwhile, the mirror PSS kept a very similar revolution reduction but nearly no power reduction (0.7%).

Paper [27] addresses the topic of a PSS in the form of controllable pre-swirl fins (CPSF), having fixed and

controllable ('flap') parts. The blades are designed via variational optimization by means of FVM simulations. The advantage of the adopted solution is that each blade can be adapted for actual vessel loading conditions to preserve the optimal propulsor operation. For the design example, a 32500 DWT bulk carrier was selected. The model tests were carried out for two draughts: 'Design' ($T = 10.0$ m, even keel) and 'Ballast' ($T_A = 7.0$ m, $T_F = 5.0$), both for the propeller operating alone and with ESD installed, at each draught. The flap angle was optimised before these tests. Power saving at a level of 2.5% for the design draught and even 4.8% for the ballast draught was declared.

Paper [15] addresses the topic of pre-swirl stator design. As in most cases in current research, it is realised via optimization by means of FVM simulation. The vessel adopted for the design example is the Chemical Tanker. Despite the model tests conducted, no complete full-scale prognosis with the ESD is provided in the paper. Only selected propulsive coefficients are compared before and after installing the ESD, and it can be stated only that the expected hull efficiency value will rise from the value of 1.170 to 1.242 due to the presence of the ESD.

In the dissertation [17], two propulsor systems are presented (along with model test results): propeller CP745 with the pre-swirl stator ST001 and propeller CP753 with the PSS ST002. Both propulsor systems were designed via a combined lifting line–lifting surface approach (the latter with its more mature version). Each PSS blade is assumed to have an elliptic loading distribution. The vessel adopted for the design case was Navigator XXI with the design speed defined as $V_s = 13.0$ knots. The model tests were conducted for cases both with and without the ESD.

The discussed propulsor systems were earlier presented in papers [16], [18], [19] and [20]. The data presented in [17] may differ slightly as it was re-calculated anew.

Paper [31] describes the PSS design procedure and analysis of its impact on the economic aspect of the vessel's exploitation. As stated in the paper, the design procedure includes:

1. RANS computation to obtain the wake field at the pre-selected PSS positions
2. BEM optimisation to obtain the optimal twist and camber of the PSS
3. Creation of parametric model for ESD
4. RANS Self-propulsion computations/optimisations to evaluate the PSS design".

For the design example, the Bulk Carrier “VALVOLINE” with the design speed of $V_s = 15.0$ knots was adopted. The design propeller rate of revolution is defined as $n_s = 123$ rpm. The FVM simulation predicted a delivered power reduction by 5.3% due to PSS installation, while sea trials revealed it to be 6.8%. The propeller rate of revolution was reduced by 5.2% due to the PSS.

In paper [32] the approach to PSS design is based on circulation distribution, replaced with the equivalent angle of attack. The detailed criteria for selecting the stator loading distribution and magnitude are not given, however. For the design example, the Kreso Container Ship (KCS) was adopted. The numerical results presented in the paper refer to the influence of the PSS on the hull resistance (resistance tests, without operating propeller), indicating a predicted effective power increase of 11% due to installation of the PSS. No self-propulsion test results or simulations were presented in this paper.

DOWNSTREAM DEVICES

Table 7 is constructed in a similar manner to Table 3 and presents corresponding data for downstream devices.

Paper [2] covers the topic of a post-swirl stator. Vortex representation of the lifting blades is utilised. The propeller is designed individually and then the stator is designed as a retrofit and the study “*therefore neglects the effect of the stator in the optimization process of the propeller*”. The design criterion for the stator demands cancellation of the fluid rotation passing through it. This criterion gives a direct relation between the bound circulation on the stator and that of the propeller. Two design examples are presented in the paper, the ‘Trawler’ and the ‘Tanker’. The particulars of the vessels are not provided; only operating parameters assumptions are given. An FVM simulation for the full scale was carried out to analyse the

designed propulsors (propeller + stator). A similar design approach to PoSS is adopted in paper [8]. A vortex model is applied and the design criterion demands rotation cancellation after the stator also. As the design example a 286 m Container Ship was adopted. The required thrust is defined as “*roughly $T = 2910416.35N$* ”. The model tests indicate 6.1% point higher efficiency for the propeller+stator system than for the equivalent stand-alone propeller.

In paper [10] the topic is a combined ESD, consisting of a wavy twisted rudder (WTR), tip raked propeller (TRP) and pre-swirl stator. The PSS design is conducted via potential code in the initial stage and is finalised with FVM. The design case adopted as the example is the Kreso Container Ship (KCS). In the first part of the paper, model tests with various rudder types are conducted to reveal the delivered power’s dependency on the selected rudder type. Based upon these results, the WTR was adopted for further work. Subsequent model tests were conducted with each ESD (PSS, TPR and WTR) installed alone and with all of them together (combined ESD), revealing that the sum of the power-saving effects of ESDs installed individually (7.16%) is notably higher than that for the combined ESD (5.36%). This is easily explained by the fact that some of the applied ESDs recover the same energy losses components.

Paper [12] covers the topic of twisted rudder design. Three types of twisted rudders were investigated in this study, including a ‘bare’ twisted rudder blade, a second one with a bulb and a third with additional fins installed on the bulb. As a reference level, a standard horn-type rudder was taken. The model tests revealed that the rudder equipped with the bulb brought the lowest saving effect (2.0%), while the one with additional fins on the bulb gave the highest effect (2.9%). The bare twisted rudder gave a 2.3% power-saving effect.

Paper [29] is focused mainly on the rudder type and the influence of its distance from the propeller on the propulsion

Tab. 7. Effect of downstream device installation

Paper	Ship type / Name	ESD type	ΔP_D [%]	V_s [kn]	n [rpm]	K_T [-]	$10K_Q$ [-]	C_T [-]	C_N [-]
[2]	Trawler	PoSS		10.0	380.0	0.104	0.117	2.792	6.388
[2]	Tanker	PoSS		12.5	247.0	0.181	0.232	2.294	4.119
[4]	Cargo Vessel A	PBCF	0.8			0.388	0.475	5.105	8.921
[4]	Cargo Vessel B	PBCF	1.8			0.385	0.475	5.058	8.923
[8]	Container Ship	none	-	22.0		0.220	0.344	1.073	1.458
[8]	Container Ship	PoSS	6.1	22.0		0.239	0.345	1.166	1.463
[10]	KCS	FSR	-	24.0	654.0 ^M				
[10]	KCS	TR	1.5	24.0	654.0 ^M				
[10]	KCS	WTR	1.8	24.0	652.2 ^M				
[12]	13,200 TEU Container Ship	none	-	20.0	477.0 ^M	0.205	0.353	1.115	1.770
[12]	13,200 TEU Container Ship	ZB-F TR	2.9	20.0	473.4 ^M	0.205	0.351	1.117	1.761
[29]	180m Diamond 34 Bulk Carrier	Orig	-	14.0	559.2	0.157	0.208		
[29]	180m Diamond 34 Bulk Carrier	Naca	0.3	14.0	557.4	0.157	0.209		

PoSS – post-swirl stator; FSR – full spade rudder; TR – twisted rudder; WTR – wavy twisted rudder;

Orig – original horn rudder; Naca – spade rudder with NACA20 section; ZB-F TR – twisted rudder with bulb and fins;

^M – model-scale value

characteristics. Moreover, the paper presents some results with the PSS installed; however, for this case only numerical results are available. For the design example a 180 m Diamond 34 Bulk Carrier was adopted. The design speed is $V = 14$ knots ($Fr = 0.173$). The model tests were conducted for two rudder types (ORIG – the original horn rudder and NACA – a spade rudder based on a NACA20 section), for three values of the propeller–rudder distance for each of them:

Tab. 8. Model test results for rudder ORIG

Rudder	$\Delta X/D$ [-]	T_M [N]	Q_M [Nm]	n_M [rps]	$2\pi Q_M n_M$ [W]	K_{T^a} [-]	K_{O^a} [-]
ORIG	0.455	42.78	1.333	9.42	78.92	0.1556	0.0205
ORIG	0.371	42.22	1.318	9.32	77.18	0.1569	0.0208
ORIG	0.286	42.97	1.331	9.32	77.96	0.1597	0.0210
NACA	0.441	41.66	1.330	9.39	78.47	0.1525	0.0206
NACA	0.357	41.75	1.323	9.35	77.68	0.1542	0.0207
NACA	0.272	41.95	1.319	9.29	76.98	0.1569	0.0209
NACA	0.272	41.95	1.319	9.29	76.98	0.1569	0.0209

a – calculated based on data provided in original paper

The influence of the pre-swirl stator was analysed via FVM simulation only for configuration with the ORIG rudder. This simulation indicated a power reduction of 1.8% and a revolution reduction of 1.61% due to PSS installation. The detailed design procedure for the PSS was not provided in the paper. It was only stated that its blades are: “*angled based on the flow direction in the region where they operate in order not to introduce extreme angles of attack and separation on the fins.*” Figures included in the paper suggest symmetric section profiles, but this is not stated directly. There must, however, be some non-zero camber and/or angle of attack, as there is a lift force generated on the PSS blades and it introduces the required counter-swirl, as stated in the paper.

In paper [4] a well-developed theoretical method for design of a propeller and dedicated propeller boss cap fins (PBCF) is provided. Preliminary calculations are based on vortex flow models, and precede more CFD calculations for verification of the produced design. In paper [22] PBCFs are analysed together with a divergent propeller hub cap. The first part of the paper is focused on representing the optimisation scheme, fuelled by CFD-derived and experimental data, where the parametrically described geometry of the PBCFs was analysed. A similar analysis was conducted for several concepts of the divergent hub cap. Another important contribution of this paper is the description of the experimental method, which is suitable for conducting an open water test for propellers equipped with PBCFs, which differs slightly from standard open water tests. The results show that the PBCFs may increase the propeller’s open water efficiency, but the divergent cap applied for the propeller with PBCFs reduced the efficiency by 7.5%, which suggests that this shape of cap was not good for this case. This conclusion is supported by the increased hub vortex reported for the model test with the divergent cap.

PROPELLER LOADING AND ENERGY-SAVING EFFECT

As one can imagine, the wide scatter of data presented above does not allow all of them to be arranged on a common base that would provide a reliable reference level for power-saving evaluation. Thus only selected values from the data presented above are taken for the analysis.

Plotting the energy-saving effect versus propeller loading (determined for ‘No ESD’ conditions), as in Fig. 2, leads to the clear conclusion that the propellers with higher loading reveal a higher potential for the energy-saving effect:

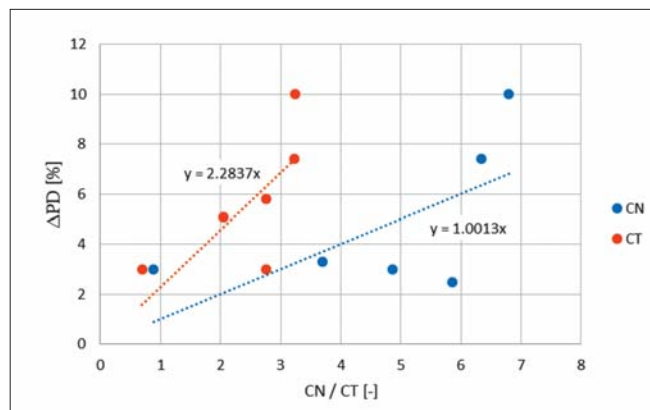


Fig. 2. Stand-alone propeller loading versus power-saving effect

Loading coefficients C_T and C_N represent the propeller loading with respect to the inflow velocity to the propeller disc. The propeller operating conditions may also be related to the rate of revolution, by coefficients K_T , K_Q . Plotting the energy-saving effect versus these, as in Fig. 3, did not allow any clear trend to be identified and hence no trend line was plotted.

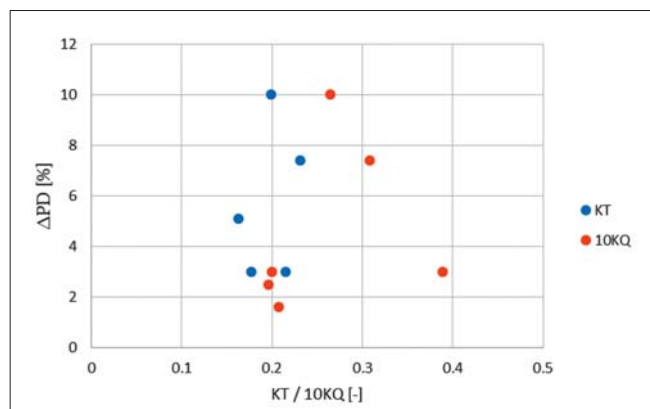


Fig. 3. Stand-alone propeller loading versus power-saving effect

The situation above is well explained by the fact that the $C_{T/N}$ coefficients relate the propeller loading to the energy brought by the inflowing stream, while $K_{T/Q}$ instead provides information on whether the propeller should be regarded as slow rotating or fast rotating. The latter concept is not necessarily directly determined by whether the propeller is highly or lightly loaded.

Another possibility for evaluating the energy-saving effect is to plot it versus the revolution reduction, as presented in Fig. 4:

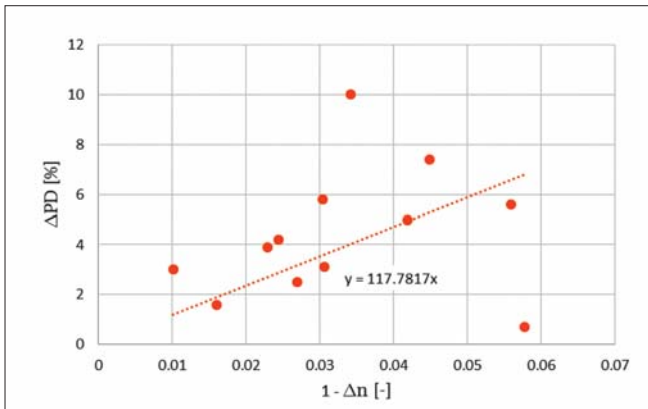


Fig. 4. Rate of revolution reduction versus power-saving effect

It has to be underlined that the latter method is not sufficient to evaluate the potential energy saving that can be expected for a particular propeller upon its stand-alone loading, but rather helps to evaluate the general quality of a particular ESD. A clear positive trend may be observed, but cases like the one described in [14] have to be kept in mind, when similar revolution reduction is accompanied by notably different power reduction values.

The analysis above was prepared for upstream devices only due to the completeness of the collected data. To evaluate the quality of the downstream devices analysed, their power savings were compared to the trend lines drawn for upstream devices:

Tab. 9. Downstream devices evaluation

Paper	Ship type / Name	ESD	Expected (trend line based on)			ΔP [%]
			C_T	C_N	$1-\Delta n$	
[8]	Container Ship	PoSS	2.5	1.5	-	6.1
[10]	KCS	TR	-	-	0.0	1.5
[10]	KCS	WTR	-	-	0.3	1.8
[12]	13,200 TEU Container Ship	ZB-F TR	2.5	1.8	0.9	2.9
[29]	180m Diamond 34 Bulk Carrier	NACA	-	-	0.4	0.3

In table 9. signs “-” were put where sufficient data was not provided in the original papers. It can be seen, however, that the post-swirl stator reveals a notably more favourable operation effect than upstream devices installed with the propellers of corresponding loading. Another observation is that the trend line relating the power-saving effect with the revolution reduction may not be sufficient for evaluation of rudders that are considered as ESDs. It seems that the problem is not that there is no data for very low values of revolution reduction (the rudders analysed in this review yield nearly no revolution reduction), but the different hydrodynamic behaviour. Proper evaluation of rudders considered as ESDs requires a greater amount of data to be collected.

CONCLUSIONS

As concluding remarks of this review, the following may be stated:

- The design of ESDs is dominated by the use of optimization algorithms. The differences between particular studies lie mainly in the flow model adopted (potential or viscous) and the particular aspect undergoing the optimization process (loading distribution or geometry).
- Vortex models are being displaced by modern CFD but they still have an important role, especially at the initial stages of the design process. However, even modern CFD has a tendency to underestimate the expected power-saving effect.
- Proper analysis of vessels equipped with ESDs requires dedicated extrapolation methods for propulsion prognosis and sometimes conducting the model tests themselves.
- The expected power-saving level for most ESDs is around 3–6%; higher propeller loading brings more potential for energy recovery. Each case should be analysed carefully to deduce the amount of energy losses that are to be recovered.
- Among the upstream devices that were analysed in this review, pre-swirl ducts revealed power savings at a similar level to pre-swirl stators. However, their additional advantage is the improvement of the axial inflow to the propeller.
- Reasonable power saving may be achieved by replacing the classical spade rudder by one with a twisted leading edge (around 3%).

ACKNOWLEDGEMENT

The research was partly financed by the National Centre for Research and Development of the Republic of Poland, within the framework of the Esthetics project (POLTUR3/ESTHETICS/1/2019).

REFERENCES

1. I. H. Abbott, A. E. Doenhoff, *Theory of wing sections including a summary of airfoil data*. New York: Dover Publications, 1959.
2. F. Celik, M. Guner, “Energy saving device of stator for marine propellers,” *Ocean Engineering*, vol. 34, pp. 850–855, 2007
3. J.P. Chen, J. Su, J.W. Jie, L. Yang, “Investigation on propulsion and flow field of ships with energy saving devices using CFD predictions and model tests,” in *12th International Conference on Hydrodynamics, Egmond aan Zee, The Netherlands, September 2016*.
4. M. Cheng, C. Hao-peng, Q. Zheng-fang, C. Ke, “The design of propeller and propeller boss cap fins (PBCF) by an integrative method,” *Journal of Hydrodynamics*, vol. 26 (4), pp. 586–593, 2014.

5. B. W. Coney, *A method for the design of a class of optimum marine propulsors*. Massachusetts Institute of Technology, 1989.
6. L. Guangnian, Q. Chen, Y. Liu, "Experimental study of dynamic structure of propeller tip vortex," *Polish Maritime Research*, vol. 27 (2), pp. 11–18, 2020.
7. P. M. Hooijmans, J. Holtrop, J. Windt, "Refitting to save fuel and new approaches in the design of new buildings," in *11th International Symposium on Practical Design of Ships and Other Floating Structures*, 2010.
8. L. X. Hou, C. H. Wang, A. K. Hu, F. L. Han, "Wake-adapted design of fixed guide vane type energy saving device for marine propeller," *Ocean Engineering*, vol. 110(B), pp 11–17, 2015
9. S. Hyun-Joon, L. Jong-Seung, L. Jang-Hoon, Myung-Ryun Han, H. Eui-Beom, S. Sung-Chul, "Numerical and experimental investigation of conventional and un-conventional preswirl duct for VLCC," *International Journal of Naval Architecture and Ocean Engineering*, vol. 5(3), pp 414–430, 2013
10. L. Joon-Hyoung, K. Moon-Chan, S. Young-Jin, K. Jin-Gu, "Study on performance of combined energy saving devices for container ship by experiments," *Fifth International Symposium on Marine Propulsors smp'17*, 2017.
11. J. E. Kerwin, W. B. Coney, C.-Y. Hsin, "Hydrodynamic aspects of propeller/stator design," The Society of Naval Architects and Marine Engineers, Propeller '88 Symposium 5th, 1988.
12. J.-H. Kim, J.-E. Choi, B.-J. Choi, S.-H. Chung, "Twisted rudder for reducing fuel-oil consumption," *Ocean Engineering*, vol. 6, pp. 715–722, 2014.
13. J.-H. Kim, J.-E. Choi, B.-J. Choi, S.-H. Chung, H.-W. Seo, "Development of energy-saving devices for a full slow-speed ship through improving propulsion performance," *International Journal of Naval Architecture and Ocean Engineering*, vol. 7, pp. 390–398, 2015.
14. M. C. Kim, H. H. Chun, Y. D. Kang, "Design and experimental study on a new concept of preswirl stator as an efficient energy-saving device for slow speed full body ship," *SNAME* vol 112, pp 111–121, 2004.
15. V. Kraslinikov, K. Koushan, M. Nataletti, L. Sileo, S. Spence, "Design and numerical and experimental investigation of pre-swirl stators PSS," in *Sixth International Symposium on Marine Propulsors SMP'19*, 2019.
16. P. Król, "Vortex model of ideal guide vane and its application to the real guide vane," in *Sixth International Symposium on Marine Propulsors SMP'19*, 2019.
17. P. Król, "A new design method of propulsor systems with optimum distribution of bound circulation," Gdańsk University of Technology, 2019.
18. P. Król, T. Bugalski, "Application of vortex flow model in propeller-stator system design and analysis," *Polish Maritime Research*, vol. 25(1), pp. 24–32, 2018.
19. P. Król, T. Bugalski, M. Wawrzusiszyn, "Development of numerical methods for marine propeller-pre-swirl stator system design and analysis," in *Fifth International Symposium on Marine Propulsors smp'17*, 2017.
20. P. Król, K. Tesch, "Pre-swirl energy saving device in marine application," in XXIII Krajowa Konferencja Mechaniki Płynów, Zawiercie, 2018.
21. L. Kwi-Joo, A. Jung-Sun, K. Han-Joung, "Comparative study between results of theoretical calculation and model test for performance confirmation of 'Crown Duct,'" *Journal of Ocean Engineering and Technology*, vol. 28(1), pp. 1–5, 2014.
22. S.-S. Lim, T.-W. Kim, D.-M. Lee, C.-G. Kang, S.-Y. Kim, "Parametric study of propeller boss cap fins for container ships," *International Journal of Naval Architecture and Ocean Engineering*, vol. 6(2), pp. 187–205, 2014; published online Epub6.
23. A. Minchev, M. Schmidt, S. Schnack, "Contemporary bulk carrier design to meet IMO EEDI requirements," *Third International Symposium on Marine Propulsors smp'13*, 2013.
24. K. Moon-Chan, S. Yong-Jin, L. Won-Joon, L. Joon-Hyoung, "Study on extrapolation method for self-propulsion test with pre-swirl device," *Fifth International Symposium on Marine Propulsors smp'17*, 2017.
25. A. Nadery, H. Ghassemi, "Numerical investigation of the hydrodynamic performance of the propeller behind the ship with and without WED," *Polish Maritime Research*, vol. 27(4), pp. 50–59, 2020.
26. H. Nouroozi, H. Zeraatgar, "Propeller hydrodynamic characteristics in oblique flow by unsteady RANSE solver," *Polish Maritime Research*, vol. 27(1), pp. 6–17, 2020.
27. J. R. Nielsen, W. Jin, "Pre-swirl fins adapted to different operation conditions," *Sixth International Symposium on Marine Propulsors SMP'19*, 2019.
28. S. Park, G. Oh, S. Rhee, B.-Y. Koo, H. Lee, "Full scale wake prediction of an energy saving device by using computational fluid dynamics," *Ocean Engineering*, vol. 101, pp. 254–263, 2015.
29. C. D. Simonsen, C. Nielsen, C. Klimt-Møllenbach, C. R. Holm, A. Minchev, "CFD based investigation of potential

power saving for different rudder types, positions and pre-swirl fins,” Siemens report, November 2012.

30. T. T. Ngoc, D. D. Luu, T. T. H. Nguyen, T. T. T. Nguyen, M. V. Nguyen, “Numerical prediction of propeller – hull interaction characteristics using RANS method,” *Polish Maritime Research*, vol. 26(2), pp. 163–172, 2019.
31. Y. Xing-Kaeding, S. Gatchell, H. Streckwall, “Towards practical design optimization of pre-swirl device and its life cycle assessment,” in *Fourth International Symposium on Marine Propulsors SMP’15*, 2015.
32. S. Yong-Jin, K. Moon-Chan, L. Won-Joon, L. Kyoung-Wan, L. Joon-Hyoung, “Numerical and experimental investigation of performance of the asymmetric pre-swirl stator for container ship,” in *Fourth International Symposium on Marine Propulsors SMP’15*, 2015.
33. J. Zou, G. Tan, H. Sun, J. Xu, Y. Hou, “Numerical simulation of the ducted propeller and application to a semi-submerged vehicle,” *Polish Maritime Research*, vol. 27(2), pp. 19–29, 2020.
34. Y. Zhang, X. Wu, M. Lai, G. Zhou, J. Zhang, “Feasibility study of RANS in predicting propeller cavitation in behind-hull conditions,” *Polish Maritime Research*, vol. 27(4), pp. 26–35, 2020.

CONTACT WITH THE AUTHOR

Przemysław Król

e-mail: przemyslaw.krol@cto.gda.pl

Ship Design and Research Centre
Szczecińska 65, 80-392 Gdańsk

POLAND

MODELLING SHIPS MAIN AND AUXILIARY ENGINE POWERS WITH REGRESSION-BASED MACHINE LEARNING ALGORITHMS

Fatih Okumuş *

Araks Ekmekçioğlu

Selin Soner Kara

Yildiz Technical University, Istanbul, Turkey

* Corresponding author: hfatihokumus@gmail.com (F.Okumus)

ABSTRACT

Based on data from seven different ship types, this paper provides mathematical relationships that allow us to estimate the main and auxiliary engine power of new ships. With these mathematical relationships we can estimate the power of the engine based on the ship's length (L), gross tonnage (GT) and age. We developed these approaches using simple linear regression, polynomial regression, K-nearest neighbours (KNN) regression and gradient boosting machine (GBM) regression algorithms. The relationships presented here have a practical application: during the pre-parametric design of new ships, our mathematical relationships can be used to estimate the power of the engines so that more environmentally friendly ships may be built. In addition, with the machine learning methodology, the prediction of the main engine (ME) and auxiliary engine (AE) powers used in the numerical calculation of ship-based emissions provides data for researchers working on emission calculations. We conclude that the GBM regression algorithm provides more accurate solutions to estimate the main and auxiliary engine power of a ship than other algorithms used in the study.

Keywords: : machine learning, regression, ship emissions, engine power, prediction

INTRODUCTION

Machine learning is a system that investigates the work and construction of algorithms that can make predictions by making inferences using mathematical and statistical methods from the available data. In machine learning, which is a sub-discipline of artificial intelligence, the algorithms work by building a model to make predictions from sample inputs with the help of computers and software.

The effects of ship-based exhaust emissions include reduction in the air quality, especially in a country's inland waters, the straits, and port areas. These emissions and greenhouse gases are also among the major factors causing global climate change. Two approaches stand out in the literature to estimate emissions from ships. One is the top-down approach, which is based on the fuel consumed by the ship, and the other is the bottom-up approach, which uses the ship's main and auxiliary machinery forces, based on the manoeuvre, cruise, and port activities.

Looking at the research on the application of machine learning in the maritime industry in the literature, Ekmekçioğlu et al. [1] calculated the exhaust emissions from ships arriving at four major ports of Turkey for a year using real numerical data such as the main engine power and speed, auxiliary engine power, and the duration of stay in port. In his study, Trozzi [2] proposed a function based on the ship type and gross tonnage in calculation of the ship's main engine power. He used non-linear regression for ship-based emission calculation. He also proposed the estimated average vessel ratios of the auxiliary engines / main engines by ship type. Yan et al. [3] proposed a two-stage fuel consumption prediction and fuel reduction model for a dry bulk ship. In the first stage, they created a fuel consumption prediction model that takes into account the ship's sailing speed, cargo weight, sea and weather conditions by using the random forest regression. In the second stage, they developed a speed optimisation model based on the prediction model proposed in the first stage. They concluded that the proposed model could reduce the ship's fuel consumption

by 2–7% and this reduction would also lead to lower CO₂ emissions. Huang et al. [4] calculated ship exhaust emissions using the activity-based STEAM (Ship Traffic Emissions Assessment Model) method. They used machine learning (80% training set, 20% test set) and the polynomial regression method to calculate the value of the unknown main engine power according to the ship's dimensions. Tran [5] emphasised the effect of fuel consumption on CO₂ emissions and used fuzzy clustering to examine the effect of loading a bulk carrier, which he took as a case study, on the fuel consumption. He concluded that the novel methodology showed that machine learning could be used to make decisions for the optimum loading of the ship, in the study where parameters such as wind speed, wave height, ship speed, distance travelled, and shaft speed were analysed.

In their studies, Yan et al. [6] applied big data analysis by considering environmental factors to optimise the engine speeds of inland ships. They proposed a distributed parallel k-means analysis for clustering environmental factors into multiple groups and a model to optimise ships' energy efficiency. They conducted a case study to verify their method on the Yangtze River, and concluded that the method they developed could increase ships' energy conservation and emission reduction. Cepowski [7] used the ship's speed and deadweight or TEU capacity properties to estimate the total machine power of bulk carriers and container vessels. Requia et al. [8] estimated and compared PM_{2.5} components with ordinary kriging (OK) interpolation, hybrid interpolation and machine learning (forest-based regression) methods. They concluded that the forest model offers the best performance because the R² value is higher than 0.7 for most of the particle components. They stated that their results may be useful for more accurate prediction of PM_{2.5} components in the air. Uyanık et al. [9] performed the fuel consumption optimisation of a container ship with machine learning using multiple linear regression, ridge and lasso regression, support vector regression, tree-based algorithms and boosting algorithms. They compared the prediction models in their studies and they found that parameters such as the main engine rpm, cylinder values, scavenge air and shaft indicators are highly correlated with fuel consumption, and stated that they found the most accurate estimate with multiple regression and ridge regression. Barua et al. [10] explored international freight transportation management through machine learning. They discussed how it is applied in the fields of maritime transport, air cargo and intermodal transport using different machine learning methods such as demand forecasting, operation and asset maintenance, vehicle trajectory and on-time performance prediction. They proposed four directions for future research. Peng et al. [11] estimated the energy consumption of ships in China's Jingtang port and discussed their strategies to reduce energy consumption and proposed prediction models. They used the gradient boosting regression, random forest regression, BP network, linear regression and K-nearest neighbour regression machine learning models and analysed 15 features that have an impact on ships' energy consumption as input. They concluded that net tonnage,

deadweight tonnage, actual weight and efficiency of facilities are the four most important features to predict the energy consumption of the ships. Jeong et al. [12] made predictions of time for shipbuilding production processes using machine learning technology. In their study, they analysed data with the R and Python programs, they created prediction models and confirmed these models using criteria such as the mean absolute percent error and root mean squared logarithmic error. Gkerekos et al. [13] investigated the effectiveness of different multiple regression algorithms to estimate ships' main engine fuel oil consumption. They considered the noon reports and automatic data logging and monitoring systems for data collection. They compared machine learning regression algorithms such as linear regression, decision tree regressors, random forest regressors, extra trees regressors, support vector regressors, K-nearest neighbours, artificial neural networks and ensemble methods, and stated that the best performance was shown by extra trees regressors and random forest regressors. Jonquais and Krempf [14] used machine learning to make predictions about shipping times between South East Asia and North America. By using the random forest algorithm and creating four models to produce estimates, they created a tool that gives superior results over traditional methods. Bodunov et al. [15] estimated a destination and an estimated time of arrival (ETA) for maritime traffic using a machine learning method using geo-spatial data, random forest, gradient boosting decision trees, XGBoost trees and extremely randomised trees models for destination prediction; they used feed forward neural networks for arrival time estimation. They achieved 97% accuracy in the destination estimate and 90% accuracy in the ETA estimate. In their study, Yuan and Nian [16] emphasised the importance of improving ship energy efficiency and reducing ship emissions, and they developed a Gaussian process metamodel to predict ships' fuel consumption in different scenarios, taking into account the operating and weather conditions such as speed, trim, wind and wave effects. With the case study, they demonstrated the accuracy and effectiveness of using the Gaussian process metamodel for the prediction of ships' energy consumption. Farag and Ölçer [17] stated that fuel consumption is a very important tool in reducing greenhouse gas emissions. They developed an estimation model for the fuel consumption of ships using artificial neural network and multiple regression techniques. Finally, they used the model they developed to estimate the fuel savings that one ship can make during a voyage. Bui-Duy and Vu-Thi-Minh [18] created a deep-based fuel consumption model for the shipping route selection of container ships in Asia. They offered an idea that helped choose the optimal route to minimise fuel costs. They stated that the model, which has five input variables, namely average velocity, sailing time, ship capacity, wind speed and wind direction, has an accuracy of close to 95%. Hao Cui et al. [19] proposed a new machine-learning-based ship design optimisation approach. They used a multi-objective particle swarm optimisation method, multi-agent system and CAE software to build an optimisation system. They conducted a dry cargo vessel design

optimisation as a case study to evaluate the conformity of the method they created to the real world. Peker et al. [20] created a model that can predict the heating and cooling load of houses by using machine learning algorithms with a data set with eight input and two output values. They used and compared machine learning algorithms such as support vector machine regression, linear regression, random forest regression and nearest neighbour regression, and concluded that the best predictive success was achieved by the random forest regression algorithm. In this study, the ship length, gross tonnage, and age data were weak in predicting the ship's main power. With KNN regression, the main engine power can be successfully estimated, but the most successful

algorithm was the GBM algorithm. Similarly, linear and polynomial regression is not sufficient for predicting auxiliary machine power. While KNN regression received a pass grade, the GBM regression algorithm predicted quite successfully.

AIM OF RESEARCH

Previous studies were examined according to their methods, inputs, outputs and R^2 values and the similarities and differences between this study and other articles were revealed. The comparison with previous studies is shown in Table 1.

Tab. 1. Comparison with previous studies.

Study	Method	Inputs	Outputs	R^2
This study	Linear regression	GRT, length, age	ME power	0.68
This study	Linear regression	ME Power, length, age	AE power	0.68
This study	Polynomial regression	GRT, length, age	ME power	0.8
This study	Polynomial regression	ME power, length, age	AE power	0.69
This study	K-nearest neighbour regression	GRT, length, age	ME power	0.86
This study	K-nearest neighbour regression	ME power, length, age	AE power	0.74
This study	Gradient boosting regression	GRT, length, age	ME power	0.95
This study	Gradient boosting regression	ME power, length, age	AE power	0.93
Yan et al. [3]	Random forest regression	Sailing speed, cargo weight, weather conditions	Fuel consumption	0.72
Huang et al. [4]	Polynomial regression	Cargo ships, length, breadth	ME power	0.91
Huang et al. [4]	Polynomial regression	Tankers, length, breadth	ME power	0.87
Requia et al. [8]	Forest model	25 predictors representing land use	PM _{2.5} emission	0.93
Peng et al. [11]	Random forest regression	15 features consisting of inherent properties of container ships and external features of ports	Ship energy consumption	0.94
Peng et al. [11]	Linear regression	15 features consisting of inherent properties of container ships and external features of ports	Ship energy consumption	0.77
Peng et al. [11]	K-nearest neighbour regression	15 features consisting of inherent properties of container ships and external features of ports	Ship energy consumption	0.62
Peng et al. [11]	Gradient boosting regression	15 features consisting of inherent properties of container ships and external features of ports	Ship energy consumption	0.91
Gkerekos et al. [13]	Random forest regression	Load conditions, weather conditions, speed, sailing distance, draft	Ship ME fuel consumption	0.87
Gkerekos et al. [13]	K-nearest neighbour regression	Load conditions, weather conditions, speed, sailing distance, draft	Ship ME fuel consumption	0.78
Gkerekos et al. [13]	Boosting	Load conditions, weather conditions, speed, sailing distance, draft	Ship ME fuel consumption	0.90
Jonquais and Krempf [14]	Random forest regression	Carrier, shipper, route	Shipping times for departure	0.88
Jonquais and Krempf [14]	Neural networks model	Carrier, shipper, route	Shipping times for departure	0.85
Farag and Ölçer [17]	Artificial neural network	Speed, depth, wind speed, wave parameters, swell parameters, sea current	Brake power	0.96
Farag and Ölçer [17]	Artificial neural network	Speed, depth, wind speed, wave parameters, swell parameters, sea current	Fuel consumption	0.89

In this study, we use different machine learning methods and comparisons in order to estimate the main and auxiliary engine powers of the ships, which are necessary for numerical calculation of the emissions of exhaust gas originating from the maritime sector.

MATERIALS AND METHOD

MODEL VALIDATION

The accuracy of the model's predictions is calculated by comparing the actual power values of the main and auxiliary engine with the corresponding predicted values. Ten-fold cross-validation was applied to check the model performance. The dataset was randomly divided into 10 parts, train the model on 9 partitions and predict the properties of the remaining set. This process was repeated 10 times for each section. The prediction ability of the model is then evaluated as the average performance of the model in all repetitions. The root mean squared error (*RMSE*), mean absolute error (*MAE*), and R-squared (R^2) were used to assess the performance of the developed regression models.

$$RMSE = \sqrt{\frac{1}{n} \sum_{i=1}^n (y_i - \hat{y}_i)^2} \quad (1)$$

As shown above, y_i and \hat{y}_i respectively represent the actual power values and estimated power values. Since the aim of training the model is to reduce the difference between these two values as much as possible, the model with a small *RMSE* value was accepted as superior.

The *MAE* measures the average magnitude of errors in a series of estimates, regardless of their direction. It is the average of the absolute differences between the estimate and the actual observation that all individual differences have equal weight on the test sample. Its analytical expression is as follows:

$$MAE = \frac{1}{n} \sum_{i=1}^n |y_i - \hat{y}_i| \quad (2)$$

The R^2 correlation coefficient is used to evaluate the performance of the models and is given as follows:

$$R^2 = 1 - \frac{\sum_{i=1}^n (y_i - \hat{y}_i)^2}{\sum_{i=1}^n (y_i - \bar{y}_i)^2} \quad (3)$$

\bar{y}_i represents the mean value of y_i . It is a measure showing how close each data point is to the regression line with the R^2 value. It is always positive and between 0 and 1.

DATA SET

In this study, data containing information from 4037 different ships were used. The dataset includes the ship type, gross tonnage, year of manufacture, length, and the main and

auxiliary engine power for each ship. While 80% of these data of these ships are used to train the model, 20% of them are used for testing. Samples were taken from seven different ship types: chemical tanker, container, general cargo, LPG tanker, oil product tanker, Ro-Ro ship, and search and rescue ship. The gross tonnage of the ships varies between 74 and 162960. The oldest ship was produced in 1925, while the newest ship was built in 2018. The lengths of the ships were kept in a wide range from 18.25 m to 368 m. The main machine power and auxiliary machine power to be estimated vary in the ranges of 147–72240 kW and 37–9600 kW, respectively. Table 2 provides statistical data on the ships.

Tab. 2. Statistical data of the data set

	Minimum	1 st . Qu.	Median	Mean	3 rd . Qu.	Maximum
Gross tonnage	74	3505	9927	21654	29982	162960
Length	18.28	106.00	141.00	154.86	189.99	368.00
ME power	147	1920	5400	8839	10500	72240
AE power	37	253	500	738	910	9600

DETERMINING THE INDEPENDENT VARIABLES

The separation of resistance components in terms of the scale effect and its first use in model–ship extrapolation was introduced by Froude. In this method, which is today called the Froude hypothesis, total resistance is divided into friction and residual resistance; the friction resistance is assumed to be equal to one equivalent plate resistance in the same area as the ship's wet area, and the difference between the total resistance and friction resistance is defined as the residual resistance. There are various methods for calculating the ship's total resistance and resistance components. CFD (computational fluid dynamics), panel methods, other numerical techniques, model experiments, empirical and statistical approaches are the main methods used in calculation. It is an undeniable fact that the total resistance of ships has improved over time with the research and development studies of researchers on these methods.

Also, the number of ship gas emissions is estimated to be around 450, but the vast majority of these are at a level that can be neglected in terms of both quantity and impact. However, carbon dioxide (CO₂), carbon monoxide (CO), nitrogen oxides (NO_x), sulphur oxides (SO_x), and particulate matter (PM) are the most common gas emissions and have the greatest impact on both human health and the ecosystem. MARPOL (International Convention for the Prevention of Pollution from Ships) is reducing the limits of these harmful emissions to ever more demanding levels. Although various internal combustion engine technologies have been developed to overcome these difficult constraints, it is difficult to do so unless there are efficient ships. For this reason, it would not be a correct approach to ignore the developments that occur over time while estimating the main engine power of the ships.

Also, the NO_x emission factors used in the calculations vary according to the shipbuilding year. As a matter of fact, when looking at the results of the relative influence of the model created with the GBM algorithm, it is seen that the age of the ship has an effect amounting to 21.86%. Fig. 1 contains the result of the relative influence of the independent variables.

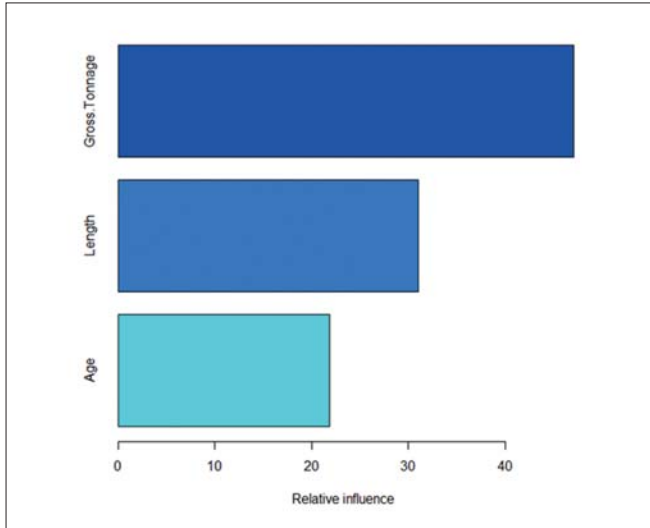


Fig. 1. Relative influence of the independent variables

The admiralty coefficient formula is one effective empirical expression that can be used to predict the power curves of ships and is expressed as in Eq. (4). Ships with a similar hull form, speed and displacement have the same admiralty coefficient.

$$P_E = \frac{\Delta^{2/3} \cdot V^3}{C} \quad (4)$$

Tab. 3. Admiralty coefficient for different ship types [21]

Ship type	Admiralty constant
General cargo ship	400±600
Bulker and tanker	600±750
Reefer	550±700
Feeder ship	350±500
Warship	150

In Eq. (4), Δ , V , P_E and C are the displacement, velocity, effective power and admiralty coefficient respectively. Table 3 contains the admiralty coefficient suggested by Schneekluth and Bertram for different ships [21]. When Table 3 is examined, the effect of the ship type on the power can be seen clearly. After the effective efficiency is calculated, the main engine power can be calculated using the efficiency of the gear box, the mechanical efficiency of the shaft line, efficiency of the hull, rotation relative efficiency, and open water efficiency of the propeller.

It is seen that two important features of ships have emerged in order to predict the main engine power in ships. The change in the admiralty coefficient of different ship types indicates that ships have different power requirements in relation to

their job description. In the study, an independent variable representing the ship type was thus needed to estimate the main engine power. For this reason, it was investigated whether the gross tonnage can represent the ship type and, for this, the gross tonnage length curves were examined depending on the ship type. In Fig. 2, the gross tonnage length distributions of different types of ships in the data set are given. In addition, the curves where the gross tonnage changes depending on the length for the same ship type are shown in Fig. 3, using the available data.

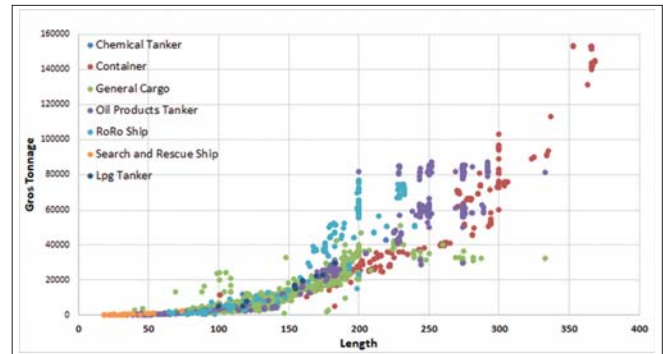


Fig. 2. Gross tonnage and length distributions of different types of ships

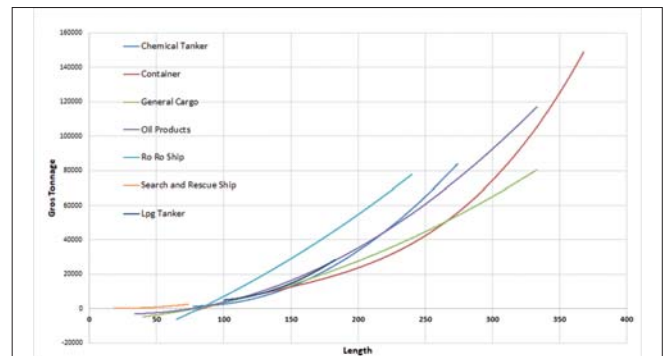


Fig. 3. Gross tonnage and length curves of different types of ships

Fig. 3 shows that the gross tonnage value shows different trends for different ship types. There are also supporting empirical statements showing that the gross tonnage and length values of the ships in the data set used differ according to the ship types. Similar to the admiralty coefficient, the empirical statement in Eq. (5) can be used to estimate the gross tonnage. Here, the gross tonnage expression is given as a function of CN (cubic number). The symbol k indicates the coefficient, which varies according to the ship type. In Eq. (6), the explicit expression of CN is given and the symbols L_{pp} , B , and D represent the values of the length between the perpendiculars, beam and depth respectively.

$$GT = k \cdot CN \quad (5)$$

$$CN = L_{pp} \cdot B \cdot D \quad (6)$$

When the friction resistance affecting the ships is examined, it is seen that it basically depends on the friction coefficient, the density of the fluid it is in, the wet surface area and the square of the speed. Among these variables, the square of the

wet surface area and velocity is directly related to the ship's design parameters. The wet surface area, defined as the area of the surface of the ship in contact with water, is one of the important parameters of the resistance and power calculation. Considering that the wet surface area is also a function of the ship's length, this length is also used as an independent variable.

It would not be right to think that the power of the ship's auxiliary engines is in a linear relationship depending on the ship's main engine power. However, the ship is not completely independent from the main engine power. While calculating the power of auxiliary machinery, many variables such as crew needs and the power requirements of the control systems should be taken into consideration. In this study, the main engine power and ship length were used as an indicator of the size and power needs of the ship to estimate the auxiliary engine power. In addition, the gross tonnage was used to symbolise the special needs of the ship type.

LINEAR REGRESSION

Linear regression is a method used to model the connection between one or more independent variables and a dependent variable. The main purpose of linear regression is to obtain the function of the relationship between parameters. Creating an appropriate model in the learning process signifies choosing the most appropriate parameters for the hypothesis function by using the training set. The hypothesis function may depend on one or more parameters. Provided that a model based on a single parameter is constructed, it is named as single regression; if it is constructed with two or more parameters, it is named as multiple regression. Single linear regression is formulated as in Eq. (7).

$$y = \beta_0 + \beta_1 x + \varepsilon \quad (7)$$

In Eq. (7), y refers to the value of the dependent variable, x refers to the value of the independent variable, β_0 is the population's y intercept, β_1 the slope of the population regression line and ε a random error term. Similarly, multiple linear regression is expressed as in Eq. (8).

$$y = \beta_0 + \beta_1 x + \dots + \beta_k x_k + \varepsilon \quad (8)$$

As distinct from Eq. (7), k represents the number of independent values. In multiple linear regression analysis, the contribution of some of the modelled independent variables to the model may be insignificant. Therefore, it is necessary to identify the independent variables that will explain the dependent variable in the most appropriate way, and remove the insignificant variables from the model. This process is called "variable selection".

Various methods have been developed for independent variable selection. These can be examined as three main groups.

- Forward selection
- Backward elimination
- Standard stepwise regression

For selection of the variables for main engine and auxiliary engine power estimates, the forward selection, backward elimination and standard stepwise selection methods have been applied to determine the contribution of our variables to the model.

According to the simple correlation matrix between the ME power dependent variable and the other independent variables for the ME, the highest correlation coefficient was found. L and GT were the highest independent correlations with ME power. The degree of significance of all independent variables p was examined separately. Then, while the L and GT variables are constant, it is necessary to find the independent variable with the highest partial correlation with ME power. For this reason, the age variable is a candidate to enter the model. Since the significance level of the L, GT and age variables is $p < 0.05$, these variables are included in the model.

According to the simple linear correlation matrix between the AE power dependent variable and other independent variables for the AE, the highest correlation coefficient was found. The independent variables with the highest correlation with AE power were ME power, L, and GT, respectively. The degree of significance of all independent variables p was examined separately. The ME power, L and age variables are included in the model because their p value is less than 0.05. The GT variable was removed from the model because its p value is greater than 0.05.

Within the scope of this study, Model.ME.1 was created to estimate the ship's main engine power. While constructing the model, the length, gross tonnage and age of the ship were used as independent variables. Moreover, the ship's auxiliary engine power was estimated by linear regression, using the main engine power, length and age. The model thus created was named as Model.AE.1. Table 4 contains the errors from the linear model's train and test sets.

Tab. 4. Error values of the linear model

	Train			Test		
	RMSE	R ²	MAE	RMSE	R ²	MAE
Model.ME.1	6592.29	0.688	4396.62	6257.2	0.684	4143.66
Model.AE.1	448.99	0.650	251.847	430.77	0.679	246.48

POLYNOMIAL REGRESSION

Independent variables are not continuously required to be in a linear relationship with the dependent variable. As a consequence, the predictive power of the linear model will weaken. In such circumstances, polynomial regression is used. For multiple exponents of the argument, the polynomial model is created as in Eq. (9).

$$y = \beta_0 + \beta_1 x + \beta_2 x^2 + \dots + \beta_p x^p + \varepsilon \quad (9)$$

In the equation, expression p refers to the polynomial degree. Polynomial regression can be applied as single or multiple regression as in linear regression.

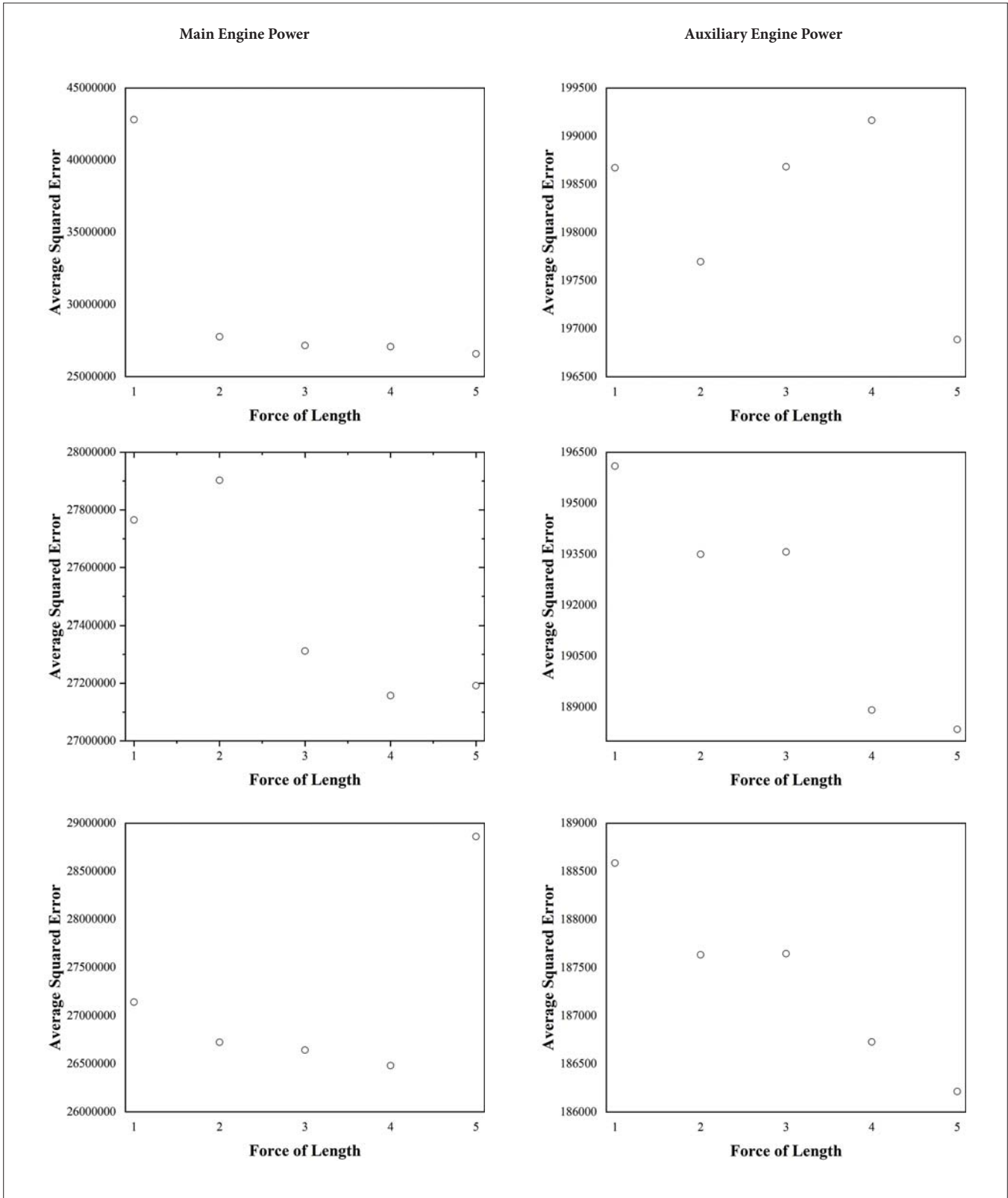


Fig. 4. Forces of independent variables

In this part of the study, the answer to the question of which polynomial levels should be created using the data in the whole data set without any test–train separation was sought. Polynomial forces between 1 and 5 were investigated for each

predictor in Model.ME.1. Average squared error values were examined for each polynomial force and, according to the results, the forces of the estimators of the final model were decided.

i , j , and k represent the polynomial degrees of the independent variables (length, gross tonnage, and age), respectively. When Fig. 4 is examined, a 2nd degree polynomial is suitable for length, 4th degree for gross tonnage and 2nd degree for age. With reference to these results, Model.ME.2 was created to estimate the ship's main engine power. Similar steps were used to estimate the auxiliary engine power, for which Model.AE.2 was created. As a consequence of the applied operations, the force of the main engine power was 5, and the force of the length and age was 4 and 5, respectively. Fig. 4 shows the average square error obtained for various forces of the independent variables. Table 5 contains the errors from the polynomial model's train and test sets.

Tab. 5. Error values of the polynomial model

	Train			Test		
	RMSE	R ²	MAE	RMSE	R ²	MAE
Model.ME.2	5174.01	0.807	3112.51	5006.42	0.800	2955.65
Model.AE.2	431.59	0.676	232.28	421.22	0.691	238.55

K-NEAREST NEIGHBOURS – REGRESSION

The K-nearest neighbours regression method is a simple algorithm that stores all available states and predicts the numerical target based on distance similarity. KNN was first used as a nonparametric technique in statistical prediction and pattern recognition in the early 1970s.

Contrary to alternative supervised learning algorithms, KNN does not have a training stage. With KNN, principally the closest points to the new point are searched. K represents the number of the closest neighbours of the unknown point. We select the amount K of the algorithm (usually an odd number) to estimate the results.

The KNN algorithm is predicted by the majority vote of its neighbours. The closest neighbours are found with a distance function. Eq. (10), (11), and (12) contain distance functions that are frequently used for regression.

$$\text{Euclidean} \quad \sqrt{\sum_{i=1}^k (x_i - y_i)^2} \quad (10)$$

$$\text{Manhattan} \quad \sum_{i=1}^k |x_i - y_i| \quad (11)$$

$$\text{Minkowski} \quad \left[\sum_{i=1}^k (|x_i - y_i|^q) \right]^{1/q} \quad (12)$$

The three distance functions above can only be used in continuous variables. To choose the most suitable value for K, the data should first be examined. In general, a large K value is more sensitive as it reduces overall noise, although no guarantee is granted. Cross-validation is another way to retrospectively determine a good K value, using an independent dataset to validate the value.

In this part of the study, the number of neighbours was determined. Model.ME.3 was designed to estimate the ship's main engine power and Model.AE.3 to estimate the auxiliary engine power. The arguments used to estimate the outputs were not changed. To determine the number of neighbours, numbers between 1 and 10 were examined and determined according to the RMSE values. Fig. 5 shows the RMSE values of the neighbour numbers.

When Fig. 5 is examined, the minimum error value for Model.ME.3 is obtained when the number of neighbours is 1. On the other hand, for Model.AE.3, the neighbour number should be 4. The Euclidean distance was used for both models. After determining the number of neighbours, the RMSE, R² and MAE errors were calculated for the test and train sets. Table 6 contains these error values.

Tab. 6. Error values of the KNN model

	Train			Test		
	RMSE	R ²	MAE	RMSE	R ²	MAE
Model.ME.3	119.46	0.999	11.36	4245.57	0.856	1372.19
Model.AE.3	350.22	0.787	173.18	385.99	0.739	220.57

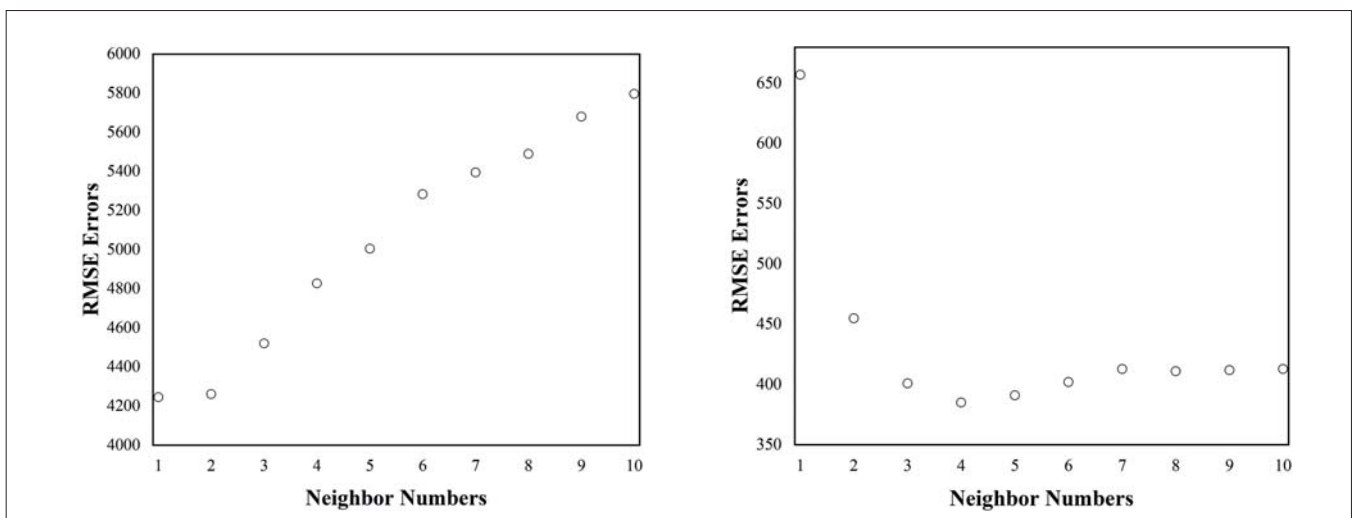


Fig. 5. RMSE values of neighbour numbers

GRADIENT BOOSTING MACHINE (GBM)

The gradient boosting machine (GBM) is a nonparametric regression technique that combines a regression tree with the gradient boosting algorithm. Unlike the regression method, which basically produces a single best model, the GBM model adaptively combines multiple classification and regression tree models using the gradient boosting technique to optimise performance. That is, unlike standard regression methods that produce a single predictive model, it fits many simple models and combines them in prediction, thereby increasing the predictive performance. In addition, it does not need any assumptions about the functional relationship between dependent and independent variables. GBM uses the gradient boost algorithm from Boost algorithms.

This method requires the most training time. Besides, a considerable amount of parameters need to be determined from the outset. Initially, Model.ME.4 was designed to estimate the ship's main engine power, and Model.AE.4 was created to estimate the power of the auxiliary engine. Interaction depth, n.trees, shrinkage and n.minobsinnode variables were determined by tuning. The interaction depth 1

through 7 in 2 increments, n.trees between 1000 and 10,000 with 1000 increments, the shrinkage value as 0.01 or 0.1, and the n.minobsinnode value between 10 and 20 were searched. The optimum values of n.trees = 0000, interaction depth = 7, shrinkage value = 0.01 and n.minobsinnode = 10 were obtained for Model.ME.4. The final values used for Model.AE.4 were n.trees = 2000, interaction depth = 7, shrinkage = 0.01 and n.minobsinnode = 11. Fig. 6 shows the effect of these variables on the RMSE for the main engine and Fig. 7 shows the effect of these variables on the RMSE for the auxiliary engine.

The error rates for the final models created after the tuning process are listed in Table 7.

Tab. 7. Error values of the GBM model

	Train			Test		
	RMSE	R ²	MAE	RMSE	R ²	MAE
Model.ME.4	1135.29	0.990	714.19	2562.01	0.947	1246.5
Model.AE.4	201.11	0.931	118.42	248.20	0.926	118.05

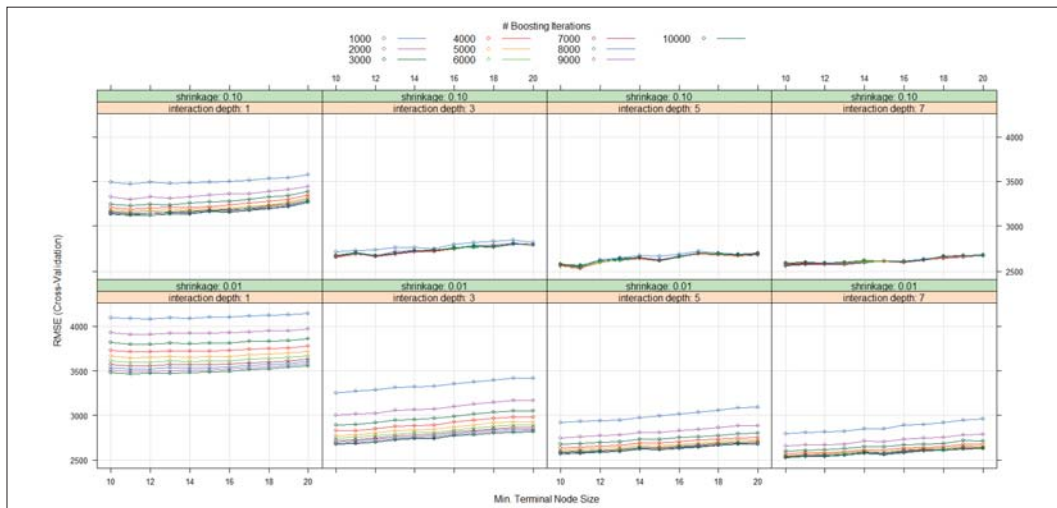


Fig. 6. Effects of variables on RMSE for ME

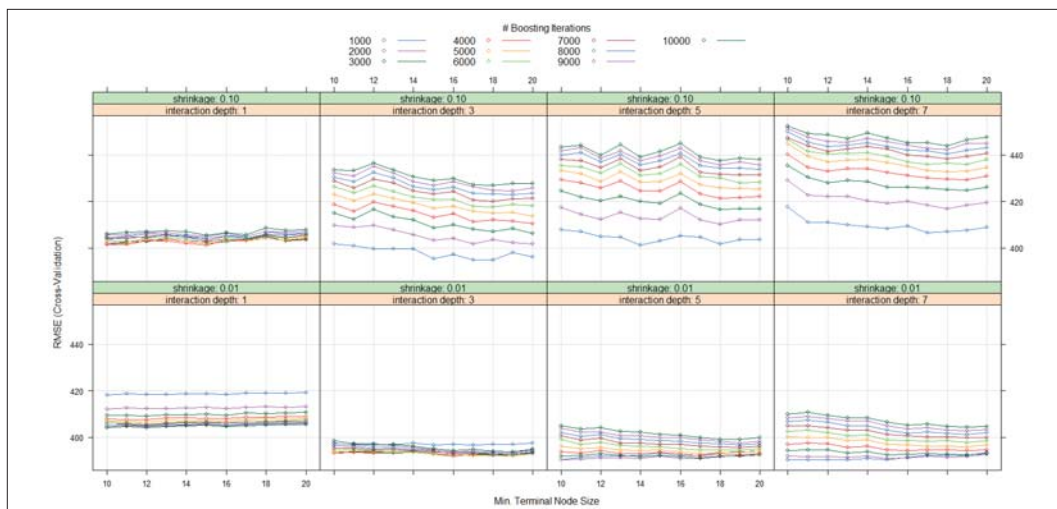


Fig. 7. Effects of variables on RMSE for AE

RESULTS AND DISCUSSION

Based on the length, gross tonnage, and age data from 4037 different ships, this study estimated the main and auxiliary engine power values. As a predictor, four different regression models, linear, polynomial, KNN and GBM, were studied. The models were trained on 80% of the data set and tested in 20%. The performance of the models was evaluated with ten-fold cross-validation and the RMSE, MAE and R^2 errors were calculated and interpreted.

In Fig. 8, a comparison chart of the coefficients of determination (R^2) of the regression algorithms is given. The fact that the coefficient of determination is close to 1 indicates that the success of the algorithm is high. As a result of the study, the best regression algorithm for main engine power prediction is the gradient boosting machine with an R^2 value of 0.947. Among the models created for estimating the auxiliary motor power, the best performing model was again the gradient boosting machine and its R^2 value is 0.926.

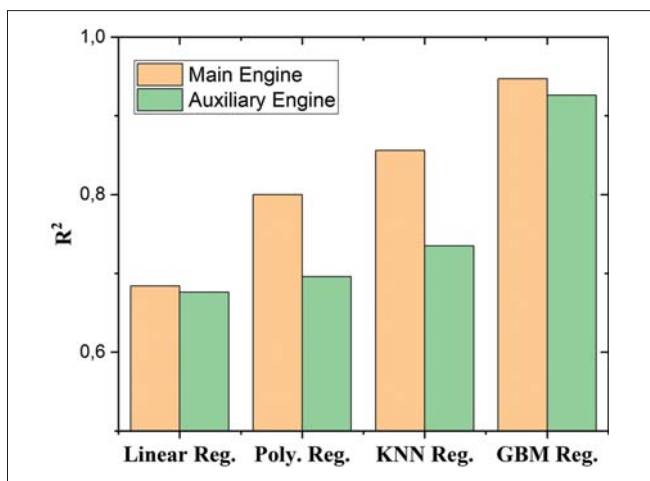


Fig. 8. Coefficients of determination of four models

In Fig. 9, the comparison chart of the mean absolute error (MAE) values of the regression algorithms is given. The fact that the mean absolute error value is close to 0 indicates that the success of the algorithm is high.

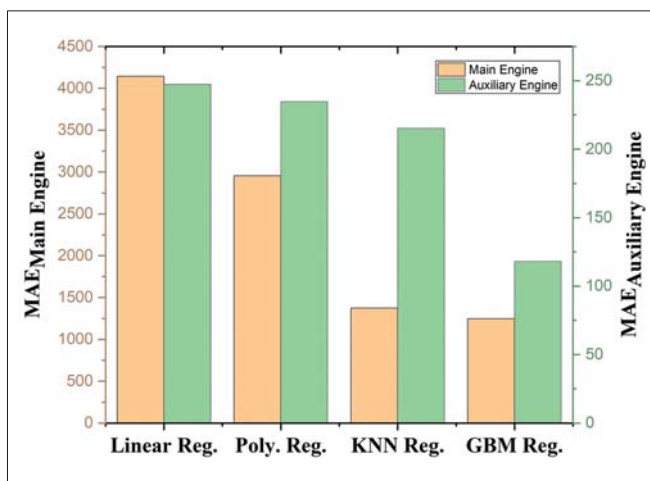


Fig. 9. Mean absolute error values of four models

The comparison graph of the root mean square error (RMSE) values of the regression algorithms is given in Fig. 10. Here too, it can be understood from the fact that the average square error value is close to 0 that the success of the algorithm is high.

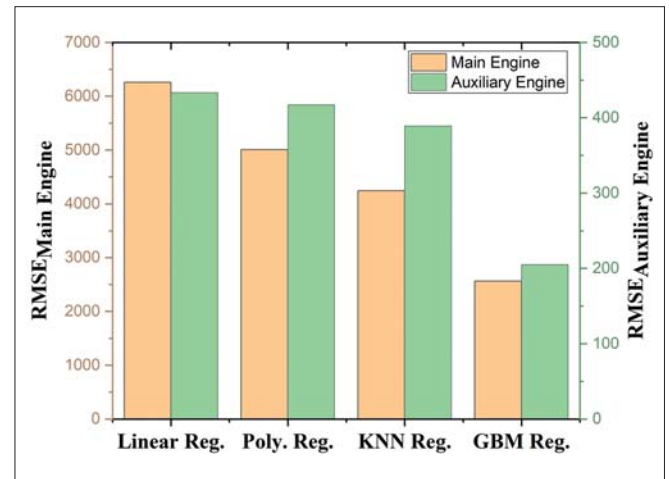


Fig. 10. Root mean squared error values of four models

The graphs showing the main and auxiliary engine power values estimated by the algorithms and the actual index values in the test data are given in Fig. 11.

Residual analysis plays an important role in verifying the regression model. The residues are the difference between the estimated value and the actual value. Graphs representing the deviation of the estimated value from the actual value are shown in Fig. 12.

Fig. 12 shows that the linear and polynomial regression algorithms with a high error rate now move away from the zero line. On the other hand, the low error rates of the GBM and KNN algorithms are somewhat closer to the zero line.

CONCLUSION

In this study, regression-based algorithms are used to estimate ships' main and auxiliary machine powers. Four different regression algorithms, linear, polynomial, KNN, and GBM, have been designed. Each method requires data pre-processing, data distribution determination, regression and performance evaluation steps, which are important stages of machine learning. K-cross-validation validity, a hyperparameter frequently used in the literature, was used to compare the performance results of the machine learning methods. For KNN regression, the optimum neighbour numbers were searched from one to ten. In addition, as GBM regression, for the interaction depth, n.trees, shrinkage and n.minobsinnode parameters tuning was performed for four, ten, two, and ten different parameters, respectively. In the study of 4037 ship samples, the algorithm that can best estimate the power of both machines compared to R^2 , RMSE and MAE was found to be the gradient boosting machine. Although this method provides good results, the number of parameters to be determined from the outset and the training

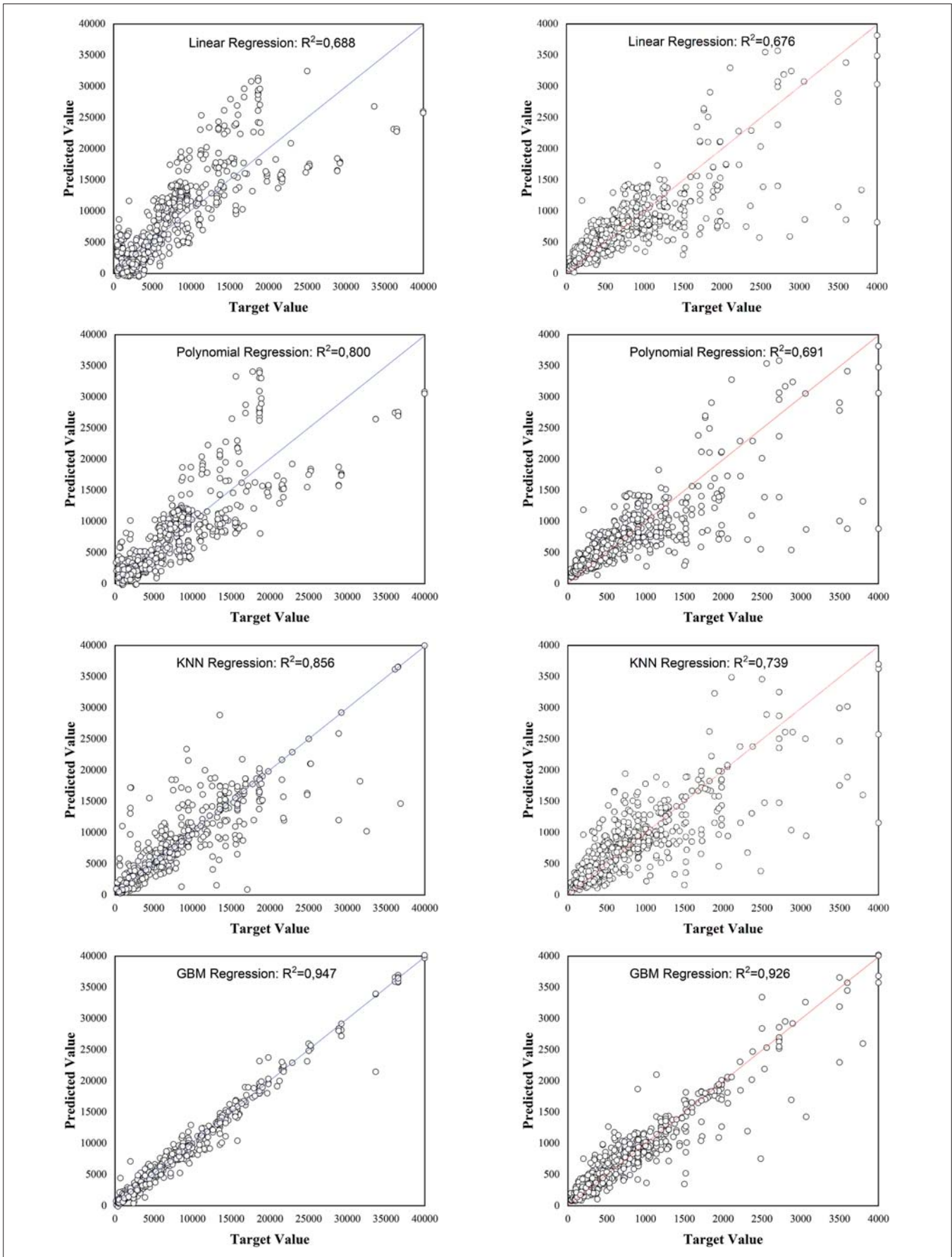


Fig. 11. Difference between target values and forecast values

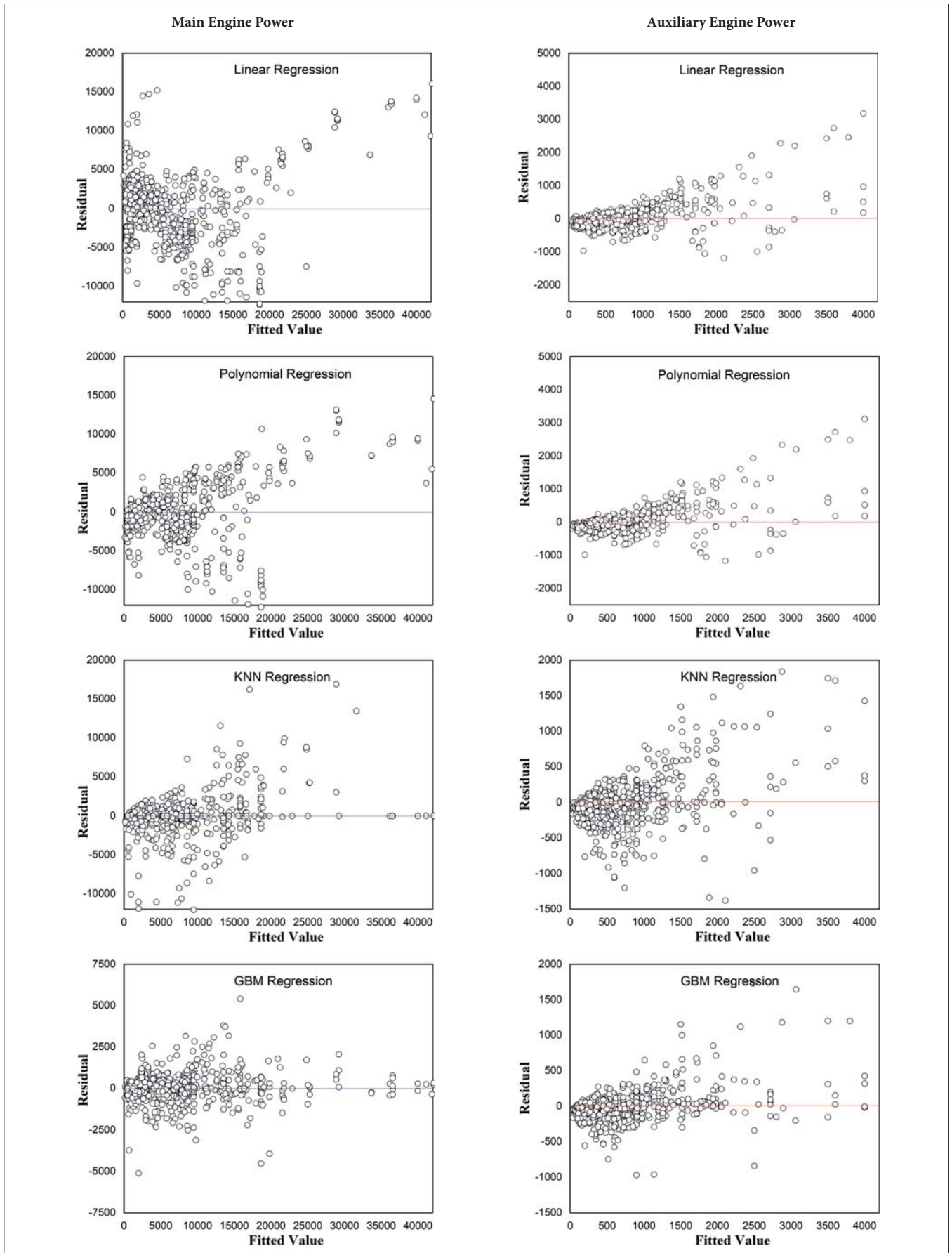


Fig. 12. Residuals

time proved to be more important as negative aspects of the method. However, the linear and polynomial regressions were not able to adapt to the data set. As a result, the GBM algorithm for estimating ships' main and auxiliary machine powers is quite suitable. It showed good results in estimating both the main power and the auxiliary machine power. The basis for this method's effectiveness is that the predictions are made in order, not independently.

REFERENCES

1. A. Ekmekçioğlu, K. Ünlügençoğlu, and U. B. Çelebi, 'Ship emission estimation for Izmir and Mersin international ports – Turkey', *Journal of Thermal Engineering*, vol. 5, no. 6, pp. 184–195, 2019, doi: 10.18186/thermal.654319.
2. C. Trozzi, 'Emission estimate methodology for maritime navigation', *Co-leader of the Combustion & Industry Expert Panel*, 2010.
3. R. Yan, S. Wang, and Y. Du, 'Development of a two-stage ship fuel consumption prediction and reduction model for a dry bulk ship', *Transportation Research Part E: Logistics and Transportation Review*, vol. 138, no. July 2019, p. 101930, 2020, doi: 10.1016/j.tre.2020.101930.
4. L. Huang, Y. Wen, Y. Zhang, C. Zhou, F. Zhang, and T. Yang, 'Dynamic calculation of ship exhaust emissions based on real-time AIS data', *Transportation Research Part D: Transport and Environment*, vol. 80, no. August 2019, p. 102277, 2020, doi: 10.1016/j.trd.2020.102277.
5. T. A. Tran, 'Effect of ship loading on marine diesel engine fuel consumption for bulk carriers based on the fuzzy clustering method', *Ocean Engineering*, vol. 207, no. January 2019, p. 107383, 2020, doi: 10.1016/j.oceaneng.2020.107383.
6. X. Yan, K. Wang, Y. Yuan, X. Jiang, and R. R. Negenborn, 'Energy-efficient shipping: An application of big data analysis for optimizing engine speed of inland ships considering multiple environmental factors', *Ocean Engineering*, vol. 169, no. August, pp. 457–468, 2018, doi: 10.1016/j.oceaneng.2018.08.050.
7. T. Cepowski, 'Regression formulas for the estimation of engine total power for tankers, container ships and bulk carriers on the basis of cargo capacity and design speed', *Polish Maritime Research*, vol. 26, no. 1, pp. 82–94, Mar. 2019, doi: 10.2478/pomr-2019-0010.
8. W. J. Requia, B. A. Coull, and P. Koutrakis, 'Evaluation of predictive capabilities of ordinary geostatistical interpolation, hybrid interpolation, and machine learning methods for estimating PM2.5 constituents over space', *Environmental Research*, vol. 175, no. April, pp. 421–433, 2019, doi: 10.1016/j.envres.2019.05.025.
9. T. Uyanık, Ç. Karatug, and Y. Arslanoğlu, 'Machine learning approach to ship fuel consumption: A case of container vessel', *Transportation Research Part D: Transport and Environment*, vol. 84, 2020, doi: 10.1016/j.trd.2020.102389.
10. L. Barua, B. Zou, and Y. Zhou, 'Machine learning for international freight transportation management: A comprehensive review', *Research in Transportation Business and Management*, no. July 2019, p. 100453, 2020, doi: 10.1016/j.rtbm.2020.100453.
11. Y. Peng, H. Liu, X. Li, J. Huang, and W. Wang, 'Machine learning method for energy consumption prediction of ships in port considering green ports', *Journal of Cleaner Production*, vol. 264, p. 121564, 2020, doi: 10.1016/j.jclepro.2020.121564.
12. J. H. Jeong, J. H. Woo, and J. G. Park, 'Machine learning methodology for management of shipbuilding master data', *International Journal of Naval Architecture and Ocean Engineering*, vol. 12, pp. 428–439, 2020, doi: 10.1016/j.ijnaoe.2020.03.005.
13. C. Gkerekos, I. Lazakis, and G. Theotokatos, 'Machine learning models for predicting ship main engine fuel oil consumption: A comparative study', *Ocean Engineering*, vol. 188, no. August, p. 106282, 2019, doi: 10.1016/j.oceaneng.2019.106282.
14. A. Jonquais and F. Krempf, 'Predicting Shipping Time with Machine Learning', 2019.
15. O. Bodunov, F. Schmidt, A. Martin, A. Brito, and C. Fetzter, 'Grand challenge: Real-time destination and ETA prediction for maritime traffic', *DEBS 2018 – Proceedings of the 12th ACM International Conference on Distributed and Event-Based Systems*, pp. 198–201, 2018, doi: 10.1145/3210284.3220502.
16. J. Yuan and V. Nian, 'Ship energy consumption prediction with Gaussian process metamodel', *Energy Procedia*, vol. 152, pp. 655–660, 2018, doi: 10.1016/j.egypro.2018.09.226.
17. Y. B. A. Farag and A. I. Ölçer, 'The development of a ship performance model in varying operating conditions based on ANN and regression techniques', *Ocean Engineering*, vol. 198, no. July 2019, 2020, doi: 10.1016/j.oceaneng.2020.106972.
18. L. Bui-Duy and N. Vu-Thi-Minh, 'Utilization of a deep learning-based fuel consumption model in choosing a liner shipping route for container ships in Asia', *Asian Journal of Shipping and Logistics*, 2020, doi: 10.1016/j.ajsl.2020.04.003.
19. H. Cui, O. Turan, and P. Sayer, 'Learning-based ship design optimization approach', *CAD Computer Aided Design*, vol. 44, no. 3, pp. 186–195, 2012, doi: 10.1016/j.cad.2011.06.011.

20. M. Peker, O. Özkaraca, and B. Kesimal, 'Modeling heating and cooling loads by regression-based machine learning techniques for energy-efficient building design', *International Journal of Informatics Technologies*, pp. 443–449, 2017, doi: 10.17671/gazibtd.310154.
21. V. Bertram and H. Schneekluth, *Ship Design for Efficiency and Economy*. Elsevier, 1998.

CONTACT WITH THE AUTHORS

Fatih Okumuş

e-mail: hfatihokumus@gmail.com

Yildiz Technical University
Besiktas, 34000 Istanbul
TURKEY

Araks Ekmekçioğlu

e-mail: araks@yildiz.edu.tr

Yildiz Technical University
Besiktas, 34000 Istanbul
TURKEY

Selin Soner Kara

e-mail: ssoner@yildiz.edu.tr

Yildiz Technical University
Besiktas, 34000 Istanbul
TURKEY

IMPROVEMENT OF THE CARGO FLEET VESSELS POWER PLANTS ECOLOGICAL INDEXES BY DEVELOPMENT OF THE EXHAUST GAS SYSTEMS

Valerii Kuznetsov*

Boris Dymo

Svitlana Kuznetsova

Mykola Bondarenko

Admiral Makarov National University of Shipbuilding, Ukraine

Andrii Voloshyn

State Research Design & Shipbuilding Centre, Ukraine

* Corresponding author: valeriy.kuznetsov@nuos.edu.ua (V. Kuznetsov)

ABSTRACT

Modernisation of the power plants of cargo fleet vessels to satisfy the requirements set out by the International Maritime Organisation is an urgent scientific and technical problem. The article presents the results of developing a solution to this problem that focuses on the exhaust gas system. We propose the use of ejection nozzles as part of this system. It was found that when the ejection coefficient in these nozzles is $n = 3$, it is possible to exclude the use of SCR reactors, thus reducing the operating costs of the marine power plant. Using a mathematical modelling method, the efficiency of operation of six types of nozzle as part of the exhaust gas system was investigated, and a constructive layout was proposed for the gas ducts and inlet louvres for supplying ambient air.

To increase the efficiency of the proposed system, we consider several options for intensifying heat transfer processes through the use of dimple systems in the nozzles and nozzles with swirling flow. We found that these technical solutions would make it possible to further increase the efficiency of the systems by up to 19% abs.

Keywords: marine power plant, emissions, gas-air cooler, nozzle, intensification

INTRODUCTION

The introduction of new requirements by the International Maritime Organisation (IMO) has given rise to a need to improve the existing cargo fleet to ensure the possibility of working under modern conditions.

The main focus of these new requirements is a significant reduction in the levels of harmful emissions of NO_x and SO_x (Fig. 1), since these constitute the highest proportion of the exhaust gases from diesel engines [1, 2].

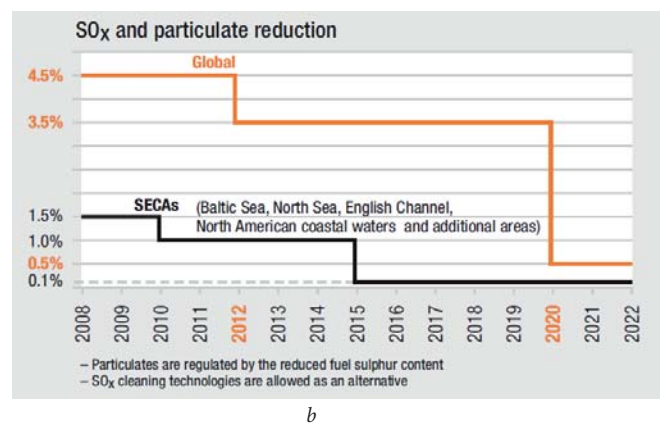


Fig. 1. Reduction of the levels of harmful emissions in accordance with the requirements of the IMO: a - NO_x emissions; b - SO_x emissions

The areas of operation of modern vessels are wide, and include special zones- (the South Sea, the Baltic Sea, the English Channel, etc.), meaning that it is necessary to implement appropriate measures to meet the requirements for emissions of harmful substances. A reduction in NO_x emissions can be achieved by reducing the level of sulphur in the fuel, for example by using light fuels. However, the presence of nitrogen in the fuel makes it necessary to reduce the level of NO_x in the exhaust gases. One option for solving this problem is to improve the exhaust gas systems of marine power plants, and the present work addresses this topic.

IDENTIFICATION OF THE INVESTIGATION OBJECT

Modern methods of reducing the emissions of harmful substances from vessels can be divided into active and passive approaches.

Active methods include those that directly affect the flow of gases, and require the installation of additional equipment in the engine room. These include thermochemical heat recovery systems, scrubber systems, SCR reactors, and the recirculation of exhaust gases from heat engines.

The thermochemical and thermoacoustic use of the heat of exhaust gases from marine power plants can be an effective way to reduce harmful emissions [3, 4, 5, 6]. However, these methods require the installation of a significant amount of equipment in the vessel's engine room.

One effective way of improving ecological indices is the use of water-fuel emulsions [7]; however, this method requires the use of a special fuel preparation system. To improve the ecological indices of marine power plants, Wartsila proposed a gas cleaning system (Fig. 2) [8]. To reduce the weight-size parameters of the system, a diffuser system with several inlets can be used (Fig. 3).

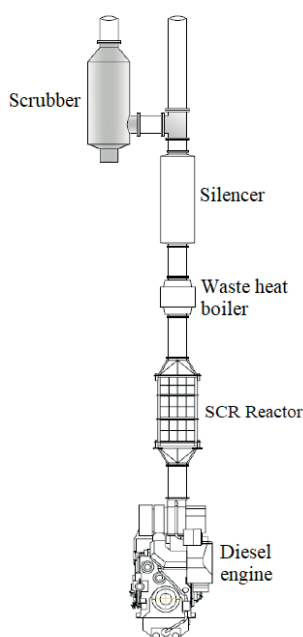


Fig.2 Direct-flow gas cleaning system



Fig.3. Diffuser system

These systems can operate on open or closed circuits, and can be installed both on newly built vessels and as part of the modernisation of existing marine power plants. One of the most significant elements of such systems are SCR reactors (Fig. 4) [9]. However, the efficiency of this approach does not exceed 95% [10], and it is therefore advisable to develop other ways of reducing the level of NO_x emissions that can help to improve the efficiency and reduce the weight-size parameters [11-14].

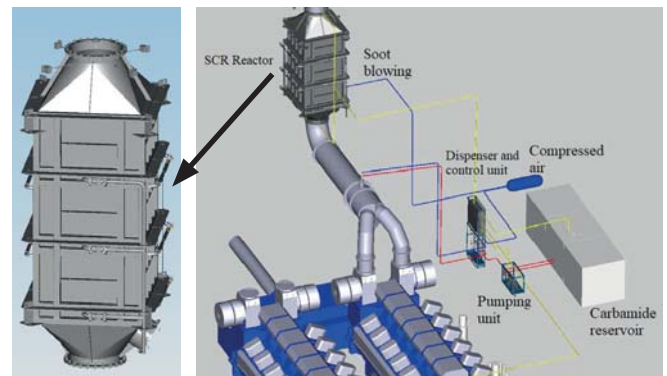


Fig.4 SCR reactor system

Alfa Laval has developed the *Pure SO_x Express* system to reduce the SO_x level, as shown in Fig. 5 [11].



Fig.5 The Pure SO_x Express system from Alfa Laval

This system allows vessels to continue to use heavy fuel oil while still meeting the Tier II and III requirements for SO_x emissions. However, the use of these scrubber systems necessitates the selection of scrubber elements, depending on the operating mode [15], and also causes problems in terms of the disposal of water from scrubber washing, especially when vessels are at sea [16].

An alternative method of absorbing SO_2 and NO from engine exhaust gases involves the use of $Na_2S_2O_8$ [17]. Reductions in early injection timing, exhaust gas recirculation, and water injection into the cylinder are other techniques that

have been considered for reducing the level of NO_x in the exhaust gases of diesel engines [10, 11]. A schematic diagram of a gas recirculation system is shown in Fig. 6.

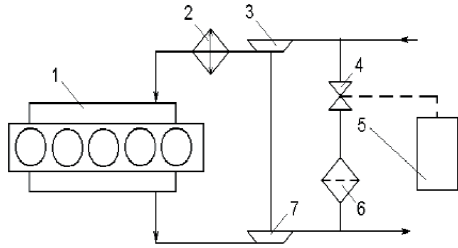


Fig. 6. Schematic diagram of a gas recirculation system: 1 – diesel engine; 2 – cooler; 3 – compressor; 4 – valve; 5 – control unit; 6 – filter; 7 – turbine

The degree of recirculation can be used as an indicator, as follows:

$$k_R = \frac{M_G}{M_G + M_A} \cdot 100\%$$

where M_G , M_A are the masses of bypass gas and air in the engine cylinder.

Gas recirculation slows down the combustion process, which leads to a decrease in the amount of NO_x emissions (Fig. 7).

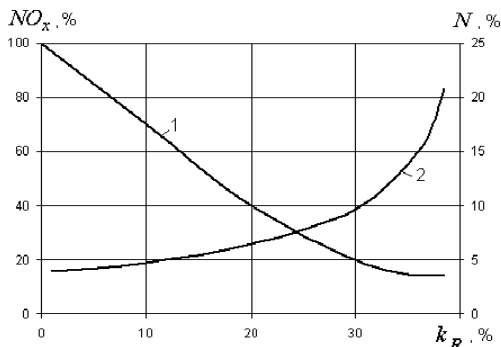


Fig. 7. Reductions in NO_x (1) and smoke (2) emissions versus the degree of recirculation [6]

Although recirculation can reduce the emissions of nitrogen oxides, the soot yield increases and the fuel efficiency of the engine decreases, and this is particularly evident at full loads. For this reason, this approach is economically justified only at partial engine operating modes and at recirculation rates of 12–20% [10, 11, 12].

When methods are used to reduce the levels of harmful emissions in the exhaust gases of marine power plants, a significant amount of space is required in the engine room to accommodate the necessary equipment and containers. These methods do not provide complete cleaning of exhaust gases from harmful emissions, and are expensive to operate. The choice of method also depends on the type and mode of operation of the vessel [13], which can significantly limit their application.

One way to solve this problem is to develop additional, passive ways of reducing the level of harmful emissions by

upgrading the gas exhaust system. These methods can be used with or without the above active techniques.

EXPERIMENTAL METHOD

The processes of movement of exhaust gases in power plants systems were investigated using a mathematical modelling method. The motion processes and heat transfer were mathematically modelled by finding numerical solutions to the following equations [18]:

Continuity:

$$\frac{\partial \rho}{\partial t} + \nabla(\rho \vec{V}) = 0 \quad (1)$$

where ρ is the mass flow density, and \vec{V} is the vector of the local fluid velocity;

Momentum:

$$\frac{\partial(\rho \vec{V})}{\partial t} + \nabla(\rho \vec{V} \vec{V}) = \nabla p + \nabla \tau + \rho \vec{g} + \vec{F} \quad (2)$$

where p is the static pressure, $\rho \vec{g}$ is the gravitational force per unit mass, \vec{F} are the external forces acting on the flow and τ is the pressure tensor;

Energy conservation:

$$\frac{\partial(\rho E)}{\partial t} + \nabla(\vec{V}(\rho E + p)) = \nabla(-\vec{J}_q + (\tau_{eff} \vec{V})) \quad (3)$$

where \vec{J}_q is the heat flow density, $E = h - \frac{p}{\rho} + \frac{V^2}{2}$ is the total

energy of the working fluid, h is the working fluid enthalpy, and the expression $\tau_{eff} \vec{V}$ represents viscous heating.

The system of equations presented above is not closed; it can be closed by adding semi-empirical equations for the pressure tensor, the heat flux, the equation of state for ideal gases, and the differential equations of the turbulence model.

Newton's law: By neglecting the bulk viscosity, the stress tensor can be represented as

$$\tau = \mu \left[\nabla \vec{V} + (\nabla \vec{V})^T - \frac{2}{3} \nabla(\vec{V} I) \right] \quad (4)$$

where μ is the coefficient of molecular viscosity, and I is the unit vector.

Fourier's law: The heat flow is determined by the expression

$$\vec{J}_q = -\lambda_{eff} \nabla T \quad (5)$$

where $\lambda_{eff} = \lambda + \lambda_t$ is the coefficient of effective conductivity.

Mendeleev-Clapeyron's law: The basic law of an ideal gas, which establishes a relationship between the main thermodynamic parameters, takes the form

$$p = R \cdot \rho \cdot T \quad (6)$$

where R is the individual gas constant for the working fluid.

On the basis of the recommendations given in [19, 20], the RSM turbulence model was used to close the system of equations (1)–(6). To solve the resulting system, the RANS approach was implemented using the *Code Saturne* software package with a free license [21] and the *SimScale* cloud service [22].

The mathematical model was verified by comparing the results of numerical modelling with experimental data from a full-scale bench test of a model of a ship's gas-air cooler. The discrepancy between the results did not exceed 5% [23].

EVALUATION OF EFFICIENCY OF USING A GAS-AIR COOLER TO IMPROVE THE ECOLOGICAL INDEXES OF POWER PLANTS

Passive methods of reducing the level of harmful substances in emissions are those that can perform their functions both with and without active methods, do not require the installation of significant additional equipment and are integrated into the existing structures of vessels without the need for significant re-design.

An example of such a system is the use of ship ejection air coolers (Fig. 8) [23, 24]. In this approach, the energy of the exhaust gases is used to operate the air cooler. The exhaust gas flow (ejection flow) is actively mixed with the external environmental flow (ejected flow), thus reducing the temperature of the gas-air flow.

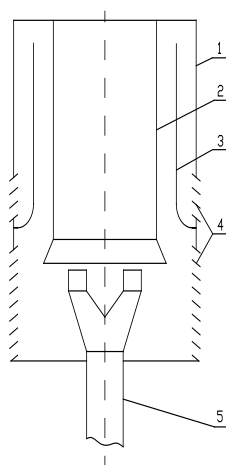


Fig. 8 Exhaust gas system with an ejection-type air cooler: 1 – casing; 2 – mixer; 3 – mixer screen; 4 – air inlet louvers; 5 – gas duct with a nozzle.

A reduction in the temperature of the exhaust gases is achieved by intensifying the process of mixing them with the ambient air, shielding a part of the exhaust gases flow and heated pipe elements with surfaces that are cooled. The disadvantages of this constructive solution include the need for a significant amount of cooling of atmospheric air to ensure the required degree of cooling of the exhaust gases, meaning that it is necessary to provide air intake louvres with a large area on the outer walls of the chimney casing. This should not pose a problem, since inlet and exit louvres for natural ventilation of the casing are installed on cargo vessels (Figs. 9 and 10).

Through the modernisation of the internal elements of the casing, ejection nozzles can be installed at the lower level of the inlet louvres, inlet louvres can be provided around the entire perimeter of the casing and a mixing chamber can be installed (Fig. 11).

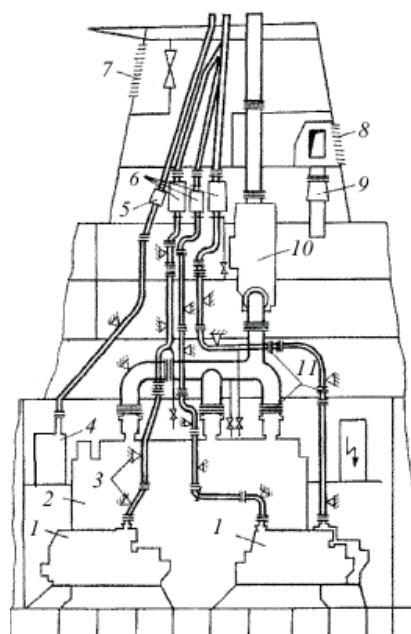


Fig. 9 Diesel plant exhaust gas system: 1 – diesel-driven alternator; 2 – main engine; 3 – support; 4 – auxiliary boiler; 5 – steam spark arrester; 6 – spark arrester-silencer; 7, 8 – inlet and outlet louvers, respectively, for natural ventilation of the chimney casing; 9 – blower fan; 10 – waste heat boiler; 11 – compensators



Fig. 10. Superstructure of a tanker with a deadweight of 45,564 t with inlet louvres

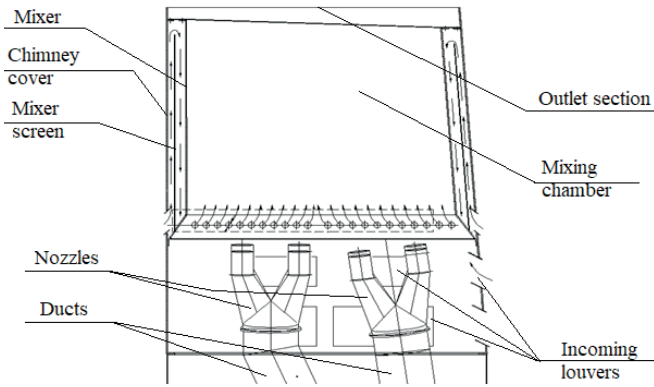


Fig.11 Structural scheme of gas ducts and incoming louvers for supplying environmental air in a gas-air cooler

The concentration of harmful emissions can be represented by a parameter that is inversely proportional to the value of the ejection coefficient n :

$$C \text{ (kg emissions / kg gas mixture)} = C_0 / (1+n) \quad (7)$$

The ejection coefficient is calculated as set out in [24]:

$$n = 1,03 \frac{1 - \hat{\delta}}{\hat{\delta} - \Theta} \quad (8)$$

where 1.03 is an empirical coefficient; $\hat{\delta} = \frac{T_3}{T_1}$, T_1, T_3 are the temperatures at the inlet and outlet of the air cooler, respectively, in degrees K; and $\Theta = \frac{T_2}{T_1}$, T_2 is the environment temperature, in degrees K.

The drag coefficient of the nozzle is calculated as follows [24]:

$$\zeta = \frac{\Delta p}{\rho w^2 / 2} \quad (9)$$

where Δp is the pressure loss in the nozzle, in Pa; ρ is the flow density, in kg/m³; and w is the flow velocity, in m/s.

The baseline emission level is $C_{NO_x} = 14$ g/(kWh), which meets the Tier II requirements of the IMO (Fig. 1a). Changes in the emission level in the range $n = 1$ to 3 are shown in Fig. 12.

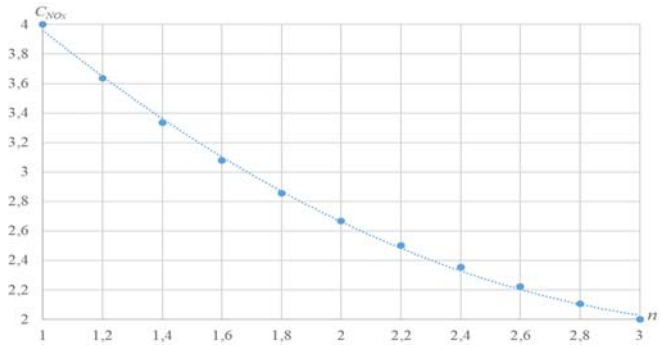


Fig. 12 Changes in the level of harmful emissions

An analysis of this graph shows that when the ejection coefficient in the nozzles is $n=3$, it is possible to meet the Tier III requirements for NO_x emissions without using SCR reactors. However, this is an ideal case, and depends on the composition and operating mode of the power plant; if this scheme cannot fully replace SCR reactors, it may be able to partially replace them.

Various types of nozzles can be used for the practical implementation of ejection cooling. The types of nozzles that can be used in air coolers are shown in Fig. 13 [24].

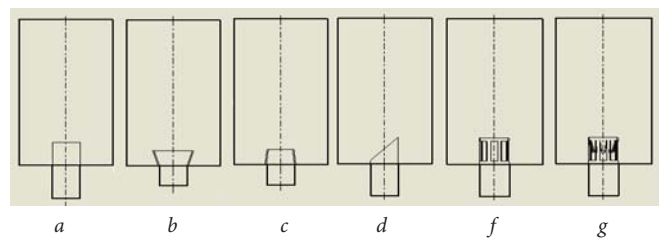


Fig.13 Structures of ejection nozzles: a - cylindrical; b - diffuser; c - confuser; d - oblique cut; f - with longitudinal perforation; g - with perforations and petals

Calculation results for each type of nozzle are shown in Table 1.

Tab. 1. Characteristics of the ejection nozzles investigated here

Type of ejection nozzle	Ejection coefficient	Drag coefficient
Cylindrical	1.15	0.01
Diffuser	1.05	0.11
Confuser	1.35	0.12
Oblique cut	2.90	0.57
With longitudinal perforation	2.40	1.30
With perforations and petals	2.27	0.80

The results in Table 1 show that the optimum statistics (the highest ejection coefficient and the lowest drag coefficient) were obtained for the nozzle with an oblique cut, meaning that the use of this tip will give the best results. However, the final choice of nozzle type will be made at the design stage of the system.

According to equation (8), an increase in the value of the ejection coefficient is possible due to a decrease in the temperature behind the nozzle. One option for implementing this condition involves the intensification of heat transfer processes in the air cooler. There are two possible methods of achieving this: the use of dimple systems, and the use of nozzles with swirling flow. A feature of dimple systems is that the increase in the heat transfer outstrips the increase in the resistance, which is important in gas release systems for vessel engines. The second method can provide better heat transfer, due to better mixing of the streams.

Fig. 14 shows a variant of the diffuser nozzle with dimples located in an area of constant diameter. We investigated options for the locations of holes in areas with constant and variable cross-sections, for diffuser, confuser and oblique cut nozzles. The parameters and the location of the dimples were set based on the recommendations given in [25].

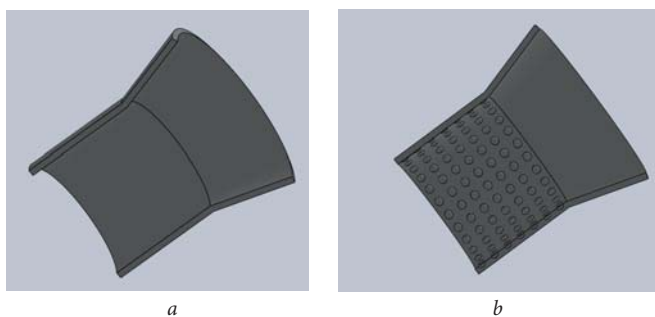


Fig. 14 Arrangement of dimples on a diffuser nozzle: a – basic version; b – variant with dimples

Figure 15 shows a nozzle with swirling flow. The packing parameters (twist angle, cut diameter) were estimated based on the recommendations set out in [26].

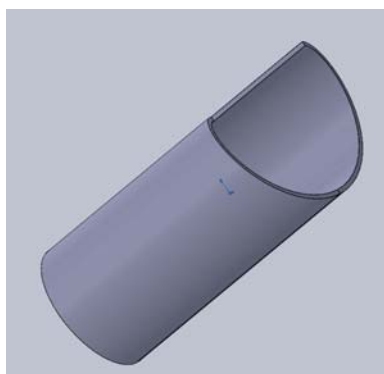


Fig. 15 Nozzle with swirling flow

Calculations were carried out for gas inlet temperatures of 300–450°C and Reynolds numbers of 6,000–20,000. The results showed that an intensification of the heat transfer processes reduces the gas temperature behind the cooler to 17% abs. when the dimple systems are used, and for swirling flow in smooth channels, this rises to 19% abs. According to equation (8), this will lead to a similar increase in the ejection coefficient and the entire ejection cooling system. However,

this is the maximum value that can be expected, and depends on the composition and operating mode of the power plant.

DISCUSSION OF RESULTS

The modernisation of marine power plants that are currently in operation to comply with the Tier III requirements of the IMO is an urgent scientific and technical problem. The results obtained here show that the cost of modernisation can be reduced by developing exhaust gas systems. This will ensure compliance with NO_x emission regulations.

The proposed design can be used either as a backup for SCR reactors or as an independent system that can significantly reduce the cost of operating a marine power plant. Intensification of heat transfer in the elements of the system can further increase its efficiency by up to 19% abs.

Further research will focus on optimising the size and locations of the dimples in the attachments, and the design characteristics of the nozzle with swirling flow, to achieve the maximum efficiency of gas exhaust devices depending on the operating mode of the power plant.

CONCLUSIONS

In this study, we propose the use of ejection cooling devices as part of an exhaust gas system to improve the ecological indices of marine power plants. The use of these devices will reduce the level of NO_x emissions in exhaust gases and the cost of operating marine SCR reactors in exhaust gas systems. It is shown here that implementation of the proposed solution will not lead to significant economic cost as part of the modernisation of an exhaust gas system.

The efficiency of various types of ejection nozzles as components of air coolers was investigated, and the results showed that it is possible to achieve compliance with Tier III IMO standards on NO_x emissions without using SCR reactors, although this depends on the power of the engines and the operating modes of the power plant.

The possibility of intensifying the heat transfer processes in the ejection nozzles is considered in terms of further improvement in ejection coolers. The use of dimple systems and flow swirling in nozzles was found to be effective. The intensification of heat transfer processes in the nozzles made it possible to increase the effects of the system by up to 19% abs.

REFERENCES

1. MARPOL 73/78 Dodatok VI (take a look) before the Convention “Rules for the protection of shipwrecking”. Retrieved from <http://docs.cntd.ua/document/499014496>.
2. Z. Yang, Q. Tan, and P. Geng, “Combustion and emissions investigation on low-speed two-stroke marine diesel engine with low sulfur diesel fuel,” *Polish Maritime Research*,

- vol. 1, no. 101, pp. 153–161, 2019. Retrieved from: <https://doi.org/10.2478/pomr-2019-0017>.
3. O. Cherednichenko and V. Mitienkova, “Analysis of the impact of thermochemical recuperation of waste heat on the energy efficiency of gas carriers,” *Journal of Marine Science and Application*, 2020. Retrieved from <https://doi.org/10.1007/s11804-020-00127-5>.
 4. O. Cherednichenko, S. Serbin, and M. Dzida, “Application of thermo-chemical technologies for conversion of associated gas in diesel-gas turbine installations for oil and gas floating units,” *Polish Maritime Research*, vol. 26, no. 3, pp. 181–187, 2019. Retrieved from <https://doi.org/10.2478/pomr-2019-0059>.
 5. Y. Kondratenko, V. Korobko, O. Korobko, G. Kondratenko, and O. Kozlov, “Green-IT approach to design and optimization of thermoacoustic waste heat utilization plant based on soft computing,” *Studies in Systems, Decision and Control*, 287–311, 2017. Retrieved from http://doi.org/doi:10.1007/978-3-319-55595-9_14.
 6. Y. Kondratenko, S. Serbin, V. Korobko, and O. Korobko, “Optimisation of bi-directional pulse turbine for waste heat utilization plant based on green IT paradigm” *Studies in Systems, Decision and Control*, pp. 469–485, 2018. http://doi.org/doi:10.1007/978-3-030-00253-4_20.
 7. V. Kornienko, R. Radchenko, A. Stachel, A. Andreev, and M. Pyrynsunko, “Correlations for pollution on condensing surfaces of exhaust gas boilers with water-fuel emulsion combustion,” *Advanced Manufacturing Processes. InterPartner-2019. Lecture Notes in Mechanical Engineering*, Springer, Cham, pp. 530–539, 2020. Retrieved from http://doi:10.1007/978-3-030-40724-7_54.
 8. Product manual scrubber (scrubber) (2013). Wartsila, 98 p. Retrieved from https://cdn.wartsila.com/docs/default-source/local-files/russia/products/project-guides/wärtsilä-scrubber-product-guide-rev-c_rus.pdf?sfvrsn=73676f44_2.
 9. Unit for reducing NOx emissions by technology SCR by WÄRTSILÄ. Retrieved from https://cdn.wartsila.com/docs/default-source/local-files/russia/products/nox_reducers-rus.pdf?sfvrsn=f1696f44_2.
 10. O.V. Serazhutdinov and V.A. Chistyakov, “Technologies for the reduction of nitrogen oxides in the exhaust gases of marine diesel engines” *Marine Intelligent Technology*, №4-1(30), pp. 23–28, 2015.
 11. V.V. Le and T.H. Truong, “A simulation study to assess the economic, energy and emissions characteristics of a marine engine equipped with exhaust gas recirculation,” *1st International Conference on Sustainable Manufacturing, Materials and Technologies*, 2020. Retrieved from <http://doi.org/doi:10.1063/5.0000135>.
 12. R. Radchenko, M. Pyrynsunko, V. Kornienko, R. Patyk, and O. Moskovko, “Improving the ecological and energy efficiency of internal combustion engines by ejector chiller using recirculation gas heat,” *ICTM 2020, Advances in Intelligent Systems and Computing*, Springer, Cham, 10 p., 2020.
 13. Y. Zhao, Y. Fan, K. Fagerholt, and J. Zhou, “Reducing sulfur and nitrogen emissions in shipping economically” *Transportation Research Part D, Transport and Environment*, vol. 90, 2021. Retrieved from <https://doi.org/10.1016/j.trd.2020.102641>.
 14. New system *PureSOx Express*. Retrieved from <https://www.alfalaval.ua/media/news/2020/new-alfa-laval-puresox-express-offers-easy-access-to-sox-scrubber-advantages/>.
 15. Y.-S. Choi, and T.-W. Lim, “Numerical simulation and validation in scrubber wash water discharge from ships,” *Journal of Marine Science and Engineering*, vol. 8, no. 4, p. 272, 2020. Retrieved from <http://doi.org/doi:10.3390/jmse8040272>.
 16. S. Endres et al., “A new perspective at the ship-air-sea-interface: The environmental impacts of exhaust gas scrubber discharge,” *Frontiers in Marine Science*, vol. 5, 2018. Retrieved from <http://doi.org/doi:10.3389/fmars.2018.00139>.
 17. H. Xi, S. Zhou, and Z. Zhang, “A novel method using $\text{Na}_2\text{S}_2\text{O}_8$ as an oxidant to simultaneously absorb SO_2 and NO from marine diesel engine exhaust gases,” *Energy & Fuels*, 2020. Retrieved from <http://doi.org/doi:10.1021/acs.energyfuels.9b03334>.
 18. Y.A. Bystrov, S.A. Isayev, N.A. Kudryavtsev, and A. I. Leont'yev, *Numerical Simulation of Heat Transfer Vortex Intensification in the Pipe Packs*. St. Petersburg: Shipbuilding, 2005.
 19. T.B. Gatski, M.Y. Hussaini, and J.L. Lumley, *Simulation and Modelling of Turbulent Flows*. Oxford, New York: Oxford University Press, 314 p., 1996. Retrieved from https://www.academia.edu/10100418/SIMULATION_AND_MODELLING_OF_TURBULENT_FLOWS (last accessed: 20.01.2021).
 20. S. Sarkar and L. Balakrishnan, *Application of a Reynolds-Stress Turbulence Model to the Compressible Shear Layer*, 1990. Retrieved from <https://apps.dtic.mil/dtic/tr/fulltext/u2/a227097.pdf> (last accessed: 20.01.2021).
 21. Introducing code_Saturne. Retrieved from <https://www.code-saturne.org/cms/>.

22. Computational Fluid Dynamics: CFD Software. Retrieved from <https://www.simscale.com/product/cfd/>.
23. B.V. Dymo, A.Y. Voloshyn, A.E. Yepifanov, and V.V. Kuznetsov, "Increase of ship power plants gas-air cooler efficiency," *Problemele Energeticii Regionale*, vol. 2, no. 34, pp. 113–124, 2017.
24. B.V. Dymo, A.Y. Voloshyn, and V.I. Kharchenko, "The research of gas-dynamic processes in the gas-air cooler of the ship power plant," *Zbirnyk Naukovykh Prats' NUK*, vol. 6, pp. 81–89, 2010.
25. A.A. Khalatov, *Heat Transfer and Fluid Mechanics over Surface Indentations (Dimples)*. Kiev: National Academy of Sciences of Ukraine, Institute of Engineering Thermophysics, 64 p., 2005.
26. V.V. Kuznetsov, "Generalization of the rules in the heat transfer of swirling flows inside the tubular channels of power plants heat transfer devices," *Collection of Scientific Papers of Admiral Makarov National University of Shipbuilding* vol. 5, pp. 46–52, 2015.

CONTACT WITH THE AUTHORS

Valerii Kuznetsov

e-mail: valeriy.kuznetsov@nuos.edu.ua
Admiral Makarov National University of Shipbuilding,
Heroyiv Ukraine av. 9, 54025 Mykolaiv,
UKRAINE

Boris Dymo

e-mail: dymobv@gmail.com
Admiral Makarov National University of Shipbuilding,
Heroyiv Ukraine av. 9, 54025 Mykolaiv,
UKRAINE

Svitlana Kuznetsova

e-mail: svitlana.kuznetsova@nuos.edu.ua
Admiral Makarov National University of Shipbuilding,
Heroyiv Ukraine av. 9, 54025 Mykolaiv,
UKRAINE

Mykola Bondarenko

e-mail: bondarenko.nikola2308@gmail.com
Admiral Makarov National University of Shipbuilding,
Heroyiv Ukraine av. 9, 54025 Mykolaiv,
UKRAINE

Andrii Voloshyn

e-mail: voloshinandrey2011@gmail.com
State Research Design & Shipbuilding Centre, Heroyiv
Ukraine av. 1E, 54025 Mykolaiv,
UKRAINE

A COMPARATIVE LIFE CYCLE ASSESSMENT OF MARINE DESOX SYSTEMS

Mengqi Cui¹

Yingwei Lu²

Jiahao He¹

Lei Ji¹

Hui Wang¹

Shaojun Liu^{*}

¹ Jiangsu university of science and technology, China

² Zhejiang University, China

* Corresponding author: phoenix205@zju.edu.cn (S. Liu)

ABSTRACT

With new sulphur oxides emission limits carried out in 2020, multiple desulphurisation methods have been proposed. The main desulphurisation scrubber systems were chosen and investigated using life cycle assessment. The whole system life is divided into the construction and operational phases. Three different systems classified by desulphurisers, namely, seawater, NaOH, and Mg-based systems, were modelled in GaBi software. Moreover, environmental, economic and energy aspects (3E model) were introduced for further analysis. Through this study, some conclusions have been drawn. As for the environmental aspect, the seawater system has the most pleasing performance since the primary emissions come from 1.24E+03 kg CO₂ and 1.48E+01 kg chloride. The NaOH system causes 1000 times more emissions than the seawater. The Mg-based system has less pollution than the NaOH system, with 5.86E+06kg CO₂ and 3.86E+03 kg chloride. The economic aspect is divided into capital expenditure (CapEx) and operational expenditure (OpEx) to estimate disbursement. The seawater system also has the most favourable cost appearance, which takes 1.7 million dollars without extra desulphuriser expenses, based on 10MW engine flue gas treatment. The next is the Mg-based system, which cost 2 million dollars in CapEx and \$ 1200/year in OpEx for the desulphuriser. NaOH uses about 2.5 million dollars for construction and \$ 30000/year in desulphuriser. As for the energy aspect, the seawater and Mg-based systems use less non-renewable energy than the NaOH system in the construction phase. In conclusion, the seawater system shows the best performance and could be an alternative in SO_x control technologies. This study sheds light on the comprehensive evaluation of marine environmental protection technologies for further optimisation.

Keywords: life cycle assessment, desulphurization, 3E model

INTRODUCTION

With the convenience of shipping transportation, an excess of vessels has caused terrible sulphur dioxide pollution with a negative effect on the ocean environment and human health. 2020 is a watershed in the controlling of marine SO₂ emissions since unprecedentedly strict regulations have taken effect. The International Maritime Organisation (IMO) stipulated that the sulphur content in fuel oil should be less than 0.5% m/m globally, starting from January 1st, 2020 [1], while in emission control areas (ECA), such as the Baltic Sea, below 0.1% m/m was adopted in 2015 [2].

In order to comply with the above standards, multiple SO₂ emission reduction methods have emerged in commercial applications. One is using low sulphur oil, but it has a higher cost with additional CO₂ emissions [3]. Another alternative is liquefied natural gas (LNG). Although LNG combustion emission is cleaner than that of fuel oils mentioned above, the structure of the ship has to be extensively modified, which increases the expenditure of design and implementation [4]. More importantly, the easily flammable property of LNG poses a threat on the operation of marine power plants [5]. Last but not least, exhaust gas cleaning systems (EGCS) have been employed which reduce SO₂ concentrations to

the level equivalent to the combustion of low sulphur oil, via wet scrubbing or dry adsorption. Extensive research has been conducted on EGCS, including design, manufacture, installation, and global service. However, seldom does the research focus on the whole process of EGCS operation, that is, the deSO_x process, which includes capital expenditure (CapEx) and operational expenditure (OpEx). Moreover, besides economic concerns, environment and energy impact should also be taken into account to appropriately evaluate the deSO_x expenditure. Under this framework, different patterns of EGCS could be literally compared and the correct strategy for SO₂ emission control could be made accordingly.

In order to progress this purpose, life cycle assessment (LCA) was introduced into our research. As a tool to synthetically evaluate the process from cradle to grave, LCA has been published in many studies. As early as 1969, Midwest Research Institute (MRI) firstly quantified the resource, the emissions, and the waste by using LCA, helping factories to make decisions [6]. It became the foundation of LCA development. In recent years, LCA has gradually received more attention and is utilised in many fields. Zheng et al. used LCA to evaluate bicycle sharing based on a survey. The results showed that it was friendly to the environment except for metal consumption. However, in the sensitive analysis, the growth of rental fees and quantity of bicycles caused negative impacts [7]. Tomporowski et al. conducted comparison analysis for blade life cycle in land-based and offshore wind power plants, and they arrived at conclusions that land-based blades caused more harmful effects to water, while the offshore blade produced a more negative influence on the atmospheric environment [8]. In the environmental protection field, Wu et al. compared several gaseous pollutant control methods, including limestone-gypsum wet flue-gas desulphurisation (WFGD), selective catalytic reduction (SCR), and electrostatic precipitators (ESP) [9]. Effects such as global warming, acidification, nutrient enrichment, photochemical ozone formation, soot and ashes were taken into consideration. It was found that SCR consumed more energy while more water was used in the WFGD process, and the ESP process possessed excellent performance in environmental and economic aspects. Lopes et al. discussed the environmental performance of the whole wastewater treatment process installed in Bahia State, Brazil and the results showed that the environmental impact in construction also had considerable significance [10]. In the marine field, a comparative study of marine power systems employing LCA was performed [11]. The results showed that a new-build system had a mitigation potential, while a retrofitted one was environmentally benign, due to incorporated emerging technologies. Hwang et al. estimated the environmental impact of ships using MGO, natural gas, and hydrogen. The results showed that the emissions from natural gas in the Well-to-Tank phase were lower than MGO and hydrogen but created more CO₂ than MGO in the Tank -to-Wake phase [12].

The aforementioned studies resorting to LCA tools have comprehensive analysis, but fewer papers concentrate on the whole life of a scrubber including construction and operation.

Based on the above experience, our study will compare different marine deSO_x systems by means of LCA from the environmental, economic, and energy aspects (3E model).

METHODOLOGY

According to the ISO 14040 issued by International Standard Organisation (ISO), four steps are involved in LCA. First, the goal and scope of the study should be defined [13]; then real data are collected to perform inventory analysis and produce an impact assessment [14]; and the last step is interpretation [15]. It has close-knit relationship between the four steps, as shown in Fig.1.

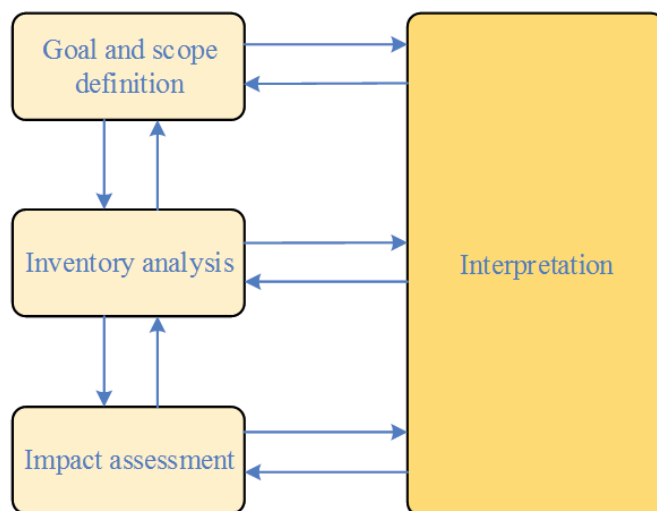


Fig.1. LCA framework

GOAL AND SCOPE DEFINITION

The goal of our study is to compare three deSO_x scrubber systems based on LCA and to come up with measures to optimise the system in terms of the results. Before we start to analyse, we need to determine the scope of the system.

For the three systems, we used a 10MW diesel engine as the function unit, from which flue gas emissions could be treated by various systems. In this respect, the performance could be equally assessed and compared. It is assumed that each deSO_x system works for 20 years and operates 7000 hours each year [16]. The system boundaries are composed of the input and output flows [17]. The input flows consist of energy and resources, while emissions such as solid waste, wastewater and air pollutants are output flows, which are described in Fig.2.

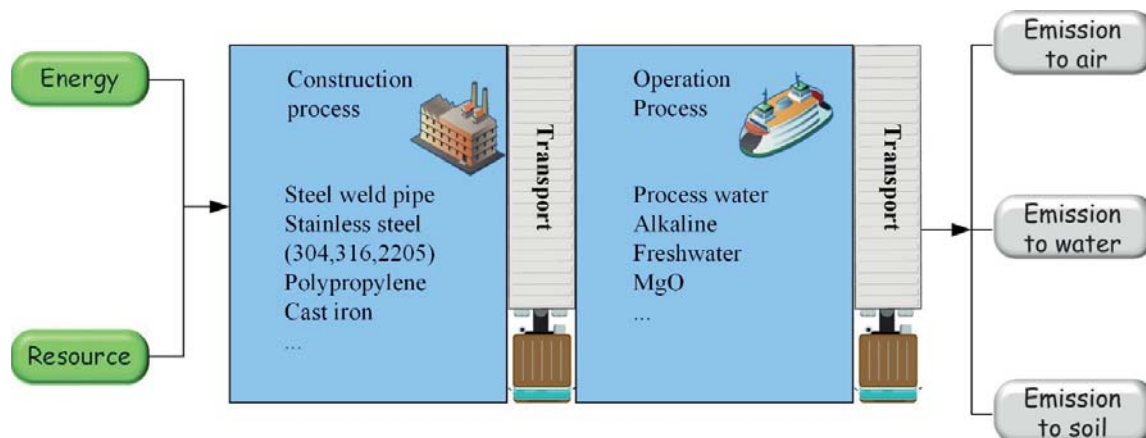


Fig. 2. System boundaries for deSO_x process

INVENTORY ANALYSIS

As shown in Fig.1, inventory analysis takes an important role in the whole LCA process, since it is the basis of the interpretation, and needs to set up models for systems. This part also needs to ensure the quality and precision of the practical data, which can help us to gain reasonable results. The following diagram shows the three different deSO_x systems investigated. They could be divided into four parts on the basis of types of desulphuriser: the blue part is the all-purpose part; the seawater system consists of the orange part and the all-purpose part. The green part plus the all-purpose part constitute the magnesium-based (Mg-based) system. The last part is the purple part, combined with the all-purpose part, representing the NaOH system.

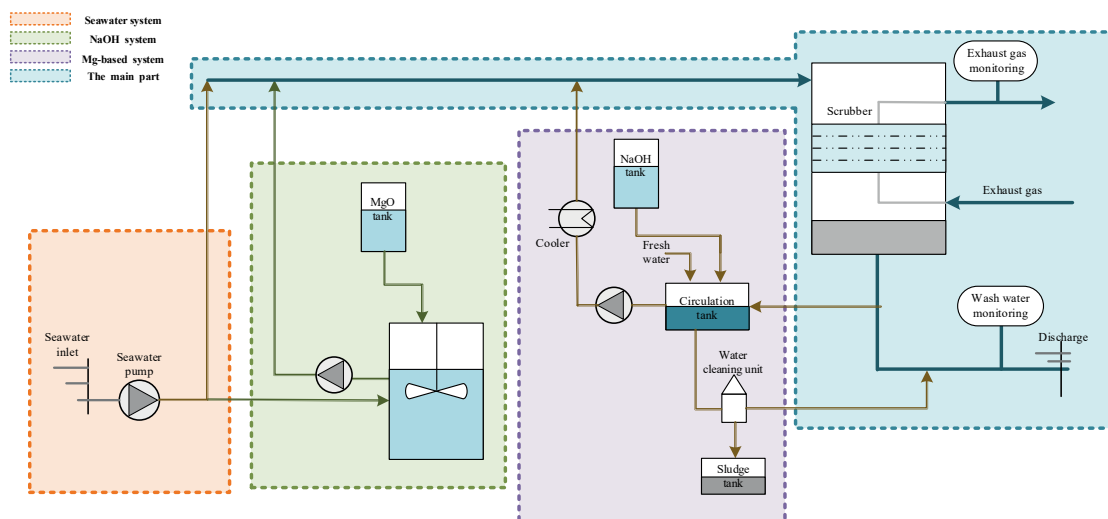
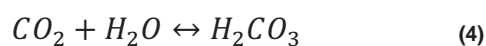
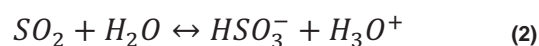
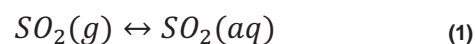


Fig. 3. The desulphurisation scrubber system of our research object

Seawater system

The seawater system, also called the open loop system, uses natural seawater to absorb SO_x and the products are directly or indirectly discharged to the surrounding environment [18]. The seawater is easily acquired while sailing and so the

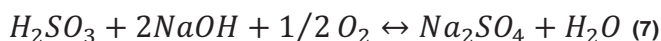
installation is easily fulfilled. The working principle of the seawater system includes SO_x directly absorbed by seawater, which is described by chemical reactions as follows [19]:



The orange part and blue part describe the subsystems of the seawater system. It can be divided into four main components—flue gas piping, the scrubber, seawater supply, and discharge pipelines. Thanks to basic soluble salts contained in seawater, the exhaust gas accesses the scrubber and could be neutralised repeatedly by seawater until the cleaned gas satisfies the emission standard, as shown above.

NaOH system

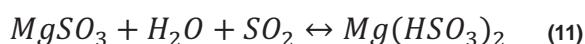
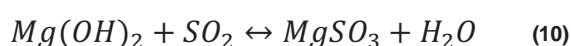
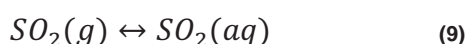
The NaOH system, also known as the closed loop system, will operate when the alkalinity of seawater is not sufficient, for example, with pH values below 6.8, or where waste-water discharge is forbidden in some special sea areas. In this case, the deSO_x process needs to use stored alkaline solution to absorb SO_x. The system is more complex than the seawater one. The principle of this mode is described as follows [20]:



The green part and the all-purpose part describe the subsystems of the NaOH system. It can be divided into five main components—flue gas piping, the scrubber, freshwater supply pipelines, lye circulation, and discharge disposal. Fuel gas comes into the scrubber and reacts with NaOH, then the wash water can be reused many times before being further processed and discharged.

Mg-based system

The Mg-based system combines the MgO with seawater to reduce the concentration of sulphur oxides due to the good solubility of seawater for MgO, and the shortage of freshwater on board. Specifically, MgO dissolves in the seawater, which largely depends on the alkalinity of the absorption liquid and then forms Mg(OH)₂ to absorb SO_x [21]. The principle of this mode is described as follows [22]:



The purple part and the blue part describe the subsystems of the Mg-based system. It consists of four main components—the flue gas piping, the scrubber, magnesium oxide slurry preparation, and washing water discharge. The magnesium oxide slurry is mixed with the seawater to form Mg(OH)₂. The mixture is conveyed to the scrubber to reduce the SO_x concentration. After absorption, the product will be directly discharged to the sea owing to the environment-friendly properties of Mg-based materials.

Application

After introducing the three systems, in this part we collect the data from a real working state as our study object. A typical flue gas from a 10MW diesel engine was used, with SO₂ concentration equivalent to combustion of 3.5% S containing

fuel oil. The whole life cycle is divided into two phases, called the construction and operation phases. The construction phase includes material preparation and transportation, while the operation phase includes desulphuriser preparation and freshwater storage.

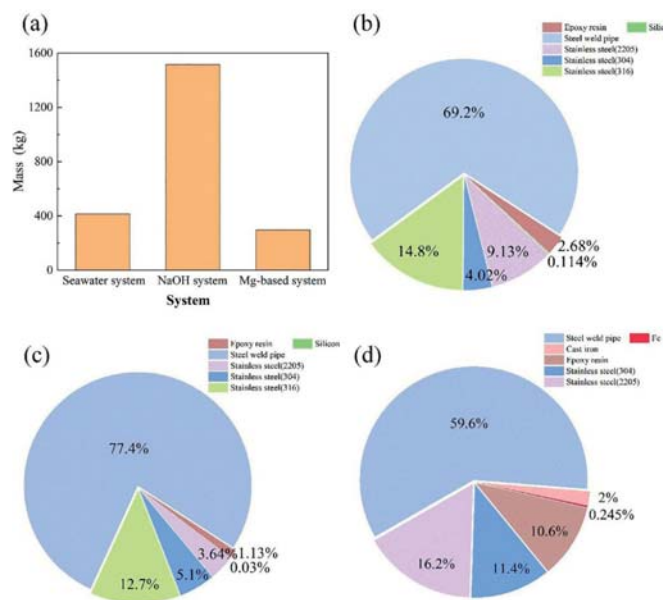


Fig. 4. Material preparation (a) sum mass; (b) seawater system; (c) NaOH system; (d) Mg-based system

Each and every system has a definite architecture utilising a different amount of materials in the construction phase. Fig.4 (a) displays the weight of materials expending each year by three deSO_x systems and the residual pictures show the portion of materials used the in respective systems. The seawater and NaOH system together use diverse stainless steels, steel weld pipe, epoxy resin and silicon, while beyond that, the Mg-based system also uses Fe and cast iron. Different types of stainless steel with various chemical compositions are used for special purposes according to the application. For example, stainless steel (2205) has better corrosion resistance than the others used in the scrubber, as shown in the following picture. Fig.5 presents the disparate stainless steels used in deSO_x systems and it is worth mentioning that more epoxy resin was used in Mg-based system instead of stainless steel (316) in construction. After collecting the practical data, the model was established in GaBi software. GaBi was used to obtain the related data, in which the original data are from industry, academia, education, and policy and regulation making departments.

IMPACT ASSESSMENT

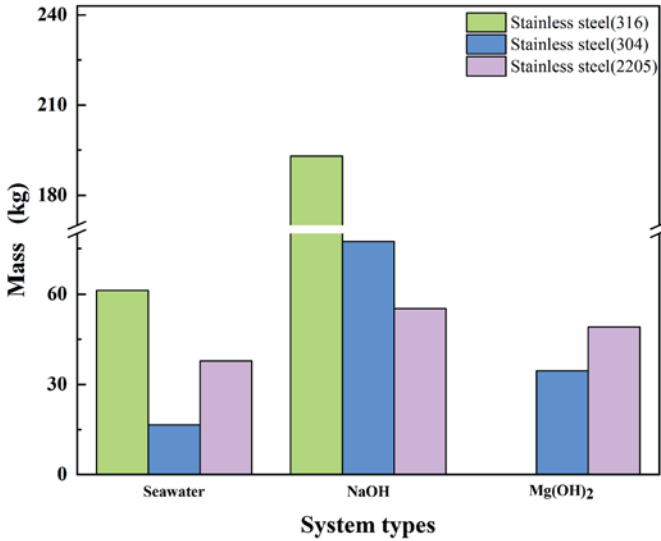


Fig. 5. Amount of different types of stainless steel used in deSOx systems

In order to assess the environmental impact, the assessment methodology should be determined. Several methodologies have been published, such as ReCiPe2016, TRACI, PEF and so on. ReCiPe2016 has been chosen to assess the impact through these data in the subsequent statement. ReCiPe2016 is an endpoint assessment model, which consists of CML2001 and Ecoindicator99 and it can be seen as a fusion of the two methodologies, taking the midpoint impact categories from CML2001 and the endpoint impact categories from Ecoindicator99 [23]. The ReCiPe2016 has three perspectives—individualist, hierarchist, and egalitarian, and we chose the hierarchist perspective to investigate the impact mechanism [24].

In more detail, the midpoint impact categories orient to the environment, such as global warming and acidification. The endpoint impact categories are split into three parts, which are human health, biodiversity, and resources. The following picture shows the relation between the midpoint and endpoint indicators in ReCiPe2016 [25].

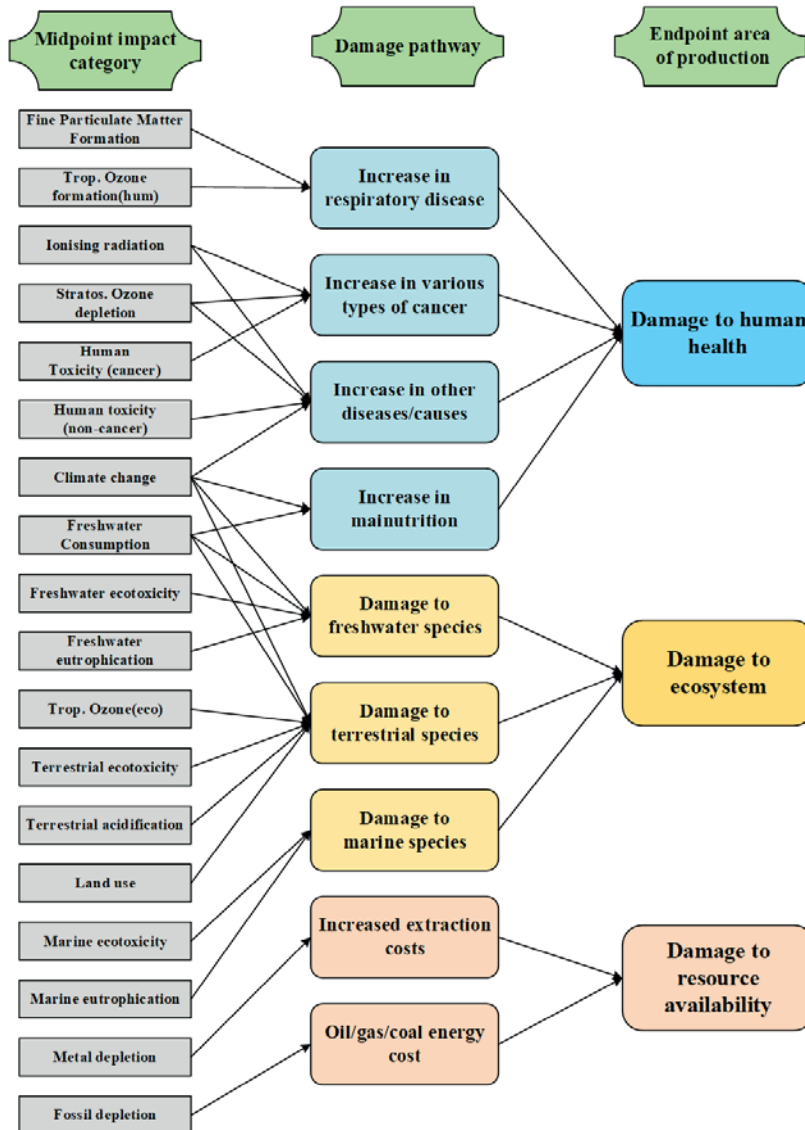


Fig. 6. Relationship between midpoint and endpoint indicators in ReCiPe2016[26]

RESULTS AND DISCUSSIONS

LIFE CYCLE INVENTORY ASSESSMENT

In the construction phase, desired materials for each deSO_x system were prepared based on design. The following operation phase relies on electricity for washing water preparation, in which seawater or freshwater is incorporated into the desulphurising agent. The transporting process is based on the following assumptions: 1) a truck was employed; 2) diesel was used as the fuel; and 3) the average distance was about 100km. As a result, the total consumption of diesel could be estimated. Note that diesel not only provides power to the truck but also delivers an influence on the surroundings during transportation. Table 1 shows the abbreviation and the assessment unit of these category indicators. It simplifies the description of indicators in the subsequent analysis.

Tab. 1 The abbreviation and the assessment unit of category indicators

Impact category	Abbr.	Unit	Impact category	Abbr.	Unit
Climate change	GWP	kg CO ₂	Land use	LOP	m ² land
Fine Particulate Matter Formation	PMFP	kg PM2.5	Marine ecotoxicity	METP	kg 1,4-DCB
Fossil depletion	FFP	kg oil	Marine Eutrophication	MEP	kg NO _x
Freshwater Consumption	WCP	m ³ water	Metal depletion	SOP	kg Cu
Photochemical Ozone Formation, Human Health	HOFP	kg NO _x	Photochemical Ozone Formation, Ecosystems	EOFP	kg NO _x
Freshwater Eutrophication	FEP	kg PM2.5	Freshwater ecotoxicity	FETP	kg 1,4-DCB
Human toxicity, cancer	HTPc	kg 1,4-DCB	Stratospheric Ozone Depletion	ODP	kg CFC-11
Human toxicity, non-cancer	HTPnc	kg 1,4-DCB	Terrestrial Acidification	TAP	kg SO ₂
Ionising Radiation	IRP	kBq Co-60	Terrestrial ecotoxicity	TETP	kg 1,4-DCB

Seawater system inventory

Table 2 shows that part of the emissions in the seawater system and primary air emission is about 1.24E+03kg carbon dioxide, which results in global warming, and the major water emission comes from chloride which is naturally present in the seawater.

Tab. 2 Emissions of the seawater system

Emission to air	Mass(kg)	Emission to water	Mass(kg)
Dust (PM10)	6.04E-01	Nitrate	7.55E-02
Dust (PM2.5)	1.76E-01	Carbonate	1.83E-01
Nitrogen oxides	2.46E+00	Calcium	6.43E-01
Methane	3.93E+00	COD	9.34E-01
Sulphur dioxide	6.70E+00	Sulphate	1.07E+00
Carbon monoxide	7.99E+00	Sodium	4.19E+00
Carbon dioxide	1.24E+03	Chloride	1.48E+01

The seawater system only has a construction phase because it works without an extra desulphuriser. In this system, seawater has a natural alkalinity to cut down the concentration of SO₂ and will be discharged into the sea for disposal. Fig.7 shows the inventory percentage of the seawater system. In general, this system is quasi self-sufficient to reduce the sulphur oxides.

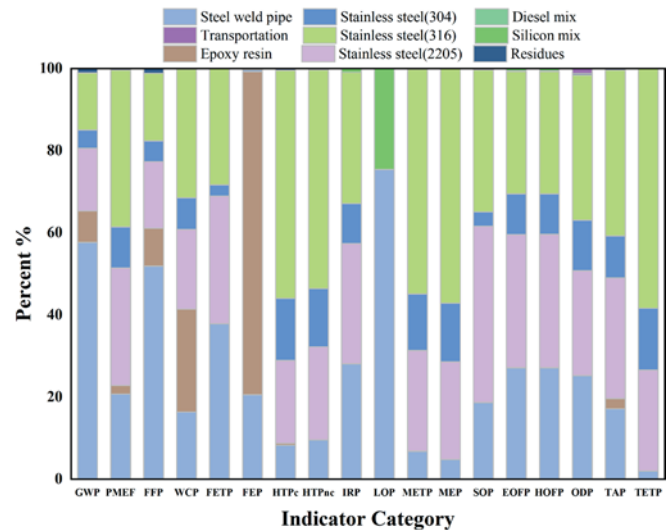


Fig. 7. Seawater system inventory in construction phase

From above, we can see that the steel weld pipe and three types of stainless steel appear in most of the indicator categories. The steel weld pipe plays the leading role in the GWP, FFP and LOP. Three kinds of stainless steel have different distributions in that 316 occupies the most ratios in the indicators, and the least one is 304. Epoxy resin holds over 78.7% parts in the FEP, and no more than 30% has an effect on GWP, PMEP, FFP, WCP and TAP. The silicon mix leads the LOP signal, accounting for 24.6%. As a result, the system is simple to install with environmental-friendly properties. Moreover, due to the seawater being adopted and discharged during sailing, less complexity can be observed in this system.

NaOH system inventory

Table 3 presents the main emissions in the NaOH system. It is obvious that carbon dioxide and nitrogen oxides discharge approximately 1000 times as much to the air as the seawater system. Furthermore, particulate matter is not neglectable, which is the origin of ozone depletion. Although some means are taken to reduce the concentration of sulphur oxides, the inescapable emissions to water show that chloride and calcium are in the majority, followed by sodium, sulphate, and COD (Chemical oxygen demand).

Tab. 3 Emissions of the NaOH system

Emission to air	Mass(kg)	Emission to water	Mass(kg)
Dust (PM10)	1.00E+00	Magnesium	8.74E+01
Hydrogen chloride	4.75E+01	Nitrate	2.71E+02
Dust (PM2.5)	1.04E+02	Iron	6.82E+02
Ammonia	1.15E+02	Fluoride	9.67E+02
Group NMVOC	2.48E+02	COD	1.35E+03
Sulphur dioxide	8.18E+02	Sulphate	2.32E+03
Methane	1.98E+03	Sodium	6.53E+03
Nitrogen oxides	2.33E+03	Calcium	1.28E+04
Carbon dioxide	1.30E+06	Chloride	4.07E+04

As mentioned above, the NaOH system could be evaluated from the construction and operation phases. On the basis of the model in GaBi, the construction phase has a total of 1516 kg materials each year, while the operation phase is composed of 2135 tons of 50% alkaline solution and 7000 tons process water as the solvent. We combine the two processes to see the whole life cycle effect. The NaOH system inventory is described in Fig.8.

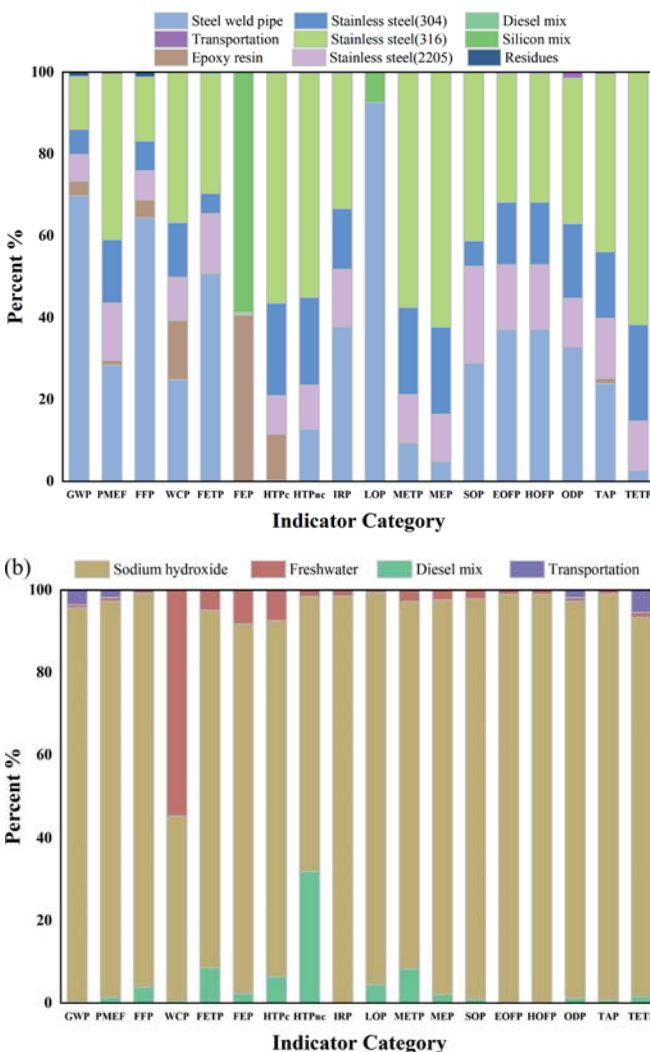


Fig. 8. NaOH system inventory (a)construction phase; (b)operation phase

From the construction phase, steel weld pipe and stainless steels are in the majority of categories except for FEP, which comprises diesel mix, epoxy resin and stainless steel (2205) in decreasing sequence. Silicon also affects LOP, while steel weld pipe and epoxy resin have influences in GWP, PMP, FFP, WCP and TAP. From the operation phase, sodium hydroxide has an effect on most of the categories, up to more than 70%. It is noticed that WCP not only consist of sodium hydroxide, but also freshwater which has over a 50% ratio. The impact of diesel-mix and transportation become more distinct compared to the construction phase.

The addition of sodium hydroxide increases the absorption of SOx. However, the chemical material has a severely harmful effect on the environment from manufacture to usage. Besides, the NaOH system needs extra freshwater to dilute the alkaline solution, which increases the transport consumption.

Mg-based system inventory

Table 4 shows the main emissions in the Mg-based system. In this system, carbon dioxide occupies about 5.86E+05kg in the contribution to the air, followed by sulphur dioxide, PM2.5 and PM10. Emissions to the water mainly stem from chloride, followed by COD, calcium, sulphate, and sodium.

Tab. 4 Emissions of the Mg-based system

Emission to air	Mass(kg)	Emission to water	Mass(kg)
Tin	4.50E+00	Nickel	6.76E-02
Manganese	7.87E+00	Manganese	2.11E-01
Nitrogen oxides	1.03E+03	Chromium	5.15E-01
Methane	1.25E+03	Magnesium	3.06E+01
Dust (PM2.5)	1.29E+03	Iron	5.98E+01
Dust (PM10)	1.29E+03	Calcium	2.20E+02
Sulphur dioxide	1.29E+03	COD	2.67E+02
Carbon dioxide	5.86E+05	Chloride	3.86E+03

The Mg-based system can be divided into two processes like the NaOH system, as shown in Fig.9. The Mg-based system also uses epoxy resin, steel weld pipe and stainless steels, the same as the NaOH system, with the addition of 122kg cast iron and 14.8kg Fe.

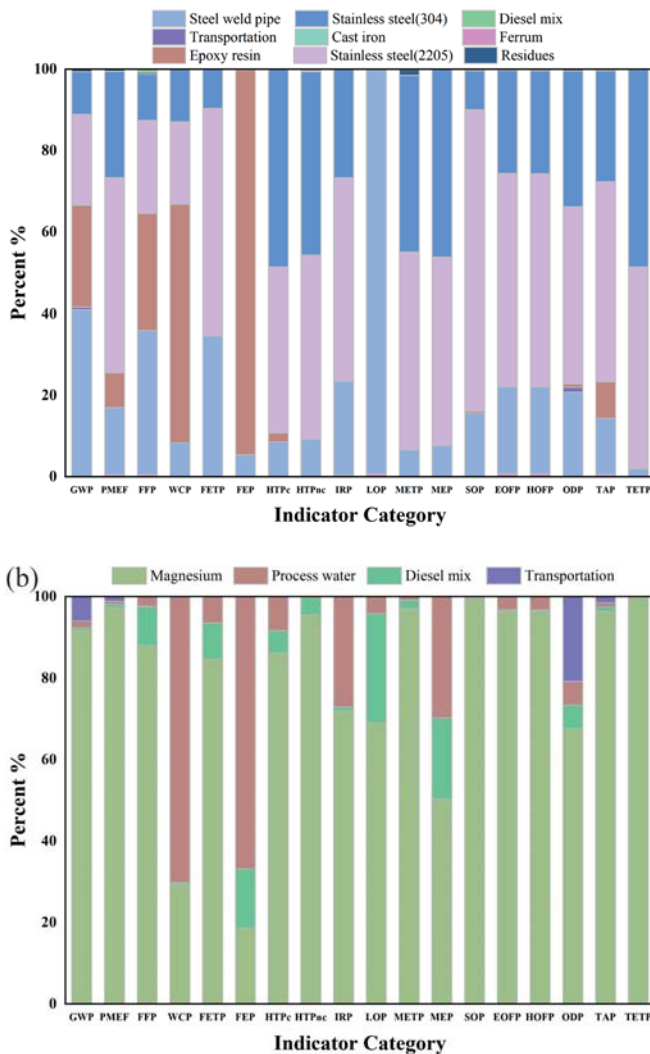


Fig. 9. Mg-base system (a) construction phase; (b) operation phase

From Fig.9 (a), it can be seen that the steel weld pipe and stainless steels play important roles in most of environment indicators. Epoxy resin has a leading role in FEP and a prominent influence in GWP, PMEP, FFP and WCP, while it has slightly less impact in HTPc, MEP and ODP compared with the NaOH system.

The Mg-based system employs seawater because freshwater is scarce when sailing. Moreover, seawater can increase the solubility of MgO. Thus, it will be cleaner and save resources. In the operation phase, magnesium occupies a large part of the affected indicators. Due to the considerable amount of materials that need to be transported, diesel mix, and transportation impacts appear in most of indicators except MEP, SOP, EOFP and TETP.

COMPREHENSIVE EFFECT BASED ON 3E MODEL

Corresponding to the ReCiPe2016 endpoint indicators, we combined the 3E model with the GaBi results for further analysis.

Environmental aspect

The environmental emissions are divided into three main parts, which are emissions to air, emissions to water, and emissions to soil. The important parts in our scope are emissions to air and emissions to water. These damages contact with our daily life and the poor environment results in the growth of disease. The analysis results could further help us to make decision to promote the quality of life. According to the LCIA result, it shows that the Mg-based system is better than the NaOH system in regard to global warming. The seawater system causes less pollution than the others because it uses less materials. More particulate matter was observed in the Mg-based system than the other systems. Chloride tends to have the leading role in emissions to water, while sodium and calcium cannot be neglected.

Above all kinds of materials used, the steel weld pipe and the stainless steel not only show a superior quantity, but also have obvious influences in most of the indicators. The smelting process in metallurgical refinery is known as the origin of abundant pollution. Due to the more radiant molecule produced, they can cause harm to humans and the ecosystem. However, steels have pretty good corrosion and abrasion resistance, and in most cases, they are often the best choice in the industry. The main FEP impact by epoxy resin during fabrication is significant on account of amine and other inactive diluents. In the operation phase, the desulphurisation agent addition causes water consumption and gives rise to the use of freshwater or seawater. Besides, the preparation of the desulphuriser is a prominent reason for the cost of the transportation and diesel mix.

Economy aspect

This part can be assessed by life cycle cost (LCC) in GaBi software, which calculates the spending in the whole life cycle process. Because of the global warming, the ecosystem verges to the poor status, meanwhile the balance is destroyed by reason of over exploitation. However, for ship owners, economy occupies a vital consideration as well as performance, hence analysing synthetically is conducive to saving economic costs. On the assumption that the cost of installation and maintenance are quantified, we primarily compared the cost of the desulphuriser to show the economic effect fairly.

Tab. 5 Expenditure comparison in CapEx and OpEx

	Seawater system	NaOH system	Mg-based system
CapEx (\$)	1.69E+06	2.49E+06	1.91E+06
OpEx (\$/year)	/	3.00E+04	1.20E+03

According to practical expenditure data incorporated with our project, CapEx and OpEx estimation is shown in Table 5. The major compared objects are the Mg-based system and the NaOH system because without the extra desulphuriser, the seawater system dispenses with OpEx. On the subject of CapEx, NaOH uses about 2.5 million dollars while the Mg-based system costs less than the NaOH system, by approximately two million dollars. As for OpEx, the expenditure of the desulphuriser is taken into consideration. NaOH is about

260\$/t and the total cost reaches \$ 30000 per year. In the Mg-based system, MgO is about 60\$/t and the total cost is no more than \$1200 per year. As for the seawater system, it takes about 1.7 million dollars to accomplish construction. In a word, the seawater system is tentatively ascribed as the best choice of the three deSOx systems from an economic aspect.

Energy aspect

Table 6 shows the primary energy used in the deSOx systems during the construction phase. The quantity of the following five kinds of fuels were estimated in the three deSOx systems. From Table 6, it can be found that the NaOH system consumes more fuel than the others. The Mg-based and seawater systems have a similar quantity of materials. These primary energies mainly provoke fossil fuel depletion (FFP) because they can provide high heat values.

Tab. 6 Primary energy consumption estimated in the deSOx systems

Material	System mass(kg)		
	Seawater system	NaOH system	Mg-based system
Crude oil	3.75E+01	1.03E+02	4.30E+01
Hard coal	3.69E+02	1.33E+03	2.77E+02
Lignite	1.86E+01	6.05E+01	1.10E+01
Natural gas	7.33E+01	2.13E+02	9.58E+01
Peat	7.70E-01	2.27E+00	6.88E-01

As the primary energy sources, crude oil, hard coal, lignite, natural gas, and peat have become the focus. They are fundamental to the production of all kinds of materials constituting the system, and also the fundamental input flows in the LCA. With a shortage of primary energy, every part needs to be used efficiently. Moreover, other alternatives are under development, such as wind and solar energy. We prefer to use cleaner energy to protect the natural environment.

CONCLUSIONS

Under established strict standards, efficient marine emissions control has been taken into account. In order to treat the exhaust gas of marine engines, the performance and economy are considered in the first place. So, this study uses LCA tools to estimate the performance of three deSOx systems, from cradle to grave, that is, seawater, NaOH, and Mg-based systems. The results were combined with the 3E model to analyse the construction and operation phases from the environmental, economy, and energy aspects.

In summary, the part we pay more attention to is the environmental effect. The emissions to air and water are predominantly caused by the NaOH system which produced the largest amount of CO₂ and chloride in the construction phase for a 10MW engine flue gas treatment, i.e. 1.30E+06kg and 4.07E+04kg, respectively. Furthermore, the results show that the seawater system seems more cleaner with 1.24E+03kg CO₂ and 1.48E+01kg chloride. Less than 450 times emissions are induced by the Mg-based system, generating 5.86E+05kg

carbon dioxide and 3.86E+03kg chloride. From the economic aspect, the least payment of desulphuriser is achieved by the seawater system, which use natural seawater without additional cost, the Mg-based system spends about \$1200 per year while the NaOH system costs \$30000 per year. From the energy aspect, the most is consumed by the NaOH system which uses more than 10 times the weight of primary energy, except for lignite, compared with the Mg-based and the seawater system in the construction process. In a word, the seawater system has the best performance among all the deSOx systems investigated in this research. However, the efficiency of seawater also needs to be considered in practical use. This work provides valuable opinions for boosting technologies of ocean environment preservation in the future.

ACKNOWLEDGEMENTS

This work was supported by Postgraduate Research & Practice Innovation Program of Jiangsu province (Grant No. SJCX_1491) and National Natural Science Foundation of China (51901088).

REFERENCES

1. Revised MARPOL Annex VI: Regulations for the prevention of air pollution from ships and NOx technical code London: IMO Marine Environmental Protection Committee (MEPC), IMO, 2008
2. Z. Yang, Q. Tan, and P. Geng, 'Combustion and emissions investigation on low-speed two-stroke marine diesel engine with low sulphur diesel fuel', Polish Maritime Research. 2019, 26(1), 153-161.
3. L. Yang, Y. Cai, Y. Wei, and S. Huang, 'Choice of technology for emission control in port areas: A supply chain perspective', Journal of Cleaner Production. 2019, 240, DOI: 10.1016/j.jclepro.2019.118105.
4. W. Zeńczak and A. K. Gromadzińska, 'Preliminary analysis of the use of solid biofuels in a ship's power system', Polish Maritime Research. 2020, 27(4), 67-79.
5. S.-I. Park, S.-K. Kim, and J. K. Paik Freng, 'Safety-zone layout design for a floating LNG-Fueled power plant in bunkering process', Ocean Engineering. 2020, 196, DOI: 10.1016/j.oceaneng.2019.106774.
6. J. B. Guinée et al., 'Life cycle assessment: past, present, and future', Environmental Science & Technology. 2011, 45(1), 90.
7. F. Zheng, F. Gu, W. Zhang, and J. Guo, 'Is bicycle sharing an environmental practice? Evidence from a life cycle assessment based on behavioural surveys', Sustainability. 2019, 11(6), DOI: 10.3390/su11061550.

8. A. Tomporowski, I. Piasecka, J. Flizikowski, R. Kasner, and K. Bieliński, 'Comparison analysis of blade life cycles of land-based and offshore wind power plants', *Polish Maritime Research*. 2018, 25(97), 225-233, DOI: 10.2478/pomr-2018-0046.
9. X. Wu et al., 'Comparative life cycle assessment and economic analysis of typical flue-gas cleaning processes of coal-fired power plants in China', *Journal of Cleaner Production*. 2017, 142, 3236-3242, DOI: 10.1016/j.jclepro.2016.10.146.
10. T. A. S. Lopes, L. M. Queiroz, E. A. Torres, and A. Kiperstok, 'Low complexity waste-water treatment process in developing countries: A LCA approach to evaluate environmental gains', *Sci Total Environ*. 2020, 720, 137593, DOI: 10.1016/j.scitotenv.2020.137593.
11. J. Ling-Chin and A. P. Roskilly, 'A comparative life cycle assessment of marine power systems', *Energy Conversion & Management*. 2016, 127, 477-493.
12. S. S. Hwang et al., 'Life cycle assessment of alternative ship fuels for coastal ferry operating in Republic of Korea', *Journal of Marine Science and Engineering*. 2020, 8(9), DOI: 10.3390/jmse8090660.
13. ISO 14041: Environmental management — life cycle assessment — goal and scope definition — inventory analysis, H. J. Klüppel, 1998.
14. ISO 14042 Environmental management • Life cycle assessment • life cycle impact assessment, S. O. Ryding, 1999.
15. ISO 14043: Environmental management • life cycle assessment • life cycle interpretation, H. Lecouls, 1999.
16. H. E. Lindstad, C. F. Rehn, and G. S. Eskeland, 'Sulphur abatement globally in maritime shipping', *Transportation Research Part D: Transport and Environment*. 2017, 57, 303-313, DOI: 10.1016/j.trd.2017.09.028.
17. S. R. Sharvini, Z. Z. Noor, C. S. Chong, L. C. Stringer, and D. Glew, 'Energy generation from palm oil mill effluent: A life cycle assessment of two biogas technologies', *Energy*. 2020, 191, 116513.1-116513.8, DOI: 10.1016/j.energy.2019.116513.
18. Lamas et al., 'Numerical model of SO₂ scrubbing with seawater applied to marine engines', *Polish Maritime Research*. 2016, 23(90), 42-47
19. D. Flagiello, A. Erto, A. Lancia, and F. Di Natale, 'Experimental and modelling analysis of seawater scrubbers for sulphur dioxide removal from flue-gas', *Fuel*. 2018, 214, 254-263, DOI: 10.1016/j.fuel.2017.10.098.
20. A. Pajdak, 'The effect of structure modification of sodium compounds on the SO₂ and HCl removal efficiency from fumes in the conditions of circulating fluidised bed', *Chemical and Biochemical Engineering Quarterly*. 2017, 31(3), 261-273, DOI: 10.15255/cabeq.2015.2305.
21. Y. Zhu et al., 'Shipboard trials of magnesium-based exhaust gas cleaning system', *Ocean Engineering*. 2016, 128, 124-131, DOI: 10.1016/j.oceaneng.2016.10.004.
22. Q. Liu, M. Sun, T. Zhang, and Y. Zhu, 'Enhanced oxidation of MgSO₃ during desulphurisation by a novel spray method in magnesium-based seawater exhaust gas clean system', *Proceedings of the Institution of Mechanical Engineers, Part M: Journal of Engineering for the Maritime Environment*. 2017, 231(4), 871-876, DOI: 10.1177/1475090216687437.
23. M. Goedkoop, R. Heijungs, M. Huijbregts, A. De Schryver, J. Struijs, and R. Van Zelm, (2009), 'ReCiPe 2008 - A life cycle impact assessment method which comprises harmonised category indicators at the midpoint and the endpoint level', Report I: Characterisation. Vol. 1. Ministerie van VROM. Den Haag
24. M. A. J. Huijbregts et al., 'ReCiPe2016: a harmonised life cycle impact assessment method at midpoint and endpoint level', *The International Journal of Life Cycle Assessment*. 2016, 22(2), 138-147, DOI: 10.1007/s11367-016-1246-y.
25. Y. H. Dong and S. T. Ng, 'Comparing the midpoint and endpoint approaches based on ReCiPe—a study of commercial buildings in Hong Kong', *The International Journal of Life Cycle Assessment*. 2014, 19(7), 1409-1423, DOI: 10.1007/s11367-014-0743-0.
26. W. Shi et al., 'Environmental effect of current desulfphurisation technology on fly dust emission in China', *Renewable and Sustainable Energy Reviews*. 2017, 72, 1-9, DOI: 10.1016/j.rser.2017.01.033.

CONTACT WITH THE AUTHORS

Mengqi Cui

e-mail: cuimengqijust@163.com

Jiangsu University of Science and Technology
No.2 Mengxi Road, 212003 ZhenJiang

CHINA

Yingwei Lu

e-mail: 260810214@qq.com

Zhejiang University,
Zheda road, 310027 Hangzhou,

CHINA

Jiahao He

e-mail: 15501527636@163.com

Jiangsu University of Science and Technology
No.2 Mengxi Road, 212003 ZhenJiang

CHINA

Lei Ji

e-mail: just_jilei@163.com

Jiangsu University of Science and Technology
No.2 Mengxi Road, 212003 ZhenJiang

CHINA

Hui Wang

e-mail: wanghuixuzhou@just.edu.cn

Jiangsu University of Science and Technology
No.2 Mengxi Road, 212003 ZhenJiang

CHINA

Shaojun Liu

e-mail: phoenix205@zju.edu.cn

Jiangsu University of Science and Technology
No.2 Mengxi Road, 212003 ZhenJiang

CHINA

THE MATTER OF DECISION-MAKING CONTROL OVER OPERATION PROCESSES OF MARINE POWER PLANT SYSTEMS WITH THE USE OF THEIR MODELS IN THE FORM OF SEMI-MARKOV DECISION-MAKING PROCESSES

Jerzy Girtler*

Jacek Rudnicki

Gdańsk University of Technology, Poland

* Corresponding author: jgirtl@pg.edu.pl (J. Girtler)

ABSTRACT

The article presents the possibility to control the real operation process of an arbitrary device installed in the marine power plant based on the four-state semi-Markov process, being the model of the process, which describes the transition process of operational states of the device (e_k , $k = 1, 2, 3, 4$), and the transition process of its technical states (s_l , $l = 1, 2, 3$). The operational states e_k ($k = 1, 2, 3, 4$) have the following interpretation: e_1 – active operation state resulting from the task performed by the device, e_2 – state of ready-to-operate stop of the device, e_3 – state of planned preventive service of the device, e_4 – state of unplanned service of the device, forced by its damage. Whereas the interpretation of the technical states s_l ($l = 1, 2, 3$) is as follows: s_1 – state of full serviceability of the device, s_2 – state of partial serviceability of the device, and s_3 – state of unavailability of the device. All these states are precisely defined for the ship main engine (SG). A hypothesis is proposed which justifies the use of this model to examine real state transitions in marine power plant device operation processes. The article shows the possibility to make operating decisions ensuring a rational course of the device operation process when the proposed model of this process and the dynamic programming method based on the Bellman's principle of optimality are applied. The optimisation criterion adopted when making operating decisions is the expected profit to be gained as a result of functioning of the device in the time interval $[\tau_o, \tau_m]$, being the sum of the expected profit gained in interval $[\tau_o, \tau_1]$ and to be gained in interval $[\tau_1, \tau_m]$.

Keywords: semi-Markov model, ship main engine, operation process, stochastic process, operational state, technical state, marine power plant equipment

INTRODUCTION

In Ref. [2], the author presents a possibility to apply the Bayesian decision-making theory for making one of two possible operating decisions when the limiting distribution of the three-state semi-Markov model of technical state transitions of the ship main engine (SG) is known. The article points out that the application of the Bayesian decision-making theory and the theory of semi-Markov processes provides an opportunity to make a choice between one of the two following decisions:

- decision d_1 – first perform the relevant preventive service of the engine to restore its state required for

performing the commissioned task, and then start performing the task within the time limit agreed by the customer,

- decision d_2 – omit the preventive service and start performing the commissioned task.

The engine user must always make one of these two decisions prior to ship's departure. In those situations, the decision-making procedure described in [2, 6, 11, 12] can be very helpful. Making a choice between these two decisions is also of high importance for other marine power plant devices. However, there are more decisions to be made in operating practice. In general, it is important that the decision made ensures that the course of the operation process of not only the

main engine but also of the remaining devices in the marine power plant is rational (preferably optimal). For an arbitrary marine power plant device, its operation process needs to be controlled. Each of these processes comprises a sequence of casually related states $z_i \in Z$ ($i = 1, 2, 3, 4$), bearing the name of operation process states and describing the simultaneous occurrence of operational states $e_k \in E$ and technical states $s_l \in S$, in which the device can stay [2, 4, 5, 6, 10, 12]. The definitions of states $z_i \in Z$ ($i = 1, 2, 3, 4$), e_k ($k = 1, 2, 3, 4$), and s_l ($l = 1, 2, 3$) are given in Chapter 2. Their interpretation is similar to that adopted for marine diesel engines [2, 5, 6].

The need to control the operation process of each device (not only the main engine) installed in the marine power plant by controlling its states $z_i \in Z$ results from the fact that during ship sailing, these devices should permanently stay in state $z_1 = (e_1, s_1)$, i.e. simultaneously in state e_1 of active operation, and state s_1 of full serviceability. Unfortunately, the wear of a device can lead to its failure, which should be avoided during ship's voyage. When any of marine power plant devices gets damaged during the storm, this leads at least to a complicated and troublesome situation in ship sailing, if not to the emergency situation [11]. In particular, the damage of such an important device as the main engine leads, as a rule, to a catastrophic situation [11]. Those situations, which most often result in ship's sinking, frequently with crew and passengers, can be avoided by applying a proper diagnosing system (*SDG*) to each device to monitor its technical condition [2, 3, 5, 7, 10, 17, 18]. This way, the times of preventive services could be rationally planned and executed to avoid possible failures during ship's voyage. When the preventive service is performed, the device is in state $z_3 = (e_3, s_2)$, being the consequence of simultaneous occurrence of state e_3 of its preventive service, and state s_2 of its partial serviceability. However, despite the use of *SDG*, the device can get damaged, and additional unplanned service caused by this damage is required. During this service the device is in state $z_4 = (e_4, s_3)$, which means that it is simultaneously in state e_4 of unplanned service, and in state s_3 of unserviceability. Certainly, the device can also be in state $z_2 = (e_2, s_1)$, which occurs when it is simultaneously in the ready-to-operate stop state e_2 , and the full serviceability state s_1 which allows the device to perform tasks for which it was intended in the design and production phases. Making decision d_i that the device should be in state z_i ($i = 1, 2, 3, 4$) will entail certain financial consequences. These consequences can be expressed as the profit, which takes into consideration both financial gains obtained when the device performs its task and the cost of the device staying in one of those states. The marine power plant user is interested in making a decision which will bring him the profit as large as possible, preferably the maximum. This is possible when using the decision-making (control) theory of semi-Markov processes for making decisions ensuring the maximum profit. These decisions create an optimum strategy, which can be determined using the dynamic programming method based on the Bellman's principle of optimality, or the iterative Howard algorithm [12, 13, 15, 16, 21]. In the monograph [12], the author describes in detail the issue of decision-making based control of the operation process of internal combustion engines used

as ship main engines, which makes use of the process model in the form of six-state semi-Markov process and Howard algorithm. With some adaptations, the proposed method can be used for an arbitrary device in an arbitrary marine power plant. However, a simpler model can also be used for this purpose [7, 10, 11, 12]. This article describes the possibility of decision-making based control of the operation process of a marine power plant device which makes use of the process model in the form of four-state semi-Markov process, along with dynamic programming and the Bellman's principle of optimality.

FORMULATING THE OPTIMISATION PROBLEM FOR THE MARINE POWER PLANT DEVICE OPERATION PROCESS BASED ON THE FOUR-STATE SEMI- MARKOV MODEL OF THIS PROCESS AS AN EXAMPLE

At an arbitrary time t of its operation, the marine power plant device, (the main or auxiliary internal combustion engine, compressor, pump, steam or water boiler, water cooler, or electric motor, etc.), can be in one of four operation process states z_i ($z_i \in Z$, $i = 1, 2, 3, 4$). The operation process states $z_i \in Z$ describe the simultaneous occurrence of operational states e_k ($k = 1, 2, 3, 4$) and technical states s_l ($l = 1, 2, 3$). Formally, the states $z_i \in Z$ can be defined as: $z_1 = (e_1, s_1)$, $z_2 = (e_2, s_1)$, $z_3 = (e_3, s_2)$, $z_4 = (e_4, s_3)$. The operational states e_k belong to the set of operational states, E ($e_k \in E$, $k = 1, 2, 3, 4$), defined by the relation (1) [10, 11, 12]:

$$E = \{e_1, e_2, e_3, e_4\} \quad (1)$$

having the following interpretation:

- state e_1 resulting from performing the intended task by the marine power plant device,
- state e_2 resulting from the ready-to-operate stop of the device waiting for start and transition to state e_1 ,
- state e_3 of planned (preventive) service of the device, performed to avoid its possible damage during state e_1 ,
- state e_4 of unplanned service of the device, forced by its damage.

The set $E = \{e_1, e_2, e_3, e_4\}$ of operational states can be considered the set of values of the stochastic process $\{X(t): t \geq 0\}$ with realisations constant in intervals and continuous on the right [10, 12].

In the phase of rational operation of all marine power plant devices, it is required that the operational state e_1 takes place only when the device is in the full serviceability state (s_1). Moreover, the existence of state e_2 is only permissible in this operation when the device is in state s_1 . When the device is in the partial serviceability state, (s_2), it must get preventive service to avoid its possible damage. Starting this service means the appearance of state e_3 . If the damage cannot be prevented and takes place, the device changes to state s_3 . In

this case, the service forced by the damage is to be performed, during which the device changes to state e_4 .

The technical states s_l ($l = 1, 2, 3$) being the condition for the existence of states e_k ($k = 1, 2, 3, 4$) belong to the set of technical states, S ($s_l \in S, l = 1, 2, 3$), defined by the relation (2) [5, 6, 10, 11, 12]:

$$S = \{s_1, s_2, s_3\} \quad (2)$$

having the following interpretation:

- state of full serviceability, s_1 , which enables the device to operate in all conditions (in the case of the main engine – in the entire load range), for which it was intended in the design and production phases;
- stan of partial serviceability, s_2 , which enables the device to operate in limited conditions, (in the case of the main engine - in the smaller load range), compared to those for which it was intended in the design and production phases,
- state of unserviceability, s_3 , which precludes the device operation (ship moving by the main engine) as intended due to its damage.

The set $S = \{s_1, s_2, s_3\}$ of technical states can be considered the set of values of the stochastic process $\{W(t): t \geq 0\}$ with realisations constant in intervals and continuous on the right [2, 5, 6, 12, 13, 14].

Consequently, the states z_i belong to the set Z of operation process states defined by the relation (3):

$$Z = \{z_1, z_2, z_3, z_4\} \quad (3)$$

having the following interpretation:

- the operation process state $z_1 = (e_1, s_1)$, which exists when the device is in full serviceability state (s_1) and is operated as intended (actively used, or working), which means that it is in operational state e_1 ,
- the operation process state $z_2 = (e_2, s_1)$, which exists when the device is in full serviceability state (s_1) and is used passively (not actively: not working) waiting for start, which means that it is in operational state e_2 ,
- the operation process state $z_3 = (e_3, s_2)$, which exists when the device is in partial serviceability state (s_2) and for this reason gets preventive service, which means that it is in operational state e_3 ,
- the operation process state $z_4 = (e_4, s_3)$, which exists when the device is in unserviceability state (s_3) due to its damage, and for this reason gets unplanned service, which means that it is in operational state e_4 ,

A more detailed interpretation of operational states e_k ($k = 1, 2, 3, 4$) of the marine power plant device was already given when discussing relation (1), while that of technical states s_l ($l = 1, 2, 3$) – for relation (2).

The above interpretation of states z_i ($i = 1, 2, 3, 4$) is fairly general, but it can be defined more precisely for an individual device: main or auxiliary internal combustion engine, steam or water boiler, impeller or positive displacement pump, radial or axial compressor, water or oil or air cooler, oil or water or fuel heater, etc.

The set of operation process states of an arbitrary marine power plant device, $Z = \{z_1, z_2, z_3, z_4\}$, can be considered the set of values of the stochastic process $\{Y(t): t \geq 0\}$ with realisations constant in intervals and continuous on the right [5, 7, 9, 10, 11, 12]. This process includes the stochastic process $\{X(t): t \geq 0\}$, with operational states e_k ($k = 1, 2, 3, 4$) as its values, and the stochastic process $\{W(t): t \geq 0\}$, with technical states s_l ($l = 1, 2, 3$) of the device as its values.

The graph of state transitions for the process $\{Y(t): t \geq 0\}$ is shown in Fig. 1. This graph has been created based on situations observed in operational practice of each marine power plant device. The states z_1 and z_2 are desirable states, while states z_3 and z_4 are undesirable, as they make it more difficult to use the power plant device as intended at arbitrary time t of its operation. States z_3 and z_4 are unavoidable evil and cannot be escaped in the operation of any device [9, 11, 12, 13, 17, 18, 24], but proper control of its operation (such as proper decision-making, for instance) can reduce negative effect of those states on operating parameters, including ship profitability.

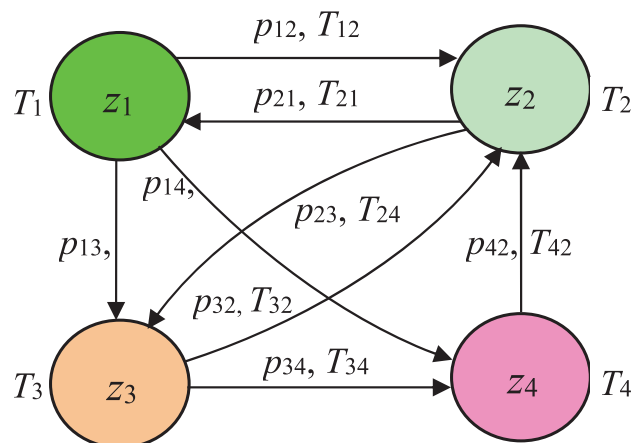


Fig.1. Graph of state transitions, $z_i \in Z$ ($i = 1, 2, 3, 4$), for the process $\{Y(t): t \geq 0\}$ of marine power plant device operation: (z_1) – state of active operation of the device with full serviceability, (z_2) – state of passive use of the device with full serviceability, (z_3) – state of planned preventive service of the device with partial serviceability, (z_4) – state of unplanned service of the device (forced by its damage), which is therefore in unserviceability state, T_i – time interval of existence of state z_i ($i = 1, 2, 3, 4$), T_{ij} – time interval of existence of state z_j provided that the next state is z_i ($i, j = 1, 2, 3, 4; i \neq j$), p_{ij} – probability of state transition from z_i to z_j in process $\{Y(t): t \geq 0\}$

Arcs in the graph shown in Fig. 1 result from the need to ensure rational operation of a device installed in an arbitrary marine power plant [2, 9, 10, 11, 12].

For the device user, the most important state is z_1 , which exists when the device performs its task. Once the task is completed, the state z_1 changes to z_2 , which occurs with probability p_{12} after time T_{12} . When the device is still in the technical state s_1 , which makes it possible to perform the next task, the user of this device may initiate this task, which will result in device's state transition from z_2 again to z_1 . This transition takes place with probability p_{21} after time T_{21} . When the user, based on diagnostic tests, concludes that the device is in technical state which precludes performing the next task, he makes a decision that the device should get preventive

service. This is equivalent with state transition from z_2 to z_3 , taking place with probability p_{23} after time T_{23} . Once the service is completed, the state z_3 changes again to z_2 , which takes place with probability p_{32} after time T_{32} . The need for preventive service can be observed by the user when the device performs its task. Then, immediately after task completion, the user initiates device's state transition from z_1 to z_3 , which takes place with probability p_{13} after time T_{13} . After completing the preventive service, the device changes state from z_3 again to z_2 , which takes place with probability p_{32} after time T_{32} . However, it is possible that the device gets damaged when performing its task. Then it should get unplanned service, forced by the damage, which changes its state from z_1 to z_4 . This transition takes place with probability p_{14} after time T_{14} . After completing the unplanned service, the device's state transition from z_4 to z_2 takes place with probability p_{42} after time T_{42} . In rational operation of the device, there is also the relation between states z_3 and z_4 which describes the situation in state z_3 , being the result of preventive service execution, during which it may turn out that the device got damaged when in state z_1 and this was not detected by the diagnosing system (SDG) being unable to detect such damage types. In that case, after completing the preventive service, the unplanned service forced by the damage is done, which changes the device's state from z_3 to z_4 . This state transition takes place with probability p_{34} after time T_{34} . Certainly, each marine power plant device can change state to z_2 from both, states z_3 and z_4 (Fig. 1).

The above-described operational situation is illustrated in Fig. 2 as the realisation $y(t)$ of the process $\{Y(t): t \geq 0\}$ of transitions of operation process states z_i ($i = 1, 2, 3, 4$) for an arbitrary device during its inter-overhaul period.

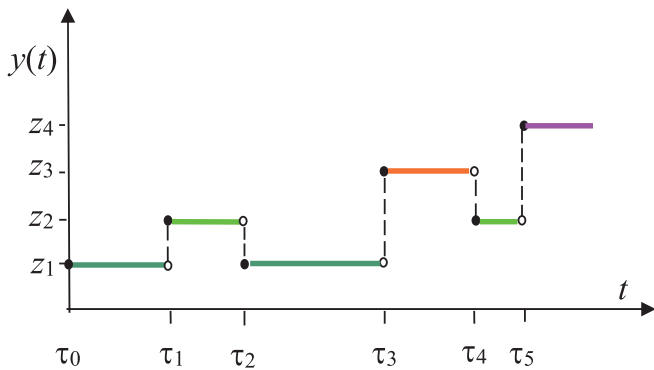


Fig. 2. Sample realisation of process $\{Y(t): t \geq 0\}$ for an arbitrary marine power plant device: t – operating time, (z_1) – state of active operation of the device with full serviceability, (z_2) – state of passive use of the device with full serviceability, (z_3) – state of planned preventive service of the device with partial serviceability, (z_4) – state of unplanned service (forced by damage) of the device being in unserviceability state

The interpretation of operation process states $z_i \in Z$ (3) can be more precise for a given marine power plant device. For the ship main engine (SG), for instance, the interpretation of these states $z_i \in Z$ ($i = 1, 2, 3, 4$) is as follows:

- state $z_1 = (e_1, s_1)$, which has place when the main engine is

simultaneously in full serviceability state (s_1) and active operation state (e_1). In this operation process state, the main engine works and generates the average torque M_o at rotational speed n at which the overall efficiency of the propulsion is $\eta_o \neq \eta_o(\max)$, or generates the average torque M_o at rotational speed n to ensure the optimal overall propulsion efficiency $\eta_o = \eta_o(\max)$, etc.,

- state $z_2 = (e_2, s_1)$, which has place when the main engine is simultaneously in passive operational state (e_2) and full serviceability state (s_1). In this operation process state, the main engine is stopped at engine room temperature $t \leq 0^\circ\text{C}$ or at temperature $t_i > 0^\circ\text{C}$, etc., and waits for start,
- state $z_3 = (e_3, s_2)$, which has place when the main engine is simultaneously in state of preventive service (e_3) and in partial serviceability state (s_2). This operation process state can result, for instance, from the need to check the quality of fuel spraying by injectors, with possible correction of injection pressure, or to adjust the fuel injection advance angle, etc.,
- state $z_4 = (e_4, s_3)$, which has place when the main engine is in state of unplanned service (e_4) forced by damage, which means that it is also in unserviceability state (s_3). This operation process state can result, for instance, from the need to replace a damaged injector, or broken piston rings, or injection pump with plunger seized in the cylinder, etc.

The performed operation tests have shown that the created model $\{Y(t): t \geq 0\}$ of a real operation process, with the values (states) $z_i \in Z$ ($i = 1, 2, 3, 4$) that describe simultaneous existence of mutually implicating technical states s_l ($l = 1, 2, 3$) and operational states e_k ($k = 1, 2, 3, 4$) taking place in the operational phase of a marine power plant device, is the semi-Markov model, as it is characterised by the following properties [7, 9, 11, 13, 14, 19, 24]:

- 1) the Markov condition for the evolution of future state transitions of the operation process $\{Y(t): t \geq 0\}$ of each marine power plant device to depend only on the state of this device at a given time and not on its functioning in the past is met; in other words: the *future* of the device depends only on its *present*, and not on its *past*;
- 2) random variables T_i (which are time intervals of existence of state z_i regardless of which state appears next) and T_{ij} (which are time intervals of existence of state z_i provided that the next process state is z_j) have distributions different than the exponential distribution.

The properties 1 and 2, which justify considering the model $\{Y(t): t \geq 0\}$ of the real operation process $\{Y^*(t): t \geq 0\}$ as the semi-Markov process, are, respectively, the consequences K_1 and K_2 of the following hypothesis: **the semi-Markov process $\{Y(t): t \geq 0\}$ can be the model of a real operation process of an arbitrary marine power plant device, as the arbitrary state z_i ($i = 1, 2, 3, 4$) of this device and the time interval of its existence depend on the state z_j ($j = 1, 2, 3, 4; j \neq i$) directly preceding it, and not on earlier states and their time intervals.**

Verifying the hypothesis H requires recognising the

correctness of the following syntactic implication [7, 10, 20, 22]:

$$H \Rightarrow K_i(i = 1, 2) \quad (4)$$

Then the non-deductive (inductive) inference conducted in accordance with the following scheme can be applied [10, 21, 22]:

$$[K_i(i = 1, 2), H \Rightarrow K_i(i = 1, 2)] \vdash H \quad (5)$$

Logical interpretation of this inference scheme is as follows: if experimental verification of consequences $K_i(i = 1, 2)$ has confirmed their truthfulness, then if the implication (4) is true then the hypothesis H is also true and can be accepted. The inductive inference conducted in accordance with the above scheme (5) bears the name of reductive inference. Certainly, like each other inference belonging to the group of inductive inferences, this inference leads only to possible, and not sure conclusions [7, 20, 22].

The property 1 is met (and hence the consequence K_1 true), as contemporary marine power plant devices are treated as diagnosed systems (SDN) which are to be equipped with advanced computer diagnosing systems (SDG). This makes a basis for formulating complete and highly reliable diagnoses (temporary diagnosis, genesis, and prognosis) concerning the technical condition of the device at arbitrary time t of its operation [4, 5, 10, 11, 12, 17, 18]. Consequently, the SDN user gets satisfactory insight into the current technical condition of each device, which allows him to make a right decision whether state z_3 or state z_4 should be introduced, as these two states cannot exist simultaneously. Therefore, if the process $\{Y(t): t \geq 0\}$ stays in one of these states, (z_3 or z_4), then its future state z_2 and time interval T_2 of its existence (Fig. 1) will depend only on the state z_3 or z_4 directly preceding it. That means that state z_2 and its time interval T_2 do not depend on state z_1 which existed before state z_3 or z_4 . But if the process $\{Y(t): t \geq 0\}$ stays first in state z_1 , and then changes to state z_2 , then the state z_2 and its time interval T_2 will depend only on state z_1 , and not additionally on one of earlier states z_3 or z_4 . Also, the state z_1 and its time interval T_1 will only depend on state z_2 directly preceding it, and not on earlier states z_3 or z_4 (Fig. 1).

The property 2 is also met (and hence the consequence K_2 true), as marine power plant devices, in particular mechanical devices, suffer damages resulting from excessive surface and/or volumetric wear caused by the action of so-called cumulative stimuli, more rarely relaxation stimuli [3, 5, 6, 11, 12]. These devices are not subject to the action of so-called stepwise stimuli, as there are not impact loads which could damage them regardless of their technical condition. Therefore, the exponential distribution cannot be used for probabilistic description of random variables $T_1, T_2, T_3,$ and T_4 . The use of this distribution would only be justified when:

- the level of strength properties (wear resistance) of the devices did not change, which means no ageing provoked damages (coming from cumulative inputs),

- device damages were caused by accidental external or internal impact actions, so-called stepwise stimuli, either being the consequence of device operation or not.

The distributions of the remaining random variables also cannot be considered exponential distributions. This results not only from technical conditions, but also from organisational and economic conditions of the existence of states $z_1, z_2, z_3,$ and z_4 [5, 6, 11, 12].

Hence, we can conclude that the developed model $\{Y(t): t \geq 0\}$ of the real operation process $\{Y^*(t): t \geq 0\}$, which is characterised by transitions of states z_i ($i = 1, 2, 3, 4$) to states z_j ($i, j = 1, 2, 3, 4; j \neq i$) taking place during the operation of marine power plant devices, is the semi-Markov model. This justifies the application of the theory of semi-Markov processes to determine reliability characteristics of these devices, while the application of decision-making (control) theories to the semi-Markov processes enable making optimal operating decisions, with profit used as the optimisation criterion. The semi-Markov models of real processes are characterised by the initial distribution and the functional matrix bearing the name of the kernel of the process [13, 14].

The initial distribution of the process $\{Y(t): t \geq 0\}$ (Fig. 2) is given by the formula:

$$P_i = P\{Y(0) = z_i\} = \begin{cases} 1 & \text{for } i = 1 \\ 0 & \text{for } i = 2, 3, 4 \end{cases} \quad (6)$$

while its functional matrix (kernel), according to the graph shown in Fig. 1, has the following form:

$$Q(t) = \begin{bmatrix} 0 & Q_{12}(t) & Q_{13}(t) & Q_{14}(t) \\ Q_{21}(t) & 0 & Q_{23}(t) & 0 \\ 0 & Q_{32}(t) & 0 & Q_{34}(t) \\ 0 & Q_{42}(t) & 0 & 0 \end{bmatrix} \quad (7)$$

where:

$Q_{ij}(t) = p_{ij} F_j(t)$ is the kernel element of the process (7), which is the conditional probability of appearance of state z_j at time not longer than t , provided that the previous process state was z_i ($i, j = 1, 2, 3, 4; j \neq i$),

p_{ij} – probability of transition of process $\{Y(t): t \geq 0\}$ from state z_i to z_j ,

$F_{ij}(t)$ – cumulative distribution function of random variable T_j ,

Methods to determine the probability p_{ij} and the cumulative distribution function $F_{ij}(t)$ are well known and have been presented in numerous publications, for instance in monographs [12, 13].

It results from the presented hypothesis that the model $\{Y(t): t \geq 0\}$ of real operation processes of marine power plant devices is the semi-Markov process, as it is characterised by the fact that the time interval of the process state existing at time τ_n and the process state which can appear at time τ_{n+1} do not depend stochastically on earlier states and their time intervals. In marine power plant device operation (Fig. 2), it is important for the realisation $y(t)$ of the process $\{Y(t): t \geq 0\}$ to be optimal. This can be achieved by applying the decision-making (control) theory of semi-Markov processes to the

analysed process $\{Y(t): t \geq 0\}$ considered as the semi-Markov decision-making process [6, 9, 12, 15, 16, 21].

The semi-Markov decision-making process $\{Y(t): t \geq 0\}$ is the process, the realisation of which depends on decisions $d_i(\tau)$ ($i = 1, 2, 3, 4$), made at times τ : first at initial time τ_0 , and then at state transition times, $\tau_1, \dots, \tau_n, \dots$ of this process. Decision $d_i(\tau_n)$ is the decision made at time, when the semi-Markov process is in the operation state z_i , which means that $Y(\tau_n) = z_i$ ($i = 1, 2, 3, 4$). In each state of process $\{Y(t): t \geq 0\}$, the decision d_i belonging to the set of decisions, D_i ($d_i \in D_i$), can be made. Making decision d_i means selecting i -th row of the functional matrix (kernel) expressed by the relation (8) which results from matrix (7).

$$Q(t) = \begin{bmatrix} 0 & Q_{12}^{d_1}(t) & Q_{13}^{d_1}(t) & Q_{14}^{d_1}(t) \\ Q_{21}^{d_2}(t) & 0 & Q_{23}^{d_2}(t) & 0 \\ 0 & Q_{32}^{d_3}(t) & 0 & Q_{34}^{d_3}(t) \\ 0 & Q_{42}^{d_4}(t) & 0 & 0 \end{bmatrix} \quad (8)$$

where:

$Q_{ij}^{d_k}(t) = p_{ij}^{d_k} F_{ij}^{d_k}(t)$ is the kernel element of the process (8), which is the conditional probability of appearance of state z_j at time not longer than t when the decision d_k is made, provided that the previous process state was z_i ,

$p_{ij}^{d_k}$ – probability of transition of process $\{Y(t): t \geq 0\}$ from state z_i to z_j when the decision d_k is made,

$F_{ij}^{d_k}(t)$ – cumulative distribution function of random variable $T_{ij}^{d_k}$,

The probabilities $p_{ij}^{d_k}$ and cumulative distribution functions $F_{ij}^{d_k}(t)$ are determined in a similar way as for the earlier mentioned probabilities p_{ij} and cumulative distribution functions $F_{ij}(t)$ characterising the functional matrix (7).

The i -th row of the functional matrix (8) defines the probabilistic mechanism of process evolution in time interval $[\tau_n, \tau_{n+1})$. This row is selected from the set:

$$\{Q_{ij}^{(d_i)}(t): t \geq 0, d_i \in D_i; i, j = 1, 2, 3, 4, i \neq j\}, \quad (9)$$

Decision $d_i(\tau_n) = z_i \in D_i$ means that the semi-Markov process evolves in such a way that, according to the distribution ($p_{il}^{(d_i)}: l = 1, 2, 3, 4$) the process state z_j is selected to which the process changes at time τ_{n+1} . The length of the time interval $[\tau_n, \tau_{n+1})$ is determined in accordance with the distribution given by the cumulative distribution function $F_{ij}^{(d_i)}(t)$. This results from the fact that $Q_{ij}^{(d_i)}(t) = p_{ij}^{(d_i)} F_{ij}^{(d_i)}(t)$ [12, 13, 15, 21].

Decisions are made in accordance with the adopted strategy

$$d = \{(d_1(\tau_1), \dots, d_N(\tau_n)) : n = 0, 1, 2, \dots\} \quad (10)$$

comprising possible decisions $d_i \in D_i$ which may be made. The elements of the decision sequence (10) are vectors with components being the decisions made in given states, at times of their transitions.

In the case of marine power plant devices, the strategy d is the *markovian* strategy, as for each state $z_i \in Z$ (3) and each state transition time $\tau_n, n = 1, 2, \dots$, the decision $d_i(\tau_n) \in D_i$ does not depend on process realisation until time τ_n . Moreover,

this decision does not depend on n , and $d_i(\tau_n) = d_i$, which means that it is also the *stationary* strategy, and the semi-Markov decision-making process $\{Y(t): t \geq 0\}$ is the uniform process. With respect to marine power plant devices, the optimisation of the semi-Markov decision-making process $\{Y(t): t \geq 0\}$ consists in selecting a strategy for which profit, being the optimisation criterion, takes the maximum value.

OPTIMISING THE SEMI-MARKOV DECISION-MAKING PROCESS AS THE FOUR-STATE MODEL OF MARINE POWER PLANT DEVICE OPERATION PROCESS

Optimisation of the semi-Markov process $\{Y(t): t \geq 0\}$ with functional matrix (8) and initial distribution (6), being the model of marine power plant device (*USO*) operation process, is always done for a given time interval $[0, \tau_m)$ of device operation. That means that the number of transitions of states $z_i \in Z$ (4) of this process is predetermined.

The optimisation criterion is the profit gained in time unit of existence of state z_i , which is given by relation [12, 13, 16, 21]:

$$r_{ij}^{(d_k)}(t), \quad i, j = 1, 2, 3, 4, d_k \in D_i \quad (11)$$

provided that at the transition time this state changes to z_j , and decision $d_k \in D_i$ was made at the time of state transition to z_i . The unit profit $r_{ij}^{(d_k)}(t)$ is the function of time t calculated from the time of appearance of state z_i until the time of appearance of state z_j .

When the marine power plant device (*USO*) is in state, the transport task is executed by the ship. Once this task is completed, the crew is paid the salary, which means that they have the unit profit $r_{1j}^{(d_k)}(t), j = 2, 3, 4$, regardless of whether the *USO* changes next to state z_2, z_3 , or z_4 . This also means that in the mathematical sense $r_{12}^{(d_k)} > 0, r_{13}^{(d_k)} > 0, r_{14}^{(d_k)} > 0$. On the other hand, the existence of states z_2, z_3 , and z_4 generates costs, which in the mathematical sense can be considered negative profits. The cost $r_{21}^{(d_k)} < 0$ (as negative profit) of *USO* state transition from z_2 to z_1 results from the need to spend financial resources to ensure that *USO* will return to the active operation state (z_1). For instance, returning the main engine (*SG*) to state z_1 requires purchasing energy media, such as fuel (heavy and/or diesel oil), lubricating oil, technical water for engine cooling, etc. Also, state transition from z_2 to z_3 of either *SG* or any other *USO* involves costs related with crew activity to prepare conditions for preventive service (z_3), hence the (negative) profit $r_{23}^{(d_k)} < 0$ is to be considered. In turn, the execution of preventive service to obtain state transition from z_3 to z_2 requires incurring the cost $r_{32}^{(d_k)} < 0$. Likewise, the unplanned service forced by its damage which is necessary to bring the device from state z_4 to z_2 requires incurring the cost $r_{42}^{(d_k)} < 0$. Also, when a damage to *SG* or another *USO* is detected when performing the planned service, the cost $r_{34}^{(d_k)} < 0$ is to be incurred to change the state from z_3 to z_4 . The

state z_4 is related with the unplanned service, forced by the damage and performed to bring the device back to state z_2 . This state transition involves the cost $r_{42}^{d_k} < 0$.

Taking into account the above characterised unit profits $r_{ij}^{d_k}(t)$, the total profit obtained until time t , as calculated from the time of appearance of state z_i of the process $\{Y(t): t \geq 0\}$ but before transition to state z_j , is given by the function [12, 13]:

$$R_{ij}^{(d_k)}(t) = \int_0^t r_{ij}^{(d_k)}(\tau) d\tau, \quad i, j = 1, 2, 3, 4, d_k \in D_i \quad (12)$$

In the economic sense, the profit is gained when the state z_i exists, while all remaining states z_i ($i = 2, 3, 4$), generate costs (losses) which, as already mentioned, can be considered in the mathematical approach as negative profits (with a minus sign). Except for the main engine (SG), this fact is not always taken into consideration, which results from the fact that the ship with non-functioning engine cannot perform transport tasks. Moreover, when the ship is at sea in rough weather conditions, the main engine failure can lead to the loss of the ship with all transported cargo, which is equivalent for the ship owner to substantial financial loss.

Along with the profit defined by relation (12), another factor which needs considering is a one-off cash inflow (profit) which gives $b_j^{d_k} > 0$, or a one-off cost, with $b_j^{d_k} < 0$. The constant one-off profit and constant one-off cost (negative profit) resulting from state transition from z_i to z_j ($i, j = 1, 2, 3, 4$) are given by the formula [12, 13]:

$$b_{ij}^{(d_k)}, \quad i, j = 1, 2, 3, 4, i \neq j, d_k \in D_i \quad (13)$$

In the model $\{Y(t): t \geq 0\}$, the cash inflows, i.e. profits $b_{12}^{d_k} > 0$, $b_{13}^{d_k} > 0$ and $b_{14}^{d_k} > 0$, are to be paid by the ship owner to the crew to ensure start-up of the works related with the appearance of states z_2 , z_3 and z_4 . For instance, when the SG stays in state z_2 , the profit $b_{12}^{d_k} > 0$, as the crew has to get financial resources to purchase fuel, lubricating oil, spare parts, etc. When in future, the ship owner is commissioned to perform the transport task, these purchases will provide the opportunity for SG state transition from state z_2 to z_1 and starting the execution of the commissioned task. Also, rational state transition of either SG, or another USO from state z_1 to z_3 requires involving financial resources to purchase spare parts for the preventive service to be started. For the SG for instance, this requires purchasing: injectors, filter cartridges, injector pumps, etc., hence $b_{13}^{d_k} > 0$. Likewise, the crew gets financial resources for necessary purchases to ensure rational state transition of either SG or any other USO from state z_1 to z_4 , hence also $b_{14}^{d_k} > 0$. In turn, state transition from z_2 to z_1 is related with the costs incurred by the crew to purchase fuel and lubricating oil, as well as crew salaries to be paid to maintain the existence of state z_1 . Therefore, state transition from z_2 to z_1 requires incurring one-off cost, hence $b_{21}^{d_k} < 0$. Moreover, the cost $b_{23}^{d_k} < 0$ should be determined which allows state transition from z_2 to z_3 , and the cost $b_{32}^{d_k} < 0$ for the transition from state z_3 to z_2 , as well as the cost $b_{34}^{d_k} < 0$ for the state transition from z_3 to z_4 .

The total profit taking into account relations (12) and (13)

is given by the function [12, 13]:

$$U_i^{(d_k)} = \sum_{j \in S} \int_0^\infty (R_{ij}^{(d_k)}(t) + b_{ij}^{(d_k)}) dQ_{ij}^{(d_k)}(t), \quad (14)$$

representing the expected profit to be gained in a single interval of realisation of state z_j , when the decision $d_k \in D_i$ was made at the beginning of this state.

Analysing profits gained from the realisation of the operation process in time interval $[0, \tau_m)$ requires defining the expected (average) profit $V_i(d_m)$, $z_i \in Z$, $i = 1, 2, 3, 4$ to be gained as a result of the adopted decision-making strategy d_m (15).

In the USO operation phase, making a decision (choosing from the set of possible decisions) at time τ_n does not depend on the past realisation of the operation process, but on the technical condition of the device. That means that the Markov strategy can be applied [12, 13]

$$d_m = \{(d_1(\tau_n), \dots, d_N(\tau_n)) : n = 0, 1, \dots, m-1\}, \quad (15)$$

provided that the initial state of the process is state $z_i \in Z$.

Then we can determine the expected (average) profit $V_i(d_m)$, $z_i \in Z$, $i = 1, 2, 3, 4$ to be gained from time $\tau_1 \in [0, \tau_m)$, i.e. in time interval $[\tau_1, \tau_m)$ when applying the strategy

$$d_{m-1} = \{(d_1(\tau_n), \dots, d_N(\tau_n)) : n = 1, \dots, m-1\}, \quad (16)$$

provided that state $z_j \in Z$ was initiated at time τ_1 .

Thus, the expected profit to be obtained as a result of realisation of the USO operation process in time interval $[\tau_0, \tau_m)$ is the sum of the expected profit gained in time interval $[\tau_0, \tau_1)$ and the profit expected to be gained in time interval $[\tau_1, \tau_m)$, which can be expressed by the formula:

$$V_{z_i}(d_m) = U_{z_i}^{(d_k)} + \sum_{z_j \in Z} p_{ij}^{(d_k)} V_{z_j}(d_{m-1}), \quad z_i \in Z. \quad (17)$$

Taking into consideration formula (14), we get the function:

$$V_{z_i}(d_m) = \sum_{z_j \in Z} \int_0^\infty (R_{ij}^{(d_k)}(t) + b_{ij}^{(d_k)}) dQ_{ij}^{(d_k)}(t) + \sum_{z_j \in Z} p_{ij}^{(d_k)} V_{z_j}(d_{m-1}), \quad z_i \in Z. \quad (18)$$

In the USO operation phase, of high importance are optimal strategies, as they provide opportunities for gaining maximum profits. Strategy d_m^* can be considered the optimal strategy when it allows the maximum profit to be gained

$$V_{z_i}(d_m^*) = \max_{d_m} [V_{z_i}(d_m)] \quad (19)$$

in time interval $[\tau_0, \tau_m)$ for the semi-Markov decision-making process starting from state e_i .

That means that the inequality [13]

$$V_{z_i}(d_m^*) \geq V_{z_i}(d_m) \quad (20)$$

is met for all possible strategies d_m .

The optimal strategy can be found using the dynamic programming method, based on a well-known Bellman's principle of optimality. In the analysed case, this principle can be formulated as follows [1, 13]:

When $z_j \in Z$ is the state of process $\{Y(t): t \geq 0\}$ existing at time τ_1 as a result of a decision made at time $\tau_0 = 0$ then, if the strategy

$$d_m^* = \{(d_1^*(\tau_n), \dots, d_N^*(\tau_n)) : n = 0, 1, \dots, m-1\}$$

is the optimal strategy, then the strategy

$$d_{m-1}^* = \{(d_1^*(\tau_n), \dots, d_N^*(\tau_n)) : n = 1, \dots, m-1\}$$

is also the optimal strategy for the process initiated from state z_j at time τ_1 .

Based on this principle and formula (17), the expected (average) profit is given as:

$$V_{z_i}(d_m^*) = \max_{d_k \in D_i} [U_i^{(d_k)} + \sum_{z_j \in Z} p_{ij}^{(d_k)} V_{z_j}(d_{m-1}^*)], \quad z_i \in Z \quad (21)$$

When at time τ_{m-1} the operation process is in state $z_i \in Z$, then the optimal strategy is determined from the relation

$$V_{z_i}(d_1^*) = \max_{d_k \in D_i} [U_i^{(d_k)}], \quad z_i \in Z \quad (22)$$

Consequently, the optimal strategy is given as:

$$d_1^* = \{(d_1^*(\tau_n), \dots, d_N^*(\tau_n)) : n = m-1\} \quad (23)$$

After calculating the maximum profit $V_i(d_1^*) = \max_{d_k \in D_i} [U_i^{(d_k)}]$ for each $z_i \in Z$ ($i = 1, 2, 3, 4$), the optimal strategy

$$d_2^* = \{(d_1^*(\tau_n), \dots, d_N^*(\tau_n)) : n = m-2, m-1\} \quad (24)$$

is determined for the operation process $\{Y(t): t \geq 0\}$, the initial time of which is τ_{m-2} . This strategy is determined from the relation

$$V_{z_i}(d_2^*) = \max_{d_k \in D_i} [U_i^{(d_k)} + \sum_{z_j \in Z} p_{ij}^{(d_k)} V_{z_j}(d_1^*)], \quad z_i \in Z \quad (25)$$

Continuing this procedure, we obtain the optimal decision-making strategy

$$d_m^* = \{(d_1^*(\tau_n), \dots, d_N^*(\tau_n)) : n = 0, 1, \dots, m-2, m-1\} \quad (26)$$

The optimal strategy of operating decision-making (26) makes it possible to determine the next state z_j , when the process is in state z_i ($i, j = 1, 2, 3, 4; i \neq j$), in such a way that the user of an arbitrary USO can gain the maximum profit. Applying the above procedure to determine the optimal strategy of operating decision-making requires taking into consideration the initial distribution of the model $\{Y(t): t \geq 0\}$ of the operation process, with the initial distribution given by formula (6) and the functional matrix (kernel) in the form (8). Certainly, matrix (8) is the matrix (7) modified such that its functions $Q_{ij}(t)$ depend on decisions d_k .

Past examinations of USO operations have shown that the time intervals of existence of states $z_i \in Z$, $i = 1, 2, 3, 4$

and the times of state transition from z_i to z_j of the process $\{Y(t): t \geq 0\}$ can be considered random variables with gamma-distribution [10, 11, 12]. Hence, the elements of matrix (8)

$$\{Q_{ij}^{(d_k)}(t) : t \geq 0, d_k \in D_i, i, j \in \{1, 2, 3, 4\}, i \neq j\} \quad (27)$$

can be expressed as

$$Q_{ij}^{(d_k)}(t) = \int_0^t q_{ij}^{(d_k)}(\tau) d\tau, \quad (28)$$

where:

$$q_{ij}^{(d_k)}(\tau) = p_{ij}^{d_k} \frac{\lambda_{ij}^{(d_k)} \alpha_{ij}^{(d_k)}}{\Gamma(\alpha_{ij}^{(d_k)})} \tau^{\alpha_{ij}^{(d_k)}-1} e^{-\lambda_{ij}^{(d_k)} \tau} \quad (29)$$

The function

$$f_{ij}^{(d_k)}(\tau) = \frac{\lambda_{ij}^{(d_k)} \alpha_{ij}^{(d_k)}}{\Gamma(\alpha_{ij}^{(d_k)})} \tau^{\alpha_{ij}^{(d_k)}-1} e^{-\lambda_{ij}^{(d_k)} \tau} \quad (30)$$

is the gamma distribution density. In this distribution, the expected value $m_{ij}^{d_k}$ and the standard deviation $\sigma_{ij}^{d_k}$ are given by formulas:

$$m_{ij}^{(d_k)} = \frac{\alpha_{ij}^{(d_k)}}{\lambda_{ij}^{(d_k)}}, \quad \sigma_{ij}^{(d_k)} = \frac{\sqrt{\alpha_{ij}^{(d_k)}}}{\lambda_{ij}^{(d_k)}} \quad (31)$$

Hence, the shape parameters $\alpha_{ij}^{(d_k)}$ and the scale parameters $\lambda_{ij}^{(d_k)}$ of this distribution can be expressed as:

$$\alpha_{ij}^{(d_k)} = \frac{[m_{ij}^{(d_k)}]^2}{[\sigma_{ij}^{(d_k)}]^2}, \quad \lambda_{ij}^{(d_k)} = \frac{m_{ij}^{(d_k)}}{[\sigma_{ij}^{(d_k)}]^2} \quad (32)$$

Applying the above procedure of making optimal decisions, i.e. decisions which will give the USO user the opportunity to gain the maximum profit, requires defining the most profitable state. In the analysed case, this state is z_j , in which the engine moves the ship, thus enabling the performance of the transport task and providing profit to the ship owner. According to the graph in Fig. 1 and the functional matrix (8), the user of an arbitrary USO being in state z_i can make one of three possible decisions: d_1 – change to state z_2 , d_2 – change to state z_3 , and d_3 – change to state z_4 . Therefore, the set of decisions for state z_i is as follows:

$$D_1 = \{d_1, d_2, d_3\} \quad (33)$$

Each decision $d_k \in D_i, k = 1, 2, 3$ (33), is attributed with time interval of operation state (z_i), probability of state transition to z_2, z_3 and z_4 , and profit gained from task realisation.

It results from the proposed four-state model of operation process of an arbitrary USO with states $z_i \in Z$ ($i = 1, 2, 3, 4$), matrix (8) and the graph shown in Fig. 1 that making a decision requires determining the following operating parameters:

1. Probabilities $p_{ij}^{d_k}$ of state transitions, i.e.:

$$p_{12}^{(1)}, p_{13}^{(1)}, p_{14}^{(1)}, p_{12}^{(2)}, p_{13}^{(2)}, p_{14}^{(2)}, p_{12}^{(3)}, p_{13}^{(3)}, p_{14}^{(3)},$$

2. Conditional expected values $m_{ij}^{d_k}$ (of operating state time intervals $T_{ij}^{d_k}$), i.e.:

$$m_{12}^{(1)}, m_{13}^{(1)}, m_{14}^{(1)}, m_{12}^{(2)}, m_{13}^{(2)}, m_{14}^{(2)}, m_{12}^{(3)}, m_{13}^{(3)}, m_{14}^{(3)},$$

3. Standard deviations $\sigma_{ij}^{d_k}$ of conditional state time intervals, i.e.:

$$\sigma_{12}^{(1)}, \sigma_{13}^{(1)}, \sigma_{14}^{(1)}, \sigma_{12}^{(2)}, \sigma_{13}^{(2)}, \sigma_{14}^{(2)}, \sigma_{12}^{(3)}, \sigma_{13}^{(3)}, \sigma_{14}^{(3)},$$

4. Average profits $r_{ij}^{d_k}$ gained in ship operation time unit, i.e.:

$$r_{12}^{(1)}, r_{13}^{(1)}, r_{14}^{(1)}, r_{12}^{(2)}, r_{13}^{(2)}, r_{14}^{(2)}, r_{12}^{(3)}, r_{13}^{(3)}, r_{14}^{(3)},$$

5. Constant one-off profits $b_{ij}^{d_k}$ obtained from single operating state realisation, i.e.:

$$b_{12}^{(1)}, b_{13}^{(1)}, b_{14}^{(1)}, b_{12}^{(2)}, b_{13}^{(2)}, b_{14}^{(2)}, b_{12}^{(3)}, b_{13}^{(3)}, b_{14}^{(3)}.$$

Moreover, the distribution parameters of conditional operating state time intervals for different decisions, which are necessary for decision-making, should be calculated from formulas (32). Therefore, we should calculate:

6. Distribution parameters $\alpha_{ij}^{d_k}$ and $\lambda_{ij}^{d_k}$ of conditional operating state time intervals, i.e.:

$$\alpha_{12}^{(1)}, \alpha_{13}^{(1)}, \alpha_{14}^{(1)}, \alpha_{12}^{(2)}, \alpha_{13}^{(2)}, \alpha_{14}^{(2)}, \alpha_{12}^{(3)}, \alpha_{13}^{(3)}, \alpha_{14}^{(3)}, \\ \lambda_{12}^{(1)}, \lambda_{13}^{(1)}, \lambda_{14}^{(1)}, \lambda_{12}^{(2)}, \lambda_{13}^{(2)}, \lambda_{14}^{(2)}, \lambda_{12}^{(3)}, \lambda_{13}^{(3)}, \lambda_{14}^{(3)}.$$

After completing the task performed by an arbitrary *USO*, but when it is still in state z_1 , the user can make a decision that the next state will be z_2 . Then, when the *USO* is already in state z_2 , the user can make, according to the graph in Fig. 1 and the functional matrix (8), one of two possible decisions: d_1 – change to state z_1 , d_2 – change to state z_3 . Therefore, the set of decisions for state z_2 is:

$$D_2 = \{d_1, d_2\} \quad (34)$$

Also in this case, each decision $d_k \in D_2, k = 1, 2$ (34) is attributed with time interval of ready-to-operate stop (z_2), probability of transition to states z_1 and z_3 , and profit related with the existence of this state. Making a proper decision requires determining the following operating parameters:

1. Probabilities $p_{ij}^{d_k}$ of state transitions, i.e.:

$$p_{21}^{(1)}, p_{23}^{(1)}, p_{21}^{(2)}, p_{23}^{(2)},$$

2. Conditional expected values $m_{ij}^{d_k}$ (of state time intervals $T_{ij}^{d_k}$), i.e.:

$$m_{21}^{(1)}, m_{23}^{(1)}, m_{21}^{(2)}, m_{23}^{(2)},$$

3. Standard deviations $\sigma_{ij}^{d_k}$ of conditional state time intervals, i.e.:

$$\sigma_{21}^{(1)}, \sigma_{23}^{(1)}, \sigma_{21}^{(2)}, \sigma_{23}^{(2)},$$

4. Average “profits” $r_{ij}^{d_k}$ gained in time unit of ready-to-operate stop, i.e.:

$$r_{21}^{(1)}, r_{13}^{(1)}, r_{21}^{(2)}, r_{13}^{(2)},$$

5. Constant one-off profits $b_{ij}^{d_k}$ obtained from single ready-to-operation stop state realisation, i.e.:

$$b_{21}^{(1)}, b_{23}^{(1)}, b_{21}^{(2)}, b_{23}^{(2)};$$

The distribution parameters of conditional ready-to-operate stop state time intervals for different decisions, which are necessary for decision-making, should be calculated from formulas (32). Therefore, we should calculate:

6. Distribution parameters $\alpha_{ij}^{d_k}$ and $\lambda_{ij}^{d_k}$ of conditional stop time intervals, i.e.:

$$\alpha_{21}^{(1)}, \alpha_{23}^{(1)}, \alpha_{21}^{(2)}, \alpha_{23}^{(2)}, \lambda_{21}^{(1)}, \lambda_{23}^{(1)}, \lambda_{21}^{(2)}, \lambda_{23}^{(2)}.$$

When the *SG* or any other *USO*, and, consequently, the process $\{Y(t): t \geq 0\}$ are in state z_3 , the user can make, according to the matrix (8) and the graph in Fig. 1, only one of two possible decisions: d_1 – change to state z_2 , d_2 – change to state z_4 . Therefore, the set of decisions for state z_3 (preventive service) is as follows

$$D_3 = \{d_1, d_2\} \quad (35)$$

Like in the previous cases, in this case each decision $d_k \in D_3, k = 1, 2$ (35) is attributed with time interval of preventive service state (z_3), probability of transition to states z_2 and z_4 , and profit related with the existence of this state. Making a proper decision requires determining the following operating parameters:

1. Probabilities $p_{ij}^{d_k}$ of state transitions, i.e.:

$$p_{32}^{(1)}, p_{34}^{(1)}, p_{32}^{(2)}, p_{34}^{(2)},$$

2. Conditional expected values $m_{ij}^{d_k}$ (of state time intervals $T_{ij}^{d_k}$), i.e.:

$$m_{32}^{(1)}, m_{34}^{(1)}, m_{32}^{(2)}, m_{34}^{(2)},$$

3. Standard deviations $\sigma_{ij}^{d_k}$ of conditional preventive service time intervals, i.e.:

$$\sigma_{32}^{(1)}, \sigma_{34}^{(1)}, \sigma_{32}^{(2)}, \sigma_{34}^{(2)},$$

4. Average “profits” $r_{ij}^{d_k}$ gained in time unit of preventive service, i.e.:

$$r_{32}^{(1)}, r_{34}^{(1)}, r_{32}^{(2)}, r_{34}^{(2)}$$

5. Constant (negative) “profits” $b_{ij}^{d_k}$ obtained from single realisation of state e_3 , i.e.:

$$b_{32}^{(1)}, b_{34}^{(1)}, b_{32}^{(2)}, b_{34}^{(2)}.$$

The distribution parameters of conditional preventive service state time intervals for different decisions, which are necessary for decision-making, should be calculated from formulas (32). Therefore, we should calculate:

6. Distribution parameters $\alpha_{ij}^{d_k}$ and $\lambda_{ij}^{d_k}$ of conditional preventive service time intervals, i.e.:

$$\alpha_{32}^{(1)}, \alpha_{34}^{(1)}, \alpha_{32}^{(2)}, \alpha_{34}^{(2)}, \lambda_{32}^{(1)}, \lambda_{34}^{(1)}, \lambda_{32}^{(2)}, \lambda_{34}^{(2)}.$$

In the case when the *SG* or any other *USO* and, consequently, the process $\{Y(t): t \geq 0\}$ are in state e_4 , the user can make, according to matrix (8) and the graph in Fig. 1, only one decision: d_1 – change to state z_2 . Therefore, the set of decisions for state z_4 (unplanned service forced by damage) has only one element:

$$D_4 = \{d_1\} \quad (36)$$

Making this decision requires the information of the values of the following operational parameters:

1. Probability $p_{ij}^{d_k}$ of state transition, i.e.: $p_{42}^{(1)} = 1$,
2. Conditional expected value $m_{ij}^{d_k}$ of time interval $T_{ij}^{d_k}$ of unplanned service forced by damage, i.e.: $m_{42}^{(1)}$,
3. Standard deviation $\sigma_{ij}^{d_k}$ of the conditional time interval of unplanned service forced by damage, i.e.: $\sigma_{42}^{(1)}$,
4. Average "profit" $r_{ij}^{d_k}$ gained in time unit of unplanned service forced by damage, i.e.: $r_{42}^{(1)}$,
5. Constant "profit" $b_{ij}^{d_k}$ (bonus) obtained from single realisation of state e_4 , i.e.: $b_{42}^{(1)}$.

The distribution parameters of conditional time interval of state e_4 , which are necessary for making decision d_1 , should be calculated from formulas (32). Therefore, we should calculate:

6. Distribution parameters $\alpha_{ij}^{d_k}$ and $\lambda_{ij}^{d_k}$ of the conditional time interval of the service forced by damage, i.e.: $\alpha_{42}^{(1)}$, $\lambda_{42}^{(1)}$.

After calculating the values of the above parameters of the operation process $\{Y(t): t \geq 0\}$ for an arbitrary USO, the procedure proposed in the article (formulas 17 ÷ 25) can be applied to determine the optimal strategy.

FINAL CONCLUSIONS AND REMARKS

Decision-making based control of the operation process of an arbitrary marine power plant device (USO), in particular the main engine (SG), is the most essential and, simultaneously, most difficult issue in operation of these devices. This results from the fact that the control is executed in a stochastic decision-making situation resulting from random conditions in which these devices operate. As a consequence, rational control of these processes requires developing stochastic decision-making models.

The article shows that these models can be developed based on the theory of semi-Markov decision-making (control) processes. To enable making operating decision which will ensure a rational course of the USO process, the model of this process is proposed in the form of a four-state semi-Markov decision-making (control) process $\{Y(t): t \geq 0\}$.

The optimisation criterion adopted when making operating decisions is the expected profit to be gained during the operation of each USO in given time interval.

The optimal decision-making strategy for the process $\{Y(t): t \geq 0\}$ is determined using profit as the optimisation criterion and the dynamic programming method making use of the well-known Bellman's principle of optimality. The developed procedure to determine the optimal strategy is as follows:

1. For each $z_i \in Z$ and $d_k \in D_i$, the profit $U_i^{d_k}$ is to be calculated from formula (14), which is the expected

profit to be gained in a single time interval of state z_i realisation when the decision $d_k \in D_i$ was made at the beginning of this realisation

2. For each $z_i \in Z$, the maximal profit $V_{z_i}(d_1^*)$ is to be calculated from formula (22) for the first decision d_1^* ,
3. In successive steps, i.e. for $l = 2, \dots, m$, and for each $z_i \in Z$, the expected (average) profit is to be calculated from formula (21), hence for $l = 2$

$$V_{z_i}(d_2^*) = \max_{d_k \in D_i} [U_i^{(d_k)} + \sum_{z_j \in Z} p_{ij}^{(d_k)} V_{z_j}(d_1^*)].$$

Calculating the expected (average) profit from formula (21) for the final step ($l = m$), when at the initial time the process $\{Y(t): t \geq 0\}$ was in state $z_i \in Z$, is equivalent to determining the optimal strategy.

Verifying and demonstrating the practical usefulness of this model requires the use of statistical methods to estimate the probabilities p_{ij} and the expectation values $E(T_{ij})$ and the parameters of the distributions of the random variables T_{ij} and other performance parameters, which are considered in this article. This is possible only in the case of obtaining the realization $y(t)$ of the process $\{Y(t): t \geq 0\}$ in a sufficiently long testing interval, that is, for $t \in [0, t_b]$, with $t_b \gg 0$. Then it is possible to determine the numbers n_{ij} ($i, j = 1, 2, 3, 4; i \neq j$), which denote the numbers of transitions from state z_i to z_j in a sufficiently long time depending on the decisions made.

REFERENCES

1. Bellman R., A.: Dynamic programming. Princeton Univ. Press. Princeton, New Jersey 1957.
2. Girtler J.: Limiting distribution of the three-state semi-Markov model of technical state transitions of ship power plant machines and its applicability in operating decision-making. Polish Maritime Research, Vol. 27, No 2(106), 2020, s. 136-144.
3. Girtler J.: Necessity for and possibility of application of the theory of semi-Markov processes to determine reliability of diagnosing systems. Journal of POLISH CIMAC, Vol. 7, No. 2 (2011), s. 45-54.
4. Girtler J.: The issue of quantum in empirical research on machines and other power systems. Journal of POLISH CIMAC, Vol. 7, No. 1 (2012), s. 57-66.
5. Girtler J.: Application of semi-Markov processes for evaluation of diesel engines reliability with regards to diagnostics. Journal of Polish CIMAC, Vol. 11, No 1, s.47-53, 2017.
6. Girtler J.: Possibility of estimating the reliability of diesel engines by applying the theory of semi-Markov processes and making operational decisions by considering reliability of diagnosis on technical state of this sort of combustion engines. Combustion Engines, Vol 163, No 4. 2015, s. 67-76.

7. Girtler J.: Usefulness of semi-Markov processes as models of the operation processes for marine main engines and other machines of ship power plants. *Journal of Polish CIMAC*, Vol. 9, No 2. 2014, s. 57-67.
8. Girtler J.: A semi-Markov model of fuel combustion process in a Diesel engine. *Polish Maritime Research*, Vol. nr S1, 2007, s.58-61.
9. Girtler J.: The semi-Markov model of energy state changes of the main marine internal combustion engine and method for evaluating its operation during ships voyage. *Polish Maritime Research*, Vol. 18, nr 4, 2011, s. 36-42.
10. Girtler J.: Diagnostics as a condition for control over the operation of marine internal combustion engine. Study No 28, WSM, Szczecin 1997 (in Polish).
11. Girtler J., Kuzmider S., Plewiński L.: Selected issues of operation of sea-going vessels in the aspect of navigation safety. Ed. WSM in Szczecin, Szczecin 2003 (in Polish).
12. Girtler J.: Control over operation process of marine internal combustion engines on the basis of a diagnostic decision-making model. *AMW Scientific Journals*, No. 100A, Gdynia 1989 (in Polish).
13. Grabski F.: The theory of semi-Markov operation processes of technical objects. *AMW Scientific Journals*, No. 75 A, Gdynia 1982 (in Polish).
14. Grabski F.: Semi-Markov models of reliability and operation. *Polish Academy of Sciences, IBS*. Warsaw 2002. Series: System Studies, vol. 30 (in Polish)
15. Howard R.A.: Research in semi-Markovian decision structures. *J. Oper. Res. Soc. Japan*, 1964, 6, nr 4, p.163-199.
16. Jewell W.S.: Markov-renewal programming. *Operation Research* 11, 1963, p.938-971.
17. Korczewski Z.: Operational diagnostics of marine engines. Ed. Gdansk University of Technology, Gdansk 2017 (in Polish).
18. Korczewski Z.: Endoscopy of marine engines. Acad. Ed. AMW, Gdynia 2008 (in Polish).
19. Koroluk V.S., Turbin A.F: Semi-Marcov processes and their applications. *Naukowa Dumka*, Kiev 1976 (in Russian).
20. Leszek W.: Empirical research. Institute of Operation Technologies, Radom 1977 (in Polish)
21. Mine H., Osaki S.: Markovian decision processes. *AEPCI*, Nev York 1970.
22. Pabis S.: Methodology and methods of empirical sciences. PWN, Warsaw 1985 (in Polish).
23. Rudnicki J.: Application issues of the semi-Markov reliability model. *Polish Maritime Research*. No 1(85)/2015, Vol. 22, pp. 55 – 64.
24. Silvestrov D.S.: Semi-Marcov processes with a discrete set of states. *Soviet Radio*, Moscow 1980 (in Russian).

CONTACT WITH THE AUTHORS

Jerzy Girtler

e-mail: jgirtl@pg.edu.pl

Jacek Rudnicki

e-mail: jacekrud@pg.edu.pl

Gdańsk University of Technology
Narutowicza 11/12
80-233 Gdańsk
POLAND

FINITE ELEMENT FATIGUE ANALYSIS OF UNSUPPORTED CRANE

Ryszard Buczkowski*

Bartłomiej Żyliński

West Pomeranian University of Technology Szczecin, Poland

* Corresponding author: rbuczkowski@ps.pl (R. Buczkowski)

ABSTRACT

The presented strength and fatigue calculations refer to an unsupported deck crane and its three distinct parts: housing, jib and column. Static loads applied to the structure were due to the crane's own weight and a maximum working load, corresponding to a maximum lifting capacity at a maximum outreach of the crane. The numerical analysis was aimed at determining the thickness of the skin plating of the column and the number, shape and distribution of stiffeners in the column, housing and jib, ensuring that the crane yields correct strength and fatigue parameters. During the process of designing marine structures, the standard numerical analysis is, in many cases, limited to calculations in the basic strength range. Even when using numerical methods of analysis, complex strength and fatigue calculations are often not performed. The modern numerical analysis chain for marine structures should concentrate not only on strength analysis, but should take a further step, which encompasses fatigue analysis. The article presents a new outlook on design methods, which should be the entry point to the design of marine structures. Based on the acquired number of cycles of fatigue life, it is possible to estimate, with a sufficient degree of accuracy, the practical service life of a structure. To solve the problem, the authors used the finite element analysis software ABAQUS supported by the fe-safe system.

Keywords: fatigue life analysis, strength analysis, fatigue factors, unsupported deck crane, FEM model

INTRODUCTION

Unsupported deck cranes are being installed more and more often on container ships all over the world. This is a response to ship owners' greater demands for larger container space on deck. More cargo room is gained by sacrificing whatever can be removed from the open deck, even by moving the superstructure further aft. For the same reason, naval architects tend to locate deck cranes on one side instead of on the ship's centre line. One such example is a new crane solution, the CBB 3800 from Liebherr, a powerful machine that can easily handle oversize cargo items.

The pursuit for greater ship efficiency leads to crane design restrictions, which may leave no space on the weather deck for the crane jib support used during the sea passage. In such a case, the installation of an unsupported deck crane is

often the only compromise solution, despite the higher cost of such cranes and related operational problems. Besides this, unsupported cranes require more precise strength and fatigue calculations for crane housings and jibs, mounted on a column higher than ten metres.

Ships and other marine structures are, obviously, subjected to fatigue damage caused by dynamically acting waves and slowly changing loads, that occur during cargo handling operations. In a recent study [17], containing projected trends in offshore structures, the authors postulated the need for further investigation of fatigue damage prediction procedures. In turn, Hirdaris et al. [10] pointed out that to correctly assess and predict fatigue phenomena in offshore structures one has to have a design philosophy based on an analysis of model test results, field measurements and simulations using up-to-date numerical modelling systems.

Today, fatigue analysis commonly makes use of two methodologies for solving problems of that type. One consists of an analysis utilising the S-N relation (stress – number of cycles to failure), the other is the fatigue crack growth (FCG) method.

Many research studies relating to fatigue analysis of various types of offshore structures have been based on these methods. Wirsching [21], for instance, presented results of fatigue tests on welded joints from steel offshore structures. The author's analysis took into account service life, wave spectra, water depth, platform dynamics and the location of the joint in the structure.

Fonte et al. [5], in turn, presented tests of welded joints and cracks on a crane pedestal of a container ship. The authors found that, although the crane column was subjected to fatigue processes, sudden loads during cargo operations and the phenomenon of crack corrosion found on the column surface may be due to normal crane operation as well as poor maintenance.

Deguchi et al. [4] examined the influence of the ultrasonic peening method on increases in the fatigue strength of welded joints in structural ship components. Taking into account changes in the distribution of stresses occurring over the entire service life of the ship, the authors proposed effective methods for using ultrasonic peening to improve fatigue strength.

Soares and Moan [20] proposed a special model of loading that should be considered when designing offshore structures. The model enables the assessment of fatigue damage in structural ship components.

Soares and Garbatov [19] presented an assessment of ship hull reliability, with respect to fatigue failure of the longitudinal stiffeners, as well as plating. Their formula allows modelling of the crack growth process.

Kvittem and Moan [13] undertook long term fatigue damage analysis for a semi-submersible wind turbine. They observed that it is essential for an analysis to adopt loading that will not cause high fatigue damage. Thus, we can obtain a reliable fatigue estimate for the adopted service life.

Lieurade [15] stated that wave loads, commonly acting on offshore structures over an assumed 20+ years of operation, caused about 1E8 cycles of stress variation and may be the main cause of potential fatigue cracking. The author referred to a number of offshore structures and the main factors affecting the formation of fatigue effects in these objects.

Hirdaris et al. [9] provided a wide overview of loads on maritime structures to support classification rule requirements and procedures. In their fatigue analysis, the authors took into consideration the loads acting on ships and offshore lifting structures.

Researchers are also interested in fatigue analysis of marine cranes. Marquez et al. [14] presented the causes of crane failures and similarities in failure circumstances. They examined a cylindrical luffing crane, designed to handle containers at a river port. Due to damaged bolts, the crane broke away from its base and collapsed into the water. The bolts fixed the non-rotating part of the crane to the base. After the

damaged parts were recovered from the water, it was found that bolt damage was due to material fatigue and occurred prior to the catastrophic failure.

Using a FEM model and the NASTRAN system, Han et al. [7] presented an analysis of an offshore platform crane, aimed at examining deformations and stress distribution. Moreover, they made fatigue estimations to determine the life cycle of the welded boom structure. The analysis took into account the crane's own weight, maximum working load, wind pressure and wave action causing the ship's rolling motion.

Examining a quayside container crane, Wu et al. [22] applied a FEM model and MSC.Adams, MSC.Patran and MSC.Fatigue systems to present the analysis chain comprising the modelling of a structure, followed by strength and fatigue analyses.

Ozguç [23] presented non-linear FE results of ship-shaped offshore vessels, where the deck structure is exposed to buckling failure. The hybrid method (combination of the deformable finite elements and the concentrated mass method) was applied in [24] to design of some offshore steel structures. Samson and Kahsin [25] described numerical and experimental results of pre-tension forces in standing rigging of a mast.

The examples presented above, often do not encompass a complex numerical analysis. The processes of analysis should be conducted with the inclusion of industry codes, standards and classification society requirements.

We will attempt to present an effective chain of engineering analysis which contains numerical analysis using the Finite Element Method in the range of fatigue analysis.

NUMERICAL MODEL OF THE UNSUPPORTED DECK CRANE

This analysis deals with an unsupported deck crane with a lifting capacity of 400 kN at a 32 m outreach, mounted on a 13.8 m column, an integral part of the ship's hull. The overall height of the crane, including the column, is 24.6 m, while the jib is 34.4 m long. The adopted model naturally distinguishes three characteristic parts of the crane: column, housing and jib, as shown in Figure 1. The figure presents a discrete, finite element mesh model of the crane.



Fig. 1. A model of an unsupported deck crane mounted on a column

The crane column functions as a base for mounting the housing at a required height so that the jib is located above the level of the top container tier. This allows maximisation of the use of space around the column by placing extra containers there. The column interior is used by crane operators to climb to the housing. The column interior comprises electric and hydraulic installations. The crane column is topped with a collar flange, to which the housing is bolted. The lower part of the housing is where the jib is attached by pins, held in a proper position by outreaching, changing ropes. Inside the housing are drive units for controlling the outreach and crane rotation and for cargo lowering and lifting. The numerical model, created with the finite element method, is composed of 17,352 elements and 64,879 nodes, which gives 365,478 degrees of freedom in total. To discretise the metal plates used for the shell and stiffeners of the housing, column and jib, we mainly used thin shell elements, denoted as S8R5, STRI65 (as in the ABAQUS system) [3].

The plate thicknesses ranged from 26 to 31 mm in the column, from 10 to 28 mm in the housing and from 10 to 25 mm in the jib (note the different colour markings in Figure 1). The stiffener distribution in the column and the jib is shown in Figure 2.

The method of modelling the crane's lifting ropes deserves special attention. The most often used ropes in rope structures are ordinary spiral or multi-strand plaited ropes, as well as prefabricated wire and rope cables [16]. Plaited ropes used in deck cranes are characterised by their high flexibility, allowing easy winding of the ropes on lead pulleys and high longitudinal deformability. The mechanical properties of ropes are substantially different from those of individual wires. The main difference is the value of Young's modulus E [16]. An arbitrary adoption of the modulus of elasticity in the numerical model may lead to significant differences between the calculated and actual states of displacements and stresses in the elements of the tie structures. When devices that may create hazardous situations are designed, the modulus of elasticity should be determined experimentally [16]. According to the Polish guidelines contained in relevant design standards [16], the values of the modulus of elasticity for plaited ropes range from 120 GPa to 195 GPa. The value of the Young's modulus adopted for the numerical calculations was $E = 120$ GPa. For rope modelling by the finite element method, the stiffness matrix of a tie element is obtained from the superposition of its elastic stiffness; it corresponds to the stiffness of a bar element and its geometrical stiffness, taking account of the longitudinal forces in a rope finite element [1, 12, 16]. For the calculations, 30 finite elements of the rope were adopted at each section from the jib end to the leading pulley block, mounted at the upper part of the housing.

Structural elements of cranes and other handling equipment are typically made of high strength, class 355 or normal strength, class 235 steel. In the DNV regulations, steels with similar strength properties (yield points) are classified as VL-36 and VL, respectively. The calculations assume that the crane is made of high strength steel (high strength, class 355). Steel grade S355J2G3 (EN10025-2) was adopted here, with

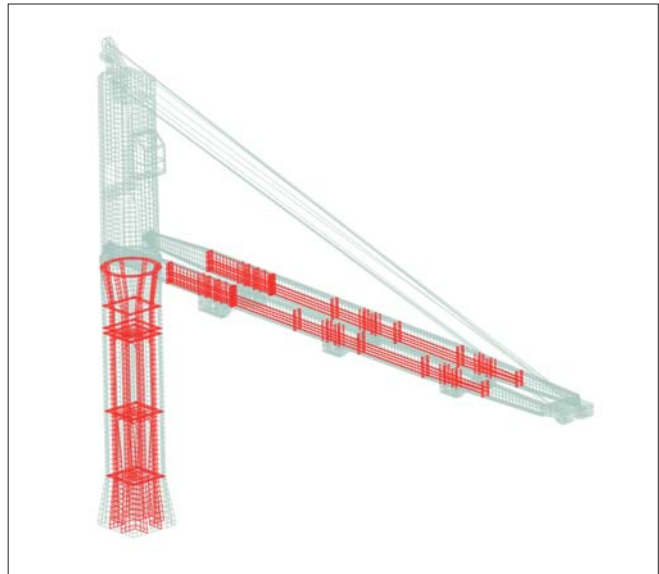


Fig. 2. Discretisation using finite elements of the column and jib internal transverse and longitudinal stiffeners

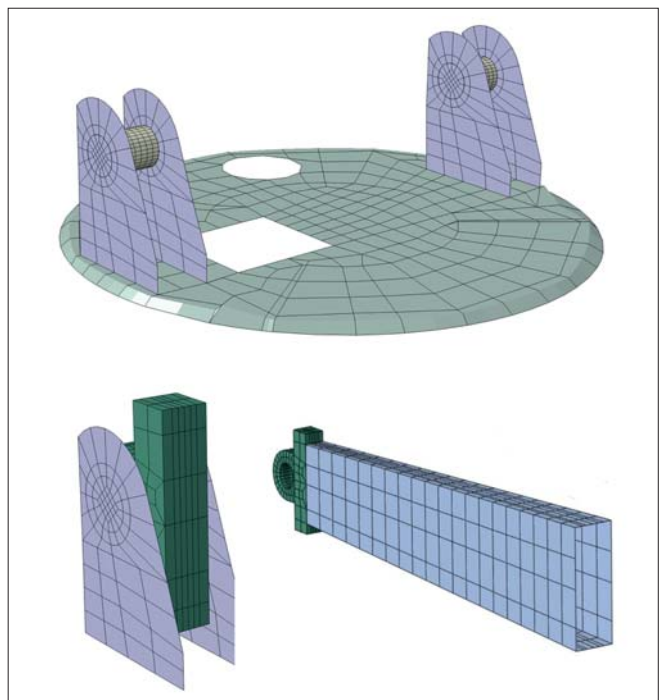


Fig. 3. A contact pin connection between the housing and the jib

a minimum yield strength of 355 MPa (for a sheet thickness up to 16 mm). For these steels, the S-N curves are published in the DNV regulations. In our calculations, it is steel marked as material B. For comparison, the possibility of using another steel material with the S-N curve provided by the manufacturer (material A) was also tested.

FATIGUE CALCULATIONS

In engineering practice, it is generally estimated that more than half of the permanent damage to machinery is caused by fatigue changes occurring in a machine's component materials. In this context, it is essential to correctly use

reliable engineering tools to assist the determination of fatigue strength. Fatigue analysis, utilising the finite element method, substantially reduces or, in some cases, eliminates the cost of re-designing or withdrawing faulty products. Besides, it is possible to curb the testing costs performed before a prototype is made. Customer satisfaction, due to solid and durable products, comes as an extra benefit.

Fatigue calculations for high cycle elements make use of a method based on assigning certain values of stress to the number of stress change cycles, this is well known to designers. Numerous sources [6, 26] state that the boundary between high cycle and low cycle fatigue life is 104 or 105 cycles. Besides the strict determination of a limit value, it is more important to accept the general principle that calculations of high cycle fatigue strength are used for work within an elastic range, while low cycle fatigue calculations refer to the elastic-plastic range.

In practical fatigue calculations, computer programs based on the finite element method (FEM) are currently used, which automates the entire calculation process. Classification institutions also offer software of this type, e.g. the SESAM system (DNV), which includes programs that enable the performance of strength calculations, in accordance with the requirements of the regulations of this institution.

The general-purpose FEM systems currently used, such as ANSYS or ABAQUS (together with the SIMULIA software package), are based on the results of static calculations, and they enable fatigue calculations to be performed. These calculations are performed by the appropriate module built into the post-processor program (see the ANSYS Workbench – fatigue module). An example of such a program is ‘fe-safe’ which is delivered as part of the SIMULIA package (the manufacturer of 3DS-Dassault Systems) in cooperation with the ABAQUS program and other significant systems (NASTRAN, ANSYS).

The fe-safe program allows fatigue calculations to be performed with a wider scope and in a more advanced way than those required by the regulations and recommendations of classification institutions. The choice is between fatigue strength models based on Wohler stress relationships (known as S-N or “Stress-Life”) and those based on deformation (known as “Strain-Life”).

For the S-N type analyses, the program enables the definition of the transformation of the mean stress according to Godman, Gerber, Soderberg and others. For Strain-life analyses, the transforms given by Morrow, Smiths and others can be used. It is possible to define any fatigue load of characteristic load cycles: alternating, zero-pulsating, non-proportional or based on the readings of real signals (loads). The program includes a ready-made material database with assigned S-N curves. It is possible to define your own material library and the corresponding S-N curves and to define the correction of these curves due to the notch effect.

Fatigue analyses based on S-N (“Stress-Life”) relationships are commonly used for high-cycle fatigue strength. As a rule, low-cycle fatigue analysis is based on deformation relationships (“Strain-Life”). As a result of the fatigue calculations, the durability (or portions of failure) is obtained according to the Palmgren-Miller hypothesis.

The capabilities of the fe-safe program (as well as the Ansys-Workbench and others) enable fatigue calculations based on S-N curves, taking into account the appropriate correction factors contained in the regulations and recommendations of classification institutions, e.g. DNV. Results of the high-cycle S-N fatigue analysis in one of the above-mentioned programs will be received in the same way as defined in the regulations of these institutions.

It should be noted that the fatigue calculation methods described above include the fatigue of the structure material. Fatigue calculations of welds are a separate issue and classification institutions have separate requirements in this regard.

FATIGUE ANALYSIS ACCORDING TO THE REGULATIONS OF CLASSIFICATION INSTITUTIONS

Classification institutions, such as Lloyd’s Register or DNV (formerly known as Det Norske Veritas and Germanischer Lloyd, prior to a merger), issue separate classification and approval rules for on-board equipment, including lifting machinery and equipment. DNV has two separate standards for lifting appliances: one for offshore lifting appliances (“DNVGL-ST-0377 Standard for offshore and platform lifting appliances”), the other for conventional deck equipment, including the design of cranes mounted on merchant ships (“DNVGL-ST-0377 Standard for shipboard lifting appliances”). All of these regulations specify the number of load cycles in the expected service life and the fatigue strength.

Now, we briefly describe the requirements according to DNV. DNV for fatigue design is mainly based on the application of the S-N stress relationship, assuming linear cumulative damage (the Palmgren-Miner rule). The methodology is also widely described in the additional recommendation DNVGL-RP-0005 “RP-C203: Fatigue design of offshore steel structures”. For ship cranes, detailed fatigue strength requirements are specified in DNVGL-ST-0377 (Chapter 4.6). If they are in agreement with the classification institution, other recognised fatigue calculations may be used. Fatigue analysis is based on nominal S-N curves for plate structures. S-N curves obtained from fatigue tests are given in the DNV regulations or recommended practice.

If the fatigue life estimation based on S-N data is insufficient for a component in which failure may lead to serious consequences, a more detailed study covering the greater part of the structure or the fracture mechanics analysis, should be performed.

In this article, we discussed the Miner’s rule of cumulative damage; it is the simplest cumulative damage model. It states that if there are K different stress levels and the average number of cycles to failure at the i -th stress, then the partial damage D_i is determined as follows:

$$D_i = \sum_{k=1}^K \frac{n_k}{N_k} \quad (1)$$

where: K is the total number of blocks of the stress range spectrum, n_k is the number of stress cycles in block k and N_k denotes the number of stress cycles determined from the S-N curve.

The above equation can be thought of as assessing the proportion of life consumed at each stress level and then adding the proportions for all the levels together. Often, an index for quantifying the damage is defined as the product of stress and the number of cycles operated under this stress, which is:

$$W_i = n_i S_i \quad (2)$$

Assuming that the critical damage is the same across all the stress levels, then:

$$W_{failure} = N_i S_i$$

Using Eq. (2) as the critical value of damage that will result in failure, Eq. (1) becomes

$$D_i = \sum_{k=1}^K \frac{n_k S_k}{N_k S_i} = \frac{\sum_{k=1}^K n_k S_k}{W_{failure}} \quad (3)$$

For example, if $W_{failure} = 50$ for a component, it means that the component will fail after 10 cycles at a stress level of 5, or after 25 cycles, at a stress level of 2.

It is assumed that the fatigue strength is achieved when the cumulative failure D meets the condition:

$$D = \sum D_i \leq 1 \quad (4)$$

When the damage fraction reaches 1, failure occurs.

THE RESULTS OF NUMERICAL CALCULATIONS

In the fe-safe program, the fatigue calculations were carried out in accordance with the requirements of the DNV classification, adopting the high-cycle fatigue analysis of the S-N type. To perform the calculations requires the definition of the input parameters for the analysis. The most important of these are material data and the definition of a fatigue load. For comparison purposes, calculations were performed for two defined materials, i.e. steel with different S-N curves. For material A (steel, $R_m = 400$ MPa), the S-N curve was taken from the fe-safe database (the selected values are shown in Table 2).

As a result of fem analysis, performed with ABAQUS, the displacement of the jib end under a maximum load of 400 kN was 1,067 mm as depicted in Figure 4.

For individual structural elements of the crane (jib, crane housing and column), the locations of the highest von Mises stresses were identified (Figure 4). These values are listed in Table 1.

Spot B in Figure 5 is located at a height of 13.9 m from the column base. The place of greatest effort in the column, marked as C in Figure 5, is found 11.5 m up from the column base, where the column changes its shape from a cuboid to a convex socket. Maximum reduced stresses in the jib are located 15.8 m from the jib end, denoted as A in Figure 5.

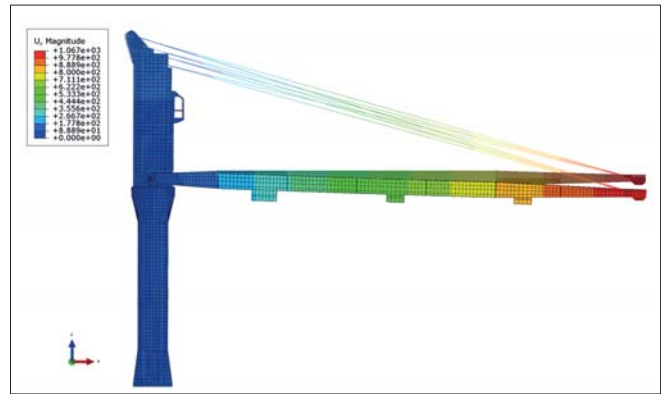


Fig. 4. Contour lines of the displacement under its own weight and working load of 400 kN (compared to the undisplaced model)

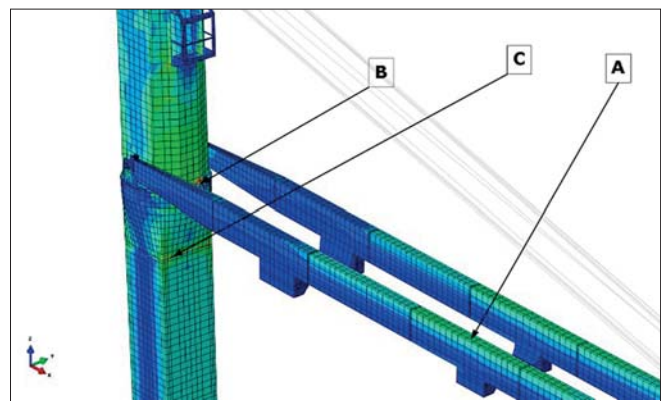


Fig. 5. Places of occurrence of the highest von Mises stresses f or individual structural elements of the crane

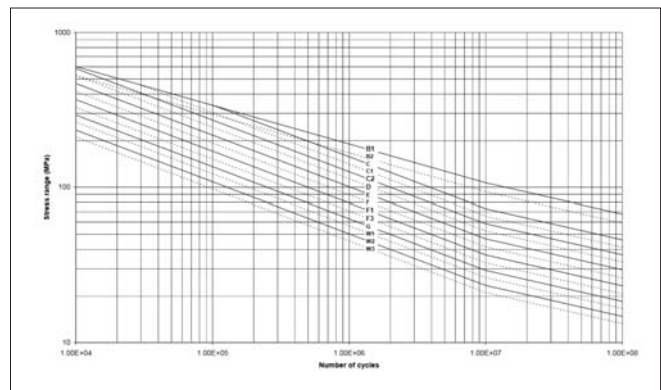


Fig. 6. S-N curves according to DNVGL ("RP C203 Fatigue design of offshore steel structures")

Tab. 1. The von Mises reduced stresses for structural elements of an individual crane

Part of the crane	Number of finite elements	Maximum von Mises stress [MPa]
Jib (A zone)	102,214	105.555
Crane housing (B zone)	300,714	368.251
Column (C zone)	203,798	281.16

Tab. 2 Material A (selected S-N values)

Number of cycles	10,000	1E7
Stresses	363 [MPa]	188.3 [MPa]

For material B, the S-N curve in the fe-safe program was defined on the basis of the DNV regulations and the curves presented therein, as in Figure 6.

Tab. 3. Results of fatigue calculations for selected points of the crane's structural elements. Material A

Part of the crane	Number of finite elements	Number of cycles	Damage/cycle
Jib (A zone)	102,214	No fatigue damage	No fatigue damage
Crane housing (B zone)	300,714	77,897	1.28E-05
Column (C zone)	203,798	2,286,472	4.37E-07

Tab. 4. Material B (selected S-N values, curve B1)

Number of cycles	10,000	1E7
Stresses	600 [MPa]	106.97 [MPa]

For material B, the S-N curve in the fe-safe program was defined on the basis of the DNV regulations and the curves presented therein, as in Figure 6.

The zero-pulsating cycle was adopted as the fatigue load (Figure 7). Therefore, calculations should take mean stress corrections into account.

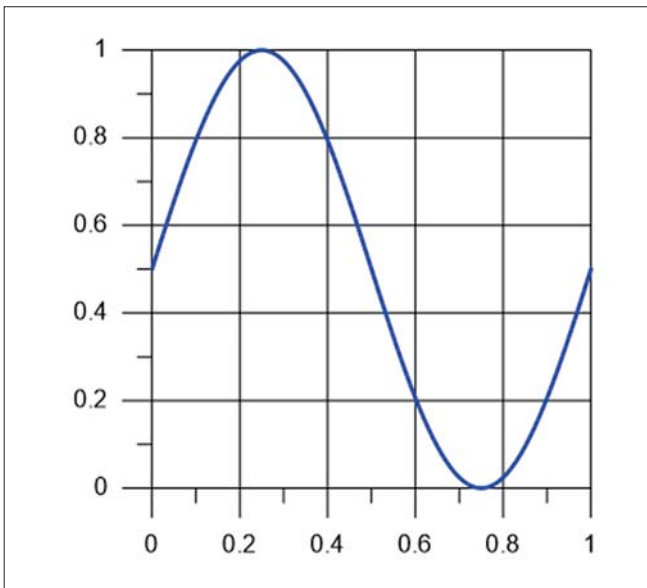


Fig. 7. The assumed fatigue load

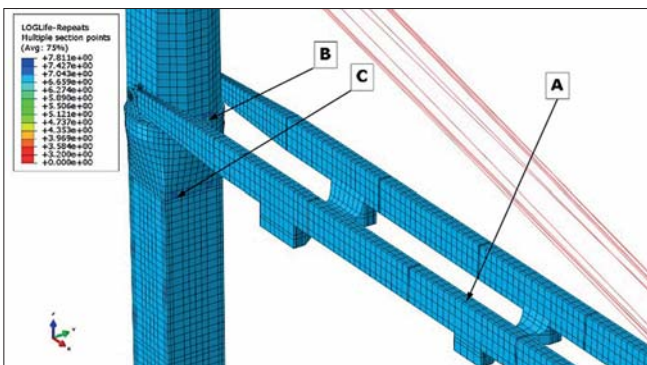


Fig. 8. Permissible number of cycles

The fe-safe system was also used to determine fatigue life (FL); it is the number of cycles (N) after which material fatigue will occur for a given value of stress. The higher the value of N means the higher the value of fatigue life. Figure 8 presents example contour lines of FL factor, determined for the surface finish factor $K_f = 1$ and $\sigma_m/\sigma_a = 1$. The higher the value of FL, the higher the value of fatigue life. For the previously selected points, the fatigue results are given in Table 3 for material A and Table 4 for material B, respectively.

Tab. 5. Results of fatigue calculations for selected points of the crane's structural elements for material B

Part of the crane	Number of finite elements	Number of cycles	Damage/cycle
Jib (A zone)	102,214	No fatigue damage	No fatigue damage
Crane housing (B zone)	300,714	163,538	6.115E-06
Column (C zone)	203,798	591,920	1.689E-06

Another widely used indicator of fatigue strength is Factor of Strength (FOS). FOS, defining the fatigue strength of a material as a function of working stress, is generally determined by using the Goodman or Soderberg formulas.

According to the Goodman formula, in the system (σ_m, σ_a) , FOS is determined from the equation

$$1/\text{FOS} = \sigma_m/\sigma_u + K_f(\sigma_a/\sigma_f) \quad (5)$$

where σ_a is stress amplitude, σ_m is mean stress, σ_u is the ultimate (tensile) strength, σ_f is the fatigue strength denoting the maximum stress at which an element will work an infinite number of cycles, and K_f denotes fatigue notch factor.

If the plasticity limit σ_y introduced into equation (3), FOS can also be determined according to the Soderberg formula

$$1/\text{FOS} = \sigma_m/\sigma_y + K_f(\sigma_a/\sigma_f) \quad (6)$$

Figure 9 presents contour lines of the FOS, that were determined by arbitrarily adopting the surface finish factor $K_f = 1$ and $\sigma_m/\sigma_a = 1$.

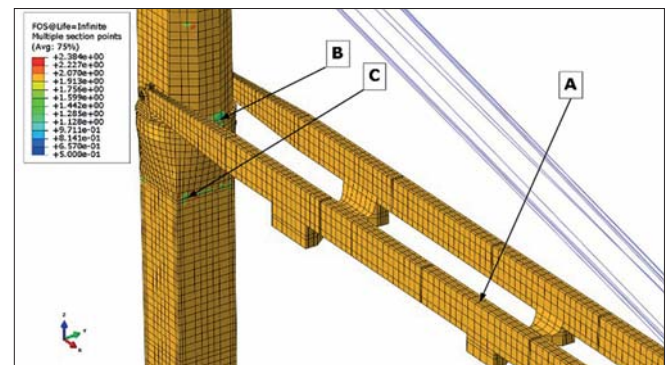


Fig. 9. Distribution of the Factor of Strength (FOS)

In the area marked B in the housing, the FOS assumes a value of 0.631. At point C on the column it is 1.218 while, at point A of the jib, FOS equals 2.0.

For the assumed zero-pulsating fatigue cycle, the influence of the average stress S_m (mean stress) was taken into account when adopting the Goodman formula. The graph of the stresses of S_a ('alternate stress') depending on the number of cycles, is shown in Figure 10.

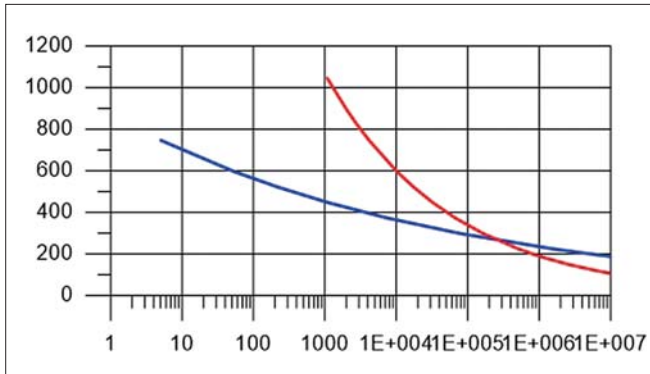


Fig. 10. Diagram of alternating stresses (S_a) versus the number of cycles (N). Material A and B

CONCLUSIONS

We determined the thicknesses of the metal plates used for the plating of the column, crane housing and the jib, and then selected and laid out the longitudinal and transverse stiffeners. Particular attention was paid to the modelling of those areas of the structure that are crucial to the safe crane operation (tie elements, pin joint connecting the jib and housing). When discretising tie elements, one should bear in mind that the mechanical properties of braided steel ropes substantially differ from the properties of individual component wires. The modelling of a structure by finite elements requires a careful choice of these elements. For instance, for a model of a girder, the ABAQUS library offers a number of plate and shell finite element types. Adopting incorrect finite elements may lead to wrong calculation results, regardless of the mesh density. According to the recommendation of the ABAQUS manual [3], thin plates (with a thickness to length ratio less than 1/15) were discretised by using shell elements marked as S8R5 (8-node tetragonal elements of a curved shell, reduced numerical integration, five degrees of freedom in a node) or STRI65 (6-node triangular elements, five degrees of freedom in a node). Thick plate elements were modelled with 8-node shell finite elements, denoted as S8R (tetragonal elements, six degrees of freedom in a node, and reduced numerical integration in calculations of the single element stiffness matrix). The fatigue analysis included examination of how the load characteristics (sinusoidal fluctuating, positive zero to tension pulsating and unilateral positive) and fatigue surface finish factor affect fatigue factors FOS and FL in selected regions of the column, the housing and the jib. The greater the values of FOS and FL are, the higher the value of fatigue life is.

Based on the acquired number of cycles of fatigue life it is possible to estimate the practical service life of a structure.

The use of advanced fatigue calculation software, such as fe-safe, allows one to automate and accelerate fatigue calculations of structures for real load cycles, measured experimentally. Such programs include advanced calculation models of fatigue strength as well as the most basic ones, which are included in the regulations and approved by classification institutions. Correctly performed numerical fatigue calculations can be accepted by classification institutions.

PRACTICAL RECOMMENDATIONS

1. Fatigue calculations (high-cycle fatigue strength) based on S-N curves are the basic calculations for the design of fatigue strength and for determining the life span of ship and offshore structures. These calculations reduce the probability of the formation and development of fatigue cracking (fracture mechanics) at the design stage (due to the probabilistic nature of loads and the dispersion of material property inaccuracies in performance).
2. Fatigue calculations of structural elements, based on the fracture mechanics according to the recommendations of classification institutions, can supplement those based on the S-N fatigue curves. For this purpose, the recommendations (according to DNV) are based on the known Paris equation describing fatigue (life expectancy and crack development) depending on the stress intensity factor K (not used here), which may be expressed as:

$$K = \sigma g \sqrt{\pi a}$$

where σ is the normal stress in the member normal to the crack, g denotes the factor depending on the geometry of the member and the crack, and a is crack depth.

3. The development of cracking usually occurs in the area of welded joints. Additional recommendations for the modelling and calculation of fatigue strength of welds are provided in the recommendations of classification institutions. According to DNV, they are also based on S-N curves (for welded joints). Numerical calculations with the use of FEM (appropriate mesh) are recommended with appropriate interpolation of the obtained numerical results regarding the nominal stresses in the area of stress concentration (notch).
4. In the case of crane fatigue strength, the calculations are reduced to fatigue calculations based on S-N curves and a comparison of the number of fatigue cycles obtained from calculations with those assumed at the design stage. In the case of ship structures, the operational period is assumed to be 20 years although, currently, there is a tendency to extend this period (up to 30 years or more).

REFERENCES

1. K.-J. Bathe, *Finite element procedures*. 2nd ed. New Jersey, Prentice Hall, 1996.
2. J. Carvill, *Mechanical engineer's data handbook*. 8th ed. Oxford, Butterworth-Heinemann, 2000.
3. Dassault Systemes Simulia Corp.: ABAQUS version 6.14: user's manual. Providence, Dassault Systemes Simulia Corp. 2014.
4. T. Deguchi, M. Mouri, J. Hara, D. Kano, T. Shimoda, F. Inamura, et al., "Fatigue strength improvement for ship structures by Ultrasonic Peening", *J Mar Sci Technol*, vol. 17(3), pp. 360–369, 2012.
5. M. Fonte, M. Freitas, B. Li, P. Duarte, L. Reis, "Welding assessment of a damaged crane pedestal of a container ship", *Ciência e Tecnologia dos Materiais*, vol. 27(1), pp. 10–14, 2015.
6. H.O. Fuchs, R.I. Stephens, *Metal fatigue in engineering*. 1st ed. New York, Wiley, 1980.
7. D.S. Han, S.W. Yoo, H.S. Yoon, M.H. Kim, S.H. Kim, J.M. Lee, "Coupling analysis of finite element and finite volume method for the design and construction of FPSO crane", *Automat Constr*, vol. 20(4), pp. 368–379, 2011.
8. R.B. Heywood, *Designing against fatigue of metals*. 1st ed. New York, Reinhold, 1962.
9. S.E. Hirdaris, W. Bai, D. Dessi, A. Ergin, X. Gu, O.A. Hermundstad, et al., "Loads for use in the design of ships and offshore structures", vol. 78, pp. 131–174, 2014.
10. S.E. Hirdaris, N.J. White, N. Angoshtari, M. Johnson, Y. Lee, N. Bakkens, "Wave loads and flexible fluid–structure interactions: current developments and future directions", *Ships Offshore Structures*, vol. 5(4), pp. 307–325, 2010.
11. R.C. Juvinall, *Engineering consideration of stresses, strain and strength*. 1st ed. New York, McGraw-Hill, 1967.
12. M. Kleiber, C. Woźniak, *Nonlinear mechanics of structures*. 1st ed. Dordrecht, Kluwer, 1991.
13. M.I. Kvittem, T. Moan, "Time domain analysis procedures for fatigue assessment of a semi-submersible wind turbine", *Mar Struct*, vol. 40, pp. 38–59, 2015.
14. A.A. Marquez, P. Venturino, J.L. Otegui, "Common root causes in recent failures of cranes", *Eng Fail Anal*, 39, pp. 55–64, 2014.
15. H.P. Lieurade, "Fatigue analysis in offshore structures", in *Advances in Fatigue Science and Technology: Proceedings of the NATO Advanced Study Institute on Advances in Fatigue Science and Technology*, Branco CM, Rosa LG, Eds. 1988 Apr 4-15; Alvor, Portugal. Dordrecht, Kluwer-NATO ASI E Series 159, 1989, pp. 585–625.
16. S. Pałkowski, *Konstrukcje ciegnowe*. 1st ed. Warszawa, WNT, 1994.
17. P.T. Pedersen, "Marine structures: future trends and the role of universities", *Engineering*, vol. 1(1), pp. 131–138, 2015.
18. Safe Technology Ltd.: Fe-safe version 6.5: user's manual. Sheffield, Safe Technology Ltd. 2014.
19. C.G. Soares, Y. Garbatov, "Fatigue reliability of the ship hull girder", *Mar Struct*, vol. 9(3–4), pp. 495–516, 1996.
20. C.G. Soares, T. Moan, "Model uncertainty in the long-term distribution of wave-induced bending moments for fatigue design of ship structures", *Mar Struct*, vol. 4(4), pp. 295–315, 1991.
21. P. Wirsching, "Fatigue reliability for offshore structures", *J Struct Eng. ASCE*, vol. 110(10), pp. 2340–2356, 1984.
22. F. Wu, W. Yao, P. Hu, "Fatigue life prediction analysis of crane structure on the basis of strain signal measure and MSC.Fatigue" in *Structural health monitoring and integrity management: Proceedings of the 2nd International Conference of Structural Health Monitoring and Integrity Management (ICSHMIM 2014)*; 2014 Sep 24–26; Nanjing, China, pp. 309–314, Boca Raton, CRC Press, 2015.
23. [O. Ozguc, "Assessment of Buckling Behaviour on an FPSO Deck Panel", *Polish Maritime Research*, vol. (3), pp. 50–58, 2020.
24. J. Łubiński, H. Olszewski, "Hybrid Finite Element Method Development for Offshore Structures. Calculation with the Implementation of Industry Standards", *Polish Maritime Research*, vol. 26(4), pp. 90100, 2019.
25. L. Samson, M. Kahsin, "A Method to Determine the Tightening Sequence for Standing Rigging of a Mast", *Polish Maritime Research*, vol. 26(4), pp. 47–55, 2019.
26. E. Zahavi, V. Torbilo, *Life expectancy of machine parts: fatigue design*, 1st ed. Boca Raton, CRC Press, 1996.

CONTACT WITH THE AUTHORS

Ryszard Buczkowski

e-mail: rbuczkowski@ps.pl

West Pomeranian University of Technology Szczecin

Piastów 41, 71-065 Szczecin

POLAND

Bartłomiej Żyliński

e-mail: bartek.zylinski@hotmail.com

West Pomeranian University of Technology Szczecin

Piastów 41, 71-065 Szczecin

POLAND

RESEARCH ON SHIP TRAJECTORY EXTRACTION BASED ON MULTI-ATTRIBUTE DBSCAN OPTIMISATION ALGORITHM

Xiaofeng Xu

Deqiang Cui*

Yun Li

Yingjie Xiao

Shanghai Maritime University, Haigang street, ShangHai

* Corresponding author: cuideqiang0213@163.com (D. Cui)

ABSTRACT

With the vigorous development of maritime traffic, the importance of maritime navigation safety is increasing day by day. Ship trajectory extraction and analysis play an important role in ensuring navigation safety. At present, the DBSCAN (density-based spatial clustering of applications with noise) algorithm is the most common method in the research of ship trajectory extraction, but it has shortcomings such as missing ship trajectories in the process of trajectory division. The improved multi-attribute DBSCAN algorithm avoids trajectory division and greatly reduces the probability of missing sub-trajectories. By introducing the position, speed and heading of the ship track point, dividing the complex water area and vectorising the ship track, the function of guaranteeing the track integrity can be achieved and the ship clustering effect can be better realised. The result shows that the cluster fitting effect reaches up to 99.83%, which proves that the multi-attribute DBSCAN algorithm and cluster analysis algorithm have higher reliability and provide better theoretical guidance for the analysis of ship abnormal behaviour.

Keywords: clustering algorithm, abnormal route, DBSCAN, Feature trajectory extraction, fitting analysis

INTRODUCTION

In the continuous development of maritime traffic, AIS (automatic identification system) data plays an extremely important role in the process of extracting ship tracks, analysing ship behaviour [1], and ensuring course safety. An AIS is an automatic identification system that can realise global coverage and send ship position information to the competent department and other ships every few minutes, so as to track the ship's trend and monitor its heading. It is an important resource for studying maritime activities [2]. AIS can be used in ship trajectory detection, ship trajectory outlier analysis and other aspects [3]. It can efficiently excavate typical sections of each characteristic pattern in the water area, and effectively use the AIS data of ship navigation to

provide great help for ship trajectory extraction [4][5], so as to guarantee the navigation safety of ships.

Scholars around the world have done a lot of research on AIS data application. Zhang et al. propose a multi-state ship trajectory reconstruction model. The model is processed in three steps, including (i) removal of outliers, (ii) estimation of the ship navigation state and (iii) ship trajectory fitting. The model allows the reconstruction of the ship's trajectory under different navigational conditions, such as berthing, manoeuvring and normal speed navigation. It is concluded that the performance of the model is better than that of the linear regression model [6]. Yan et al. propose a ship traffic route extraction method based on automatic ship history identification system (AIS) data. In this method, the ship trajectory with rich position information is transformed

into a ship navigation semantic object (STSO) with semantic information, and each ship navigation is abstracted into a stop-waypoint-stop navigation object. In addition, based on graph theory, STSO is further integrated into nodes and edges of directed maritime traffic charts to realise the extraction and expression of routes [7]. Wei et al. propose a new AIS trajectory compression algorithm based on ship behaviour characteristics, which takes into account the spatial and motion characteristics of the trajectory. The algorithm is mainly composed of two parts: one is to simplify the trajectory by using the Douglas-Peucker (DP) algorithm according to the spatial characteristics; the other is to simplify the trajectory by using a sliding window based on the motion characteristics. In addition, statistical theory is applied to determine the threshold of motion characteristics in the sliding window algorithm. The two results are combined to form a trajectory simplification algorithm considering ship behaviour [8]. Li et al. put forward the problem that AIS redundant information can reduce the accuracy of trajectory clustering. In order to improve the calculation accuracy and reduce the amount of calculation, the merged distance can be used to measure the similarity between tracks, and the low-dimensional spatial expression of the similarity between tracks can be used in multi-dimensional zoom (MDZ). Lin M.L used language to design and realise a prototype system of ship track clustering, so as to mine and analyse the important information in the AIS data and obtain the behavioural patterns of ships [22]. Sheng and Yin put forward a clustering model based on the track of the AIS data applied to the analysis of transport routes, where the entire model includes four main parts: data pre-processing, similarity measurement structure and typical path extraction, and clustering. The model considers the ship trajectory through geospatial information where different transport routes can be automatically classified. It allows experimental verification through specific waters. The results show that the model is effective, and helps to further understand the route model [10].

However, due to the impact of objective factors such as the environment, climate and the crew's subjective behaviour when the ship is underway, abnormal data will appear in the process of AIS data generation, and the accuracy and navigation under direct AIS data processing will be improved. Therefore, the detection of outliers in AIS data can better ensure navigation safety and make the processing of AIS data more accurate.

In AIS data processing research, a clustering algorithm is often used to process the ship trajectory, equipment and other data. Clustering algorithms have been widely used in various aspects such as ship trajectory extraction, ship anomaly detection and ship evaluation. Scholars around the world have conducted a large number of studies on this. Xiao et al. designed a ship track clustering algorithm based on AIS information. This clustering algorithm used the change of heading to obtain a candidate set of feature points, and determined the final feature points by the Minimum Description Length (MDL) criterion, so as to classify ship track class clusters, clustering large ships in specific waters

and obtaining the typical representative trajectories of ships [11]. Zhou et al., based on AIS data of a large number of ships, measured the trajectory similarity by fusion distance (MD). Aiming at the problem that the traditional DBSCAN algorithm needs to query the neighbourhood of each sample repeatedly, an improved DBSCAN algorithm is proposed to reduce the number of regional queries, thus improving the time efficiency of the algorithm and completing the clustering of the existing trajectory [12]. Cui has done much work and in his paper the characteristics and structure of the ship AIS trajectory data are summarised, a ship trajectory prediction model is established by using the related method of machine learning, and the future trajectory of the ship is predicted. The main research work includes data completion and exception handling methods. Based on the original AIS data, data completion and abnormal data processing were carried out. The work also includes a clustering and regression method for ship trajectory prediction. Combined with the classification idea, the K-medoids method is used to cluster the trajectory samples, and a regression prediction is made in each class to effectively reduce the difference between the trajectory samples. The experimental results show that the clustering regression method can improve the accuracy of prediction [13]. Liu and Shi use a new way to solve the problem. The skeleton extraction technology used for model reconstruction is used to carry out trajectory clustering analysis on the historical data of ships, which lays a foundation for studying the behaviour pattern of ships, and then provides a new method for regional navigational goods supervision. In view of the problem that the current trajectory clustering algorithm consumes a lot of computing resources and cannot process the trajectory quickly, the trajectory is converted into images for gradient compression and extraction clustering. The thermal surface of the track line was constructed by relying on the thermal distance field, and then the Laplacian operator was used to iteratively shrink the meshing thermal surface, and the profile skeleton line was obtained as the clustering effect picture [14].

In numerous studies, many extended algorithms have been developed based on clustering algorithms, among which the DBSCAN algorithm is widely used in ship trajectory extraction. Jiang, Xiong and Tang proposed an improved DBSCAN clustering algorithm. The ship trajectory was segmented by taking the angle and speed change as information measures, and the discrete Frechet distance was used as a trajectory similarity measure. The DBSCAN algorithm was used to cluster the trajectory segments, and the typical trajectory of ship movement was obtained [15]. Zhao, Shi and Yang proposed an adaptive hierarchical clustering method for the ship trajectory based on DBSCAN. By analysing the characteristics of the DBSCAN algorithm, the parameters are determined according to the internal distribution law of the data set and the change law of the quasi-clustering effect. Hierarchical clustering is carried out with statistical theory to adapt to ship trajectory data with an uneven density distribution [16]. Peng et al., based on the AIS data, used cloud computing and a clustering algorithm

to carry out trajectory clustering analysis on the historical data of ships and build the normal trajectory model of ship navigation, which lays a foundation for real-time detection of abnormal ship trajectories, and then provide a new method for improving the intelligent level of water traffic supervision. Aiming at the low efficiency of the current trajectory clustering algorithm, an improved parallel DBSCAN of sub-trajectory clustering algorithm SPDBSCANST (Parallel DBSCAN of sub-trajectory based on Spark) was proposed, based on Spark memory computing technology and data partitioning in order to mine the important AIS information [17]. Jiang, Xiong and Tang used an improved DBSCAN algorithm based on the turning angle and speed change rate of ships, combined with the Frechet Distance (FD) to measure the distance, and divided the track sections of ships. After realising the clustering results, typical representative tracks of ships' navigation were extracted, using a particular body of water for experiments. The experimental results show that the algorithm can improve the clustering effect and accuracy, and lay a foundation for the detection of ship trajectory anomalies [15]. Li et al. proposed that the redundant information of the AIS would reduce the accuracy of trajectory clustering. In order to improve the accuracy and reduce the amount of calculation, the similarity between trajectories was measured by combining the distance, and the low-dimensional space expression of the similarity between trajectories used multi-dimensional zoom (MDZ). The fusion between MDZ and the improved DBSCAN algorithm can identify the trajectory route well, and through the sampling data of specific waters, the DBSCAN algorithm is used to cluster the spatial points to verify the effectiveness and accuracy of the algorithm [9].

The existing clustering algorithms are mostly K-means, Spark, etc., compared with which DBSCAN has higher accuracy and a wider application range. However, the existing DBSCAN algorithm still needs to divide the ship trajectory, which will cause the loss of the ship trajectory and decrease the accuracy. Therefore, this paper proposes a multi-attribute DBSCAN extension algorithm, which vectorises the ship trajectory and avoids having to divide it, thus ensuring the complete ship trajectory and improving the calculation accuracy.

MULTI-ATTRIBUTE DBSCAN OPTIMISATION ALGORITHM FOR SHIP TRAJECTORY CLUSTERING

SHIP TRAJECTORY CLUSTERING BASED ON MULTI-ATTRIBUTE DBSCAN OPTIMISATION ALGORITHM

Currently, there are two main two research ideas about trajectory analysis and trajectory extraction: one idea is to target the trajectory as a whole for cluster analysis, which can better dig out the trajectory of the key path, but its existence may lose some general sub-tracks defects as shown in Fig. 1.

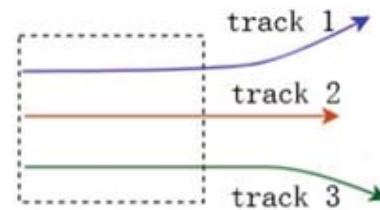


Fig. 1. Locally similar trajectories

Track 1, track 2 and track 3 have short movements with a similar general trajectory, as shown in the dotted box of the figure. If the clustering trajectory is treated as a whole, it could cause the loss of some similar sub-tracks, leading to a lack of important information. Another research idea is to divide the whole ship track into several sub-tracks. This method can effectively avoid missing sub-track information, but it also damages the integrity of the track.

SHIP TRAJECTORY CLUSTERING MODEL

Formula and similarity measure of distance between ship track points

The division of data needed to calculate the similarity between samples and the similarity calculation method between samples can be abstracted as a sample distance function. In order to calculate the distance between samples and the similarity between samples from a distance matrix, assuming that the extracted sample is X , the number of samples is n , the dimensions p , the distance matrix can be expressed in the following form:

$$\begin{bmatrix} X_{11} & \cdots & X_{1p} \\ \vdots & \ddots & \vdots \\ X_{n1} & \cdots & X_{np} \end{bmatrix}$$

where X_{ij} represents the j -th dimension data of the i -th sample.

Design of structural similarity distance formula

In the distance calculation, the following formulas are needed: Euclidean distance [18], Manhattan distance [19], Chebyshev distance and Minkowski distance [21].

1) Euclidean distance

Used to represent the distance between two points. In n -dimensional space, the Euclidean distance formula can be expressed as

$$d_{ij} = (P_i, P_j) = \left(\sum_{k=1}^m |x_{ik} - x_{jk}|^2 \right)^{1/2}$$

2) Manhattan distance

Used to represent the sum of the absolute values of the wheelbase of two points in the standard coordinate system. In n-dimensional space, the Manhattan distance calculation formula is expressed as

$$d_{ij} = (P_i, P_j) = \sum_{k=1}^m |x_{ik} - x_{jk}|$$

3) Chebyshev distance

Used to represent the maximum value of each coordinate. In n-dimensional space, the Chebyshev calculation formula is expressed as

$$d = \text{Max}(|x_{1_1} - x_{1_2}|, |x_{2_1} - x_{2_2}|, \dots, |x_{n_1} - x_{n_2}|)$$

4) Minkowski distance

When n=1, the Minkowski distance is the Manhattan distance; when n=2, the Minkowski distance is the Euclidean distance. The calculation formula is as follows:

$$d_{ij} = (P_i, P_j) = \left(\sum_{k=1}^m |x_{ik} - x_{jk}|^n \right)^{1/n}$$

The Manhattan distance, also known as the “taxi distance”, depends heavily on the coordinate system. The distance between points changes as the coordinate axis changes. The Euclidean distance refers to the distance between two points.

In order to solve the problem of trajectory loss caused by trajectory similarity, the concept of structural distance is introduced, and different weights are assigned to different attributes of the trajectory according to the actual scene, so as to comprehensively judge the similarity between trajectories. The distance between ship tracks is abstractly defined as the distance between vector points by using the position, speed and heading attributes contained in the ship track data. Thus, the formula of the structural similarity distance between two vector points is given as follows:

$$D_{\text{dist}}(P1, P2) = \frac{w1 * d1(P1, P2) + w2 * d2(P1, P2) + w3 * d3(P1, P2)}{w1 + w2 + w3 = 1}$$

where:

$D_{\text{dist}}(P1, P2)$ represents the structural distance between the vector points P1 and P2;

$d1(P1, P2)$ represents the spatial distance between the vector points P1 and P2;

$d2(P1, P2)$ represents the speed deviation between P1 and P2;

$d3(P1, P2)$ represents the course deviation between the vector points P1 and P2;

w_n represents the weight of the attribute N of the trajectory over the structural distance.

DBSCAN OPTIMISATION ALGORITHM

DBSCAN is one of the most widely used and referenced clustering algorithms. In density-based clustering, the phenomenon of clustering is that high-density regions are separated by low-density regions. Compared with other types of clustering, the density-based clustering algorithm is an unsupervised clustering algorithm, which is not sensitive to noise data and can find clusters of any shape and size without setting the number of clusters in advance. It is very suitable for clustering in the case of AIS trajectory data with many noise points and a highly uncertain trajectory pattern. The following describes the relevant definitions involved in density-based clustering:

1 Eps fields

Given an object P, with P as the centre, the area with a radius of eps (epsilon) becomes the eps domain of object P. The expression of the definition is as follows:

$$N_{\text{eps}}(P) = \{d \in D | \text{dist}(P, Q) \leq \text{eps}\}$$

where D is the given data set, and $\text{dist}(P, Q)$ represents the distance between P and Q in the data set.

2 Core objects

If the eps domain of an object P includes at least minPts objects (minPts represents the minimum number of points), then P is called the core object.

3 Direct density can be reached

In a given object data set D, if P exists in the eps field of Q, where P is a core object, the object P to object Q is directly denser.

4 The indirect density is achievable

If there is an object chain $P1, P2, \dots, Pn, P1=q, Pn=P$, for $P_i \in D, 1 \leq i \leq n$, if P_{i+1} and P_i from eps and minPts are directly accessible, then the density of object P to object Q is reachable, and it is an indirect density.

5 Densities are connected

If there is an object O in the given object set D, for objects P and Q, from object Q about eps and minPts are density-accessible, then it means that objects P and Q are connected about the eps and minPts density.

The DBSCAN algorithm requires two parameters (eps and minPts) and works by differentiating between core points, border points and noise. The concept relationship of the DBSCAN algorithm is shown in Fig. 2. The operation effect of the DBSCAN algorithm is shown in Fig. 3.

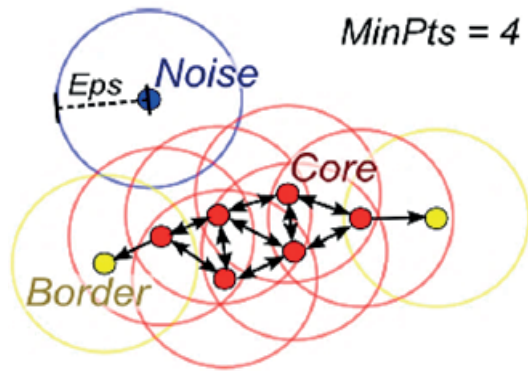


Fig. 2. DBSCAN algorithm concept relationship

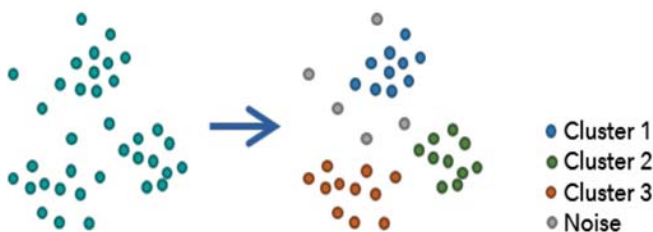


Fig. 3. DBSCAN algorithm running effect

The pseudocode of the DBSCAN algorithm is shown in Table 1.

Tab. 1. DBSCAN algorithm pseudocode

DBSCAN Algorithm
Input: data object D, object radius eps, minimum number of minPts
Output: Clustering results
Algorithm start:
1: Initialise a new class cluster C
2: for each object that is not marked in the data set P do
3: if Neps(p) Contained object \geq minPts then
4: Add all the points in P to C
5: for all unprocessed objects in Neps(p) the q do
6: if Neps(q) contains at least minPts objects
7: Objects in Neps(q) that do not belong to the class cluster are added to C
8: end if
9: end for
10: else Label P for noise
11: end for
END

MULTI-ATTRIBUTE DBSCAN OPTIMISATION ALGORITHM

Trace clustering follows the law of “birds of a feather flock together”, which divides a bunch of unmarked data into piles after some similarity measurement method, which is called clustering. Each cluster comprises trajectory data points with high similarity. When the similarity between points is higher and the similarity between clusters is lower, the overall clustering effect will be better.

The original DBSCAN algorithm is a clustering algorithm based on density. The core of the algorithm is two parameters, namely the eps field and the minimum number of points, minPts. The eps field represents the field within the object radius eps, and Neps(p) is used to represent the set within the eps radius of point P. An object is called a core object if it contains at least minPts of other objects within the eps domain of the object. In this paper, the DBSCAN algorithm is extended on the basis of the AIS data set, making full use of the three attributes of ship position, speed and heading, and simplifying the originally complex trajectory segment to the similarity measure between vector points. In order to conform to the reality of the more complex marine traffic flow situation, two control variables SpdRange and DirRange are added to the input variables of the model, to control the ship’s speed range and scope of course, according to the practical application scenarios. In the process of ship’s trajectory clustering, constraints of the ship speed and the range of the course must be considered, because it may enter port at a low speed, and may also have left port at a high speed, so SpdRange and DirRange are considered. Ship trajectory points that are not only similar in spatial position but also have little difference in ship speed and basically the same ship direction are gathered into a cluster. The pseudocode of this algorithm is shown in Table 2 below.

Tab. 2 Multi-attribute DBSCAN extension algorithm pseudocode

Multi-attribute DBSCAN extension algorithm
Model inputs: data object D, object radius eps, minimum number of points minPts, speed threshold range SpdRange, ship direction threshold value DirRange
Model output: clustering results
start:
1: Definition of method 1: multi-attribute DBSCAN extension algorithm (dataSet D, P, eps, minPts, SpdRange, DirRange)
2: Initialise an empty clusterList
3: for each point P in dataset D do
4: queryNeighbourPoints(dataSet D, P, eps, minPts, SpdRange, DirRange)
5: if neighbourPts not NULL then
6: neighbourPts add to clusterList 中
7: for each cluster C in clusterList do
8: for each clusterC'' in clusterList do
9: if C and C'' && mergeCluster(C, C'') is TRUE
10: clusterList.remove(C'')
11: return clusterList
12: Define Method 2: queryNeighbourPoints(data, P, eps, minPts, SpdRange, DirRange)
13: Initialise an empty set cluster
14: for each point Q in data do
15: if distance(P,Q)<eps && P.SOG-Q.SOG <SpdRange && P.COG-Q.COG <DirRange
16: add Q to cluster
17: if cluster.size>minPts
18: Mark point P as the core object
19: return cluster
20: or return NULL
21: Define Method 2: mergeClusters(cluster A, cluster B)
22: merge=FALSE
22: for each point Q in cluster B do
23: if point Q is the core object && cluster A contains the point Q
24: merge=TRUE
25: All objects in cluster B are added to cluster A
END

The purpose of Method 2 (QueryNeighbourPoints) is to compare point P with all other ship track points to find track points similar to it. The core idea of this method is as follows: first, to judge whether there is a point-point P relationship in the ship trajectory data set that conforms to the designed similarity structure. The second step is to judge whether the number of track points contained in the cluster is greater than minPts. The third step is to judge whether the cluster contains at least minPts track points. If so, it means that the cluster is reasonable. Otherwise, the return object is null.

In the pseudocode, short $(P, Q) < eps \ \&\& \ | p. OG - Q.S OG | < SpdRange \ \&\& \ | P.C OG - Q.C OG | < DirRange$'s role is to judge a vector points with another vector in line with the similarity measure scheme. With the formula expressed as follows:

$$D_{dist}(P,Q) = w1 * d1(P,Q) + w2 * d2(P,Q) + w3 * d3(P,Q)$$

$$w1 + w2 + w3 = 1$$

Given $D_{dist}(P, Q)$, the structural distance between points P and Q, the structural distance between two points needs to meet conditions: short $(P, Q) < eps \ \&\& \ | p. OG - Q.S OG | < SpdRange \ \&\& \ | P.C OG - Q.C OG | < DirRange$, where short (P, Q) is the space distance between points P and Q; $| p. OG - Q.S OG |$ is the speed deviation of the points P and Q; $| P.C OG - Q.C OG |$ indicates points P and Q of the ship to the deviation range.

Method 3 (mergeClusters) consolidates the cluster of classes obtained through method 2 (queryNeighbourPoints). If the core point of class cluster A happens to be the boundary point of class cluster B, then according to the merge condition of the DBSCAN algorithm, class cluster A and class cluster B need to be fused.

SHIP SIMULATION

The improved multi-attribute DBSCAN extension algorithm is applied to ship trajectory extraction in waters near the main waterway of Jintang Bridge to carry out a simulation verification of the algorithm.

AIS DATA PRE-PROCESSING

By 1 June 2017 solstice JCP 4, AIS data after being decoded pre-treatment according to the ship MMSI number matching with AIS static information table are not accessible. Therefore, some static information is inaccurate and it required to adopt the method of manual entry of real AIS data.

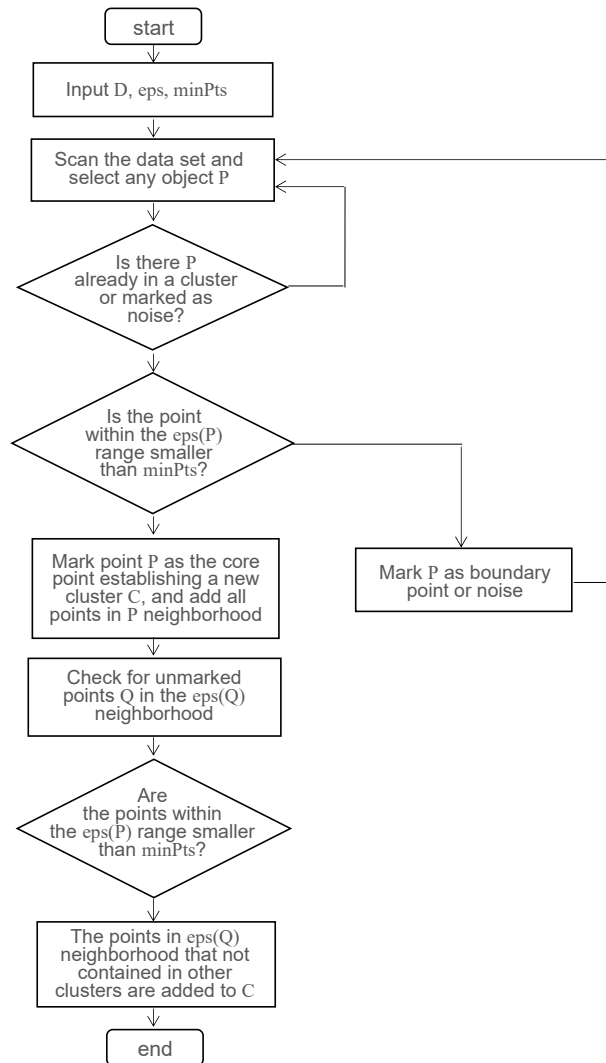


Fig. 4. Algorithm flow chart

After correction of AIS information that were incorrect for 221217 real AIS data of 638 ships, we removed redundant AIS data information used in the simulation. For the obtained AIS data samples, the proportions of each ship type were calculated statistically. The distribution of ships is shown in Fig. 5.

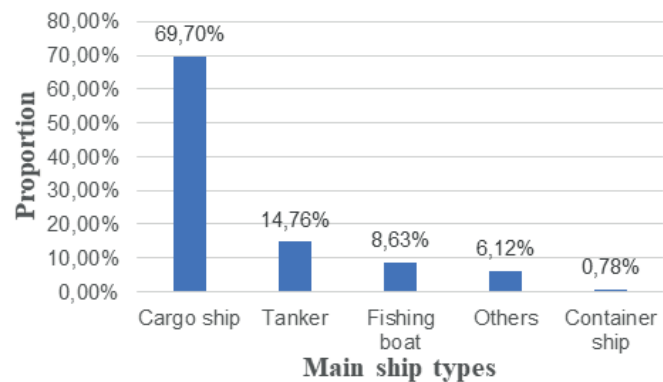


Fig. 5. Distribution of ships

As can be seen from Fig. 5, the main types of ships in the study area from large to small are: cargo ships (mainly liquid cargo ships and dry cargo ships), oil tankers, fishing ships and other types of ships (mainly pilot ships, dredging ships and tugboats). Among them, cargo ships, oil tankers and fishing vessels account for the majority, at 70.49%, 14.76% and 8.63% respectively, and amounting to 91.79% of the total number of ships.

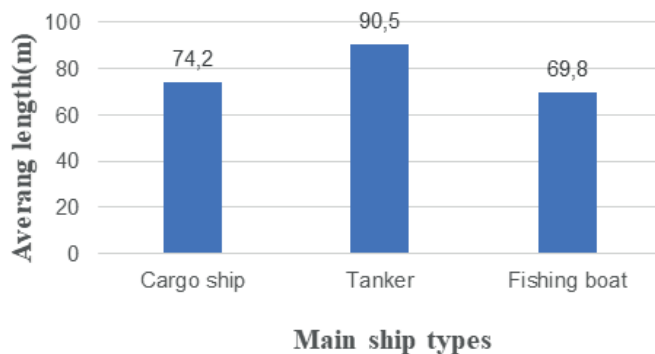


Fig. 6. Average ship length distribution

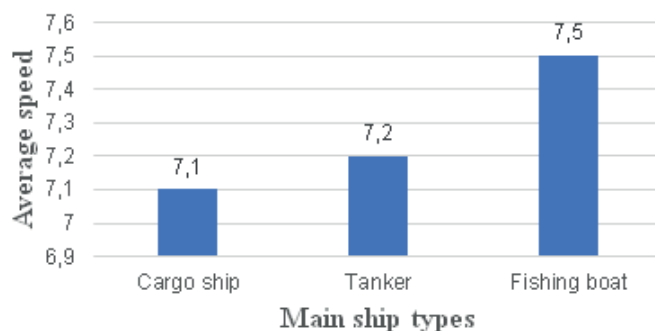


Fig. 7. Distribution of average ship speed

After screening, counting and calculating the lengths of the three ship types (cargo ships, oil tankers and trawlers), the average length distribution of all kinds of ships can be obtained, as shown in Fig. 6.

After screening, counting and calculating the speed of the top three types of ships (cargo ships, oil tankers and trawlers), the average speed distribution of all kinds of ships can be obtained, as shown in Fig. 7.

In order to analyse the main features of ship navigation in the water area, the multi-dimensional ship information in the water area is visualised and a four-dimensional ship information parallel coordinate chart is made. The relevant information of different types of ships is divided into four categories (cargo ship, oil tanker, fishing ship and others) in different colours. For each type of ship there are three corresponding attributes: speed, length and ship width, as shown in Fig. 8.

Ships of different tonnage have different requirements for speed control and water depth. In the process of entering and leaving port, the inertia and draft depth of large ships are larger, and the elimination of residual velocity is slower. Navigation must be in strict accordance with the regulations

of the port authorities. The draft depth of small ships is relatively shallow and the manoeuvrability is good, which will cause small ships to travel too fast and be unable to enter or leave ports according to the requirements of ports. If the AIS data is not screened in advance, the clustering results will be very confusing, making it difficult to show the clustering effect, so the validity and correctness of the clustering results cannot be accurately judged.

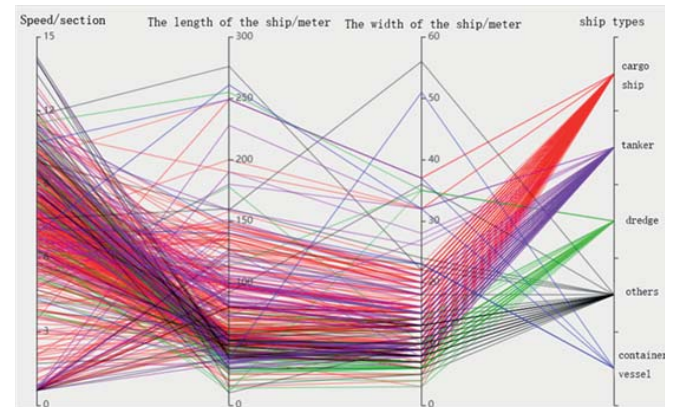


Fig. 8. Parallel coordinate chart of ship data

According to the distribution of ship types in the study area, their different ship track density and different ship lengths were displayed with the help of the BDP visual tool at the distance of 50 m and analysed according to the different ship lengths, so as to determine that the main objects of study were cargo ships and oil tankers. The process is as follows:

The track points of this water area are divided into two types: ship shelving point and ship movement point. In determining the speed threshold values of the shelving points and movement points of the ships in the study waters, it was found that when the sailing speed was within the range of 0-1 kn, the ship tracks presented the largest number of scatter points, and there were no continuous track points. These scatters were thus judged to be shelving points. If the filter speed value range is 0-1.1 kn, there will be continuous trajectory points, indicating that the current 1.1 kn is not the optimal speed threshold. Therefore, the optimal speed threshold is set as 1 kn to distinguish the shelving points and movement points. Track density visualisation is carried out for the shelving points of freighters and oil tankers with different lengths, showing the distribution of the ship track density when the speed is 0-1 kn. From the ship track density distribution, the hot spots of shelving points of different types of ships with different lengths can be intuitively found.

The following is a visual analysis of the trajectory density of the shelving points of cargo ships and oil tankers. First, the distribution of the trajectory density of the cargo ships' shelving points is shown in Fig. 9, Fig. 10 and Fig. 11. When the speed distribution is 0-1 kn, it is found from these three figures that the shelving point of each length presents a scattered distribution. Among them, 0-50 m and 50-100 m cargo ships are mainly anchored near Taepokou. The 100-150 m cargo ships are mainly anchored near the Yongjiang waterway.

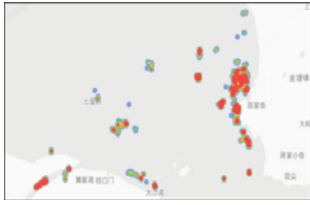


Fig. 9. Track density distribution of lay down points of 0-50m long cargo ship

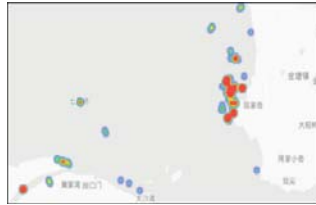


Fig. 10. Track density distribution of lay down points of 50-100m long cargo ship

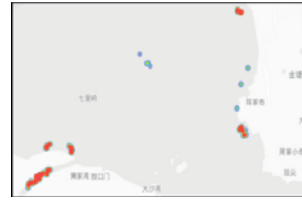


Fig. 11. Track density distribution of lay down points of 100-150m long cargo ship

Fig. 12 and Fig. 13 show the distribution of the trajectory density of the shelving points of oil tankers.

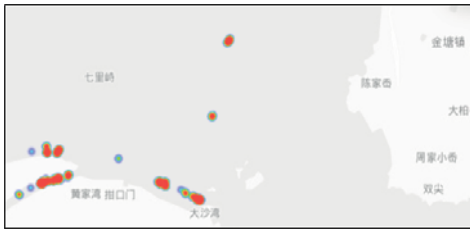


Fig. 12. Track density distribution of lay down points of 50-100m oil tankers



Fig. 13. Track density distribution of lay down points of 100-150m oil tankers

When the speed distribution is 0-1 kn, it can be seen from the above figures that the shelving points of each ship length also present a scattered distribution. As tankers with a length of 0-50 m do not have a shelving point, they are not shown. The 50-100 m and 100-150 m vessels are mainly anchored near Zhenhai, Beilun and the Yongjiang waterway. Visual analysis of the trajectory density of the movement points of cargo ships and oil tankers is carried out. The motion point trajectory density distribution of the cargo ships is shown in Fig. 14, 15 and 16.



Fig. 14. Trajectory density distribution of 0-50m cargo ship

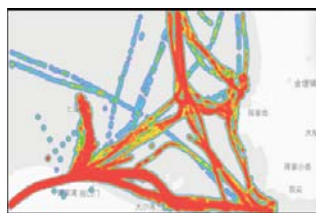


Fig. 15. Trajectory density distribution of 50-100m cargo ship

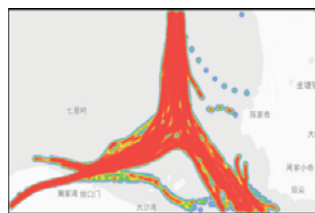


Fig. 16. Trajectory density distribution of 100-150m cargo ship

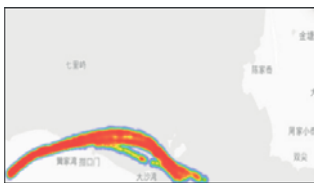


Fig. 17. Trajectory density distribution of 0-50m oil tanker

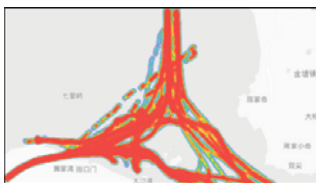


Fig. 18. Trajectory density distribution of 50-100m oil tanker

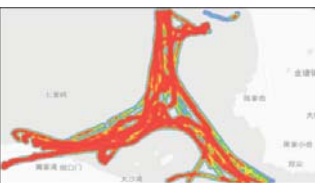


Fig. 19. Trajectory density distribution of 100-150m oil tanker

It can be seen from Figs. 14, 15 and 16 that the movement track of the 0-50 m ships is very similar to that of the 50-100 m ships, but the movement track distribution is chaotic. Comparatively speaking, ships with a length of 100-150 m

have the most concentrated and regular movement tracks. Next, the trajectory density of the movement points of oil tankers was analysed visually as shown in Fig. 17, 18 and 19.

It can be seen from Figs. 17, 18 and 19 that the movement points of the tankers with a length of 0-50 m are distributed in a concentrated way, mainly in the channel near Beilun. The trajectory distribution of 50-100 m and 100-150 m length tankers is similar and relatively regular. However, from the comprehensive consideration of the track number, track density and track regularity, 100-150 m long cargo ships are more dominant and more representative in the study

area. To sum up, in order to avoid the poor display of the ship trajectory clustering results, the cargo ships with a length of 100-150 m are selected as the research objects of this clustering experiment. These research objects are representative, and the clustering results can be used as a reference for future channel planning research of this study area.

CLUSTERING ANALYSIS

By 1 June 2017 solstice 4 JCP 4, a total of 221217 AIS data after decoding and data pre-processing, and removal of incorrect AIS data we selected the research object. It was ships of lengths of 100-150 m with the set speed threshold of 0-1 kn. After extracting the movement track points, a total of 40147 AIS data were used. The daily AIS data statistics are as shown in Table 3.

The ship shelving points and movement points are treated differently. According to the navigation speed threshold of 1 kn, the ship shelving point or the ship movement point in the water area of interest in this study is regarded as the critical value. Collision hazards are more likely to occur when

the ship is moving, and the damage caused by an impact at speed is greater. Therefore, compared with the shelving point, analysis of the ship's movement point is more important. Therefore, trajectory clustering analysis is mainly carried

out for ship movement points. In this study, there are 511 AIS data of ship shelving points and 36,719 AIS data of ship movement points in total. The trajectory data sets of each ship trajectory cluster were obtained by inputting the optimal parameters obtained from multiple experiments through the ship trajectory cluster model ($\text{eps} = 0.015$, $\text{minPts} = 45$, $\text{DirRange} = 1.5$, $\text{SpdRange} = 2$), and the trajectory data sets of each ship trajectory cluster were visualised through the BDP visualisation platform, distinguished in different colours.

Tab. 3. AIS data statistics table

Time	June 1	June 2	June 3	June 4
AIS numbers	10420	9380	10693	9654

The traffic flow in this water area involves an intersection of three directions, which resembles the shape of a “man”, and the traffic flow at the middle crossing is relatively complex. This paper simplifies the complex problem, divides the whole traffic flow into three data sets, and conducts clustering for each segment, each with its own route segment characteristics, as shown in Fig. 20.

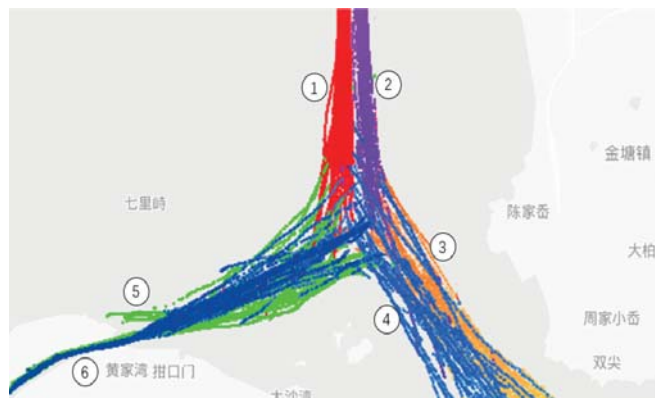


Fig. 20. Results of ship trajectory clustering

A total of 6 ship track class clusters were obtained, represented in different colours and numbered 1-6 respectively. The main channel of the bridge in and out of the Jintang Water area has been separated and is navigable, while the remaining sections have not been set up yet. Based on the analysis of the experimental results of ship trajectory clustering, ship trajectory clusters 1 and 2 of the main channel are found. Due to the implementation of the lane separation and navigation system in this water area, the ship trajectory cluster is relatively regular. All the ships passing through this area can navigate well within the established channel range, and the ship trajectory clustering results are consistent with the actual traffic flow.

Ship trajectory clusters 3 and 4 respectively represent the clusters entering and leaving the waters near Tapukou. Since the traffic separation system has not been implemented in this area, as shown in Fig. 18, some ship trajectories will deviate from the usual navigation tracks of most ships. It is found from the result of ship track clustering that the implementation of a traffic separation system is of positive

significance to the regulation of ships entering and leaving ports.

Trajectory cluster 5 represents the cluster in the direction of Zhenhai. A small number of ships enter the Yongjiang Channel. Trajectory cluster 6 indicates that the river flows out of Yongjiang in other directions.

Based on the main channel clustering results (track clusters 1 and 2) in the water area of Jintang Bridge, the speed and course frequency of each track cluster are statistically analysed. The results are shown in Fig. 21 and Fig. 22.

It can be seen from Figs. 23 and 24 that, in track cluster 1, the average speed is 9.67 kn, and the interval with the most frequent occurrence of speed value is [5.0,7.7], [7.7,10.4], [10.4,13.1], which is similar to the southbound track cluster, with a large range of speed variation. Ships belonging to this track cluster also have significant speed reductions or increases while moving. Due to the particularity of the traffic flow direction in this water area, it is shaped like a “man”. After a section of direct travel, ships often need to turn sharply, which has a great impact on their speed. The average course is 355.76° . The maximum range of course is from 154° to 189° , among which the ranges with the highest frequency of course values are [349,355], [355,0] and [0,5], which are in line with the actual direction of traffic flow.

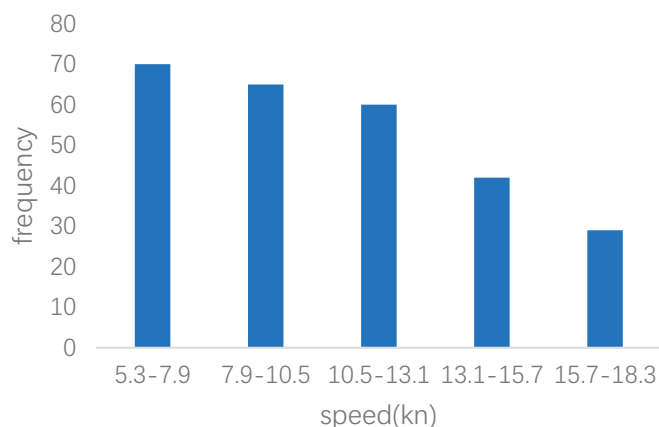


Fig. 21. Speed frequency distribution of trajectory class cluster 1

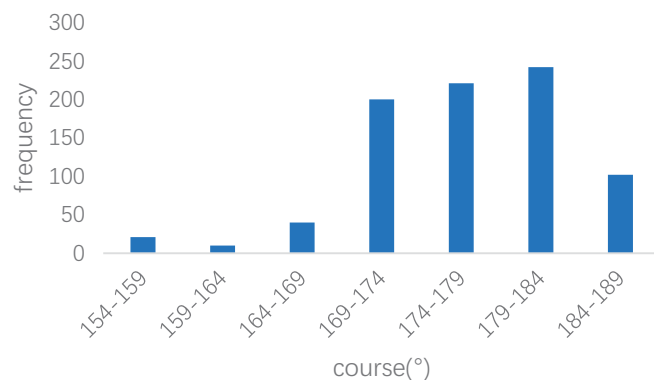


Fig. 22. Course frequency of trajectory class cluster 1

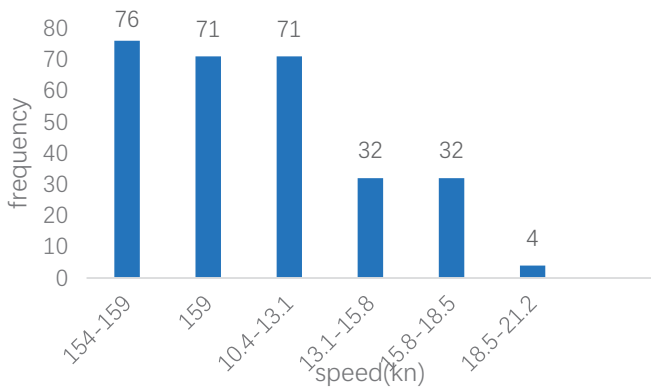


Fig. 23. Speed frequency distribution of trajectory class cluster 2

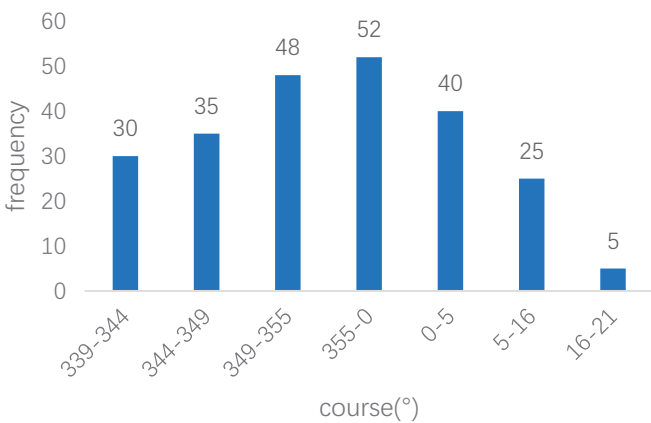


Fig. 24. Course frequency of trajectory class cluster 2

To sum up, the average speeds of ships heading south and north do not differ much, at 8.12 kn and 9.67 kn respectively and the average speed of ships heading north will be greater. The average heading of ships heading south and north is approximately opposite, which is 179.39° and 355.76° respectively. The analysis of the other four track clusters is the same as above. The ship navigation profile of each track cluster can be obtained by analysing the distribution of the speed and course frequency of each track cluster.

REPRESENTATIVE TRAJECTORY EXTRACTION

In order to further verify the reliability and accuracy of the multi-attribute DBSCAN algorithm, representative trajectories of class clusters are extracted for fitting. Each ship trajectory cluster has three attributes: position, speed and heading. Combined with the characteristics of vectors, a concept similar to representing vector points is proposed to compress the number of track points in the trajectory cluster. Existing studies have introduced the clustering method based on the trajectory line. In this paper, the method is the point-based clustering algorithm, so the output result of the algorithm is a collection of multiple trajectory points. The process is to calculate the average direction of all trajectory points of each trajectory cluster. In this direction, the trajectory cluster is divided into multiple parallel blocks, using

the interval as the normal line. The width is determined based on domain knowledge or the results of multiple experiments. Finally, the parameter eps value used in the clustering algorithm is 0.15 as the block length. Each parallel block is calculated to represent the vector points, in which Avg(LAT) and Avg(LON), the central positions of all locus points, are taken as the starting points of the representative vector points. The average speed Avg(SOG) of all trajectory points is used as the magnitude of vector points. Avg(COG), the average course of all track points, is used as the direction to represent the vector points, and the three dimensions (centre position, average speed and average heading) together constitute the vector track points. After calculating the representative vector points of all parallel blocks, all the representative vector points are connected to form the representative trajectory, as shown in Figs. 23 to 34. In this paper, only the trajectory fitting to the represented trajectory cluster 1 and 2 is listed, and the remaining trajectories are similar to these.

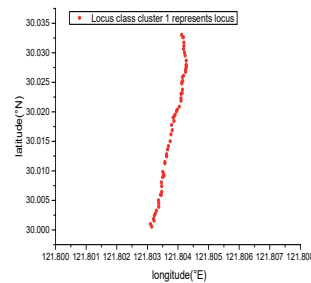


Fig. 23. Class cluster 1 represents the trajectory

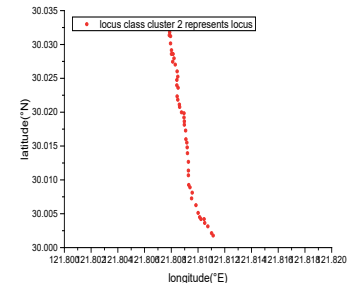


Fig. 24. Cluster 2 represents trajectory

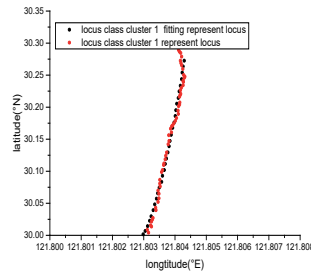


Fig. 25. Cluster 1 northbound of main channel represents trajectory fitting

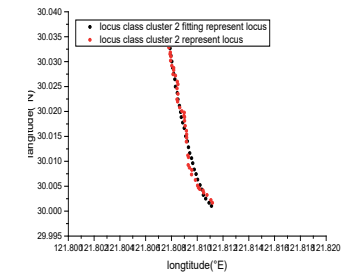


Fig. 26. Cluster 2 main channel southward represents trajectory fitting

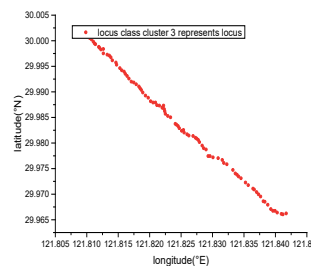


Fig. 27. Cluster 3 represents the trajectory

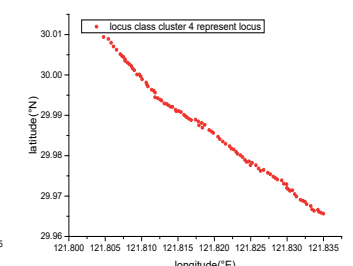


Fig. 28. Cluster 4 represents the trajectory

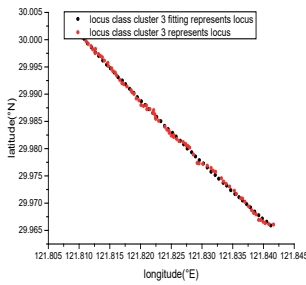


Fig. 29. Cluster 3 Dapu estuary represents the water area fitting

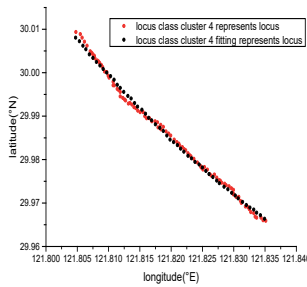


Fig. 30. Cluster 4 Dapokou represent the water area

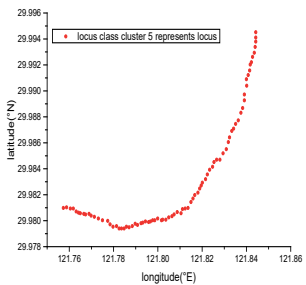


Fig. 31. Class cluster 5 represents the trajectory

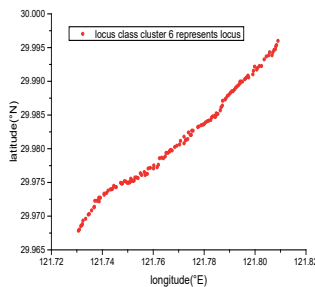


Fig. 32. Class cluster 6 represents the trajectory

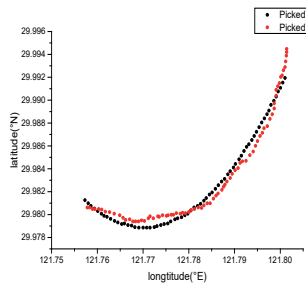


Fig. 33. Cluster 5 represents trajectory fitting

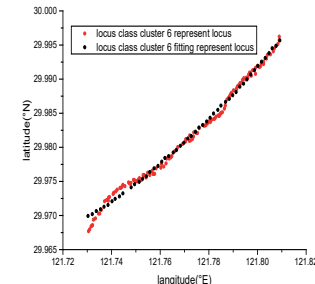


Fig. 34. Curve fitting of class cluster 6 out of Town harbor

RESULTS

From 40147 AIS data, 579 effective representative trajectory points were extracted to form 6 representative trajectory lines, accounting for about 1.44% of the total points.

The locus cluster 1 represents the starting position of the locus (30.033285°N, 121.804102°E) and the ending position (29.995572°N, 121.80227°E). At the same altitude, the distance between two points in geographical space is 2.266 nautical miles, and the azimuth angle formed between two points is 182.4°. By means of the regression model, the fitting degree of the original representative trajectory was calculated to be about 96.37%.

The locus class cluster 2 represents the starting position of the locus (30.00184°N, 121.811125°E) and the ending position is (30.032807°N, 121.8078°E). At the same altitude, the distance between two points in geographical space is 1.869 nautical miles, and the azimuth angle formed between two points is 349.1°. By means of the regression model, the original trajectory fitting degree is about 97.62%.

The locus class cluster 3 represents the starting position of the locus (30.001808°N, 121.809547°E) and the ending

position (29.966182°N, 121.841095°E). At the same altitude, the distance between two points in geographical space is 2.696 nautical miles, and the azimuth angle formed between the two points is 142.5°. By means of the regression model, the original trajectory fitting degree is about 99.89%.

The locus class cluster 4 represents the starting position of the locus (29.965868°N, 121.835008°E) and the ending position (30.009402°N, 121.804738°E). At the same altitude, the distance between the two points in geographical space is 3.052 nautical miles, and the azimuth angle formed between the two points is 328.9°. By means of the regression model, the original trajectory fitting degree is about 99.55%.

The locus class cluster 5 represents the locus starting position of (29.994542°N, 121.801375°E), and the ending position of (29.980973°N, 121.75394°E). At the same altitude, the distance between two points in geographical space is 2.599 nautical miles, and the azimuth angle formed between the two points is 251.7°. By means of the regression model, the original trajectory fitting degree is about 97.12%.

The locus class cluster 6 represents the locus whose starting position is (29.967733°N, 121.730498°E) and ending position is (29.996267°N, 121.8094°E). At the same altitude, the distance between the two points in geographical space is 4.448 nautical miles, and the azimuth angle formed between the two points is 67.3°. By means of the regression model, the original trajectory fitting degree is about 99.44%.

To sum up, after calculation by the polynomial regression equation, the trajectory fitting degree of the 6 trajectory class clusters is respectively 96.37%, 97.62%, 99.89%, 99.55%, 97.12%, 99.44%, and the average fitting degree is 98.33%. The closer the value of R is to 1, the better the fitting degree of the regression equation for the observed value is, which indicates that the fitting degree of the ship representative tracks extracted is at a high level, and also reflects the feasibility and effectiveness of the ship representative track extraction algorithm. It is also proved that the multi-attribute DBSCAN extension algorithm has a high degree of fit. The representative trajectory results of the six ship trajectory clusters are shown in Figs. 26. The experimental results show that the clustering operation conducted by the multi-attribute DBSCAN extended algorithm has a very high degree of fitting.

CONCLUSION

The density-based clustering method is extended, and the multi-attribute DBSCAN extension algorithm suitable for ship trajectory clustering is introduced to establish an effective ship trajectory clustering model, after which the ship trajectories are analysed by using the ship automatic identification system AIS data. Combined with the idea of representing vector points, the representative trajectories of the ship trajectory class clusters are extracted, which proves that the multi-attribute DBSCAN algorithm has reliability and accuracy.

1. After decoding and pre-processing the AIS data, they are divided according to different ship types and lengths. Through

visual analysis of the ship trajectory density distribution, the type of ship object to be studied is determined.

2. A multi-attribute DBSCAN extension algorithm is proposed. The original DBSCAN algorithm is extended by combining the three attributes of ship position, speed and heading in the AIS data, and a multi-attribute DBSCAN extension algorithm is established. The ship trajectory clustering model is used to carry out experiments in the waters of the Jintang Bridge area. Ship trajectory clustering is carried out for ships with a length of 100-150 meters in this water area. The trajectory clustering results show that six ship trajectory clusters are obtained.

3. Corresponding to the actual ship traffic flow pattern in this water area, the feasibility of the multi-attribute DBSCAN extension algorithm is verified. The representative trajectory extraction algorithm was proposed, which combined the idea of representing vector points to extract the representative trajectories of six ship trajectory class clusters. The polynomial regression model was used to calculate the similarity fitting degree of each representative trajectory, verify the feasibility of the representative trajectory extraction algorithm, and prove the reliability and accuracy of the multi-attribute DBSCAN algorithm.

4. Using the ideas of representative vector points, the trajectory extraction algorithm is put forward, The average direction of all trajectory points of each trajectory class cluster is calculated. In this direction, the trajectory class cluster is divided into several parallel blocks with the width of λ , taking the interval λ as the normal. The width is determined by domain knowledge or the results of many experiments. Finally, the parameter EPS value of 0.15 used in the clustering algorithm is selected as the length of λ . Then, the representative vector points are calculated for each parallel block, and the center positions AVG (LAT) and AVG (lon) of all trajectory points in the parallel block are taken as the starting points of the representative vector points; the average speed AVG (SOG) of all trajectory points is taken as the size of the representative vector points; the average direction AVG (COG) of all trajectory points is taken as the direction of the representative vector points, with three dimensions (center position, average speed and average speed) The vector trajectory points are composed of two parts. After calculating the representative vector points of all parallel blocks, connect all the representative vector points to form the representative trajectory

5. Compared with the traditional DBSCAN algorithm, the multi-attribute DBSCAN extension algorithm proposed in this paper simplifies the originally complex trajectory segment to the similarity measure between vector points. In order to better conform to the complex marine traffic flow situation in reality, two control variables, SpdRange and DirRange, are added to the input variables of the model to control the range of ship speed and heading range, which is more in line with the environmental changes of sea navigation and makes the clustering accuracy higher.

6. Although the algorithm is not sensitive to noise, clustering of arbitrary shapes can be found, but the result

of clustering has a good relationship with the parameters. DBSCAN uses fixed parameters to identify clustering, but when the sparsity of clustering is different, the same criteria may destroy the natural structure of the clustering; that is, sparse clustering will be divided into multiple clusters or dense and close clusters will be merged into one cluster.

REFERENCES

1. Yang, B. International standard of automatic ship identification system and its formulation. *Standardization of Transportation*, 2002 (01):42-44.
2. Zhao, L., Shi, G. A method for simplifying ship trajectory based on improved Douglas-Peucker algorithm. *Ocean Engineering*, Vol. 166, 2018: 37-46.
3. Zhao, L., Shi, G., Yang, J. Ship trajectories pre-processing based on AIS data. *Journal of Navigation*, 2018.
4. Wang, J., Zhu, C., Zhou, Y., Zhang, W. Vessel Spatio-temporal Knowledge Discovery with AIS Trajectories Using Co-clustering. *Journal of Navigation*, Nov 2017.
5. Zhang, Y., Shi, G., Li, S., Zhang, S. Vessel trajectory online multi-dimensional simplification algorithm. *Journal of Navigation*, 2020.
6. Zhang, L., Meng, Q., Xiao, Z., Fu, X. A novel ship trajectory reconstruction approach using AIS data. *Ocean Engineering*, 2018.
7. Yan, Z., Xiao, Y., Cheng, L., He, R., Ruan, X., Zhou, X., Li, M., Bin, R. Exploring AIS data for intelligent maritime routes extraction. *Applied Ocean Research*, 2020.
8. Wei, Z., Xie, X., Zhang, X. AIS trajectory simplification algorithm considering ship behaviours. *Ocean Engineering*, 2020.
9. Li, H., Liu, J., Wu, K., Yang, Z., Liu, R.W., Xiong, N. Spatio-temporal vessel trajectory clustering based on data mapping and density. *IEEE Access*, 2018, 6:58939-58954.
10. Sheng, P., Yin, J. Extracting shipping route patterns by trajectory clustering model based on AIS data. *Sustainability*, 2018, 10(2018):2327.
11. [11]Xiao, X., Shao, Z., Pan, J., Ji, X. Ship trajectory clustering model based on AIS information and its application. *China Navigation*, 2015, 38(02):82-86.
12. Zhou, H., Chen, Y., Chen, L. Clustering analysis and application of ship trajectory. *Computer Simulation*, 2020, 37(10):113-118+199.

13. Cui, K. Research on ship AIS trajectories prediction method based on machine learning. Zhengzhou University, 2020.
14. Liu, Y., Shi, B. Research on ship track clustering technology based on skeleton extraction. Information Technology, 2020, 44(03):50-53+58.
15. Jiang, Y., Xiong, Z., Tang, J. Ship trajectory clustering algorithm based on trajectory segment DBSCAN. China Navigation, 2019, 42(03):1-5.
16. Zhao, L., Shi, G., Yang, J. Adaptive hierarchical clustering of ship trajectory based on DBSCAN algorithm. China Navigation, 2018, 41(03):53-58.
17. Peng, X., Gao, S., Chu, X., He, Y., Lu, C. Clustering method of ship trajectory based on Spark. China Navigation, 2017, 40(03):49-53+68
18. Frey, B.J., Dueck, D. Clustering by passing message between data points. Science, 2007, 315(5814):972-976.
19. Jain, A.K., Dubes, R.C. Algorithms for clustering data. Technometrics, 2015, 32(32):227-229.
20. Yang, W., Long, H., Shao, Y., Du, Q. Research on density calculation based on Chebyshev distance and clustering method of K-means. Communications Technology, 2019, 52(04):833-838.
21. Chen, B. Research on spatio-temporal similarity of vehicle trajectories based on clustering algorithm. Fujian Normal University, 2015.
22. Design and implementation of ship trajectory clustering system based on bright [AIS]. Dalian University, 2016

CONTACT WITH THE AUTHORS

Deqiang Cui

e-mail: cuideqiang0213@163.com
 Shanghai Maritime University,
 Haigang street, 201306 ShangHai,
CHINA

Xiaofeng Xu

e-mail: xfxu@shmtu.edu.cn
 Shanghai Maritime University,
 Haigang street, 201306 ShangHai,
CHINA

Yun Li

e-mail: liyun@shmtu.edu.cn
 Shanghai Maritime University,
 Haigang street, 201306 ShangHai,
CHINA

Yingjie Xiaoi

e-mail: xiaoyj@shmtu.edu.cn
 Shanghai Maritime University,
 Haigang street, 201306 ShangHai,
CHINA

METHOD OF COOPERATIVE FORMATION CONTROL FOR UNDERACTUATED USVS BASED ON NONLINEAR BACKSTEPPING AND CASCADE SYSTEM THEORY

Zaopeng Dong^{1,2}

Yang Liu^{1,2}

Hao Wang^{1,2}

Tao Qin^{3*}

¹ Key Laboratory of High Performance Ship Technology (Wuhan University of Technology), Ministry of Education, Wuhan University of Technology, Wuhan, China

² School of Transportation, Wuhan University of Technology, Wuhan, China

³ School of Mechanical Engineering, Hubei University of Arts and Sciences, Xiangyang, China

* Corresponding author: e-mail: heu_qt@163.com (T. Qin)

ABSTRACT

This paper presents a method for the cooperative formation control of a group of underactuated USVs. The problem of formation control is first converted to one of stabilisation control of the tracking errors of the follower USVs using system state transformation design. The followers must keep a fixed distance from the leader USV and a specific heading angle in order to maintain a certain type of formation. A global differential homeomorphism transformation is then designed to create a tracking error system for the follower USVs, in order to simplify the description of the control system. This makes the complex formation control system easy to analyse, and allows it to be decomposed into a cascaded system. In addition, several intermediate state variables and virtual control laws are designed based on nonlinear backstepping, and actual control algorithms for the follower USVs to control the surge force and yaw moment are presented. A global system that can ensure uniform asymptotic stability of the USVs' cooperative formation control is achieved by combining Lyapunov stability theory and cascade system theory. Finally, several simulation experiments are carried out to verify the validity, stability and reliability of our cooperative formation control method.

Keywords: unmanned surface vehicle (USV), cooperative formation control, underactuated system, nonlinear backstepping, cascade system theory

INTRODUCTION

An unmanned surface vehicle (USV) is an intelligent autonomous surface vessel, of a type that has played an indispensable role in several fields such as science, economics and the military [1-3]. The problem of cooperative formation tracking control of multiple USVs has attracted increasing amounts attention from researchers from all over the world over recent years, since a team of USVs working together is often more effective than a single vehicle for challenging missions such as surveillance, hydrographic surveys, autonomous exploration of ocean resources, reconnaissance, rescue operations and perimeter security [4-6]. It is well-known that the control system of an USV is generally underactuated,

since the number of control inputs is less than the degrees of freedom and there is an unintegrable acceleration constraint on the system. Kinematic and dynamic models of cooperative formation tracking for USVs are highly nonlinear and coupled [7-10]; this means that classic linear methodologies cannot be applied, and more advanced methods need to be developed to achieve cooperative formation tracking control of USVs.

Several exploratory algorithms have been proposed for this problem. A leader-follower formation tracking control algorithm was presented for an underactuated USV in [2, 11], in which a radial basis function neural network and adaptive robust control techniques were adopted to preserve the robustness of the controller against unmodelled dynamics and environmental disturbances induced by waves and ocean

currents. Another control strategy was proposed in [12], in which each follower was designed to track a virtual vehicle and the formation control problem was transformed into a set of position (including heading) tracking problems. In [13], cooperative formation control was formulated as an adaptive feedback control problem for a line of sight (LOS)-based configuration of a leader and a follower, and asymmetric barrier Lyapunov functions were used in the design of the controller to account for time-varying constraints on the LOS and bearing angle. An approach based on model prediction control was proposed in [14] to address the vessel train formation problem. This method considered cooperative collision avoidance and the grouping of vessels, and a single-layer serial iterative architecture was adopted to reduce the communication requirements and ensure robustness against failure. The leader-follower formation control problem for USVs with unknown nonlinear dynamics and actuator faults was addressed in [15], and a low-complexity prescribed performance controller was proposed without the help of auxiliary neural/fuzzy systems or adaptive mechanisms. The authors of [16] explored the problem of finite-time extended state observer-based distributed formation control for USVs with input saturation and external disturbances, and a novel finite-time extended state observer was proposed to estimate the unavailable velocity measurements and external disturbances. A novel nonlinear sliding mode control method for dealing with the formation control of underactuated ships was presented in [17], in which the state space of the system was partitioned into two regions, and in [18], the dynamic equations for the position and attitude were analysed using a coordinate transformation with the aid of the backstepping technique. In [19], the platoon formation control problem for USVs in the presence of modelling uncertainties and time-varying external disturbances was studied, and performance guarantees were enforced in the control design to provide transient performance specifications for formation errors, including errors related to the LOS range and angle. A novel robust adaptive formation control scheme based on a minimal learning parameter (MLP) algorithm and a disturbance observer (DOB) was presented in [20], and a novel disturbance rejection control was designed in [21] that took into account the disturbance caused by the formation adjustment among ships. A system for motion planning, collision avoidance, guidance and control for a formation of autonomous surface vehicles navigating in a complex marine environment was presented in [6]; the motion planning unit was based on an angle-guidance fast-marching square method, while the control unit is composed of a PID heading controller and a speed controller. The authors of [4] presented a coordinated tracking strategy with swarm centre identification, self-organised aggregation, collision avoidance and a distributed controller design for multiple USVs, while an adaptive observer based on a neural network was designed to estimate the velocity information of USVs in [22]. Decentralised finite time formation control of underactuated USVs in the presence of model uncertainty and environmental disturbance was addressed in [23], and in [24],

the authors presented an approach for the distributed time-varying formation control of a swarm of underactuated USVs subject to unknown input gains, model uncertainties and ocean disturbances. A robust control scheme was developed for the time-varying formation of multiple underactuated autonomous underwater vehicles (AUVs) with environment disturbances and input saturation in [25]. A new robust model predictive control (MPC) algorithm for trajectory tracking of an autonomous surface vehicle (ASV) in the presence of time-varying external disturbances was proposed in [5], and a high-performance super-twisting sliding mode control method for a maritime autonomous surface ship (MASS) using approximate dynamic programming (ADP)-based adaptive gains and time delay estimation was presented in [26]. Although MPC is a superior method for motion control of a ship, especially when the model is unknown, the design process of constraint conditions is strict and the calculation of the system is complex in some cases.

Despite the multitude of research results in the literature on the cooperative formation control of USVs, the design process of the controller is often too complicated for calculation and analysis, and the performance of the controller needs to be further improved. In this paper, we present innovative work on the transformation of the cooperative formation control problem, and propose some design ideas for maintaining a formation and applying control methods and stability theories. Compared with existing studies, the main contributions of this paper can be summarised as follows: (i) we present a novel description of the cooperative formation control problem for a group of USVs, in which the desired positions and attitude angles of the follower USVs are transformed into intermediate variables that can help in the design of the controller; (ii) we design a new kind of global differential homeomorphism transformation for the tracking error system of the follower USVs, which simplifies the description of the control system, thus making the complex formation control system easy to analyse and allowing it to be decomposed into a cascaded system; (iii) we propose an improved controller for the cooperative formation control of a group of underactuated USVs by combining a backstepping technique with Lyapunov's direct method and cascade system theory, and devise some intermediate state variables and virtual control laws for the design process of the control algorithm.

PROBLEM FORMULATION

A. USV MODELING

When designing a cooperative formation controller for a group of underactuated USVs, mathematical models are used, including kinematic and dynamic models, which can be expressed as follows [27]:

$$\begin{cases} \dot{x}_j = u_j \cos \varphi_j - v_j \sin \varphi_j \\ \dot{y}_j = u_j \sin \varphi_j + v_j \cos \varphi_j \\ \dot{\varphi}_j = r_j \\ \dot{u}_j = \frac{m_{22j}}{m_{11j}} v_j r_j - \frac{d_{11j}}{m_{11j}} u_j + \frac{1}{m_{11j}} \tau_{uj} \\ \dot{v}_j = -\frac{m_{11j}}{m_{22j}} u_j r_j - \frac{d_{22j}}{m_{22j}} v_j \\ \dot{r}_j = \frac{m_{11j} - m_{22j}}{m_{33j}} u_j v_j - \frac{d_{33j}}{m_{33j}} r_j + \frac{1}{m_{33j}} \tau_{rj} \end{cases} \quad (1)$$

where $j = k + 1, k=1, \dots, N$. This means that there is one leader USV and N follower USVs in this group. x_j and y_j denote the position coordinates of each USV in the earth-fixed frame; φ_j is the heading angle; u_j, v_j and r_j represent the velocity vectors for each USV in the surge, sway and yaw directions in the body-fixed frame, respectively. The surge force τ_{uj} and the yaw moment τ_{rj} are considered as control inputs which drive the USV to move. $m_{11j}, m_{22j}, m_{33j}$ express the inertia coefficients of the USV, including added mass effects, and $d_{11j}, d_{22j}, d_{33j}$ represent hydrodynamic damping coefficients.

B. PROBLEM FORMULATION

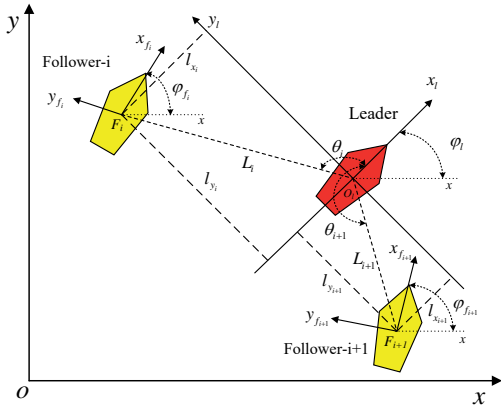


Fig. 1 Cooperative formation control of USVs based on a leader-follower scheme

The cooperative formation control of a group of USVs using a leader-follower approach is illustrated in Fig. 1, which shows one leader and two followers. As we can see from the figure, $\{x_l, y_l\}$ denotes the body-fixed frame of the leader USV, while $\{x_{fi}, y_{fi}\}$ and $\{x_{fi+1}, y_{fi+1}\}$ represent the body-fixed frames of the two follower USVs, and $\varphi_l, \varphi_{fi}, \varphi_{fi+1}$ indicate their heading angles. All of the headings are defined in the same direction, with a rotation from the earth-fixed frame to the body-fixed frame; the clockwise direction is negative, and the counterclockwise direction is positive. The leader-follower scheme for cooperative formation control of the USVs can then be formulated as follows: if the distance between each follower i and the leader L_i , and the angle θ_i between the lines $o_l x_l$ and $o_l F_i$ shown in Fig. 1, can be kept to certain

values, then the follower and the leader will sail in a specific formation, and cooperative formation control is achieved.

We assume that the desired trajectory, heading angle and velocities of the leader USV can be expressed as $\{x_{ld}, y_{ld}, \varphi_{ld}, u_{ld}, v_{ld}, r_{ld}\}$, while the desired state of the follower USV can be represented as $\{x_{fd}, y_{fd}, \varphi_{fd}, u_{fd}, v_{fd}, r_{fd}\}$. From the geometric description in Fig. 1, we can deduce the following mathematical expression, in which the heading angles are defined in the range from $-\pi$ to π , and the positions of the leader USV and the follower USVs can be arbitrarily chosen according to the requirements of the task:

$$\begin{cases} l_{x_i} = (x_{f_i} - x_l) \cos \varphi_l + (y_{f_i} - y_l) \sin \varphi_l \\ l_{y_i} = -(x_{f_i} - x_l) \sin \varphi_l + (y_{f_i} - y_l) \cos \varphi_l \\ \varphi_i = \varphi_{f_i} - \varphi_l \end{cases} \quad (2)$$

We can see that L_i and the angle θ_i should be kept at certain values, and this also means that $l_{x_i}, l_{y_i}, \varphi_i$ need to be maintained in a specific state. The desired outcome can be expressed as $l_{x_{i,d}}, l_{y_{i,d}}, \varphi_{i,d}$. We then obtain the following equations, which express the desired stable positional relationship between the leader and follower USVs when USVs' formation control has been realised:

$$\begin{cases} l_{x_{i,d}} = (x_{f_{i,d}} - x_{l,d}) \cos \varphi_{l,d} + (y_{f_{i,d}} - y_{l,d}) \sin \varphi_{l,d} \\ l_{y_{i,d}} = -(x_{f_{i,d}} - x_{l,d}) \sin \varphi_{l,d} + (y_{f_{i,d}} - y_{l,d}) \cos \varphi_{l,d} \\ \varphi_{i,d} = \varphi_{f_{i,d}} - \varphi_{l,d} \end{cases} \quad (3)$$

The following expressions can be obtained from a system state transformation:

$$\begin{cases} x_{f_{i,d}} = l_{x_{i,d}} \cos \varphi_{l,d} - l_{y_{i,d}} \sin \varphi_{l,d} + x_{l,d} \\ y_{f_{i,d}} = l_{x_{i,d}} \sin \varphi_{l,d} + l_{y_{i,d}} \cos \varphi_{l,d} + y_{l,d} \\ \varphi_{f_{i,d}} = \varphi_{l,d} + \varphi_i \end{cases} \quad (4)$$

In order to keep the overall formation of the USVs in line with the expected form, the real state variables for the leader USV, such as its position, heading angle and velocities $\{x_l, y_l, \varphi_l, u_l, v_l, r_l\}$, are used as a reference for the desired values $\{x_{ld}, y_{ld}, \varphi_{ld}, u_{ld}, v_{ld}, r_{ld}\}$. To achieve overall cooperative formation control, the desired position and heading angle of follower i can be described as follows, i.e. the desired state of the follower USVs that will be used in the actual formation tracking control process:

$$\begin{cases} x_{f_{i,d}} = l_{x_{i,d}} \cos \varphi_l - l_{y_{i,d}} \sin \varphi_l + x_l \\ y_{f_{i,d}} = l_{x_{i,d}} \sin \varphi_l + l_{y_{i,d}} \cos \varphi_l + y_l \\ \varphi_{f_{i,d}} = \varphi_{l,d} + \varphi_i \end{cases} \quad (5)$$

Taking derivatives of both sides of the above equations and applying a mathematical conversion gives:

$$\begin{cases} \dot{x}_{f_i,d} = -r_l l_{x,d} \sin \varphi_l - r_l l_{y,d} \cos \varphi_l + u_l \cos \varphi_l - v_l \sin \varphi_l \\ \dot{y}_{f_i,d} = r_l l_{x,d} \cos \varphi_l - r_l l_{y,d} \sin \varphi_l + u_l \sin \varphi_l + v_l \cos \varphi_l \\ \dot{\varphi}_{f_i,d} = r_l \end{cases} \quad (6)$$

The desired velocities of a follower i can be expressed as:

$$\begin{cases} u_{f_i,d} = \dot{x}_{f_i,d} \cos \varphi_{f_i,d} + \dot{y}_{f_i,d} \sin \varphi_{f_i,d} = r_l l_{x,d} \sin \varphi_{id} - r_l l_{y,d} \cos \varphi_{id} + u_l \cos \varphi_{id} + v_l \sin \varphi_{id} \\ v_{f_i,d} = -\dot{x}_{f_i,d} \sin \varphi_{f_i,d} + \dot{y}_{f_i,d} \cos \varphi_{f_i,d} = r_l l_{x,d} \cos \varphi_{id} + r_l l_{y,d} \sin \varphi_{id} - u_l \sin \varphi_{id} + v_l \cos \varphi_{id} \\ r_{f_i,d} = \dot{\varphi}_{f_i,d} \end{cases} \quad (7)$$

In this way, the problem of formation control of the underactuated USVs can be converted to the problem of designing control inputs (τ_{ui}, τ_{ri}) for each individual follower USV. This can help in achieving the following goal:

$$\lim_{t \rightarrow \infty} \|\eta_i - \eta_{id}\| = 0 \quad (8)$$

where $\eta_i = [x_{f_i}, y_{f_i}, \varphi_{f_i}, u_{f_i}, v_{f_i}, r_{f_i}]^T$ are the real state variables of the follower USV i , including its position, heading angle and velocities, while $\eta_{id} = [x_{f_i,d}, y_{f_i,d}, \varphi_{f_i,d}, u_{f_i,d}, v_{f_i,d}, r_{f_i,d}]^T$ represent the desired state variables of the USV, as shown below:

$$\begin{cases} x_{f_i,d} = l_{x,d} \cos \varphi_l - l_{y,d} \sin \varphi_l + x_l \\ y_{f_i,d} = l_{x,d} \sin \varphi_l + l_{y,d} \cos \varphi_l + y_l \\ \varphi_{f_i,d} = \varphi_{id} + \varphi_l \\ u_{f_i,d} = r_l l_{x,d} \sin \varphi_{id} - r_l l_{y,d} \cos \varphi_{id} + u_l \cos \varphi_{id} + v_l \sin \varphi_{id} \\ v_{f_i,d} = r_l l_{x,d} \cos \varphi_{id} + r_l l_{y,d} \sin \varphi_{id} - u_l \sin \varphi_{id} + v_l \cos \varphi_{id} \\ r_{f_i,d} = \dot{\varphi}_{f_i,d} \end{cases} \quad (9)$$

CONTROLLER DESIGN

In this section, a cooperative formation control algorithm is proposed for underactuated USVs based on nonlinear backstepping and cascade system theory. The main process of this algorithm is illustrated in Fig. 2.

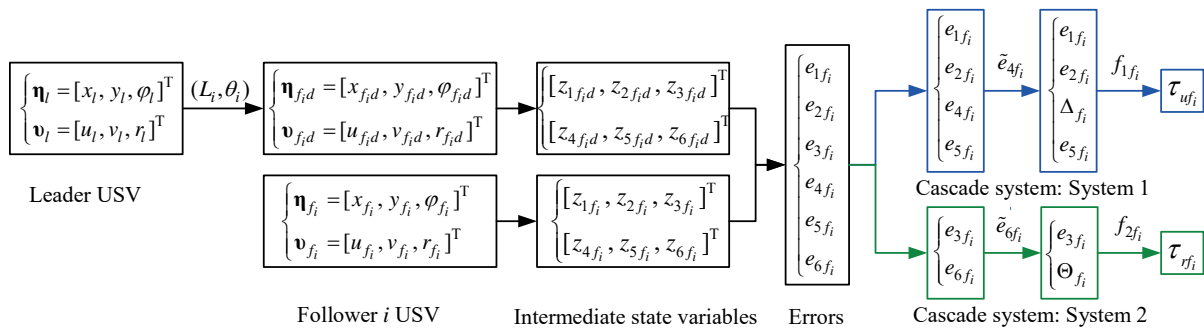


Fig. 2. Main process of the controller algorithm

The expected tracking state information for the follower USV can be obtained based on the state information for the leader USV and the desired formation. The intermediate variables can then be designed and the tracking errors obtained, and the model of the cooperative formation control error system can be established. Finally, the control algorithm is designed based on nonlinear backstepping and cascade system theory.

A. GLOBAL DIFFERENTIAL HOMEOMORPHISM TRANSFORMATION DESIGN

In order to create a better description and to carry out an analysis of the state variables of the follower USV, the following differential homeomorphic intermediate state variables $z_{nf_i}, n=1, \dots, 6$ are proposed based on the kinematics and dynamics equations expressed in (1). The main goal is to transform the system into a form that can be expressed as a cascading system.

$$\begin{cases} z_{1f_i} = x_{f_i} \cos \varphi_{f_i} + y_{f_i} \sin \varphi_{f_i} \\ z_{2f_i} = -x_{f_i} \sin \varphi_{f_i} + y_{f_i} \cos \varphi_{f_i} + m_{22f_i} v_{f_i} / d_{22f_i} \\ z_{3f_i} = \varphi_{f_i} \\ z_{4f_i} = -m_{11f_i} u_{f_i} / d_{22f_i} - x_{f_i} \cos \varphi_{f_i} - y_{f_i} \sin \varphi_{f_i} \\ z_{5f_i} = v_{f_i} \\ z_{6f_i} = r_{f_i} \end{cases} \quad (10)$$

Differentiating each equation in (10) leads to the following expressions:

$$\begin{aligned} \dot{z}_{1f_i} &= \dot{x}_{f_i} \cos \varphi_{f_i} - \dot{\varphi}_{f_i} x_{f_i} \sin \varphi_{f_i} + \dot{y}_{f_i} \sin \varphi_{f_i} + \dot{\varphi}_{f_i} y_{f_i} \cos \varphi_{f_i} \\ &= (u_{f_i} \cos \varphi_{f_i} - v_{f_i} \sin \varphi_{f_i}) \cos \varphi_{f_i} - r_{f_i} x_{f_i} \sin \varphi_{f_i} + (u_{f_i} \sin \varphi_{f_i} + v_{f_i} \cos \varphi_{f_i}) \sin \varphi_{f_i} + r_{f_i} y_{f_i} \cos \varphi_{f_i} \\ &= u_{f_i} \cos^2 \varphi_{f_i} - v_{f_i} \sin \varphi_{f_i} \cos \varphi_{f_i} - v_{f_i} x_{f_i} \sin \varphi_{f_i} + u_{f_i} \sin^2 \varphi_{f_i} + v_{f_i} \sin \varphi_{f_i} \cos \varphi_{f_i} + r_{f_i} y_{f_i} \cos \varphi_{f_i} \\ &= u_{f_i} (\cos^2 \varphi_{f_i} + \sin^2 \varphi_{f_i}) - r_{f_i} (x_{f_i} \sin \varphi_{f_i} - y_{f_i} \cos \varphi_{f_i}) \\ &= u_{f_i} - r_{f_i} (x_{f_i} \sin \varphi_{f_i} - y_{f_i} \cos \varphi_{f_i}) \\ &= -d_{22f_i} (z_{1f_i} + z_{4f_i}) / m_{11f_i} - z_{6f_i} (m_{22f_i} z_{5f_i} / d_{22f_i} - z_{2f_i}) \end{aligned} \quad (11)$$

$$\begin{aligned}
\dot{z}_{2f_i} &= -\dot{x}_{f_i} \sin \varphi_{f_i} - \dot{\varphi}_{f_i} x_{f_i} \cos \varphi_{f_i} + \dot{y}_{f_i} \cos \varphi_{f_i} - \dot{\varphi}_{f_i} y_{f_i} \sin \varphi_{f_i} + m_{22f_i} \dot{v}_{f_i} / d_{22f_i} \\
&= -(u_{f_i} \cos \varphi_{f_i} - v_{f_i} \sin \varphi_{f_i}) \sin \varphi_{f_i} - r_{f_i} x_{f_i} \cos \varphi_{f_i} + (u_{f_i} \sin \varphi_{f_i} + v_{f_i} \cos \varphi_{f_i}) \cos \varphi_{f_i} - r_{f_i} y_{f_i} \sin \varphi_{f_i} + \\
&\quad m_{22f_i} (-m_{11f_i} u_{f_i} r_{f_i} / m_{22f_i} - d_{22f_i} v_{f_i} / m_{22f_i}) / d_{22f_i} \\
&= -u_{f_i} \cos \varphi_{f_i} \sin \varphi_{f_i} + v_{f_i} \sin^2 \varphi_{f_i} - r_{f_i} x_{f_i} \cos \varphi_{f_i} + u_{f_i} \sin \varphi_{f_i} \cos \varphi_{f_i} + v_{f_i} \cos^2 \varphi_{f_i} - r_{f_i} y_{f_i} \sin \varphi_{f_i} - \\
&\quad m_{11f_i} u_{f_i} r_{f_i} / d_{22f_i} - v_{f_i} \\
&= -r_{f_i} (x_{f_i} \cos \varphi_{f_i} + y_{f_i} \sin \varphi_{f_i}) - m_{11f_i} u_{f_i} r_{f_i} / d_{22f_i} \\
&= -z_{6f_i} z_{1f_i} + (z_{1f_i} + z_{4f_i}) z_{6f_i} \\
&= z_{4f_i} z_{6f_i}
\end{aligned} \tag{12}$$

$$\dot{z}_{3f_i} = \dot{\varphi}_{f_i} = r_{f_i} = z_{6f_i} \tag{13}$$

$$\begin{aligned}
\dot{z}_{4f_i} &= -m_{11f_i} \dot{u}_{f_i} / d_{22f_i} - \dot{z}_{1f_i} \\
&= -m_{11f_i} \dot{u}_{f_i} / d_{22f_i} - (-d_{22f_i} z_{1f_i} / m_{11f_i} - d_{22f_i} z_{4f_i} / m_{11f_i} + z_{2f_i} z_{6f_i} - d_{22f_i} z_{5f_i} z_{6f_i} / m_{22f_i}) \\
&= -m_{11f_i} \dot{u}_{f_i} / d_{22f_i} + d_{22f_i} (z_{1f_i} + z_{4f_i}) / m_{11f_i} - z_{2f_i} z_{6f_i} + m_{22f_i} z_{5f_i} z_{6f_i} / d_{22f_i}
\end{aligned} \tag{14}$$

$$\begin{aligned}
\dot{z}_{5f_i} &= -m_{11f_i} u_{f_i} r_{f_i} / m_{22f_i} - d_{22f_i} v_{f_i} / m_{22f_i} \\
&= -m_{11f_i} [-d_{22f_i} (z_{1f_i} + z_{4f_i}) / m_{11f_i}] z_{6f_i} / m_{22f_i} - d_{22f_i} z_{5f_i} / m_{22f_i} \\
&= d_{22f_i} (z_{1f_i} + z_{4f_i}) z_{6f_i} / m_{22f_i} - d_{22f_i} z_{5f_i} / m_{22f_i}
\end{aligned} \tag{15}$$

$$\dot{z}_{6f_i} = \dot{r}_{f_i} \tag{16}$$

Using equations (14) and (16), the virtual intermediate control input variables, f_{1f_i} and f_{2f_i} , can be expressed as follows:

$$\begin{cases} f_{1f_i} = -m_{11f_i} \dot{u}_{f_i} / d_{22f_i} + d_{22f_i} (z_{1f_i} + z_{4f_i}) / m_{11f_i} - z_{2f_i} z_{6f_i} + m_{22f_i} z_{5f_i} z_{6f_i} / d_{22f_i} \\ f_{2f_i} = \dot{r}_{f_i} \end{cases} \tag{17}$$

Based on the above design and analysis, our mathematical model of the USVs can be converted into the following form, which is differentially homeomorphic with the system expressed in (1):

$$\begin{cases} \dot{z}_{1f_i} = -d_{22f_i} z_{1f_i} / m_{11f_i} - d_{22f_i} z_{4f_i} / m_{11f_i} + z_{2f_i} z_{6f_i} - m_{22f_i} z_{5f_i} z_{6f_i} / d_{22f_i} \\ \dot{z}_{2f_i} = z_{4f_i} z_{6f_i} \\ \dot{z}_{3f_i} = z_{6f_i} \\ \dot{z}_{4f_i} = f_{1f_i} \\ \dot{z}_{5f_i} = d_{22f_i} (z_{1f_i} + z_{4f_i}) z_{6f_i} / m_{22f_i} - d_{22f_i} z_{5f_i} / m_{22f_i} \\ \dot{z}_{6f_i} = f_{2f_i} \end{cases} \tag{18}$$

B. DEVELOPING THE TRACKING ERROR SYSTEM

The expected trajectory of the follower USV i described in (9) also needs to comply with the kinematic and dynamic expressions in (1), since otherwise the required trajectory will not be followed. The desired state variables and control inputs of follower i described in (9), namely $(x_{fd}, y_{fd}, \varphi_{fd}, u_{fd}, v_{fd}, r_{fd})$ and (τ_{ufd}, τ_{rfd}) , could be similarly transformed to z_{nfd} , $n=1, \dots, 6$ and (f_{1fd}, f_{2fd}) as shown in expressions (10) and (17). Thus, the desired trajectory of the follower i can be expressed as follows:

$$\begin{cases} \dot{z}_{1fd} = -d_{22f_i} z_{1fd} / m_{11f_i} - d_{22f_i} z_{4fd} / m_{11f_i} + z_{2fd} z_{6fd} - m_{22f_i} z_{5fd} z_{6fd} / d_{22f_i} \\ \dot{z}_{2fd} = z_{4fd} z_{6fd} \\ \dot{z}_{3fd} = z_{6fd} \\ \dot{z}_{4fd} = f_{1fd} \\ \dot{z}_{5fd} = d_{22f_i} (z_{1fd} + z_{4fd}) z_{6fd} / m_{22f_i} - d_{22f_i} z_{5fd} / m_{22f_i} \\ \dot{z}_{6fd} = f_{2fd} \end{cases} \tag{19}$$

$$\text{where: } \begin{cases} f_{1fd} = -m_{11f_i} \dot{u}_{fd} / d_{22f_i} + d_{22f_i} (z_{1fd} + z_{4fd}) / m_{11f_i} - z_{2fd} z_{6fd} + m_{22f_i} z_{5fd} z_{6fd} / d_{22f_i} \\ f_{2fd} = \dot{r}_{fd} \end{cases}$$

We define the following cooperative formation tracking control error variables for follower i :

$$e_{nf_i} = z_{nf_i} - z_{nf_i d}, \quad n = 1, \dots, 6 \tag{20}$$

Differentiation and analysis of the error variables in (20) leads to the following equations for the cooperative formation tracking control error system:

$$\begin{cases} \dot{e}_{1f_i} = -d_{22f_i} e_{1f_i} / m_{11f_i} - d_{22f_i} e_{4f_i} / m_{11f_i} + (e_{2f_i} e_{6f_i} + e_{2f_i} z_{6fd} + e_{6f_i} z_{1fd}) - m_{22f_i} (e_{5f_i} e_{6f_i} + e_{5f_i} z_{6fd} + e_{6f_i} z_{5fd}) / d_{22f_i} \\ \dot{e}_{2f_i} = e_{4f_i} e_{6f_i} + e_{4f_i} z_{6fd} + e_{6f_i} z_{4fd} \\ \dot{e}_{3f_i} = e_{6f_i} \\ \dot{e}_{4f_i} = f_{1f_i} - f_{1fd} \\ \dot{e}_{5f_i} = d_{22f_i} (e_{4f_i} e_{6f_i} + e_{4f_i} z_{6fd} + e_{6f_i} z_{4fd} + e_{1f_i} e_{6f_i} + e_{1f_i} z_{6fd} + e_{6f_i} z_{1fd}) / m_{22f_i} - d_{22f_i} e_{5f_i} / m_{22f_i} \\ \dot{e}_{6f_i} = f_{2f_i} - f_{2fd} \end{cases} \tag{21}$$

This means that if the cooperative formation-tracking control error system mentioned above can be stabilised globally and asymptotically, we can achieve stable cooperative formation control of the USVs. The error system can be decomposed into the cascading system shown in (22) and (23):

$$\begin{bmatrix} \dot{e}_{1f_i} \\ \dot{e}_{2f_i} \\ \dot{e}_{4f_i} \\ \dot{e}_{5f_i} \end{bmatrix} = \begin{bmatrix} -\frac{d_{22f_i}}{m_{11f_i}} e_{1f_i} - \frac{d_{22f_i}}{m_{11f_i}} e_{4f_i} + e_{2f_i} z_{6fd} - \frac{m_{22f_i}}{d_{22f_i}} e_{5f_i} z_{6fd} \\ e_{4f_i} z_{6fd} \\ f_{1f_i} - f_{1fd} \\ -\frac{d_{22f_i}}{m_{22f_i}} e_{5f_i} + \frac{d_{22f_i}}{m_{22f_i}} (e_{4f_i} z_{6fd} + e_{1f_i} z_{6fd}) \end{bmatrix} + \begin{bmatrix} 0 & e_{2f_i} + z_{2fd} - \frac{m_{22f_i}}{d_{22f_i}} (e_{5f_i} + z_{5fd}) \\ 0 & e_{4f_i} + z_{4fd} \\ 0 & 0 \\ 0 & \frac{d_{22f_i}}{m_{22f_i}} (e_{4f_i} + z_{4fd} + e_{1f_i} + z_{1fd}) \end{bmatrix} \begin{bmatrix} e_{3f_i} \\ e_{6f_i} \end{bmatrix} \tag{22}$$

$$\begin{bmatrix} \dot{e}_{3f_i} \\ \dot{e}_{6f_i} \end{bmatrix} = \begin{bmatrix} e_{6f_i} \\ f_{2f_i} - f_{2fd} \end{bmatrix} \tag{23}$$

C. DESIGN OF A CONTROL LAW FOR f_{1f_i}

Based on the system of equations in (22), we first take the system in (24):

$$\begin{bmatrix} \dot{e}_{1f_i} \\ \dot{e}_{2f_i} \\ \dot{e}_{4f_i} \\ \dot{e}_{5f_i} \end{bmatrix} = \begin{bmatrix} -d_{22f_i} e_{1f_i} / m_{11f_i} - d_{22f_i} e_{4f_i} / m_{11f_i} + e_{2f_i} z_{6fd} - m_{22f_i} e_{5f_i} z_{6fd} / d_{22f_i} \\ e_{4f_i} z_{6fd} \\ f_{1f_i} - f_{1fd} \\ -d_{22f_i} e_{5f_i} / m_{22f_i} + d_{22f_i} (e_{4f_i} z_{6fd} + e_{1f_i} z_{6fd}) / m_{22f_i} \end{bmatrix} \tag{24}$$

We then design the following virtual input variable \tilde{e}_{4f_i} for e_{4f_i} as follows:

$$\tilde{e}_{4f_i} = k_{1f_i} e_{1f_i} - k_{2f_i} z_{6fd} e_{2f_i} - k_{3f_i} z_{6fd} e_{5f_i} \tag{25}$$

where k_{1f_i} , k_{2f_i} and k_{3f_i} are all positive definite parameters.

We define the virtual input variable error between \tilde{e}_{4f_i} and e_{4f_i} as Δ_{f_i} :

$$\Delta_{f_i} = e_{4f_i} - \tilde{e}_{4f_i} \quad (26)$$

Differentiating the error variable in (26) yields:

$$\dot{\Delta}_{f_i} = \dot{e}_{4f_i} - \dot{\tilde{e}}_{4f_i} = f_{1f_i} - f_{1f_i,d} - (k_{1f_i}\dot{e}_{1f_i} - k_{2f_i}\dot{z}_{6f_i,d}e_{2f_i} - k_{2f_i}z_{6f_i,d}\dot{e}_{2f_i} - k_{3f_i}\dot{z}_{6f_i,d}e_{5f_i} - k_{3f_i}z_{6f_i,d}\dot{e}_{5f_i}) \quad (27)$$

Combining expressions (24), (25), (26) and (27) gives the following new error system:

$$\begin{cases} \dot{e}_{1f_i} = -d_{22f_i}(1+k_{1f_i})e_{1f_i}/m_{11f_i} + (k_{2f_i}d_{22f_i}/m_{11f_i} + 1)e_{2f_i}z_{6f_i,d} + (k_{3f_i}d_{22f_i}/m_{11f_i} - m_{22f_i}/d_{22f_i})e_{5f_i}z_{6f_i,d} - d_{22f_i}\Delta_{f_i}/m_{11f_i} \\ \dot{e}_{2f_i} = -k_{2f_i}z_{6f_i,d}^2e_{2f_i} + k_{1f_i}z_{6f_i,d}e_{1f_i} - k_{3f_i}z_{6f_i,d}^2e_{5f_i} + z_{6f_i,d}\Delta_{f_i} \\ \dot{\Delta}_{f_i} = f_{1f_i} - f_{1f_i,d} - (k_{1f_i}\dot{e}_{1f_i} - k_{2f_i}\dot{z}_{6f_i,d}e_{2f_i} - k_{2f_i}z_{6f_i,d}\dot{e}_{2f_i} - k_{3f_i}\dot{z}_{6f_i,d}e_{5f_i} - k_{3f_i}z_{6f_i,d}\dot{e}_{5f_i}) \\ \dot{e}_{5f_i} = -d_{22f_i}(1+k_{3f_i}z_{6f_i,d}^2)e_{5f_i}/m_{22f_i} + d_{22f_i}(1+k_{1f_i})e_{1f_i}z_{6f_i,d}/m_{22f_i} - d_{22f_i}k_{2f_i}z_{6f_i,d}^2e_{2f_i}/m_{22f_i} + d_{22f_i}z_{6f_i,d}\Delta_{f_i}/m_{22f_i} \end{cases} \quad (28)$$

A candidate Lyapunov function for the system in (28) could be designed as follows:

$$V_{1f_i} = \frac{1}{2}\lambda_{1f_i}e_{1f_i}^2 + \frac{1}{2}\lambda_{2f_i}e_{2f_i}^2 + \frac{1}{2}\Delta_{f_i}^2 + \frac{1}{2}\lambda_{3f_i}e_{5f_i}^2 \quad (29)$$

where λ_{1f_i} , λ_{2f_i} and λ_{3f_i} are all positive definite parameters. Differentiation of the Lyapunov function in (29) gives:

$$\begin{aligned} \dot{V}_{1f_i} &= \lambda_{1f_i}e_{1f_i}\dot{e}_{1f_i} + \lambda_{2f_i}e_{2f_i}\dot{e}_{2f_i} + \Delta_{f_i}\dot{\Delta}_{f_i} + \lambda_{3f_i}e_{5f_i}\dot{e}_{5f_i} \\ &= -\lambda_{1f_i}d_{22f_i}(1+k_{1f_i})e_{1f_i}^2/m_{11f_i} + \lambda_{1f_i}(k_{2f_i}d_{22f_i}/m_{11f_i} + 1)z_{6f_i,d}e_{1f_i}e_{2f_i} + \lambda_{1f_i}(k_{3f_i}d_{22f_i}/m_{11f_i} - m_{22f_i}/d_{22f_i}) \times \\ &\quad z_{6f_i,d}e_{1f_i}e_{5f_i} - \lambda_{1f_i}d_{22f_i}\Delta_{f_i}e_{1f_i}/m_{11f_i} - k_{2f_i}\lambda_{2f_i}z_{6f_i,d}^2e_{2f_i}^2 + k_{1f_i}\lambda_{2f_i}z_{6f_i,d}e_{1f_i}e_{2f_i} - k_{3f_i}\lambda_{2f_i}z_{6f_i,d}^2e_{2f_i}e_{5f_i} + \lambda_{2f_i}z_{6f_i,d} \times \\ &\quad \Delta_{f_i}e_{2f_i} + \Delta_{f_i}[f_{1f_i} - f_{1f_i,d} - (k_{1f_i}\dot{e}_{1f_i} - k_{2f_i}\dot{z}_{6f_i,d}e_{2f_i} - k_{2f_i}z_{6f_i,d}\dot{e}_{2f_i} - k_{3f_i}\dot{z}_{6f_i,d}e_{5f_i} - k_{3f_i}z_{6f_i,d}\dot{e}_{5f_i})] - \lambda_{3f_i}d_{22f_i}(1 + \\ &\quad k_{3f_i}z_{6f_i,d}^2)e_{5f_i}^2/m_{22f_i} + \lambda_{3f_i}d_{22f_i}(1+k_{1f_i})z_{6f_i,d}e_{1f_i}e_{5f_i}/m_{22f_i} - \lambda_{3f_i}k_{2f_i}d_{22f_i}z_{6f_i,d}^2e_{2f_i}e_{5f_i}/m_{22f_i} + \lambda_{3f_i}z_{6f_i,d}\Delta_{f_i} \times \\ &\quad e_{5f_i}/m_{22f_i} \quad (30) \\ &= -\lambda_{1f_i}d_{22f_i}(1+k_{1f_i})e_{1f_i}^2/m_{11f_i} - k_{2f_i}\lambda_{2f_i}z_{6f_i,d}^2e_{2f_i}^2 - \lambda_{3f_i}d_{22f_i}(1+k_{3f_i}z_{6f_i,d}^2)e_{5f_i}^2/m_{22f_i} + [\lambda_{1f_i}(k_{2f_i}d_{22f_i}/m_{11f_i} + \\ &\quad 1)z_{6f_i,d} + k_{1f_i}\lambda_{2f_i}z_{6f_i,d}e_{1f_i}e_{2f_i} + \lambda_{1f_i}(k_{3f_i}d_{22f_i}/m_{11f_i} - m_{22f_i}/d_{22f_i})z_{6f_i,d} + d_{22f_i}\lambda_{3f_i}(1+k_{1f_i})z_{6f_i,d}/m_{22f_i}]e_{1f_i} \times \\ &\quad e_{5f_i} + (-k_{3f_i}\lambda_{2f_i}z_{6f_i,d}^2 - \lambda_{3f_i}k_{2f_i}d_{22f_i}z_{6f_i,d}^2/m_{22f_i})e_{2f_i}e_{5f_i} + \Delta_{f_i}[f_{1f_i} - f_{1f_i,d} - (k_{1f_i}\dot{e}_{1f_i} - k_{2f_i}\dot{z}_{6f_i,d}e_{2f_i} - k_{2f_i}z_{6f_i,d}\dot{e}_{2f_i} \times \\ &\quad \dot{e}_{2f_i} - k_{3f_i}\dot{z}_{6f_i,d}e_{5f_i} - k_{3f_i}z_{6f_i,d}\dot{e}_{5f_i})] - \lambda_{1f_i}d_{22f_i}e_{1f_i}/m_{11f_i} + \lambda_{2f_i}z_{6f_i,d}e_{2f_i} + \lambda_{3f_i}d_{22f_i}z_{6f_i,d}e_{5f_i}/m_{22f_i} \end{aligned}$$

According to the expression in (30), a control law for f_{1f_i} can be proposed as follows:

$$f_{1f_i} = f_{1f_i,d} + (k_{1f_i}\dot{e}_{1f_i} - k_{2f_i}\dot{z}_{6f_i,d}e_{2f_i} - k_{2f_i}z_{6f_i,d}\dot{e}_{2f_i} - k_{3f_i}\dot{z}_{6f_i,d}e_{5f_i} - k_{3f_i}z_{6f_i,d}\dot{e}_{5f_i}) + \lambda_{1f_i}d_{22f_i}e_{1f_i}/m_{11f_i} - \lambda_{2f_i}z_{6f_i,d}e_{2f_i} - \lambda_{3f_i}d_{22f_i}z_{6f_i,d}e_{5f_i}/m_{22f_i} - k_{4f_i}\Delta_{f_i} \quad (31)$$

where k_{4f_i} are all positive definite parameters and $f_{1f_i,d}$ is as shown in (19).

D. DESIGN OF A CONTROL LAW FOR f_{2f_i}

According to the system of equations in (23), the virtual input variable \tilde{e}_{6f_i} for e_{6f_i} can be designed as follows:

$$\tilde{e}_{6f_i} = -k_{5f_i}e_{3f_i} \quad (32)$$

where k_{5f_i} are all positive definite parameters. We define the virtual input variable error between \tilde{e}_{6f_i} and e_{6f_i} as Θ_{f_i} :

$$\Theta_{f_i} = e_{6f_i} - \tilde{e}_{6f_i} \quad (33)$$

Differentiation of the error variable in (33) yields:

$$\dot{\Theta}_{f_i} = \dot{e}_{6f_i} - \dot{\tilde{e}}_{6f_i} = f_{2f_i} - f_{2f_i,d} - \dot{\tilde{e}}_{6f_i} \quad (34)$$

Combining expressions (23), (32), (33) and (34) gives the following new error system:

$$\begin{cases} \dot{e}_{3f_i} = e_{6f_i} - k_{5f_i}e_{3f_i} \\ \dot{\Theta}_{f_i} = f_{2f_i} - f_{2f_i,d} - \dot{\tilde{e}}_{6f_i} \end{cases} \quad (35)$$

A candidate Lyapunov function for the system in (35) could be designed as follows:

$$V_{2f_i} = \frac{1}{2}k_{6f_i}e_{3f_i}^2 + \frac{1}{2}\Theta_{f_i}^2 \quad (36)$$

where k_{6f_i} are all positive definite parameters. Differentiation of the Lyapunov function in (36) leads to:

$$\begin{aligned} \dot{V}_{2f_i} &= k_{6f_i}e_{3f_i}\dot{e}_{3f_i} + \Theta_{f_i}\dot{\Theta}_{f_i} \\ &= k_{6f_i}e_{3f_i}(\Theta_{f_i} - k_{5f_i}e_{3f_i}) + \Theta_{f_i}(f_{2f_i} - f_{2f_i,d} - \dot{\tilde{e}}_{6f_i}) \quad (37) \\ &= -k_{5f_i}k_{6f_i}e_{3f_i}^2 + \Theta_{f_i}(f_{2f_i} - f_{2f_i,d} - \dot{\tilde{e}}_{6f_i} + k_{6f_i}e_{3f_i}) \end{aligned}$$

Based on the expression for \dot{V}_{2f_i} in (37), a control law for f_{2f_i} can be proposed as follows:

$$\begin{aligned} f_{2f_i} &= -k_{7f_i}\Theta_{f_i} + f_{2f_i,d} + \dot{\tilde{e}}_{6f_i} - k_{6f_i}e_{3f_i} \\ &= -k_{7f_i}(\Theta_{f_i} + k_{5f_i}e_{3f_i}) - k_{5f_i}\dot{e}_{3f_i} - k_{6f_i}e_{3f_i} + f_{2f_i,d} \quad (38) \\ &= -k_{7f_i}\Theta_{f_i} - (k_{6f_i} + k_{7f_i}k_{5f_i})e_{3f_i} - k_{5f_i}\dot{e}_{3f_i} + f_{2f_i,d} \end{aligned}$$

where k_{7f_i} are all positive definite parameters and $f_{2f_i,d}$ is as shown in (19).

STABILITY ANALYSIS

A. STABILITY THEORIES

In order to better describe the stability analysis process of the control algorithm presented here, the following two classic stability analysis theories are applied.

Theorem 1[28] Consider the system:

$$\begin{cases} \dot{x} = f_1(t, x) + g(t, x, y) \\ \dot{y} = f_2(t, y) \end{cases} \quad (39)$$

where $x \in \mathbb{R}^n$, $y \in \mathbb{R}^m$, $f_1(t, x)$ is continuously differentiable with respect to (t, x) and $f_2(t, y)$, $g(t, x, y)$ are continuous in their arguments and are locally Lipschitz in y and (x, y) respectively. We can view the system in (39) as:

$$\dot{x} = f_1(t, x) \quad (40)$$

which is perturbed by the output of the system:

$$\dot{y} = f_2(t, y) \quad (41)$$

The cascaded system in (39) is globally uniformly asymptotically stable (GUAS) if the following three assumptions hold:

Assumption 1: The system (40) is GUAS and there exists a continuously differentiable function $V(t, x): \mathbb{R} \geq 0 \times \mathbb{R}^n \rightarrow \mathbb{R}$ that satisfies:

$$\begin{cases} W(x) \leq V(t, x) \\ \frac{\partial V}{\partial t} + \frac{\partial V}{\partial x} \cdot f_1(t, x) \leq 0, \forall \|x\| \geq \eta \\ \left\| \frac{\partial V}{\partial x} \right\| \|x\| \leq cV(t, x), \forall \|x\| \geq \eta \end{cases} \quad (42)$$

where $W(x)$ is a positive definite proper function and $c > 0$ and $\eta > 0$ are constants.

Assumption 2: For all $t > t_0$, the function $g(t, x, y)$ satisfies

$$\|g(t, x, y)\| \leq \theta_1(\|y\|) + \theta_2(\|y\|) \|x\| \quad (43)$$

where $\theta_1, \theta_2: \mathbb{R}_{\geq 0} \rightarrow \mathbb{R}_{\geq 0}$ are continuous functions.

Assumption 3: The system (41) is GUAS and for all $t_0 \geq 0$,

$$\int_{t_0}^{\infty} \|y(t, t_0, y(t_0))\| dt \leq \kappa(\|y(t_0)\|) \quad (44)$$

where the function $\kappa(\cdot)$ is a class κ function.

Theorem 2[29] Consider the nonautonomous system

$$\dot{x} = f(t, x) \quad (45)$$

where $f: [0, \infty) \times D \rightarrow \mathbb{R}^n$ is piecewise continuous in t and is locally Lipschitz in x on $[0, \infty) \times D$, and $D \subset \mathbb{R}^n$ is a domain that contains the origin $x = 0$. The origin is an equilibrium point for (45) at $t = 0$ if $f(t, 0) = 0, \forall t \geq 0$. Let $x = 0$ be an equilibrium

point for (45) and let $D \subset \mathbb{R}^n$ be a domain containing $x = 0$. Let $V: [0, \infty) \times D \rightarrow \mathbb{R}$ be a continuously differentiable function such that

$$\begin{cases} k_1 \|x\|^a \leq V(t, x) \leq k_2 \|x\|^a \\ \frac{\partial V}{\partial t} + \frac{\partial V}{\partial x} f(t, x) \leq -k_3 \|x\|^a \end{cases} \quad \forall t \geq 0, \forall x \in D \quad (46)$$

where k_1, k_2, k_3 and are positive constants.

Then $x = 0$ is exponentially stable. If these assumptions hold globally, then it is globally exponentially stable.

B. STABILITY ANALYSIS

By combining the expressions (22), (23), (25), (26) and (27), the following system can be derived:

$$\begin{cases} \dot{\mathbf{x}}_{f_i} = f_{1f_i}(t, \mathbf{x}_{f_i}) + g_{f_i}(t, \mathbf{x}_{f_i}, \mathbf{y}_{f_i}) \mathbf{y}_{f_i} \\ \dot{\mathbf{y}}_{f_i} = f_{2f_i}(t, \mathbf{y}_{f_i}) \end{cases} \quad (47)$$

where $\mathbf{x}_{f_i} = [e_{1f_i}, e_{2f_i}, \Delta_{f_i}, e_{5f_i}]^T$, $\mathbf{y}_{f_i} = [e_{3f_i}, e_{6f_i}]^T$, and

$$\begin{aligned} f_{1f_i}(t, \mathbf{x}_{f_i}) &= [-d_{22f_i}(1+k_{1f_i})e_{1f_i}/m_{1f_i} + (k_{2f_i}d_{22f_i}/m_{1f_i} + 1)e_{2f_i}z_{6f_i,d} + (k_{3f_i}d_{22f_i}/m_{1f_i} - m_{22f_i}/d_{22f_i})e_{3f_i}z_{6f_i,d} - d_{22f_i}\Delta_{f_i}/m_{1f_i}, \\ &-k_{2f_i}z_{6f_i,d}^2e_{2f_i} + k_{1f_i}z_{6f_i,d}e_{1f_i} - k_{3f_i}z_{6f_i,d}^2e_{3f_i} + z_{6f_i,d}\Delta_{f_i}, J_{1f_i} - f_{11d} - (k_{1f_i}e_{1f_i} - k_{2f_i}z_{6f_i,d}e_{2f_i} - k_{3f_i}z_{6f_i,d}e_{3f_i} - k_{4f_i}z_{6f_i,d}e_{5f_i}) \\ &- d_{22f_i}(1+k_{3f_i}z_{6f_i,d}^2)e_{3f_i}/m_{22f_i} + d_{22f_i}(1+k_{1f_i})e_{1f_i}z_{6f_i,d}/m_{22f_i} - k_{2f_i}d_{22f_i}z_{6f_i,d}^2e_{2f_i}/m_{22f_i} + d_{22f_i}z_{6f_i,d}\Delta_{f_i}/m_{22f_i}]^T \\ f_{2f_i}(t, \mathbf{y}_{f_i}) &= [e_{6f_i}, J_{2f_i} - f_{2f_i,d}]^T \\ g_{f_i}(t, \mathbf{x}_{f_i}, \mathbf{y}_{f_i}) &= \{[0, e_{2f_i} + z_{2f_i,d} - m_{22f_i}(e_{3f_i} + z_{3f_i,d})/d_{22f_i}], [0, \Delta_{f_i} + k_{1f_i}e_{1f_i} - k_{2f_i}z_{6f_i,d}e_{2f_i} - k_{3f_i}z_{6f_i,d}e_{3f_i} + z_{4f_i,d}], [0, 0], \\ &[0, d_{22f_i}[\Delta_{f_i} + (k_{1f_i} + 1)e_{1f_i} - k_{2f_i}z_{6f_i,d}e_{2f_i} - k_{3f_i}z_{6f_i,d}e_{3f_i} + z_{4f_i,d} + z_{1f_i,d}]/m_{22f_i}]\}^T \end{aligned}$$

Three steps are taken to prove that the system in (47) satisfies all the conditions of **Theorem 1**, as follows.

Step 1: In order to make the subsequent calculations more straightforward, we define the parameters shown in expression (48):

$$\begin{cases} c_{1f_i} = \lambda_{1f_i}(k_2d_{22f_i}/m_{1f_i} + 1) + k_{1f_i}\lambda_{2f_i} \\ c_{2f_i} = \lambda_{1f_i}k_{3f_i}d_{22f_i}/m_{1f_i} - \lambda_{3f_i}d_{22f_i}(1+k_{1f_i})/m_{22f_i} \\ c_{3f_i} = k_{3f_i}\lambda_{2f_i} - \lambda_{3f_i}k_{2f_i}d_{22f_i}/m_{22f_i} \\ c_{4f_i} = \lambda_{1f_i}m_{22f_i}/d_{22f_i} \end{cases} \quad (48)$$

By combining the control law in (31) for f_{1f_i} with the Lyapunov function in (30), we obtain:

$$\begin{aligned} \dot{V}_{f_i} &= -(1+k_{1f_i})\lambda_{1f_i}e_{1f_i}^2/d_{22f_i} - k_{2f_i}\lambda_{2f_i}z_{6f_i,d}^2e_{2f_i}^2 - \lambda_{3f_i}d_{22f_i}(1+k_{3f_i}z_{6f_i,d}^2)e_{3f_i}^2/m_{22f_i} + c_{1f_i}z_{6f_i,d}e_{1f_i}e_{2f_i} + \\ &c_{2f_i}z_{6f_i,d}e_{1f_i}e_{3f_i} - c_{3f_i}z_{6f_i,d}e_{2f_i}e_{3f_i} - c_{4f_i}z_{6f_i,d}e_{1f_i}e_{5f_i} - k_{4f_i}\Delta_{f_i}^2 \\ &\leq -(1+k_{1f_i})\lambda_{1f_i}e_{1f_i}^2/d_{22f_i} - k_{2f_i}\lambda_{2f_i}z_{6f_i,d}^2e_{2f_i}^2 - \lambda_{3f_i}(1+k_{3f_i}z_{6f_i,d}^2)e_{3f_i}^2/d_{22f_i} + c_{1f_i}(e_{1f_i}^2 + \\ &z_{6f_i,d}^2e_{2f_i}^2)/2 + c_{2f_i}(e_{1f_i}^2 + z_{6f_i,d}^2e_{3f_i}^2)/2 - c_{4f_i}(e_{1f_i} + z_{6f_i,d}e_{3f_i})^2/2 + c_{4f_i}e_{1f_i}^2/2 + c_{4f_i}z_{6f_i,d}^2e_{3f_i}^2/2 - \\ &c_{3f_i}z_{6f_i,d}(e_{2f_i} + e_{3f_i})^2/2 + c_{3f_i}z_{6f_i,d}^2e_{2f_i}^2/2 + c_{3f_i}z_{6f_i,d}^2e_{3f_i}^2/2 - k_{4f_i}\Delta_{f_i}^2 \quad (49) \\ &\leq -[(1+k_{1f_i})\lambda_{1f_i}d_{22f_i}/m_{1f_i} - (c_{1f_i} + c_{2f_i} + c_{4f_i})/2]e_{1f_i}^2 - [k_{2f_i}\lambda_{2f_i} - (c_{1f_i} + c_{3f_i})/2]z_{6f_i,d}^2e_{2f_i}^2 - [\lambda_{3f_i}(1 + \\ &k_{3f_i}z_{6f_i,d}^2)d_{22f_i}/m_{22f_i} - (c_{2f_i} + c_{3f_i} + c_{4f_i})z_{6f_i,d}^2/2]e_{3f_i}^2 - k_{4f_i}\Delta_{f_i}^2 \\ &= -\omega_{1f_i}e_{1f_i}^2 - \omega_{2f_i}z_{6f_i,d}^2e_{2f_i}^2 - \omega_{3f_i}e_{3f_i}^2 - \omega_{4f_i}\Delta_{f_i}^2 \end{aligned}$$

$$\text{where } \begin{cases} \omega_{1f_i} = [(1+k_{1f_i})\lambda_{1f_i}d_{22f_i}/m_{11f_i} - (c_{1f_i} + c_{2f_i} + c_{4f_i})/2] \\ \omega_{2f_i} = [k_{2f_i}\lambda_{2f_i} - (c_{1f_i} + c_{3f_i})/2]z_{6f_i,d}^2 \\ \omega_{3f_i} = [\lambda_{3f_i}d_{22f_i}(1+k_{3f_i}z_{6f_i,d}^2)/m_{22f_i} - (c_{2f_i} + c_{3f_i} + c_{4f_i})z_{6f_i,d}^2/2] \\ \omega_{4f_i} = k_{4f_i} \end{cases}$$

If parameters such as k_{1f_i} , k_{2f_i} , k_{3f_i} , k_{4f_i} , λ_{1f_i} , λ_{2f_i} and λ_{3f_i} are selected appropriately, then the parameters ω_{1f_i} , ω_{2f_i} , ω_{3f_i} and ω_{4f_i} can be guaranteed to be non-negative. The following results can then also be derived:

$$\begin{cases} V_{f_i}(t, \mathbf{x}_{f_i}) = V_{f_i} \geq \min\{\lambda_{1f_i}, \lambda_{2f_i}, 1, \lambda_{3f_i}\} \|\mathbf{x}_{f_i}\|^2 \geq \frac{1}{2} \min\{\lambda_{1f_i}, \lambda_{2f_i}, 1, \lambda_{3f_i}\} \|\mathbf{x}_{f_i}\|^2 = W_{f_i}(\mathbf{x}_{f_i}) \\ \dot{V}_{f_i} = \frac{\partial V_{f_i}}{\partial t} + \frac{\partial V_{f_i}}{\partial \mathbf{x}_{f_i}} f_{f_i}(t, \mathbf{x}_{f_i}) \leq 0, \quad \|\mathbf{x}_{f_i}\| \geq \eta_{f_i} \end{cases} \quad (50)$$

where $W_{f_i}(\mathbf{x}_{f_i})$ are positive definite proper functions and $\eta_{f_i} > 0$ are constants. Since

$$\left\| \frac{\partial V_{f_i}}{\partial \mathbf{x}} \right\| \leq \max\{\lambda_{1f_i}, \lambda_{2f_i}, 1, \lambda_{3f_i}\} \|\mathbf{x}_{f_i}\| \quad (51)$$

the following expression can be obtained:

$$\left\| \frac{\partial V_{f_i}}{\partial \mathbf{x}_{f_i}} \right\| \|\mathbf{x}_{f_i}\| \leq \max\{\lambda_{1f_i}, \lambda_{2f_i}, 1, \lambda_{3f_i}\} \|\mathbf{x}_{f_i}\|^2 \leq \frac{2 \max\{\lambda_{1f_i}, \lambda_{2f_i}, 1, \lambda_{3f_i}\}}{\min\{\lambda_{1f_i}, \lambda_{2f_i}, 1, \lambda_{3f_i}\}} V_{f_i} = c_{f_i} V_{f_i}(t, \mathbf{x}_{f_i}) \quad (52)$$

where $c_{f_i} = 2 \max\{\lambda_{1f_i}, \lambda_{2f_i}, 1, \lambda_{3f_i}\} / \min\{\lambda_{1f_i}, \lambda_{2f_i}, 1, \lambda_{3f_i}\}$ are positive constants. Thus, **Assumption 1** of **Theory 1** has been satisfied.

Step 2: In this step, the correlation function $g_{f_i}(t, \mathbf{x}_{f_i}, \mathbf{y}_{f_i})$ in (47) is analysed. This can be expressed as follows:

$$\begin{aligned} g_{f_i}(t, \mathbf{x}_{f_i}, \mathbf{y}_{f_i}) &= \{[0, z_{2f_i,d} - m_{22f_i} z_{5f_i,d} / d_{22f_i}; [0, z_{4f_i,d}]; [0, 0]; [0, d_{22f_i}(z_{4f_i,d} + z_{1f_i,d}) / m_{22f_i}]\} + \\ &\quad \{[0, e_{2f_i} - m_{22f_i} e_{5f_i} / d_{22f_i}]; [0, \Delta + k_{1f_i} e_{1f_i} - k_{2f_i} z_{6f_i,d} e_{2f_i} - k_{3f_i} z_{6f_i,d} e_{5f_i}]; [0, 0]; \\ &\quad [0, d_{22f_i}[\Delta_{f_i} + (k_{1f_i} + 1)e_{1f_i} - k_{2f_i} z_{6f_i,d} e_{2f_i} - k_{3f_i} z_{6f_i,d} e_{5f_i}] / m_{22f_i}]\} \\ &= g_{1f_i}(t, \mathbf{x}_{f_i}, \mathbf{y}_{f_i}) + g_{2f_i}(t, \mathbf{x}_{f_i}, \mathbf{y}_{f_i}) \end{aligned} \quad (53)$$

where,

$$\begin{aligned} g_{1f_i}(t, \mathbf{x}_{f_i}, \mathbf{y}_{f_i}) &= \{[0, z_{2f_i,d} - m_{22f_i} z_{5f_i,d} / d_{22f_i}]; [0, z_{4f_i,d}]; [0, 0]; [0, d_{22f_i}(z_{4f_i,d} + z_{1f_i,d}) / m_{22f_i}]\} \\ g_{2f_i}(t, \mathbf{x}_{f_i}, \mathbf{y}_{f_i}) &= \{[0, e_{2f_i} - m_{22f_i} e_{5f_i} / d_{22f_i}]; [0, \Delta + k_{1f_i} e_{1f_i} - k_{2f_i} z_{6f_i,d} e_{2f_i} - k_{3f_i} z_{6f_i,d} e_{5f_i}]; [0, 0]; [0, d_{22f_i}[\Delta_{f_i} + (k_{1f_i} + 1)e_{1f_i} - \\ &\quad k_{2f_i} z_{6f_i,d} e_{2f_i} - k_{3f_i} z_{6f_i,d} e_{5f_i}] / m_{22f_i}]\} \end{aligned}$$

From norm theory, we can show that:

$$\|g_{f_i}(t, \mathbf{x}_{f_i}, \mathbf{y}_{f_i})\| \leq \|g_{1f_i}(t, \mathbf{x}_{f_i}, \mathbf{y}_{f_i})\| + \|g_{2f_i}(t, \mathbf{x}_{f_i}, \mathbf{y}_{f_i})\| \quad (54)$$

$$\begin{aligned} \text{where } \|g_{1f_i}(t, \mathbf{x}_{f_i}, \mathbf{y}_{f_i})\| &\leq \|z_{2f_i,d}\| + m_{22f_i} \|z_{5f_i,d}\| / d_{22f_i} + (1 + d_{22f_i} / m_{22f_i}) \|z_{4f_i,d}\| + d_{22f_i} \|z_{1f_i,d}\| / m_{22f_i} = \theta_{1f_i}(\|\mathbf{y}_{f_i}\|), \\ \|g_{2f_i}(t, \mathbf{x}_{f_i}, \mathbf{y}_{f_i})\| &\leq \|e_{2f_i}\| + m_{22f_i} \|e_{5f_i}\| / d_{22f_i} + (1 + d_{22f_i} / m_{22f_i}) \|\Delta_{f_i}\| + [k_{1f_i} + d_{22f_i}(k_{1f_i} + 1) / m_{22f_i}] \|e_{1f_i}\| + (d_{22f_i} / m_{22f_i} + \\ &\quad 1) k_{2f_i} \|z_{6f_i,d}\| \|e_{2f_i}\| + (d_{22f_i} / m_{22f_i} + 1) k_{3f_i} \|z_{6f_i,d}\| \|e_{5f_i}\| \\ &\leq [1 + m_{22f_i} / d_{22f_i} + 1 + d_{22f_i} / m_{22f_i} + k_{1f_i} + d_{22f_i}(k_{1f_i} + 1) / m_{22f_i} + (d_{22f_i} / m_{22f_i} + 1) k_{2f_i}] \|z_{6f_i,d}\| + (d_{22f_i} / m_{22f_i} + \\ &\quad 1) k_{3f_i} \|z_{6f_i,d}\| \|\mathbf{x}_{f_i}\| \\ &= \theta_{2f_i}(\|\mathbf{y}_{f_i}\|, \|\mathbf{x}_{f_i}\|) \end{aligned}$$

and $\theta_{1f_i}(\|\mathbf{y}_{f_i}\|, \|\mathbf{x}_{f_i}\|), \theta_{2f_i}(\|\mathbf{y}_{f_i}\|, \|\mathbf{x}_{f_i}\|): \mathbf{R}(\geq 0) \rightarrow \mathbf{R}(\geq 0)$ are continuous functions. The following expression therefore holds:

$$\|g_{f_i}(t, \mathbf{x}_{f_i}, \mathbf{y}_{f_i})\| \leq \theta_{1f_i}(\|\mathbf{y}_{f_i}\|) + \theta_{2f_i}(\|\mathbf{y}_{f_i}\|, \|\mathbf{x}_{f_i}\|) \quad (55)$$

which satisfies **Assumption 2** of **Theory 1**.

Step 3: Combining the control law in (38) for f_{2f_i} with the Lyapunov function in (37) leads to:

$$\dot{V}_{2f_i} = -k_{5f_i} k_{6f_i} e_{3f_i}^2 - k_{7f_i} \Theta_{f_i}^2 \leq -\min\{k_{5f_i}, k_{6f_i}, k_{7f_i}\} \| [e_{3f_i}, \Theta_{f_i}] \|^2 = -\sigma_{3f_i} \| [e_{3f_i}, \Theta_{f_i}] \|^2 \quad (56)$$

and

$$\min\{k_{6f_i} / 2, 1 / 2\} \| [e_{3f_i}, \Theta_{f_i}] \|^2 \leq V_{2f_i} \leq \max\{k_{6f_i} / 2, 1 / 2\} \| [e_{3f_i}, \Theta_{f_i}] \|^2 \quad (57)$$

where $\sigma_{1f_i} = \min\{k_{6f_i} / 2, 1 / 2\}$, $\sigma_{2f_i} = \max\{k_{6f_i} / 2, 1 / 2\}$.

According to **Theory 2**, $[e_{3f_i}, \Theta_{f_i}] = \mathbf{0}$ is globally exponentially stable. If we combine the expressions in (32) and (33), we can show that $[e_{3f_i}, e_{6f_i}] = \mathbf{0}$ is globally exponentially stable.

$$\|\mathbf{y}_{f_i}(t, t_0, \mathbf{y}_{f_i}(t_0))\| \leq k_{f_i} \|\mathbf{y}_{f_i}(t_0)\| e^{-\lambda_{f_i}(t-t_0)}, \forall \|\mathbf{y}_{f_i}(t_0)\| \leq \delta_{f_i} \quad (58)$$

where k_{f_i} , λ_{f_i} and δ_{f_i} are positive constants and δ_{f_i} can be arbitrarily small. Then

$$\int_{t_0}^{\infty} \|\mathbf{y}_{f_i}(t, t_0, \mathbf{y}_{f_i}(t_0))\| \leq \int_{t_0}^{\infty} k_{f_i} \|\mathbf{y}_{f_i}(t_0)\| e^{-\lambda_{f_i}(t-t_0)} = k_{f_i} \|\mathbf{y}_{f_i}(t_0)\| / \lambda_{f_i} = \kappa_{f_i}(\|\mathbf{y}_{f_i}(t_0)\|) \quad (59)$$

where the function $\kappa_{f_i}(\cdot)$ is a class κ function.

Hence, the system described in (47) satisfies all the conditions of **Theory 1**. The system in (47) is GUAS, and the variables \mathbf{x}_{f_i} and \mathbf{y}_{f_i} are GUAS to $\mathbf{0}$. By combining expressions (25) and (26), we see that $[e_{1f_i}, e_{2f_i}, e_{3f_i}, e_{4f_i}, e_{5f_i}, e_{6f_i}] = \mathbf{0}$ is GUAS. Based on the tracking error system described in (21), stable cooperative formation control of the USVs can be realised using the control law expressed in (31) and (38).

SIMULATION EXPERIMENT

Several simulation experiments were carried out to verify the effectiveness and reliability of our cooperative formation control algorithm. The mathematical model for the USVs is taken from [30], and the parameter values are shown in Table 1.

Tab. 1. Model parameters

Parameters	Value	Parameters	Value
m_{11}	25.8	d_{11}	12
m_{22}	33.8	d_{22}	17
m_{33}	2.76	d_{33}	0

The trajectory of the leader USV is generated by the following expression, which can be used to design different forms of leader trajectory.

$$\begin{cases} \dot{x}_d = u_d \cos \varphi_d - v_d \sin \varphi_d \\ \dot{y}_d = u_d \sin \varphi_d + v_d \cos \varphi_d \\ \dot{\varphi}_d = r_d \\ \dot{v}_d = -m_{11}u_d r_d / m_{22} - d_{22}v_d / m_{22} \end{cases}$$

Three USVs with same model parameters (a leader USV and two follower USVs) were used in the simulation experiment, and three kinds of trajectory (a straight line, a circular trajectory and a general S-shaped trajectory) were designed to demonstrate the performance of our control algorithm. In order to verify the robustness and stability of the proposed algorithm, a stable disturbance and a sinusoidal disturbance were added in the longitudinal and steering control directions. Disturbances of $d_u = 2 + 0.1\sin(0.2t)$ in the longitudinal direction and $d_r = 1 + 0.1\sin(0.5t)$ in the heading control direction were also added.

Since there are numerous control parameters that need to be set for the control system, several basic principles were followed: (a) all the parameters should be positive, since they are all defined as positive; (b) the parameters for each follower should be the same except for k_{1f_i} , since different speeds are needed for different followers; (c) k_{6f_i} should be small, since a higher value of k_{6f_i} means a lower convergence speed, as can be seen from (56) and (57); (d) λ_{nf_i} can be chosen arbitrarily, as this has a minor impact on the system.

Case 1: A straight line trajectory is designed for the leader USV, and in order to ensure a cooperative formation, the positional information of the follower USVs relative to the leader USV is determined based on the parameters in Table 2. The initial states of the USVs and the control parameters are also shown in Table 2, and the simulation results are presented in Figs. 3 and 4.

Tab. 2. Initial states and control parameters

Symbol	Value	Symbol	Value	Symbol	Value
u_{ld}	10 m/s	L_1	5 m	L_2	5 m
r_{ld}	0	θ_1	$\pi / 2$	θ_2	$-\pi / 2$
$x_l(0)$	15 m	$x_{f_1}(0)$	9 m	$x_{f_2}(0)$	20 m
$y_l(0)$	-6 m	$y_{f_1}(0)$	8 m	$y_{f_2}(0)$	-7 m
$\varphi_l(0)$	0.7 rad	$\varphi_{f_1}(0)$	0.3 rad	$\varphi_{f_2}(0)$	0.3 rad
$u_1(0)$	0.5 m/s	$u_{f_1}(0)$	0.5 m/s	$u_{f_2}(0)$	0.5 m/s
$v_1(0)$	0.5 m/s	$v_{f_1}(0)$	0.5 m/s	$v_{f_2}(0)$	0.5 m/s
(0)	0	$r_{f_1}(0)$	0	$r_{f_2}(0)$	0
k_{1l}	2.3	k_{1f_1}	1.6	k_{1f_2}	0.03
k_{2l}	5	k_{2f_1}	15	k_{2f_2}	15
k_{3l}	5	k_{3f_1}	15	k_{3f_2}	15
k_{4l}	3	k_{4f_1}	15	k_{4f_2}	13
k_{5l}	25	k_{5f_1}	20	k_{5f_2}	20

Symbol	Value	Symbol	Value	Symbol	Value
k_{6l}	1	k_{6f_1}	0.001	k_{6f_2}	5
k_{7l}	1	k_{7f_1}	1	k_{7f_2}	1
λ_{1l}	1	λ_{1f_1}	1	λ_{1f_2}	1
λ_{2l}	1	λ_{2f_1}	1	λ_{2f_2}	1
λ_{3l}	1	λ_{3f_1}	1	λ_{3f_2}	1

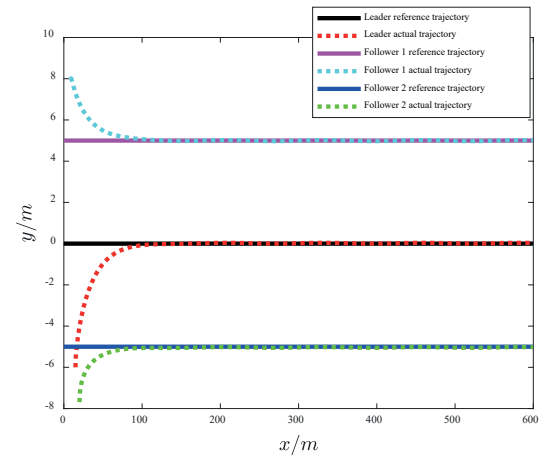
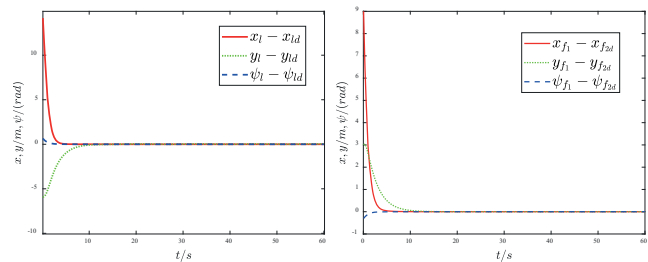
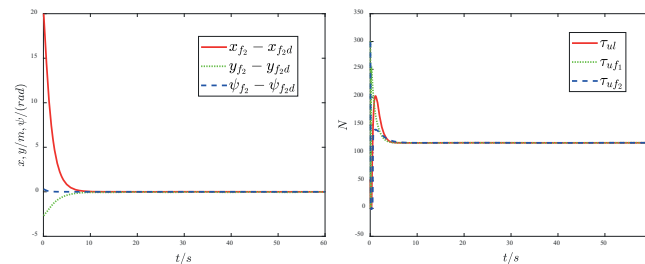


Fig. 3. Results from our cooperative formation control algorithm for a straight line trajectory



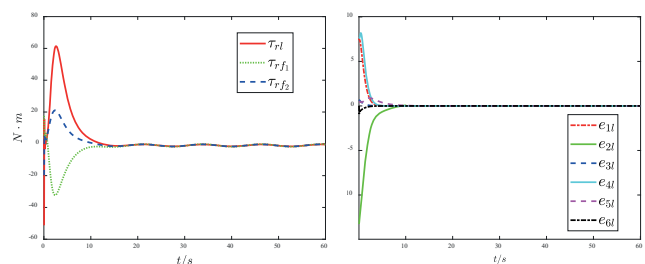
(a) Convergence curve for the position and heading angle of the leader USV

(b) Convergence curve for the position and heading angle of the Follower 1 USV



(c) Convergence curve for the position and heading angle of the Follower 2 USV

(d) Surge control forces for the three USVs



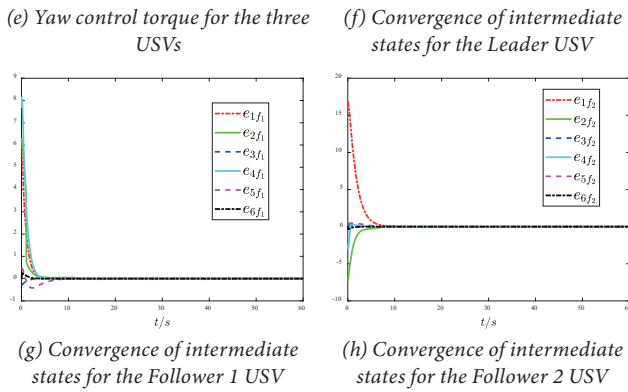


Fig. 4 Detailed error convergence curves and control forces for Case 1

Case 2: A circular trajectory was designed for the leader USV, and in order to ensure a cooperative formation, the positional information for the follower USVs relative to the leader was designed as shown by the initial states in Table 3. The initial states of the USVs are also shown in Table 3, and the results of the simulation are presented in Figs. 5 and 6.

Tab. 3. Initial states for Case 2

Symbol	Value	Symbol	Value	Symbol	Value
u_{ld}	10 m/s	L_1	20 m	L_2	20 m
r_{ld}	0.1 rad/s	θ_1	$\pi / 2$	θ_2	$-\pi / 2$
$x_l(0)$	15 m	$x_{f_1}(0)$	9 m	$x_{f_2}(0)$	20 m
$y_l(0)$	-6 m	$y_{f_1}(0)$	15 m	$y_{f_2}(0)$	-25 m
$\varphi_l(0)$	0.7 rad	$\varphi_{f_1}(0)$	0.3 rad	$\varphi_{f_2}(0)$	0.7 rad
$u_1(0)$	0	$u_{f_1}(0)$	0	$u_{f_2}(0)$	0
$v_1(0)$	0	$v_{f_1}(0)$	0	$v_{f_2}(0)$	0
$r_1(0)$	0	$r_{f_1}(0)$	0	$r_{f_2}(0)$	0

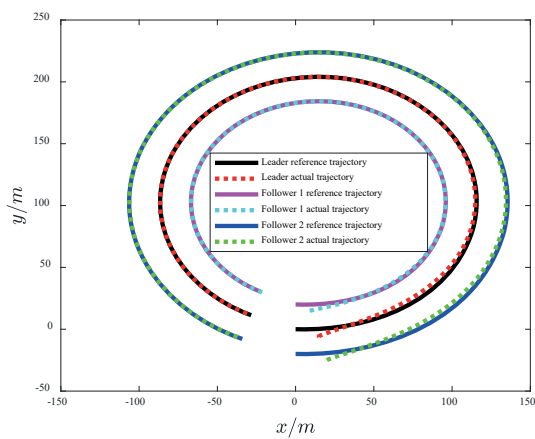
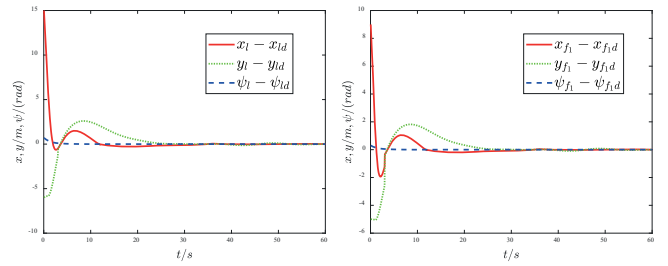
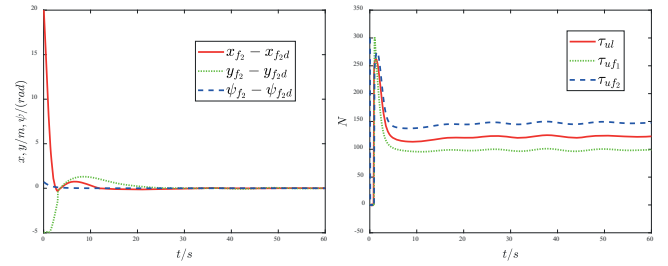


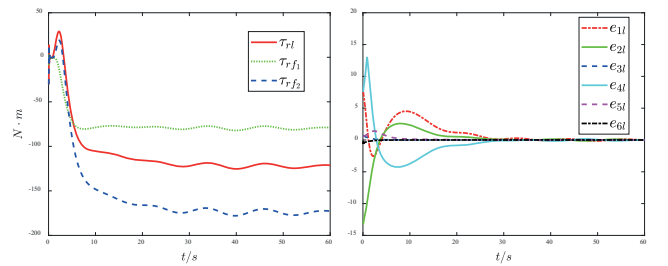
Fig. 5. Results of our cooperative formation control algorithm for a circular trajectory



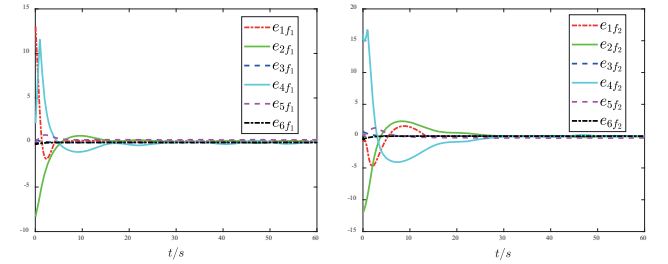
(a) Convergence curve for the position and heading angle of the leader USV (b) Convergence curve for the position and heading angle of the Follower 1 USV



(c) Convergence curve for the position and heading angle of the Follower 2 USV (d) Surge control forces for the three USVs



(e) Yaw control torque for the three USVs (f) Convergence of intermediate states for the Leader USV;



(g) Convergence of intermediate states for the Follower 1 USV; (h) Convergence of intermediate states for the Follower 2 USV

Fig. 6. Detailed error convergence curves and control forces for Case 2

Case 3: A general S-shaped trajectory was designed for the leader USV by setting $u_{ld} = 10 \text{ m/s}$, $r_{ld} = 0.1 \text{ rad/s}$, $t \leq 30$ and $r_{ld} = -0.05 \text{ rad/s}$, $t > 30$. In order to ensure a cooperative formation, the positional information for the follower USVs relative to the leader USV was designed based on the parameters shown in Table 4. The initial states of the USVs are also shown in Table 4, and the results of the simulation are presented in Figs. 7 and 8.

Tab. 4. Initial states for case 3

Symbol	Value	Symbol	Value	Symbol	Value
u_{ld}	10 m/s	L_1	30 m	L_2	30 m
r_{ld}	0.1/-0.05	θ_1	$\pi / 2$	θ_2	$-\pi / 2$
$x_l(0)$	15 m	$x_{f_1}(0)$	0	$x_{f_2}(0)$	20 m
$y_l(0)$	-6 m	$y_{f_1}(0)$	20 m	$y_{f_2}(0)$	-45 m
$\varphi_l(0)$	0.7 rad	$\varphi_{f_1}(0)$	0.7 rad	$\varphi_{f_2}(0)$	0.7 rad
$u_1(0)$	0	$u_{f_1}(0)$	0	$u_{f_2}(0)$	0
$v_1(0)$	0	$v_{f_1}(0)$	0	$v_{f_2}(0)$	0
$r_1(0)$	0	$r_{f_1}(0)$	0	$r_{f_2}(0)$	0

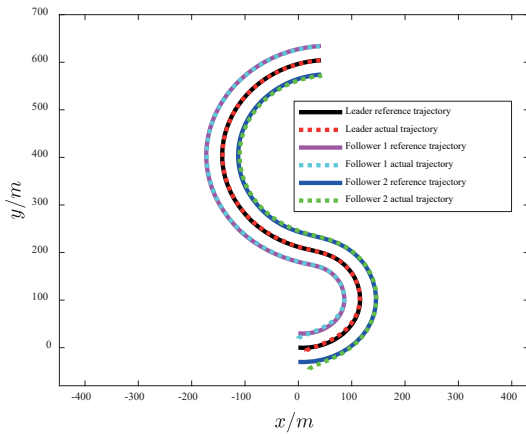


Fig. 7 Results from our cooperative formation control algorithm for a general S-shaped trajectory

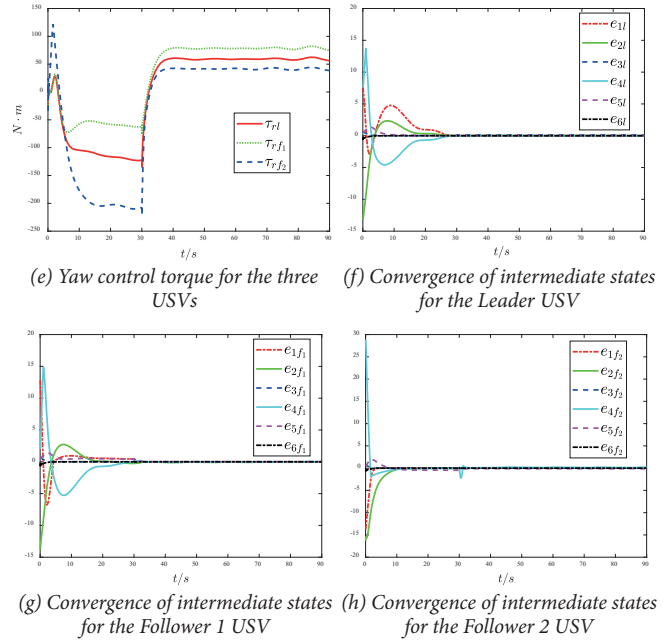
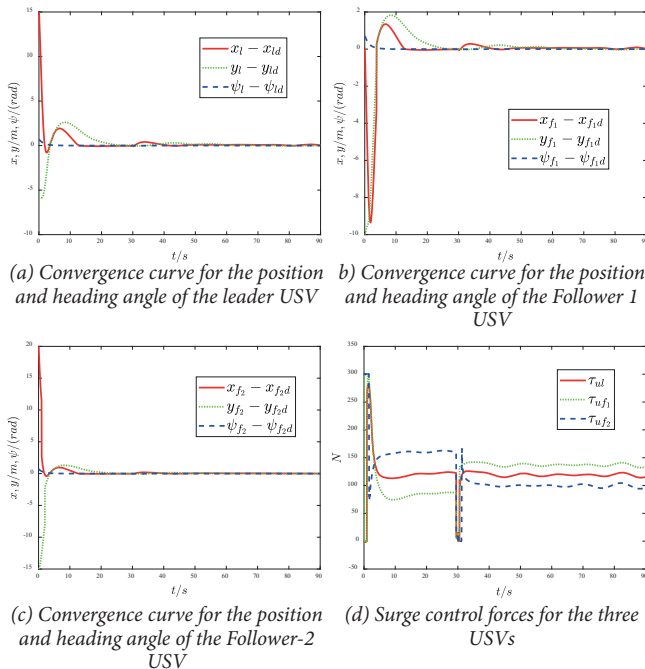


Fig. 8 Detailed error convergence curves and control forces of Case 3

The simulation results shown above in Figs. 3 to 8 indicate that the necessary system convergence time for each kind of trajectory tracking processes is within the range 10–30 seconds, and there are no instabilities or divergences after the system has converged. It is therefore obvious that the cooperative formation control algorithm proposed in this paper is stable, reliable and effective. Tracking control was successful for all three kinds of formation trajectories examined here, indicating that the general applicability of our control method is superior to conventional algorithms. From the simulation results presented above, and compared with the results reported in the literature [11] and [22], we can see that the convergence time of the proposed control algorithm is shorter, and the stability of control is better in our simulation results. In addition, the actual tracking trajectory of the USVs is smoother, and our algorithm has a wider range of applications for different kind of trajectories.

In Cases 2 and 3, the control inputs of surge control force and yaw control torque do not converge to zero, since the reference trajectories are curved in these cases, and certain control inputs in terms of both the surge control force and yaw control torque are required to ensure the sailing formation of the USVs. In addition, the actual control inputs are different, since the length of each trajectory is not the same and the necessary velocities are different. In Case 3, a state switch occurs in the middle part of the reference trajectory (that is, a change in the desired angular velocity), meaning that both the surge control force and yaw control torque undergo an abrupt adjustment process, as shown in Figs. 8(d) and (e). From the results for Case 3, we know that in order to change the formation of the USVs, the control inputs for both the surge and yaw vary rapidly due to the fast convergence of the control algorithm; if the desired trajectory is smooth transition designed then this sudden adjustment could be

avoided. In an actual application, the rate of change could be set to an even value based on the change rate of the propulsion devices of USVs. In addition, for USVs that are not equipped with reversible propellers, the surge control force could also be set to a non-negative value throughout the cooperative formation control process of the underactuated USVs.

CONCLUSION

A method of cooperative formation control is proposed in this paper for a group of underactuated USVs based on nonlinear backstepping and cascade system theory. A novel description of the problem of cooperative formation control of a group of USVs is presented, and the desired positions and attitude angles of the follower USVs are transformed into intermediate variables that facilitate the design of the controller. A new type of global differential homeomorphism transformation is put forward for the tracking error system of the follower USVs in order to simplify the description of the control system; this makes the complex formation control system easy to analyse and means that it can be decomposed into a cascaded system. In order to improve the stability of the cooperative formation controller, novel intermediate state variables and virtual control laws are devised for use in design process of the control algorithm. By combining the backstepping technique, Lyapunov's direct method and cascade system theory, we develop an improved controller for cooperative formation control of a group of underactuated USVs. We prove that our cooperative formation control algorithm for USVs is GUAS, and a variety of simulation experiments are carried out to verify the validity, stability and reliability of the algorithm, which show that the general applicability of the control method designed is superior to conventional algorithms. Some interference factors such as actual ocean environmental disturbances and uncertainties in the USV models are not fully considered in this paper, and we intend to focus on these in future research work.

ACKNOWLEDGEMENTS

This research was funded by the National Natural Science Foundation of China (Grant No. 51709214, 51809203, 51879210), Xiangyang Science and Technology Plan Project (Grant No. 2017YL12, 2019ZD03, Hubei Superior and Distinctive Discipline Group of „Mechatronics and Automobiles“ (Grant No. XKQ2021012)

REFERENCES

1. J. F. Jimenez and J. M. Giron-Sierra, "USV based automatic deployment of booms along quayside mooring ships: Scaled experiments and simulations," *Ocean Engineering*, vol. 207, pp. 1–12, Jul. 2020. doi:10.1016/j.oceaneng.2020.107438.
2. J. Y. Zhuang, L. Zhang, Z. H. Qin, H. B. Sun, B. Wang, and J. Cao, "Motion control and collision avoidance algorithm for unmanned surface vehicle swarm in practical maritime environment," *Polish Maritime Research*, vol. 26, no. 1, pp.107–116. doi: 10.2478/pomr-2019-0012.
3. B. C. Shah and S. K. Gupta, "Long-distance path planning for unmanned surface vehicles in complex marine environment," *IEEE Journal of Oceanic Engineering*, vol. 45, no. 3, pp. 813–830, Jul. 2020. doi:10.1109/JOE.2019.2909508.
4. X. Liang, X. R. Qu, Y. H. Hou, Y. Li, and R. B. Zhang, "Distributed coordinated tracking control of multiple unmanned surface vehicles under complex marine environments," *Ocean Engineering*, vol. 205, pp. 1–9, Jun. 2020. doi:10.1016/j.oceaneng.2020.107328.
5. H. N. Esfahani and R. Szlapczynski, "Model predictive super-twisting sliding mode control for an autonomous surface vehicle," *Polish Maritime Research*, vol. 26, no. 3, pp. 163–171, Sept. 2019. doi: 10.2478/pomr-2019-0057.
6. M. A. Hinostroza, H. T. Xu, and C. G. Soares, "Cooperative operation of autonomous surface vehicles for maintaining formation in complex marine environment," *Ocean Engineering*, vol. 183, pp. 132–154, Jul. 2019. doi:10.1016/j.oceaneng.2019.04.098.
7. R. V. C. Vid, J. P. V. S. Cunha, and P. B. Garcia-Rosa, "Stabilizing control of an unmanned surface vehicle pushing a floating load," *International Journal of Control, Automation and Systems*, vol. 18, pp. 1–10, Jun. 2020. doi:10.1007/s12555-019-0677-1.
8. S. S. Wang and Y. L. Tuo, "Robust trajectory tracking control of underactuated surface vehicle with prescribed performance," *Polish Maritime Research*, vol. 27, no. 4, pp. 148–156, Dec. 2020. doi: 10.2478/pomr-2020-0075.
9. C. Paliotta, E. Lefeber, K. Y. Pettersen, J. Pinto, M. Costa, and J. T. D. B. Sousa, "Trajectory tracking and path following for underactuated marine vehicles," *IEEE Transactions on Control Systems Technology*, vol. 27, no. 4, pp. 1423–1437, Jul. 2019. doi:10.1109/TCST.2018.283-4518.
10. J. Han and J. Kim, "Three-dimensional reconstruction of a marine floating structure with an unmanned surface vessel," *IEEE Journal of Oceanic Engineering*, vol. 44, no. 4, pp. 984–996, Oct. 2019. doi:10.1109/JOE.2018.2862618.
11. K. Shojaei, "Leader–follower formation control of underactuated autonomous marine surface vehicles with limited torque," *Ocean Engineering*, vol. 105, pp. 196–205, Jun. 2015. doi:10.1016/j.oceaneng. 2015.06.026.
12. Z. Y. Gao and G. Guo, "Adaptive formation control of autonomous underwater vehicles with model uncertainties,"

- Int. J. Adapt. Control Signal Process*, vol. 32, pp. 1067–1080, Mar. 2018. doi:10.1002/acs. 2886.
13. J. Ghommam and M. Saad, “Adaptive leader–follower formation control of underactuated surface vessels under asymmetric range and bearing constraints,” *IEEE Transactions on Control Systems Technology*, vol. 67, no. 2, pp. 852–865, Feb. 2018. doi:10.1109/TVT. 2017.2760367.
 14. L. Y. Chen, H. Hopman, and R. R. Negenborn, “Distributed model predictive control for vessel train formations of cooperative multi-vessel systems,” *Transportation Research Part C-Emerging Technologies*, vol. 92, pp. 101–118, May 2018. doi:10.1016/j.trc.2018. 04.013.
 15. J. X. Zhang and G. H. Yang, “Fault-tolerant leader-follower formation control of marine surface vessels with unknown dynamics and actuator faults,” *Int. J. Robust Nonlinear Control*, vol. 28, pp. 4188–4208, Apr. 2018. doi:10.1002/rnc.4228.
 16. M. Y. Fu and L. L. Yu, “Finite-time extended state observer-based distributed formation control for marine surface vehicles with input saturation and disturbances,” *Ocean Engineering*, vol. 159, pp. 219–227, Apr. 2018. doi:10.1016/j.oceaneng.2018.04.016.
 17. T. S. Li, R. Zhao, C. L. P. Chen, L. Y. Fang, and C. Liu, “Finite-time formation control of under-actuated ships using nonlinear sliding mode control,” *IEEE Transactions on Cybernetics*, vol. 48, no. 11, pp. 3243–3253, Nov. 2018. doi:10.1109/TCYB.2018.2794968.
 18. Z. J. Sun, G. Q. Zhang, Y. Lu, and W. D. Zhang, “Leader-follower formation control of underactuated surface vehicles based on sliding mode control and parameter estimation,” *ISA Transactions*, vol. 72, pp. 15–24, Nov. 2017. doi:10.1016/j.isatra.2017.11.008.
 19. S. L. Dai, S. D. He, H. Lin, and C. Wang, “Platoon formation control with prescribed performance guarantees for USVs,” *IEEE Transportation on Industrial Electronics*, vol. 65, no. 5, pp. 4237–4246, May 2018. doi:10.1109/TIE.2017.2758743.
 20. Y. Lu, G. Q. Zhang, Z. J. Sun, and W. D. Zhang, “Robust adaptive formation control of underactuated autonomous surface vessels based on MLP and DOB,” *Nonlinear Dynamics*, vol. 94, pp. 503–519, Jun. 2018. doi:10.1007/s11071-018-4374-z.
 21. Y. Li and J. Zheng, “The design of ship formation based on a novel disturbance rejection control,” *International Journal of Control, Automation and Systems*, vol. 16, no. 4, pp. 1833–1839, Feb. 2018. doi: 10.1007/s12555-017-0424-4.
 22. B. S. Park and S. J. Yoo, “Adaptive-observe-based formation tracking of networked uncertain underactuated surface vessels with connectivity preservation and collision avoidance,” *Journal of the Franklin Institute-Engineering and Applied Mathematics*, vol. 356, pp. 7947–7966, Apr. 2019. doi:10.1016/j.jfranklin.2019.04.017.
 23. C. F. Huang, X. K. Zhang, and G. Q. Zhang, “Improved decentralized finite-time formation control of underactuated USVs via a novel disturbance observer,” *Ocean Engineering*, vol. 174, pp. 117–124, Jan. 2019. doi:10.1016/j.oceaneng.2019.01.043.
 24. Z. H. Peng, N. Gu, Y. Zhang, Y. J. Liu, D. Wang, and L. Liu, “Path-guided time-varying formation control with collision avoidance and connectivity preservation of under-actuated autonomous surface vehicles subject to unknown input gains,” *Ocean Engineering*, vol. 191, pp. 1–10, Oct. 2019. doi:10.1016/j.oceaneng.2019.106501.
 25. J. Li, J. L. Du, and W. J. Chang, “Robust time-varying formation control for underactuated autonomous underwater vehicles with disturbances under input saturation,” *Ocean Engineering*, vol. 179, pp. 180–188, Mar. 2019. doi:10.1016/j.oceaneng.2019.03.017.
 26. H. N. Esfahani, R. Szlapczynski and H. Ghaemi, “High performance super-twisting sliding mode control for a maritime autonomous surface ship (MASS) using ADP-based adaptive gains and time delay estimation”, *Ocean Engineering*, vol. 191, no. 106526, pp.1–19, Nov. 2019. doi:10.1016/j.oceaneng.2019.106526.
 27. T. Fossen, “*Handbook of Marine Craft Hydrodynamics and Motion Control*”, New York: Wiley, 2011.
 28. E. Panteley, E. Lefeber, A. Loria and H. Nijmeijer, “Exponential tracking control of a mobile car using cascaded approach,” *IFAC Proceedings*, vol. 31, no. 27, pp. 201–206, 1998. doi: 10.1016/S1474-6670(17)40028-0.
 29. H. K. Khalil, “*Nonlinear Systems*” 3rd ed., New Jersey: Prentice Hall, 2002.
 30. K. D. Do and J. Pan, “Global robust adaptive path following of underactuated ships,” *Automatica*, vol. 42, no. 10, pp.1713–1722, Oct. 2006. doi: 10.1016/j.automatica.2006.01.026.

CONTACT WITH THE AUTHORS

Tao Qin

e-mail: heu_qt@163.com

School of Mechanical Engineering
Hubei University of Arts and Sciences
Xiangyang, No.296
Longzhong Road, 441053,
CHINA

Zaopeng Dong

e-mail: dongzaopeng@whut.edu.cn

Key Laboratory of High Performance Ship Technology
(Wuhan University of Technology)
Ministry of Education
Wuhan University of Technology
Wuhan, No. 1178
Heping Avenue 430063
CHINA

School of Transportation
Wuhan University of Technology
Wuhan, No. 1178
Heping Avenue, 430063
CHINA

COMPUTATIONAL INTELLIGENCE IN MARINE CONTROL ENGINEERING EDUCATION

Józef Lisowski
Gdynia Maritime University, Poland

ABSTRACT

This paper presents a new approach to the existing training of marine control engineering professionals using artificial intelligence. We use optimisation strategies, neural networks and game theory to support optimal, safe ship control by applying the latest scientific achievements to the current process of educating students as future marine officers. Recent advancements in shipbuilding, equipment for robotised ships, the high quality of shipboard game plans, the cost of overhauling, dependability, the fixing of the shipboard equipment and the requesting of the safe shipping and environmental protection, requires constant information on recent equipment and programming for computational intelligence by marine officers. We carry out an analysis to determine which methods of artificial intelligence can allow us to eliminate human subjectivity and uncertainty from real navigational situations involving manoeuvring decisions made by marine officers. Trainees learn by using computer simulation methods to calculate the optimal safe traverse of the ship in the event of a possible collision with other ships, which are mapped using neural networks that take into consideration the subjectivity of the navigator. The game-optimal safe trajectory for the ship also considers the uncertainty in the navigational situation, which is measured in terms of the risk of collision. The use of artificial intelligence methods in the final stage of training on ship automation can improve the practical education of marine officers and allow for safer and more effective ship operation.

Keywords: ship control, marine engineering curriculum, computational intelligence, game theory, computer simulation

INTRODUCTION

This paper addresses the theoretical and practical training of students as future ship officers in the field of ship control engineering and its functional facilities and processes. Control engineering includes the fundamentals of automation and specialist subjects in the field of automation, computer science, electronics, optimisation and artificial intelligence (AI). Knowledge in the field of control engineering is acquired successively, through the following stages: lectures, laboratory work, simulations and operational practice on a ship.

In laboratory sessions dealing with the fundamentals of automation, students become acquainted with the two main decision support tools of AI and game theory. These

are represented by two exemplary control algorithms, which allow for a better understanding and application of training in simulator sessions.

The purpose of control engineering training within marine territories is to pass on information on the development of ship computerisation frameworks and associated tasks, as set out by the International Maritime Organisation in the STCW-95 convention. The training of marine officers on automation should include the modern equipment carried on ships, in addition to control engineering theory and modern control engineering techniques, and may follow the textbook by Nise [19]. Heiselberg and Stateczny [7], Huang et al. [10], Lazarowska [13], Lebkowski [14] and Zhuang et al. [32] have shown that computer-aided navigation training on safe ship

controls that involves computational intelligence methods and game theory has become important. Annual statistical studies prepared by the European Maritime Safety Agency (EMSA), have demonstrated that around 80% of maritime accidents are caused by the subjectivity of a navigator when assessing the navigation situation, and before making the final manoeuvring decision.

An analysis by Ahn et al. [1] has shown that the use of AI methods in the form of a neural network to decide on the correct direction for the ship during situations of excessive proximity to others allows for the consideration of the navigator's subjectivity during the impact on the final safe manoeuvre.

Liu et al. [16] demonstrated that the use of game hypothesis to decide on a safe direction for a ship in a collision event allows for the consideration of uncertainty when encountering large numbers of nearby ships, especially in areas of limited visibility. In both cases, there are many solutions for determining safe directions for ships, and the best of these solutions should be selected, i.e. the optimal solution based on a particular criterion, such as extending the cruise route to ensure safe avoidance of other ships. As reported by Guenin et al. [5], Speyer et al. [24], Szlapczynska et al. [25], Witkowska et al. [30] and Yong [31], both static and dynamic optimisation methods can be used.

The aim of this research is to present two control algorithms to represent the two main components that are important when making decisions in simulator training: the subjectivity of decisions, which can be described by an artificial neural network model, and the uncertainty of navigation situations, as measured by the possible risk of collision, which can be mapped using a model of an appropriate game. These studies can be very valuable both when designing of new versions of simulators and when using them for training.

These new elements link the Bellman optimality principle with a neural network model to generate domains for ships and a matrix game, with collisional risk to the synthesis of safe steering of the ship's movement.

CONTROL ENGINEERING

Control engineering is taught within the Faculties of Navigation, Marine Engineering and Electrical Engineering at the Maritime University. Cwilewicz et al. [4] found that the curriculum grades within each department were different, and addressed both the explicit responsibilities of graduates when on board and the requirements arising from maritime conventions.

Cadets in the Faculties of Navigation and Marine Engineering mainly receive instruction in the single subject of automation fundamentals, while those in the Faculty of Electrical Engineering receive a broader range of training in automation due to their wider range of official duties when operating devices onboard. Based on the principles identified by Borrego et al. [3], Henri et al. [8] and Lattuca et al. [12], it is possible to design curricula in such a way that cadets receive

practical instruction in automatic control techniques, which is more useful within the profession of ship electroautomatics. The two-level system for training in automation within the Faculty of Electrical Engineering includes the following topics, delivered via lectures and laboratories:

- At the basic engineering level:
 - Basics of Automatics
 - Electronics and Power Electronics
 - Digital Technology
 - Mechatronics and Robotics
 - Devices and Control Systems Engineering
 - Automated Electrical Ship Power Drives
 - Automation of Ship Power Systems
 - Programmable Logic Controllers
 - Visualisation of Control Processes
- At the more advanced Master's level:
 - Advanced Control Engineering Methods
 - Optimisation Methods
 - AI Methods
 - Digital Control Systems
 - Automation of Electrical Power Plants
 - Distributed Control Systems
 - Computer Control Support.

FUNDAMENTALS OF AUTOMATION

The course on the Basics of Automatics includes the following themes:

- 1) Theory and techniques of automation:
 - Principles of automation-basic definitions, open and closed-loop feedback control systems, types of automatic control;
 - Methods of describing the static and dynamic properties of the physical elements of control systems: transfer function, time and frequency responses, state equations;
 - Basic physical elements of control systems and their features;
 - Characteristics of typical industrial control objects;
 - Identification of control objects;
 - Structural block diagrams of automatic control systems;
 - The requirements that should be met by automatic control systems-stability margins, quality control within transitory states, accepted steady-state errors, correction of control systems;
 - PID controllers-structures and characteristics, selection of optimal settings;
 - Direct digital control;
 - Complex systems of automatic control-cascade control, closed-open systems, multivariable control systems;
 - Nonlinear systems, relay control, two-set controllers, three-set controllers, step controllers.
- 2) Modern control systems:
 - Extremal control;
 - Optimal control;
 - Adaptive control;
 - Game control;

- Computational intelligence control-expert systems, fuzzy control, artificial neural networks, evolutionary algorithms.
- 3) Systems engineering for control of ship movement:
- Methods for describing the dynamics of a ship as an automatically controlled object;
 - Ship control systems-maintenance of course and trajectory, control of the ship's speed, dynamic positioning, precise ship steering via thrusters, roll stabilisation, safe control in collision situations, optimisation of the ship's route.
- 4) Shipboard control systems:
- Main propulsion system of a ship with adjustable pitch propeller;
 - Power generation plant;
 - Cargo refrigerated hold;
 - Ballast and bilge systems;
 - Thruster system;
 - Fire detection, alarm and fighting system;
 - Microprocessor system for monitoring and control of the engine room.

PRACTICAL EDUCATION

Trussell et al. [28] and Weisner et al. [29] report that the teaching process takes place in the following three forms:

- Lectures, exercises and laboratory exercises;
- Operating experience through a school (seafaring and manoeuvring practices) and on board commercial ships (operational practices);
- Exercises on training simulators (navigational, radar, cargo and specialist).

Based on experience, Guzey et al. [6], Nikolic [18] and Trevelyan [27], from the perspective of the forthcoming work of a graduate as an administrator of control frameworks onboard a ship, the training on ships and test system practices play a key role.

COMPUTER SUPPORT FOR OPTIMAL AND SAFE SHIP CONTROL

Safe ship control relies upon constant monitoring of the conditions at sea, anti-collision manoeuvres, its acknowledgement and the safe control to the closest return point, recently assigned on the electronic map. These factors are crucial when deciding on a safe trajectory for a ship, since a ship's single-manoeuve system or potential speed is a multi-stage decision-making process, as discussed by Bellman [2].

The implementation of a multi-stage safety control system is difficult, due to the complex properties of the control process. In training strategies that involve the selection of a manoeuvre or trajectory, one should expect the control algorithms programmed within the microprocessor controller, which defines the anti-collision framework of the ARPA radar, as illustrated in Figure 1.

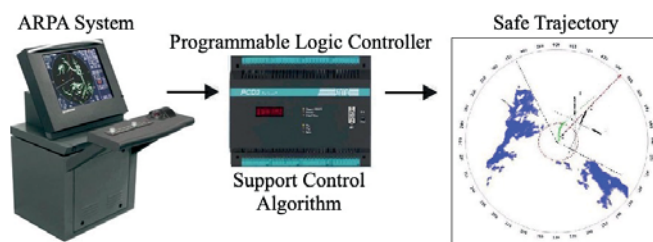


Fig. 1. Computer navigator decision support system in a collision situation at sea.

Ship control relies on the accuracy of traffic data, and uses mathematical descriptions of control processes. These descriptions consist of three components: kinematic and dynamic equations for the motion of the ship, sea waves, and complex navigational situations, as determined by the number of ships passed and the visibility at sea.

Kula [11], Liu [17] and Nise [19] show how a wide variety of models have different impacts on the synthesis of various control algorithms and the impact of safe ship motion controls.

The aim of this article is to show that it is possible to determine the single best solution from the many possible alternatives for calculating the safe trajectory of a ship, i.e. the one that ensures the least loss of the way to the safe passing of the encountered ships.

COMPUTER SIMULATION OF A NEURO-OPTIMAL SAFE TRAJECTORY THAT TAKES ACCOUNT OF NAVIGATOR SUBJECTIVITY

Over 80% of ship collisions are caused by human factors arising from subjective assessments of navigational situations and manoeuvring decisions. It is estimated that about half of these losses could be avoided by using computer programmes to support manoeuvring decisions by the navigator, based on AI, game theory and optimisation methods. When educating students as future officers for sea-going vessels, computer simulations or programmes should be included that take into consideration both the subjectivity of the navigator when making the final manoeuvring decision and the characteristics of the real and often complex navigational situation at sea.

The basic criterion used to ensure the quality of ship steering is the safe movement of ships within a given area, and this is considered by the simulation algorithm in the form of limitations on the state of the steering process. Optimisation of this control task is achieved by minimising the changes needed to the cruise route in order to safely pass all encountered ships. Since most anti-collision manoeuvres are performed in practice by changing the course while maintaining a constant speed, this task is reduced to one of time-optimal control.

Hongguang and Yong [9] illustrate the danger of ship collisions, and show that it is possible to assign certain areas to each ship in the form of domains. These domains may have fixed or variable shapes depending on the collisional

risk, and an artificial neural network implemented in Matlab software can be used to generate these. Figure 2 shows four types of ship domains, for which values are assigned based on the dimensions and speed of the ship and the safe distance at which other ships should be passed under real visibility conditions at sea.

As described in [9], the domains used for the ships may be in the form of a circle, a hexagon, an ellipse or a parabola; the choice depends on the relative speed of other passing ships, and can be changed based on the responses from an appropriately designed neural network that assesses the level of collision risk.

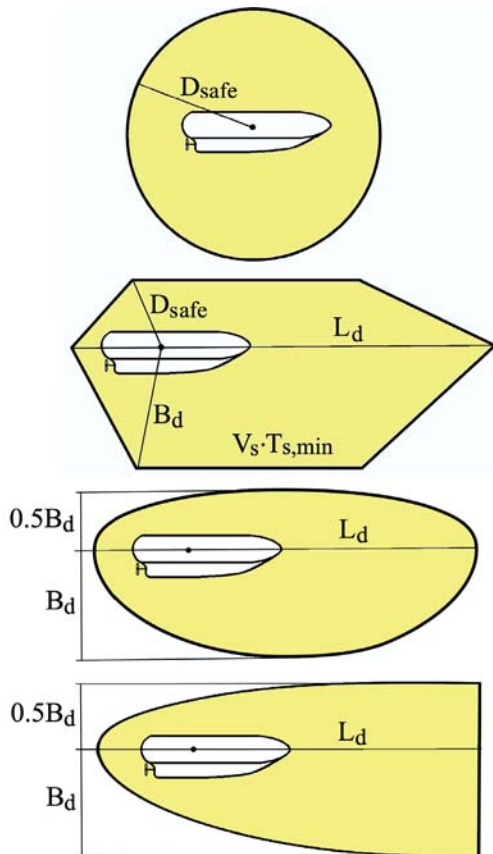


Fig. 2. Shapes of neural encountered ships domains: D_{safe} - safe distance, B_d - dynamic length of the ship, L_d - dynamic beam of the ship, V_s - speed of met s ship, $T_{s,min}$ - minimum time to approach with s met ship.

The neural network is characterised by six input quantities \mathbf{u} that describe the current collision situation, and which are gathered from measuring devices such as radar, logs, and gyrocompasses. These are combined to form a single output quantity \mathbf{r} that represents the risk of collision:

$$\mathbf{r} = A[W\mathbf{u}] \quad (1)$$

$$\mathbf{u} = [D_j, N_j, V_j, \psi_j, V, \psi] \quad (2)$$

$$\mathbf{r} = \left\{ \begin{array}{l} 0.1 \rightarrow \text{safe situation} \\ 0.3 \rightarrow \text{attention} \\ 0.5 \rightarrow \text{collision risk} \\ 0.7 \rightarrow \text{dangerous situation} \\ 0.9 \rightarrow \text{collision} \end{array} \right\} \quad (3)$$

This leads to the following equation:

$$I^* = \min_A \Sigma(r_i - r_{ei})^2 \quad (4)$$

where A are the activation functions of the neural network layers; r_i and r_{ei} are the real and expected network responses; Σ is a mathematical measurement of the neural network learning processes; and i is the time parameter.

Figure 3 shows the structure of a neural network with three layers: the input and hidden layers have activation functions with a digressional nature and the output layers have sigmoidal activation functions.

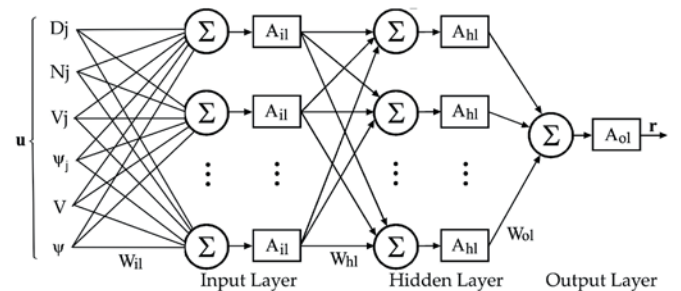


Fig. 3. Neural network for generating ship domains: W_{il} - weight factors of the input layer; W_{hl} - weight factors of the hidden layer; W_{ol} - weight factors of the output layer; A_{il} - activation functions of the input layer; A_{hl} - activation functions of the hidden layer; A_{ol} - activation function of the output layer.

When mapping current navigational situations using a neural network, a backpropagation error algorithm with comprehensive learning and moment indicators is used. The data needed for this learning process were prepared using an ARPA system simulator by 285 navigators.

The ship's dynamics can be described by the state equations in discrete form:

$$\left. \begin{array}{l} \dot{x}_{i+1}^0 = x_i^0 + V_i \Delta t_{i+1} \sin \psi_i \\ \dot{y}_{i+1}^0 = y_i^0 + V_i \Delta t_{i+1} \cos \psi_i \\ \dot{\psi}_{i+1} = \psi_i + \dot{\psi}_i \Delta t_{i+1} \\ \dot{\dot{\psi}}_{i+1} = \dot{\psi}_i + \frac{1}{T_1} (-\dot{\psi}_i - k_1 \dot{\psi}_i^2 + k_2 \alpha_i) \Delta t_{i+1} \\ \dot{V}_{i+1} = V_i + \dot{V}_i \Delta t_{i+1} \\ \dot{\dot{V}}_{i+1} = \dot{V}_i + \frac{1}{T_2 T_3} [-(T_2 + T_3) \dot{V}_i - V_i + k_3 n_i] \Delta t_{i+1} \end{array} \right\} \quad (5)$$

where:

(x^0, y^0) are the coordinates of the ship's position, ψ is the ship's course, $\dot{\psi}$ is the angular turning speed, $\dot{\dot{\psi}}$ is the angular acceleration of the ship, V is the ship's speed, \dot{V} is its acceleration, $\dot{\dot{V}}$ is the change in the acceleration, α is

the rudder angle, n is the rotational speed of the screw propeller, (k_1, k_2, k_3) are proportionality parameters, and (T_1, T_2, T_3) are the time parameters of the dynamic model.

Determining the optimal route for the ship can be treated as a multi-stage decision-making process, and can be solved using Bellman's dynamic programming method. We use a quality criterion Q , which represents the smallest extension to the voyage route that is necessary to safely pass encountered ships, leading to time-optimal steering while matching the speed of the other ships:

$$Q(\alpha, n) = \int_0^{t_K} V dt \cong V \int_0^{t_K} dt = Q_{min} \quad (6)$$

Bellman's method defines the principle of optimality, stating the optimal strategy characterises that whatever the initial state or steering may be, the remaining controls must form the optimal strategy from the point of view of the state resulting from the first control:

$$Q_{min,k} = \left\{ \begin{array}{l} Q_{min,k-1} [x_k^0, y_k^0, \psi_{k-1}, \dot{\psi}_{k-1}, V_{k-1}, \dot{V}_{k-1}] + \\ x_k^0, y_k^0, x_{k+1}^0 \left(\begin{array}{l} \psi_{k-1}, \dot{\psi}_{k-1} \\ \dot{\psi}_{k-2}, \alpha_{k-2}, \Delta t_{k-2} \end{array} \right), \Delta t_{k-1} \\ y_{k+1}^0 \left(\begin{array}{l} \psi_{k-1}, \dot{\psi}_{k-1} (\dot{\psi}_{k-2}, \alpha_{k-2}, \Delta t_{k-2}, \Delta t_{k-1}) \\ V_k (V_{k-1}, \dot{V}_{k-1} (\dot{V}_{k-2}, n_{k-2}, \Delta t_{k-2}), \Delta t_{k-1}) \end{array} \right) \end{array} \right\} \quad (7)$$

$k = 3, 4, \dots, K$

The time required to reach the k -th stage can be determined as follows:

$$\Delta t_k = \frac{\Delta s_k(x_k^0, y_k^0, x_{k+1}^0, y_{k+1}^0)}{V_k} \quad (8)$$

It results from this how calculations utilising this strategy are typically started from the last stage, and afterwards the procedure goes towards the first. According to Bellman's theorem [2], the collision avoidance procedure meets the conditions of duality, and according to this principle, the optimal trajectory for a ship in a collision situation can also be determined using the optimisation principle, starting with the calculation of the first stage before coordinated towards the last stage, as illustrated in Figure 4.

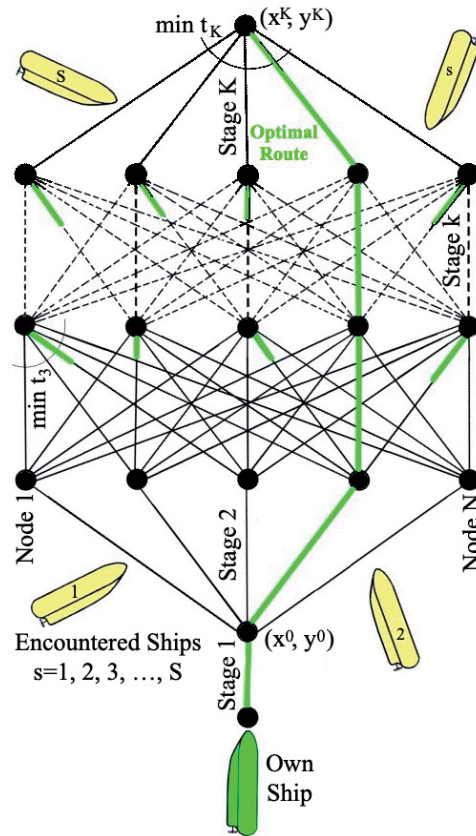


Fig. 4. Multi-stage decision-making process involving dynamic programming of the optimal voyage route, in which the domains of passed ships are mapped.

The navigation situation in Kattegat Strait is shown in Figure 5, and was used in simulation tests of the safe ship control algorithm, as recorded in the ARPA anti-collision system and installed on the research-training vessel.

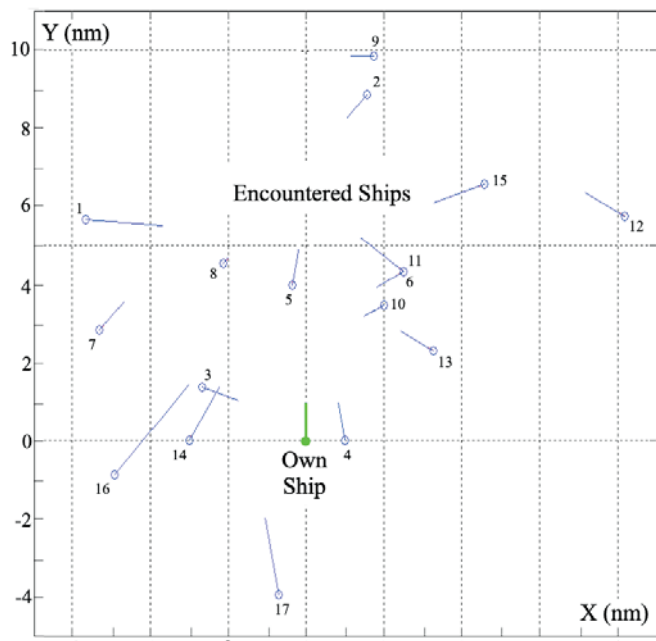


Fig. 5. Navigational situation affecting the movement of a ship between seventeen passing vessels.

Figures 6 and 7 show the neuro-optimal safe trajectories for ships under conditions of good and restricted visibility, which were processed using a programme implemented in Matlab.

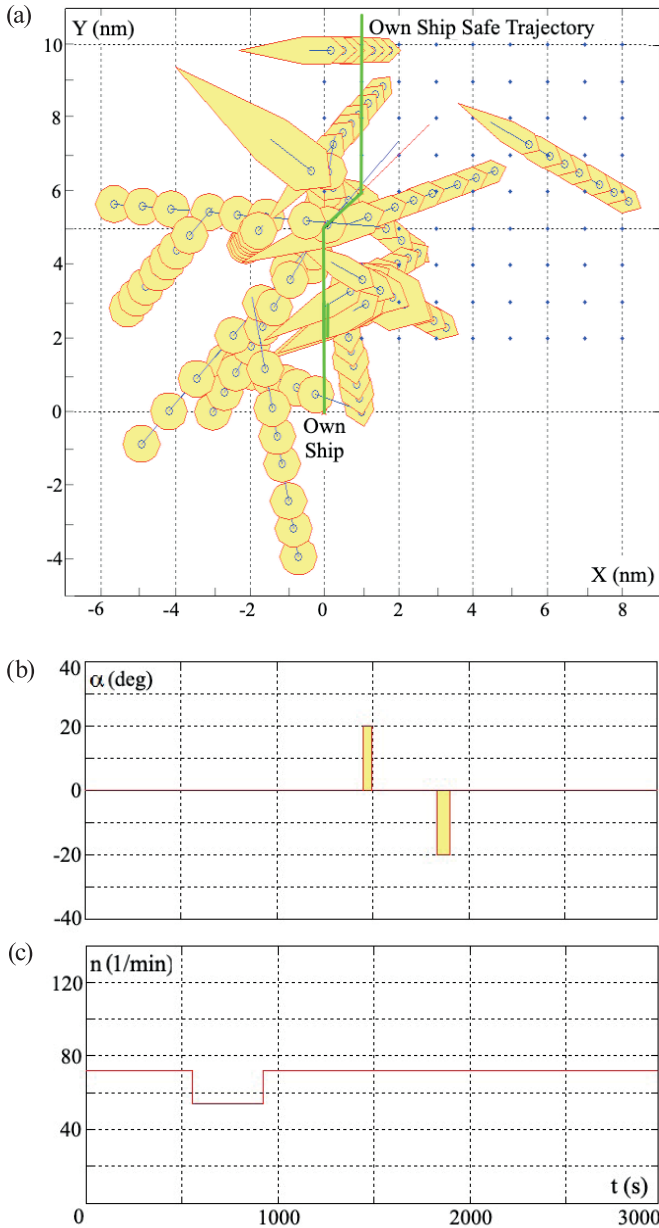


Figure 6. Results of a computer simulation of the neuro-optimal safety of a ship's trajectory and control sequence under good visibility conditions at sea for $D_s = 0.5$ nm, with circular and hexagonal domains, $Q_{min} = 2678$ s: (a) - safe trajectory of own ship, (b) - changes in the rudder angle, (c) - changes in the rotational speed of the propeller.

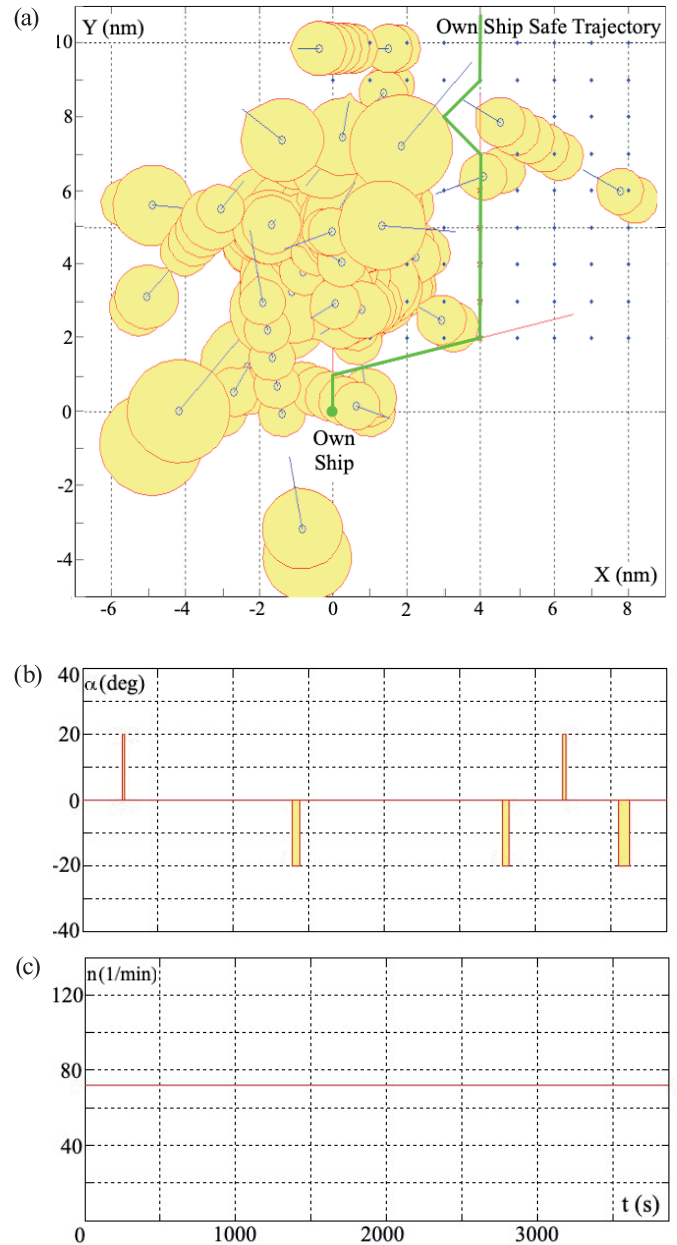


Figure 7. Computer simulation results for the neuro-optimal safety of a ship's trajectory and control sequence under conditions of restricted visibility at sea for $D_s = 1.5$ nm, with circular domains, $Q_{min} = 4033$ s: (a) - safe trajectory of own ship, (b) - changes in the rudder angle, (c) - changes in the rotational speed of the propeller.

COMPUTER SIMULATION OF A GAME-OPTIMAL SAFE TRAJECTORY THAT CONSIDERS THE UNCERTAINTY IN THE NAVIGATIONAL SITUATION

According to Lisowski [15], Song [23], Szlapczynska et al. [25] and Wang [26], the definition of the collision avoidance problem may be obvious, ignoring data sensitivity which may result from external elements dictated by climatic conditions and the state of the ocean, insufficient knowledge concerning other ships and imprecise proposals of international conflict of law rules (COLREGs).

The first approach, which involves using the theory of differential games in steering as described by Reddy et al. [21], allows for control of the ship to be considered under conditions of uncertainty in navigational situations.

Single procedure models have been helpful in training students as future seagoing officers and allowing for the selection of algorithms for safe ship control in collision situations. For the practical synthesis of control algorithms, the positional and matrix game models presented by Sanchez-Soriano [22] can be used.

The model that is closest to real situations is the matrix game model, which uses a risk matrix of ship collisions to identify various manoeuvring strategies in terms of changing courses or speeds.

The control variables of the ship are represented by the course ψ and the speed V , while for s met ship by course ψ_s and speed V_s . The state variables for the ship are represented by the risk of collision r_s , while for the met ship by distance D_s and bearing N_s .

The risk of collision with the s -th ship encountered, r_s , is a relative assessment of the current situation of the approach characterised by the quantities $D_{s,min}$ and $T_{s,min}$, compared to the expected safe situation characterised by the previously adopted safe values of D_{safe} and T_{safe} .

In most real control processes, the matrix game does not reach the saddle point, and does not guarantee balance when used in pure object strategies. The approximate solution of the real game, according to Osborne [20], constitutes a component of the mixed strategy, which expresses the probability distribution p_s of the players' pure strategies.

The optimal game control of the ship is the strategy of the highest probability to use is as follows:

$$u_{0,opt} = u_0 \left[\left(p_s^{(\sigma_0, \sigma_s)} \right)_{max} \right] \quad (9)$$

where:

σ_0 – single strategies for controlling the ship's movement to avoid collisions; in game theory, these are called 'pure strategies',

σ_s – single strategies for controlling the movement of the s -th ship that is cooperating to avoid collisions or scenarios leading to collisions for various reasons; in game theory, these are called 'pure strategies'.

In a non-cooperative game, the quality index Q for optimal ship control can be formulated as follows:

$$Q^{n-c}(\sigma_0, \sigma_s) = \min_{\sigma_0} \max_{\sigma_s} p_s(\sigma_0, \sigma_s) \quad (10)$$

However, in a cooperative game, this can be expressed as follows:

$$Q^c(\sigma_0, \sigma_s) = \min_{\sigma_0} \min_{\sigma_s} p_s(\sigma_0, \sigma_s) \quad (11)$$

Our computer simulation of cooperative and non-cooperative game control algorithms was implemented in Matlab for the navigational situation illustrated in Figure 5.

Figures 8 and 9 show the optimal safe voyage routes under good and restricted shipping conditions, respectively, for cooperation and no cooperation between ships in terms of avoiding collisions.

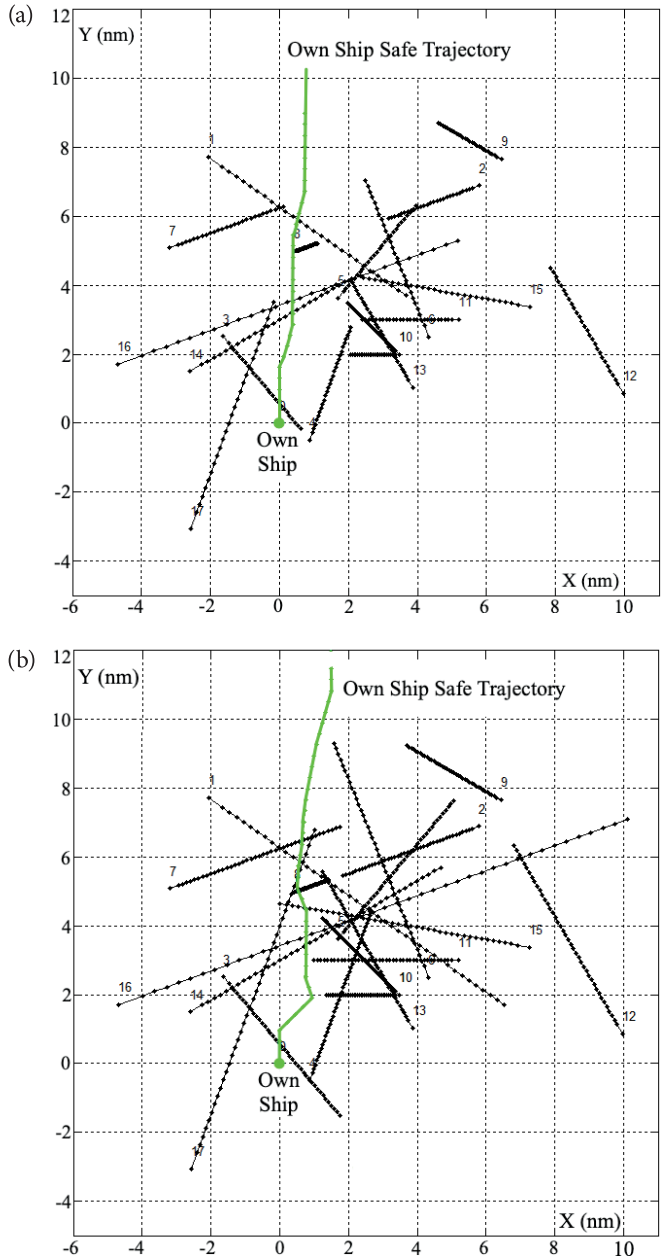


Fig. 8. Game-optimal safe ship trajectories in a computer simulation of navigational in good shipping conditions for $D_s = 0.5$ nm: (a) in a cooperative matrix game, $Q_{min} = 3312$ s; and (b) in a non-cooperative matrix game, $Q_{min} = 3660$ s.

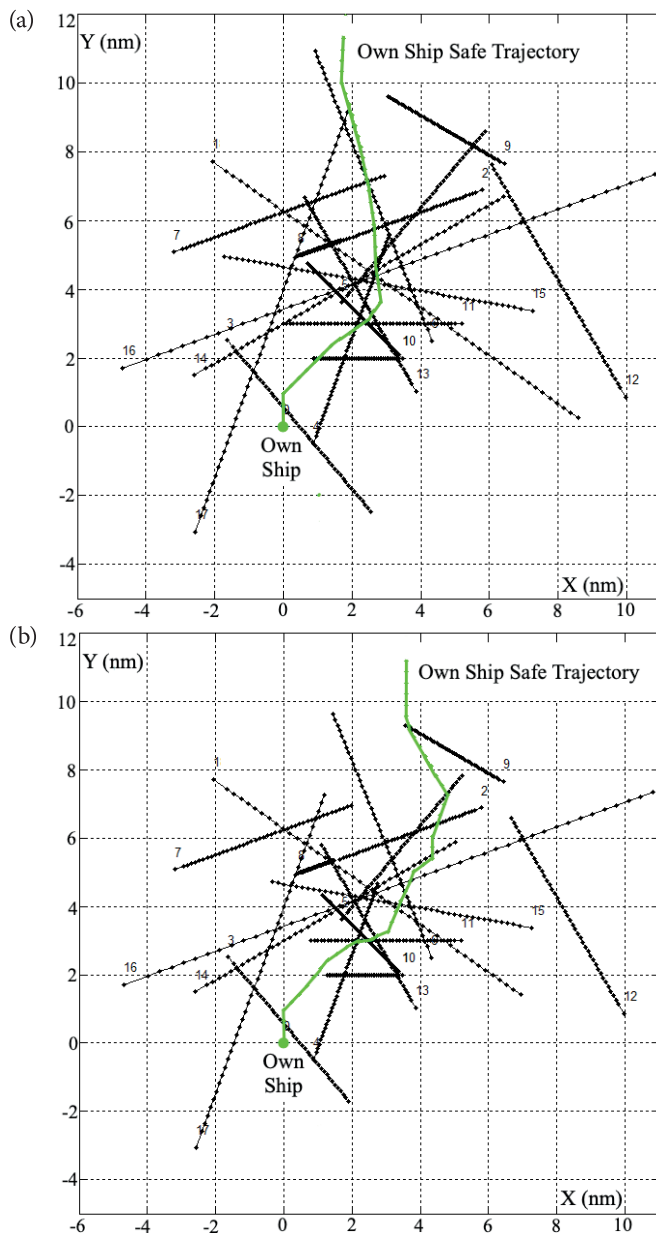


Fig. 9. Game-optimal safe ship trajectories in a computer simulation of navigation with restricted shipping conditions for $D_s = 1.5$ nm: (a) in a cooperative matrix game, $Q_{min} = 3990$ s; and (b) in a non-cooperative matrix game, $Q_{min} = 4896$ s.

CONCLUSIONS

An analysis of our research results in an effort to determine a safe and optimal route for a ship based on the use of selected computational intelligence methods allows us to draw the following conclusions.

In terms of calculating the neuro-optimal safe trajectory, the use of ARPA radar to identify object movement parameters allowed us to develop an algorithm to support the navigator in determining a safe trajectory, as a sequence of changes in the course and speed of the ship. Representing the movements of encountered ships in the form of moving

neural domains of variable size, depending on the distance and time between approaching ships, allowed us to take into account the subjectivity of the navigator when assessing the risk of collision. The use of several hundred navigator officers to teach an artificial neural network allowed the computational algorithm to interpret the domain in which there is a danger of encountering ships better than if only a single experienced navigator had been used. An analysis of the possible domain shapes shows that they can be adapted to open or restricted waters. The node density in the dynamic programming trajectory of the ship is a compromise between calculation time and ship-route accuracy.

When calculating the game-optimal safe trajectory, our algorithm takes into account both the COLREG rules when starting the game and the dynamics of the ships, in the form of the advance manoeuvring time, their degree of cooperation and the end game when the risk of collision becomes zero. A new definition of ship collision risk was also presented here based on two assessments of the same navigational situation: the real situation regarding the proximity of objects, and the safe situation as determined by the reference parameters.

This work does not cover all of the issues associated with the safe management of the movement of ships at sea. Subsequent studies will include an analysis of the sensitivity of safe ship control to inaccurate information from navigation devices, changes in the parameters of the ship dynamics, and the impact of hydrometeorological disturbances.

Future papers on computational intelligence in marine control engineering education should focus on additional groups of ship officers, such as mechanics and electricians.

ACKNOWLEDGEMENTS

This research was funded as part of a research project in the Marine Electrical Engineering Faculty, Gdynia Maritime University, Poland, No. WE/2021/PZ/02, entitled “Control theory and artificial intelligence techniques in optimal and safe ship operation”.

REFERENCES

1. J.H. Ahn, K.P. Rhee, and Y.J. You, “A study on the collision avoidance of a ship using neural networks and fuzzy logic,” *Applied Ocean Research*, vol. 37, pp. 162–173, 2012. DOI: 10.1016/j.apor.2012.05.008
2. R.E. Bellman, *Dynamic Programming*. New York: Dover Publications, 2003. ISBN 0-486-42809-5
3. M. Borrego, E.P. Douglas, and C.T. Amelink, “Quantitative, “Qualitative and mixed research methods in engineering education,” *Journal of Engineering Education*, vol. 98, no. 1, pp. 53–66, 2009. DOI: 10.1002/j.2168-9830.2009.tb01005.x
4. R. Cwilewicz and J. Lisowski, “The integrated maritime education and research activity of Gdynia Maritime

- University,” in *12th Annual General Assembly of IAMU - Green Ships, Eco Shipping, Clean Seas*, Gdynia Maritime University, Gdynia, 17 June 2011, pp. 87–98.
5. B. Guenin, J. Konemann, and L.A. Tuncel, *Gentle Introduction to Optimization*. Cambridge, UK: Cambridge University Press, 2014. ISBN 978-1-107-05344-1
 6. S.S. Guzey and M. Aranda, “Student participation in engineering practices and discourse: An exploratory case study,” *Journal of Engineering Education*, vol. 106, no. 4, pp. 585–606, 2017. DOI: 10.1002/jee.20176
 7. H. Heiselberg and A. Stateczny, “Remote sensing in vessel detection and navigation,” *Sensors*, vol. 20, pp. 1–9, 2020. DOI: 10.3390/s20205841
 8. M. Henri, M.D. Johnson, and B. Nepal, “A review of competency-based learning: Tools, assessments, and recommendations,” *Journal of Engineering Education*, vol. 106, no. 4, pp. 607–638, 2017. DOI: 10.1002/jee.20180
 9. L. Hongguang and Y. Yong, “COLREGS-constrained real-time path planning for autonomous ships using modified artificial potential fields,” *Journal of Navigation*, vol. 71, pp. 1–21, 2018. DOI: 10.1017/S0373463318000796
 10. Y. Huang, L. Chen, P. Chen, R.R. Negenborn, and P.H.A.J.M. van Gelder, “Ship collision avoidance methods: State-of-the-art,” *Safety Science*, vol. 121, pp. 451–473, 2020. DOI: 10.1016/j.ssci.2019.09.018
 11. K.S. Kula, “Automatic control of ship motion conducting search in open waters,” *Polish Maritime Research*, vol. 27, no. 4, pp. 157–169, 2020. DOI: 10.2478/pomr-2020-0076
 12. L.R. Lattuca, D.B. Knight, H.K. Ro, and B.J. Novoselich, “Supporting the development of engineers’ interdisciplinary competence,” *Journal of Engineering Education*, vol. 106, no. 1, pp. 71–97, 2017. DOI: 10.1002/jee.20155
 13. A. Lazarowska, “Comparison of discrete artificial potential field algorithm and wave-front algorithm for autonomous ship trajectory planning,” *IEEE Access*, vol. 8, pp. 221013–221026, 2020. DOI: 10.1109/ACCESS.2020.3043539
 14. A. Lebkowski, “Evolutionary methods in the management of vessel traffic,” in *Proc. Int. Conf. on Marine Navigation and Safety of Sea Transportation*, Gdynia, Poland, 17 June 2015, pp. 259–266. DOI: 10.12716/1001.12.01.13
 15. J. Lisowski, “Multi-criteria optimization of multi-stage positional game of vessels,” *Polish Maritime Research*, vol. 27, no. 1, pp. 46–52, 2020. DOI: 10.2478/pomr-2020-0005
 16. Z. Liu, Z. Wu, and Z. Zheng, “A cooperative game approach for assessing the collision risk in multi-vessel encountering,” *Ocean Engineering*, vol. 187, pp. 1–12, 2019. DOI: 10.1016/j.oceaneng.2019.106175
 17. Z. Liu, “Pre-filtered backstepping control for underactuated ship path following,” *Polish Maritime Research*, vol. 26, no. 2, pp. 68–75, 2019. DOI: 10.2478/pomr-2019-0026
 18. S. Nikolic, “Improving the laboratory learning experience: A process to train and manage teaching assistants,” *IEEE Transaction on Education*, vol. 58, no. 2, pp.130–139, 2015. DOI: 10.1109/TE.2014.2335712
 19. N.S. Nise, *Control Systems Engineering*. New York: John Wiley & Sons, 2019. ISBN 978-1-119-72140-6
 20. M.J. Osborne, *An Introduction to Game Theory*. New York: Oxford University Press, 2004.
 21. P.V. Reddy and G. Zaccour, “Feedback Nash equilibria in linear-quadratic difference games with constraints,” *IEEE Transactions on Automatic Control*, vol. 62, pp. 590–604, 2016. DOI: 10.1109/TAC.2016.2555879
 22. J. Sanchez-Soriano, “An overview of game theory applications to engineering,” *International Game Theory Review*, vol. 15, pp. 1–18, 2013. DOI: 10.1142/S0219198913400197
 23. L. Song, H. Chen, W. Xiong, et al., “Method of emergency collision avoidance for unmanned surface vehicle (USV) based on motion ability database,” *Polish Maritime Research*, vol. 26, no. 2, pp. 55–67, 2019. DOI: 10.2478/pomr-2019-0025
 24. J.L. Speyer and D.H. Jacobson, *Primer on Optimal Control Theory*. Toronto, Canada: SIAM, 2010. ISBN 978-0-898716-94-8
 25. J. Szlapczynska and R. Szlapczynski, “Preference-based evolutionary multi-objective optimization in ship weather routing,” *Applied Soft Computing*, vol. 84, pp. 1–21, 2019. DOI: 10.1016/j.asoc.2019.105742
 26. S. Wang, Y. Tuo, “Robust trajectory tracking control of underactuated surface vehicles with prescribed performance,” *Polish Maritime Research*, vol. 27, no. 4, pp. 148–156, 2020. DOI: 10.2478/pomr-2020-0075
 27. J. Trevelyan, “Technical coordination in engineering practice,” *Journal of Engineering Education*, vol. 96, no. 3, pp. 191–204, 2007. DOI: 10.1002/j.2168-9830.2007.tb00929.x
 28. H.J. Trussell and E.J. Dietz, “A study of the effect of graded homework in a preparatory math course for electrical engineers,” *Journal of Engineering Education*, vol. 92, no. 2, pp. 141–146, 2003. DOI: 10.1002/j.2168-9830.2003.tb00752.x

29. T.F. Weisner and W. Lan, "Comparison of student learning in physical and simulated unit operations experiments," *Journal of Engineering Education*, vol. 3, no. 3, pp. 5–12, 2004. DOI: 10.1002/2168-9830.2004.tb00806.x
30. A. Witkowska and R. Smierzchalski, "Adaptive dynamic control allocation for dynamic positioning of marine vessel based on backstepping method and sequential quadratic programming," *Ocean Engineering*, vol. 163, pp. 570–582, 2018. DOI: 10.1016/j.oceaneng.2018.05.061
31. J. Yong, *Optimization Theory – A Concise Introduction*. New Jersey: World Scientific, 2018. ISBN 978-981-3237-64-3
32. J. Zhuang, L. Zhang, Z. Qin, et al., "Motion control and collision avoidance algorithms for unmanned surface vehicle swarm in practical maritime environment," *Polish Maritime Research*, vol. 26, no. 1, pp. 107-116, 2019. DOI: 10.2478/pomr-2019-0012

CONTACT WITH THE AUTHOR

Józef Lisowski
e-mail: j.lisowski@we.umg.edu.pl

Uniwersytet Morski w Gdyni,
Morska 83,
81-225 Gdynia,
POLAND